UNIVERSITY OF OKLAHOMA

GRADUATE COLLEGE

PULSE COMPRESSION WAVEFORMS AND APPLICATIONS FOR WEATHER RADAR

A DISSERTATION

SUBMITTED TO THE GRADUATE FACULTY

in partial fulfillment of the requirements for the

Degree of

DOCTOR OF PHILOSOPHY

By

JAMES MICHAEL KURDZO

Norman, Oklahoma

2015

PULSE COMPRESSION WAVEFORMS AND APPLICATIONS FOR WEATHER RADAR

A DISSERTATION APPROVED FOR THE
SCHOOL OF METEOROLOGY

BY

_____
Dr. Robert Palmer, Chair

_____
Dr. Boon Leng Cheong

_____
Dr. Howard Bluestein

_____
Dr. Guifu Zhang

_____
Dr. Joseph Havlicek

Dedication

For my family: Emily, Jim, Kathy, Tim, Susan, Gerry, Scott, and Nathan.

Acknowledgements

I would like to thank my advisors, Dr. Robert Palmer and Dr. Boon Leng Cheong. Their leadership, mentorship, and professionalism have molded me into a capable and articulate scientist. Dr. Palmer, who also served as my M.S. advisor, has been my guide through the entirety of graduate school. He has pushed me to my limits to achieve more than I ever thought possible, and has afforded me as many opportunities as a graduate student could possibly ask for. Dr. Palmer was the number one supporter of my foray into electrical engineering, an opportunity that would not have been possible in this capacity anywhere else. Dr. Cheong has served as an exemplary role model and has provided me a vision for the type of career that I want to someday achieve. His knowledge, skills, and approachability have guided my progress on this degree. Both Dr. Palmer and Dr. Cheong pushed me when it was appropriate, and picked me up when I needed it the most. I would never have gotten to where I am now without the help of these advisors.

I am grateful to my doctoral committee members, Dr. Howard Bluestein, Dr. Guifu Zhang, and Dr. Joseph Havlicek. Dr. Bluestein has provided invaluable guidance on field projects, radar operations, and my sometimes irresponsible speculation regarding tornado theories. Dr. Zhang was instrumental to the original development of our pulse compression techniques and provided thoughtful discussions on comparing our methodologies with other techniques. Dr. Havlicek was my first professor in electrical engineering courses, and was a remarkably accepting and understanding guide through a new and, at times, frightening world of mathematics. All off these members provided guidance and support in the best times and the worst.

I am indebted to numerous ARRC, SoM, and ECE faculty, staff, and students. Redmond Kelley, John Meier, and Matt McCord have become very close friends of mine, while also serving as some of the most helpful go-to mentors I have had in

my time at OU. Redmond, John, and Matt have provided incredible support with the AIR, PX-1000, and other platforms that were instrumental to my research. They also supported me mentally, as friends, when I needed it the most. Dr. Caleb Fulton, Dr. Tian Yu, and Dr. Alan Shapiro were some of the most important role models that I looked up to at OU. Dr. Fulton reminded me of myself and who I want to be as a professional. Dr. Yu was my interdisciplinary companion who always supported my stretch into electrical engineering. Dr. Shapiro was the most consistent and supportive leader that I had in SoM, and was someone I turned to often in times of need. The ARRC/SoM staff, Jo Ann Mehl, Krysta Bruehl, Lauren White, Kayla Cervi, Kacie Shoemaker, Celia Jones, Nancy Campbell, and Christie Upchurch made my life so much easier than it could have been. Jo Ann and Celia, specifically, were my graduate school "mothers," and bailed me out of trouble numerous times. I am forever grateful to the ARRC and SoM for this assistance and support.

This degree would have been much more difficult without the support of my friends and colleagues in the ARRC, SoM, and ECE. My officemates David Bodine and Feng Nai are two of the most intelligent, hard-working scientists/engineers I have ever had the pleasure to work with. I can not begin to describe the discussions, help, and support provided by these two and what it means to me. I will never forget the friendships forged between us and the support they provided. A number of current and past ARRC and SoM students and scientists provided important discussions that helped me shape my dissertation, and in some cases, my career goals. These helpful people include, but are not limited to, Zach Dunn, Matt Kumjian, Fanxing Kong, Tim Bonin, Vivek Mahale, Bryan Putnam, Derek Stratman, Jen Newman, Blake Allen, Phil Stepanian, Dan Thompson, Andrew Byrd, Andrew Mahre, Javier Lujan, Jon Christian, Blake James, Qing Cao, Lei Lei, Brad Isom, Blake McGuire, Ariel Cohen, Nick Gasperoni, David Gagne, Eric Jacobson, Kyle Thiem, Zach Weinhoff, and

Yadong Wang. Additionally, I owe a lifetime of thanks to my undergraduate advisors at Millersville University, Dr. Richard Clark and Dr. Sepi Yalda. The support and encouragement provided to me by my Millersville professors has been empowering throughout my academic career.

I am grateful to my family for their support and understanding as I spent year after year in school. My parents, Jim and Kathy, never wavered in their support as I pursued my dreams. They were the ones I could talk to every step of the way. Finally, I am in awe of the unfathomable support, encouragement, and love given to me day after day for over a decade by my wonderful wife Emily. It is difficult to put what Emily has meant to me and this process into words. She has been my number one supporter every minute of every day. She picked me up when I was down, brought me back to earth when I needed it, and pushed me constantly to overcome my fears and anxiety. I can not state clearly enough that this degree would have been impossible without my wife by my side. Emily, you are my ultimate role model, the love of my life, and my hero. Thank you so much.

Contents

List Of Tables

List Of Figures

Abstract

The progression of phased array weather observations, research, and planning over the past decade has led to significant advances in development efforts for future weather radar technologies. However, numerous challenges still remain for large-scale deployment. The eventual goal for phased array weather radar technology includes the use of active arrays, where each element would have its own transmit/receive module. This would lead to significant advantages, however, such a design must be capable of utilizing low-power, solid-state transmitters at each element in order to keep costs down. In order to provide acceptable sensitivity, as well as the range resolution needed for weather observations, pulse compression strategies are required. A robust optimization technique for pulse compression waveforms with minimalistic windowing using a genetic algorithm is presented. A continuous nonlinear frequency modulated waveform which takes into account transmitter distortion is shown, both in theory and in practical use. Measured pulses and weather observations from the Advanced Radar Research Center's dual-polarized PX-1000 transportable radar, which utilizes dual 100-W solid-state transmitters, are presented. Development of waveform groups for increased isolation is presented as a proxy for multi-sector array design and spectral savings, and waveforms for convective storm observations and clear air observations during the PECAN project

are discussed. A detailed analysis of the 20 May 2013 Moore, Oklahoma tornado is presented as an example of research-grade quality pulse compression weather data, including the characterization of rear flank gust front surges co-located with debris ejections. A failed occlusion hypothesis is discussed as a possible reason for a looping pattern at the Moore Medical Center. Numerous examples from the Atmospheric Imaging Radar (AIR) convective field program are also presented as examples of pulse compression capabilities. With a 20-deg vertical fan beam, the AIR is capable of volumetrically scanning a storm of interest in under 10 seconds at 1-deg by 1-deg by 30-m spatial resolution, but requires pulse compression for adequate sensitivity due to the wide transmit beam. This technique is used to analyze the tilting characteristics of two major spring 2015 tornadoes as well as other cases since 2012.

Chapter 1

Introduction

The United States of America (USA) is home to the widest array of severe weather impacts on Earth. Its large size and location stretches from nearly sub-tropical regimes, to mid-latitude marine- and continental-based climates, poleward to, at times, arctic landmasses. Due to these vast differences, the USA is subject to floods, droughts, hurricanes, blizzards, tornadoes, hail, wind, and intense lightning. Additionally, many areas of the country can experience nearly all of these types of events in a year, including many combined events in a relatively short period of time. An illustration of the mean number of tornado days per year in the USA based on data from 1980-1999 from Brooks et al. (2003) is presented in Fig. 1.1. Not only are there multiple maxima in number of tornado days, but the coverage of greater than 0.25 days is exceptionally large, covering more than 2/3 of the nation. Each and every type of extreme weather is responsible for multiple deaths annually, and weather and climate combine for an estimated $500B impact on the USA economy alone each year (Lazo et al. 2011). In many cases, a single event has been responsible for tens or even hundreds of billions of dollars in damages and losses (Willoughby

and Black 1996; McTaggart-Cowan et al. 2007). Recent tornadoes, relatively short-term events compared to hurricanes and droughts, have been responsible for up to 162 deaths in a single event (Neblett Fanfair et al. 2012; Kanti Paul and Stimers 2014), while recent hurricanes, relatively long-term events, have been responsible for upwards of 1,800 deaths in a single event (Schmidlin 2006).

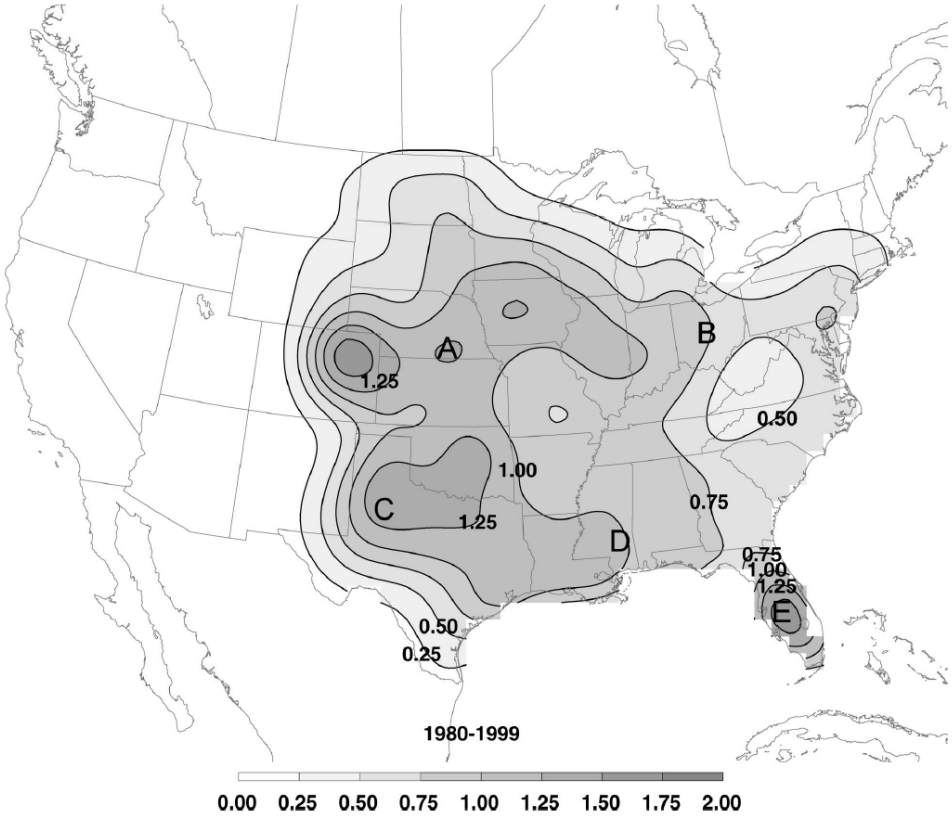

Figure 1.1: *Mean number of tornado days per year in the USA based on data from 1980-1999. Image is from Brooks et al. (2003).*

Especially with climate models predicting more common (and in some cases, stronger) extreme weather across the nation (Shein 2006), the importance of a national forecasting and warning center is becoming more and more critical (Friday 1994). The National Weather Service (NWS), originally the United States Weather Bureau, was first developed in 1870 as part of a strategy to mitigate losses to life and property, providing forecasts, watches, and warnings to the nation's growing population. In the 145 years since the inception of the NWS concept, the agency has grown to include forecasts and warnings for aviation, oceans, fire hazards, space weather, and climate prediction in addition to its traditional tropospheric forecasting responsibilities. The NWS is also responsible for upper air observations and modeling of the atmosphere, as well as the maintenance and operation of the nation's fleet of weather radars. These capabilities make the NWS uniquely capable to provide specialized forecasts and warnings to the nation.

One of the most high-impact, costly, and deadly weather events that the USA faces each year is tornadoes (Bradford 2001). Unfortunately, our knowledge of tornado formation ("tornadogenesis") and tornadic dissipation lags behind our knowledge of many other more commonly observed weather phenomena (Markowski and Richardson 2014). This is due to many reasons; first, tornadoes do not happen very often, leaving a very small dataset relative to

events such as snow storms, ordinary thunderstorms, and even supercells. Second, our observations of tornadoes generally lack in low-level wind field data due to the sparseness of our observations. As is discussed in the following paragraphs, even 159 weather radars across the vast size of the USA is not a high enough density to observe low-level characteristics of severe storms on a wide scale. Finally, it is always desirable to have the highest possible temporal and spatial resolutions. With volumetric update rates as poor as 4 minutes or more, it is impossible to routinely observe the complex evolution of a budding supercell to a strong mesocyclone to tornadogenesis and dissipation on the timescales necessary for enhanced understanding. For these reasons, our tornado warning lead time still hovers around 14 min, with many cases being much lower or even non-existent (Simmons and Sutter 2008).

While increasing tornado warning lead time is an important goal for the NWS, another key aspect to the future of meteorology is the concept of Warn-on-Forecast (WoF). Currently, severe thunderstorm warnings are issued only after storms have formed and are approaching severe criteria. In many cases, tornado warnings are not issued until after storm spotters have already reported a tornado on the ground. WoF aims to utilize high-resolution, rapid-update mesoscale models to predict severe weather at a high enough confidence level for forecasters to issue warnings long before a storm becomes severe (Stensrud et al. 2009). In some cases, it is believed that the WoF concept may be capable

of allowing forecasters to issue tornado warnings *hours* in advance (i.e., before storms have even formed). As part of the WoF effort, the mesoscale models used require very high resolution and rapidly updating low-level wind field data. A radar network capable of providing nationwide coverage at sub-1 km height levels would be an important tool for such a method.

As a method for providing the necessary information for the understanding of tornadoes and other atmospheric phenomena, the theory of radio detection and ranging (radar) has been used for over a century to detect, observe, and analyze fixed objects, moving/airborne targets, and volumetric targets such as weather (Skolnik 2002). Through the transmission of electromagnetic energy from an antenna-based source, absorbed and re-scattered energy by targets are detected by either a co-located or separated antenna and receiver for ranging, location, velocity, and other purposes. For nearly 80 years, this methodology has been used for weather observations in the USA (Watson Jr. 2009). Weather radars were first used in World War II, and beginning in the 1950s, meteorologists in the USA used radar systems to detect thunderstorms, hurricanes, and flash flooding. The first national weather radar network in the USA, the Weather Surveillance Radar 1957 (WSR-57) provided power returns to the user, allowing for the identification of storm cells before impact on major population centers (Rockney 1958; Whiton et al. 1998).

In the mid-1970s, the Weather Surveillance Radar 1974 (WSR-57) was deployed across the USA to augment and eventually replace the WSR-57 network. By 1985, a total of 83 WSR-57 radars were in operation across the nation, along with a sizable number of pre-existing WSR-57 systems, making for the largest weather radar network in the world (Whiton et al. 1998). By the early 1980s, the benefits of Doppler radial velocity estimates had become abundantly clear to the nation as a useful tool for detecting and warning for severe convective storms such as tornadoes (Brown et al. 1978) and microbursts (Wilson et al. 1984; Wolfson et al. 1994). The Weather Surveillance Radar 1988 Doppler (WSR-88D) was developed as a the next full-scale weather radar network for the USA, and by 1997, 159 Doppler radars covered the USA (Crum and Alberty 1993). The current WSR-88D coverage at 3-km height and below across the nation is shown in Fig. 1.2. These radars operate at S band (10-cm wavelength), providing large-scale coverage for weather observation, forecasting, and warning across the USA.

In the early 2000s, the benefits of polarimetric weather estimates began to take hold in the research community, creating a push to upgrade the nation's weather radars (Zahrai and Zrnić 1993; Doviak et al. 2000). In addition to the standard horizontal reflectivity factor (Z_{HH}), radial velocity (v_r), and spectrum width (W) moments, polarimetric capabilities for weather radar allowed for

estimates of differential reflectivity (Z_{DR}), correlation coefficient (ρ_{HV}), and differential phase (ϕ_{DP}).

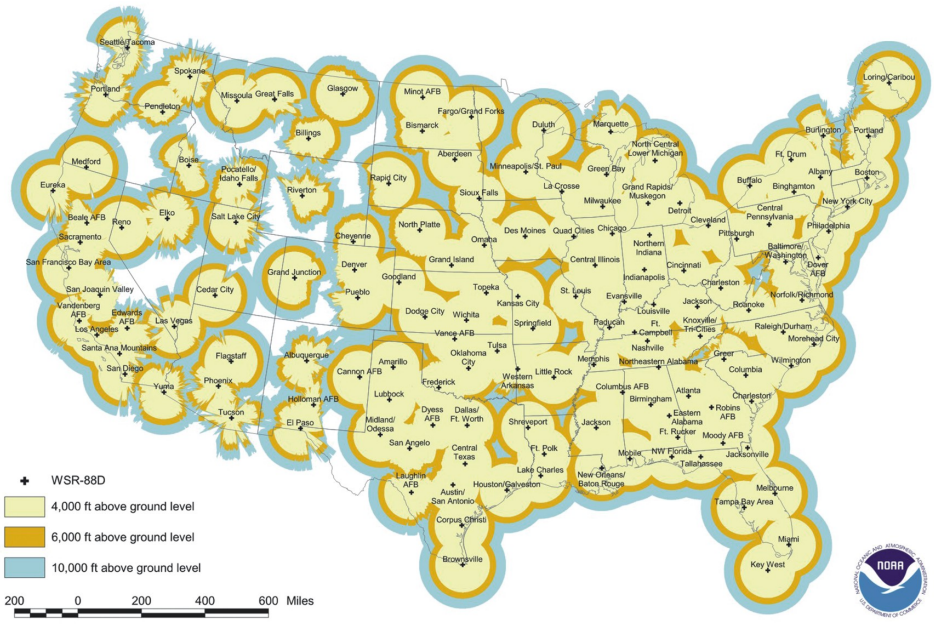

Figure 1.2: *Current WSR-88D coverage at 4,000, 6,000, and 10,000 ft above ground level (in yellow, gold, and blue shadings, respectively). Calculations are based on the radar beam height approximation in Doviak and Zrnić (1993), and the image was provided by the National Oceanic and Atmospheric Administration (NOAA).*

These added moment estimates allow for better hydrometeor classification (Bringi and Chandrasekar 2001; Park et al. 2009), including rain rates (Ryzhkov et al. 2005a), drop size distribution (Brandes et al. 2004b,a; Cao et al. 2010; French et al. 2015), hail detection (Ryzhkov et al. 2002; Kumjian and Ryzhkov 2008), tornadic debris detection (Ryzhkov et al. 2005b; Bodine et al. 2013), and biological scatterer studies (Chilson et al. 2012; Frick et al. 2012; Horton et al. 2015; Stepanian and Horton 2015). These advantages led

to all 159 WSR-88D sites being upgraded to dual-polarimetric capability by 2013 (Crum et al. 2013).

In addition to the WSR-88D network, the FAA operates 45 Terminal Doppler Weather Radar (TDWR) systems at C band (5 cm) for weather and wind shear detection near major airports (Michelson et al. 1990). While the WSR-88D provides base scan updates as fast as every 2 min (with SAILS/AVSET; Crum et al. 2013) and volume updates as fast as 4.2 min (Brown et al. 2000), the TDWR provides base updates every 1 min and volumes every 2.5 min (Vasiloff 2001). Both networks serve as the main identification tools of hazardous weather that can cause danger to life and property, such as severe convective storms, tornadoes, hurricanes, winter weather, and wind shear. The TDWR network is especially useful for the detection of microbursts at major airports, a source of deadly aviation accidents in the past (Fujita and Byers 1977). Additionally, a multitude of research radars across the country operate at S, C, X, Ka, and W bands with varying specifications and missions (e.g., Palmer et al. 2011; Isom et al. 2013; Pazmany et al. 2013; Zhang et al. 2013).

The USA currently employs the use of two other radar networks to cover the missions of air traffic control (the Airport Surveillance Radar (ASR) series; Weber and Stone (1995)) and air route surveillance (Air Route Surveillance Radar (ARSR) series; Taylor and Brunins (1975)). These networks operate at S band and L band (30-cm wavelength), respectively. A map of all USA

radar networks is shown in Fig. 1.3. Operating, maintaining, and upgrading these systems, which total 513 individual radar sites (Weber et al. 2005), is a costly endeavor for the nation. Additionally, despite the nearly constant upgrades which have been installed on the WSR-88D network by the NWS Radar Operations Center (ROC), the WSR-88D network will eventually reach the end of its expected lifetime (Yussouf and Stensrud 2008). This inevitability offers an opportunity to add advanced features as part of a new network, in order to further aid forecasters in the forecast and warning processes.

Due to the desire for cost savings, as well as holistic performance enhancements, the next generation of radar in the USA has been proposed to be a multifunction phased array radar (MPAR) network (Weber et al. 2007). In order to provide the necessary performance characteristics in a next-generation radar network (Zrnić and Doviak 2005; FAA 2012), the MPAR concept is a rapidly evolving area of research in the weather, air traffic control, and air surveillance sectors (Zrnić et al. 2007). Phased array radars operate via electronic beam steering, allowing for rapid sampling without the effects of beam smearing caused by mechanically scanning antennas (Mailloux 2005). Since rapid sampling is of principal concern for a next-generation radar network (Heinselman and Torres 2011), this makes the use of phased arrays appealing for such a system. In order to test this concept, the National Weather Radar Testbed

(NWRT) MPAR, a converted SPY-1A phased array antenna, has been operational for testing next-generation MPAR concepts related to weather (Heinselman et al. 2008), air traffic control (Torres et al. 2013b), and various other areas of research (e.g., Cheong et al. 2008), Curtis (2009), Le et al. (2009).

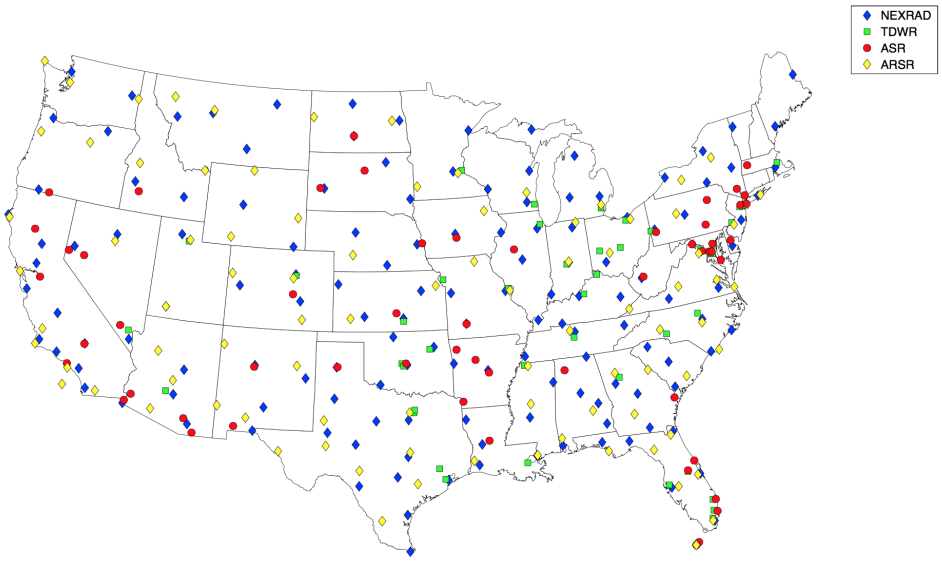

Figure 1.3: *All current NWS/FAA radar sites across the USA, including WSR-88D/NEXRAD, TDWR, ASR, and ARSR radars.*

Over the past decade, testing and development of the NWRT has lead to numerous advances that will be useful in a future MPAR network, however, when the notional functional requirements (FAA 2012) are taken into consideration, it is clear that there are many areas of research that must still be developed. Some of these areas include the implementation of dual-polarized antennas (Zhang et al. 2011), time-based resource management (Miranda et al. 2006; Reinoso-Rondinel et al. 2010), adaptive scanning (Torres et al. 2013a),

and waveform design (Keeler et al. 1999). The development and progress in these areas of research are critical for the success of the MPAR program due to the expected performance that a new national radar network would provide (Doviak 2014). A critical aspect to future radar enhancements is the necessary volumetric weather update rate (<1 min), a significant departure from the current WSR-88D value (>4 min). The desire for rapid updates stems primarily from the enhanced observation, warning, and research capabilities related to weather, with a specific focus on severe convective storms (Carbone et al. 1985; Palmer et al. 2011; Bluestein et al. 2010; Nai et al. 2013). Additionally, the update needs of air traffic control (ATC) operators, for terminal aircraft (5 s) and weather tracking (1 min at low levels), as well as long-range aircraft surveillance (12 s), must be met at or greater than current system standards.

As research and development of phased array systems and architecture move forward toward the goal of MPAR, a key research area is the inherent low sensitivity in an array of low-power transmit/receive elements. While current WSR-88D systems employ a 750-kW Klystron transmitter, an MPAR system would likely consist of thousands of individual transmit/receive elements co-located with patch antennas that could have power as low as 1-10 W each. The concept of individual transmit/receive elements exists due to the extreme flexibility afforded by a fully digital array (Fulton 2011), allowing eventual applications for digital beamforming (Yu and Palmer 2001; Cheong et al. 2004;

Palmer et al. 2005; Isom et al. 2013; Nai et al. 2013), adaptive nulling (Baird and Rassweiler 1976; Haupt 1997; Chen et al. 2008), and adaptive waveforms (Blunt and Gerlach 2006; Haykin 2007; Gini and Rangaswamy 2008), among others. With thousands of transmitters on a face at S band for the necessary beamwidth, issues such as size, cost, and heat dissipation become very important factors in element peak and average power. For these reasons, even an array of 10,000 individual elements at 10 W peak power would only provide a total peak power of 100 kW without beam pattern weighting, and as low as 50 kW or less with an appropriate beam pattern. This level of power is more than an order of magnitude lower than current WSR-88D systems, making sensitivity a significant issue for MPAR risk mitigation.

A successful MPAR design must be capable of utilizing these low-power, solid-state transmitters at each element in order to keep costs down. In order to provide acceptable sensitivity, a high enough average power must be provided, meaning that a long transmit pulse with a high duty cycle is paramount to the success of MPAR (or any inexpensive weather radar). However, long transmit pulses at a constant frequency, as shown in Chapter 2, result in poor range resolution. Based on the sensitivity levels needed to be recovered, the pulse length relevant for low-powered systems would render a traditional Doppler weather radar useless in terms of resolution. In order to deal with this issue,

pulse compression has been used for decades in military applications, providing acceptable sensitivity while keeping costs down (Cook 1960). Pulse compression typically uses a frequency-modulated pulse in order to decouple pulse length and range resolution, instead determining range resolution based on the bandwidth of the frequency change, or the "chirp."

Pulse compression has yielded a successful and wide-reaching area of research and development in the defense sectors, but is yet to be applied on a broad scale to weather radar (Bucci and Urkowitz 1993; Keeler and Hwang 1995; Mudukutore et al. 1998; Bharadwaj and Chandrasekar 2012). One of the main reasons for this disparity includes concerns regarding sensitivity loss caused by pulse windowing, or amplitude modulation (Kurdzo et al. 2014). While significant recovery of power and acceptable range resolution are possible with traditional pulse compression techniques, the heavy amplitude modulation typically used results in an inherent loss of efficiency, making the allure of extremely low-power transmitters less appealing. Additionally, weather radar systems traditionally operate with lower bandwidth and relatively low range resolution requirements compared with most defense-related radars, meaning that the types of pulse compression waveforms appropriate for the weather radar sector have scarcely been investigated. Finally, although pulse compression is often lumped into the phrase "waveform," the term waveform applies in a holistic sense, and includes numerous other aspects of the

system. These considerations can include scanning strategies, pulse repetition frequency (PRF) differences, and duty cycle decisions, but can even have an effect on post-processing algorithms such as clutter filtering and oversampling techniques. Therefore, the general waveform for a weather radar using pulse compression is a largely undeveloped topic, ripe for development and discovery.

This research presents a robust optimization technique for pulse compression waveforms with minimalistic windowing using a genetic algorithm. A continuous nonlinear frequency modulated pulse is developed, both in theory and in practical use scenarios. The Advanced Radar Research Center's (ARRC) dual-polarized PX-1000 radar, which utilizes dual 200-W solid-state transmitters, is used as a primary testbed for weather measurements. PX-1000 is also used to demonstrate a simple version of pre-distortion, which corrects inherent transmit chain distortions as part of the optimization process. Additionally, the ARRC's Atmospheric Imaging Radar (AIR) is used as a testbed for holistic waveform design, development, and optimization. Despite a 3.5-kW peak power on transmit, the AIR's fan beam architecture and desire for use in extremely chaotic weather scenarios (i.e., observations of tornadoes) make pulse compression and the entirety of the waveform design exceedingly important for proper operation. Both PX-1000 and the AIR are

used to show real-world observations of weather, including stratiform precipitation, convective storms, and tornadoes (Kurdzo et al. 2015a,c). These observations demonstrate not only significant improvement in sensitivity over previous pulse compression methods, but also unequivocally demonstrate the potential for pulse compression waveforms to be used for weather observations, forecasting, and research.

Chapter 2

Fundamentals and Background

2.1 Overview of Radar Fundamentals

2.1.1 Radar Block Diagram

A pulsed Doppler radar system, either for point or volumetric targets, can be broken down into a block diagram that has 8 main parts (Fig. 2.1): a stable local oscillator (STALO), a modulator, a high-gain amplifier, and an antenna make up the transmit chain; and an antenna, a low-noise amplifier, a mixer/filter combination, and a signal processor make up the receive chain. In most fixed monostatic radars, especially for weather observations, the antenna is shared between the transmit and receive chains, requiring a duplexer but saving in cost, size, and complexity. The STALO generates an initial signal, usually at an intermediate frequency, that is "pulsed" by the modulator and amplified by the power amplifier to an appropriate transmit power. The intermediate frequency is typically mixed with an additional frequency stage (not shown) to achieve the desired microwave radio frequency (RF) that is then transmitted through the antenna. A typical high-power weather radar may

transmit on the order of 1 MW peak power in short bursts. These transmit bursts may last on the order of 1-2 μs, followed by roughly 1 ms of "listening" time. This switch between transmitting and receiving in a system that uses a single antenna is achieved via a duplexer that switches the antenna feed between the transmit and receive chains very rapidly.

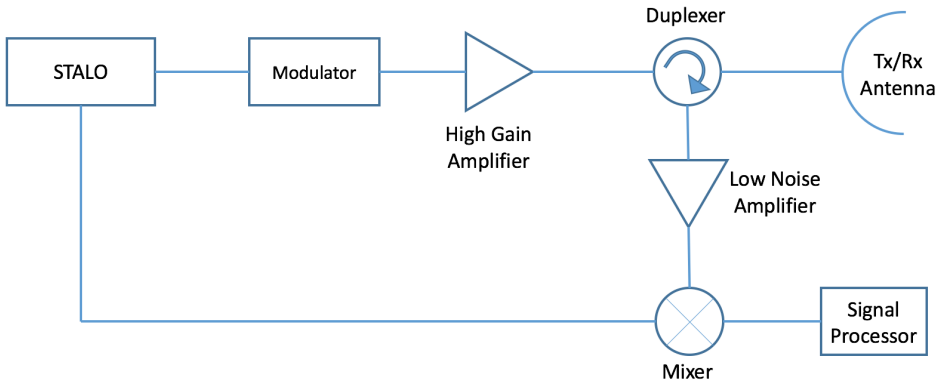

Figure 2.1: *Simple block diagram for a pulsed Doppler radar. The STALO generates a signal that is modulated/pulsed, amplified, and transmitted through the antenna. Received energy is passed through a duplexer in the opposite direction so that it can be received with the same antenna. It is then amplified and mixed with a copy of the STALO signal for filtering. Finally, a signal processor generates moments for the end user.*

After transmission, RF energy travels at close to the speed of light before being absorbed and scattered by targets as far as 500 km in range. A small amount of the scattered energy from these targets, which can be airplanes, vehicles, rain drops, hail, tornadic debris, insects, birds, or even the ground, then returns at close to the speed of light to the radar antenna during the receive

stage. An atmospheric radar must be remarkably sensitive on receive, as return powers can be as low as 10^{-13} W, marking up to a 10^{19} W dynamic range between peak transmit power and minimum receive sensitivity. After reception at the antenna, a low-noise amplifier is used to amplify the received signal for a lower noise floor and to maintain the noise figure. The original intermediate frequency is then mixed with the received signal, providing baseband components of Doppler shift, followed by down-conversion to baseband. The combination of these components allows for the determination of the sign of the Doppler shift along a radial. The signal processor then generates moments from the raw time series data, as well as heavier-processed algorithmic data for display and ingest by other algorithms and users.

2.1.2 Radar Transmitters

Of primary interest to this research is the type of transmitter used in a radar system. A number of transmitter options exist for radars, but four specific types will be detailed here: the magnetron, the klystron, the traveling wave tube (TWT), and solid-state power amplifiers (SSPAs). These transmitters are listed in Table 2.1. The most common transmitter types in use around the world for fixed-site weather radars are magnetrons and klystrons, primarily due to their capability for very high peak transmit powers. In a pulsed Doppler radar, as will be detailed later in this section, a short burst of high

Table 2.1: *Comparison of common transmitter types used in radar systems.*

Transmitter Type	**Peak Power**	**Major Pros**	**Major Cons**
Magnetron	1 MW	High Power, Inexpensive	Spectral Leakage, Random Phase
Klystron	1 MW	High Power, Steady Phase	Large Size, High Cost
Traveling Wave Tube (TWT)	10 kW	Small Size, Steady Phase	Low Power, High Distortion
Solid-State Power Amplifier (SSPA)	100 W	Small Size, Steady Phase, Low Distortion, Inexpensive	Low Power

power is ideal for a traditional radar design. However, these transmitter types have drawbacks as well. Magnetrons tend to leak power across a wide spectrum, a concern for many governments where spectral privileges are in high demand. Additionally, magnetrons have random initial phase, making advanced signal processing and certain polarimetric estimates difficult or impossible to implement. Klystrons address the issue of random phase, but at a substantial cost and increase in size, making them unsuitable for mobile or active array applications.

TWT transmitters are an ideal tradeoff for smaller systems such as mobile radars due to their small size and steady phase, but typically have much lower peak transmit powers than klystrons and magnetrons (possibly as much as two orders of magnitude difference). Additionally, TWTs typically have high distortion rates in amplitude and phase relative to SSPAs, causing difficulty with techniques such as arbitrary waveform generation and distortion correction. Finally, SSPAs provide even smaller size, steady phase, low distortion, and

low cost, but at the penalty of extremely low peak transmit powers on the order of 100s of W (maximum without "stacking"). As will be discussed later in this chapter, there are many positives that SSPAs afford radar engineers and users, but overcoming the very low power is a challenge of great importance to the MPAR mission.

2.1.3 Radar Sampling and Resolution

While some radar systems operate in a continuous and/or bistatic mode (with separate transmit and receive antennas in constant operation), pulsed Doppler radar allows for simple ranging based on the time it takes for the transmitted energy to return to the receiver. This two-way path can be determined via the propagation speed of the electromagnetic wave. However, a pulsed radar results in numerous tradeoffs that must be accounted for in the design of the radar, its waveforms, and its anticipated performance. Of principal concern among these tradeoffs is the Nyquist-Shannon sampling theorem, which states: "If a function $x(t)$ contains no frequencies higher than b hertz, it is completely determined by giving its ordinates at a series of points spaced $1/(2b)$ seconds apart" (Shannon 1949). In short, this theorem indicates that a signal must be sampled at a minimum of $2b$ samples per second in order to resolve the signal properly.

This ties into pulsed Doppler radar in two ways: the maximum unambiguous range and the maximum unambiguous velocity. Both depend on the "sampling rate" of the radar, also known as the pulse repetition frequency (PRF; the inverse of the PRF is also commonly used, and is known as the pulse repetition time, or PRT, T_s). The PRF determines how often the radar sends a pulse. The maximum unambiguous range, or r_a, is determined by the time it takes for the transmitted pulse to travel the maximum range (and return to the radar) before the next pulse is transmitted. This range is represented mathematically by:

$$r_a = \frac{c}{2\text{PRF}} \tag{2.1}$$

where c is the speed of light in m s^{-1}. The maximum unambiguous velocity, or v_a, is determined by the sampling rate of the velocity moment. This sampling rate is also determined by the PRF, and can be represented by:

$$v_a = \frac{\lambda \text{PRF}}{4} \tag{2.2}$$

where λ is the wavelength of the radar center frequency in m. A cursory look at Eqs. (2.1) and (2.2) show that r_a and v_a, which are both desired to be maximized, are inversely proportional when solving for PRF. This result is termed the "Doppler dilemma" and is represented mathematically by:

$$v_a r_a = \frac{c\lambda}{8} \tag{2.3}$$

Although radar waveforms from a pulse-perspective will be detailed in the following subsection, it is important to note that a "waveform" holistically considers the PRF, the transmitted pulse, and all of their respective inter-relations. Therefore, in addition to the PRF, an important aspect of the waveform is the pulse length, or τ. τ is important to the radar in many ways, including the duty cycle, resolution, and sensitivity. Each of these considerations will be detailed in the following paragraphs.

Duty cycle is the relation between pulse length and T_s and represents the percentage of time that the radar is transmitting. Duty cycle is an important consideration in pulsed Doppler radars due to issues such as heat dissipation. Depending on the type of transmitter, as detailed previously, the available duty cycle can range from as low as 0.1% (in *typical* Doppler radar-specified TWTs, for example), to as high as 20% or more (in SSPAs) and even 100% in continuous-wave radars. Given that the chosen T_s for the necessary combination of r_a and v_a is tied to the pulse length via a maximum duty cycle limitation in all radars, and pulse length is tied to sensitivity, it will be shown in later chapters that the entirety of the waveform must be chosen carefully based on the desired goal of the system. These goals can change drastically, even within the realm of meteorological missions (e.g., from stratiform precipitation to tornadic observations).

Resolution along the radial dimension (Δr) is traditionally determined in weather radar systems by the pulse length. As long as a constant frequency is used in the transmit pulse, the range resolution is determined by:

$$\Delta r = \frac{c\tau}{2} \tag{2.4}$$

This relation says that the length of the transmit pulse can be tied to distance based on the speed of light and a two-way trip back to the receiver. For every 1 μs of τ added, the Δr increases by a factor of 150 m. Δr is a measure of the ability for the radar to discern two distinct targets at different ranges. For a given Δr, any targets within that distance cannot be separated in processing, meaning they will appear as one target. Δr determines what radar engineers typically refer to as a "range gate," or the spacing along the radial dimension. An illustration of Δr and the ability to discern targets is shown in Fig. 2.2. Although individual targets are used in the illustration of Fig. 2.2, volumetric targets (e.g., weather) work in the same way; all volumetric targets, such as hydrometeors, in a range gate are summed together for an estimate. One can imagine that, similar to a television or computer screen with poor or "standard definition" resolution, high values of Δr will lead to less information for the radar user, so it is prudent to keep Δr values as small as possible.

Figure 2.2: *Illustration of range resolution in traditional radar (not using pulse compression). Pulse length determines the range gate size. If more than two targets are present in a single range gate, they cannot be discerned and are melded together in the moment estimate. Isolated targets that are separated by range gates are discernible.*

It is also prudent to detail resolution in the azimuthal/elevation dimensions. Due to the desire to get the highest possible resolution in all dimensions, pencil beam antennas are typically used in weather radar systems. The most common way to achieve this effect is through the use of a dish antenna or a planar array for transmit and receive. The azimuthal/elevation dimensions are then determined by the aperture size, or size of the dish/array. A simple relation for 3-dB beamwidth (also known as half-power beamwidth), which represents the cross-radial resolution, is given by:

$$\theta = 1.27\lambda/D \tag{2.5}$$

where θ is the half-power beamwidth and D is the diameter of the aperture in m. While beyond the scope of in-depth discussion for this research, it is important to mention the effects of refraction in the radar beam. Due to refractivity gradients in the atmosphere, the energy transmitted by the radar rarely travels

in a straight line; it typically curves downward (superrefraction) or upward (subrefraction). In addition, the Earth's curvature generally causes the radar "beam" to rise in elevation relative to ground level with increasing distance from the radar. Finally, also due to refractive gradients, the energy transmitted and received by the radar always moves slightly slower than the speed of light. The actual speed is on the order of 2.99703×10^8 m s^{-1} due to the increased time it takes for electromagnetic waves to travel through a denser medium than a vacuum (e.g., the Earth's atmosphere).

2.1.4 Sensitivity and the Radar Equation

Putting all of these pieces together, the radar equation for a point target can be derived. The radar equation is extremely useful for determining sensitivity, or the *minimum* detectable signal. This is important for determining the impact of lower peak transmit power from a SSPA and ways to mitigate the sensitivity loss. The radar equation for a point target can be derived starting with an isotropic radiator:

$$S_i = \frac{P_t}{4\pi r^2} \tag{2.6}$$

where S_i is the incident energy on the target (in W), P_t is the peak transmit power (W m^{-2}), and r is range from the radar to the target (m). The power

received at the target, P_σ (in W) must include the transmit gain, g_t (no units), and the target cross-section, σ (in m^2):

$$P_\sigma = S_i \cdot g_t \cdot \sigma = \frac{P_t g_t \sigma}{4\pi r^2} \tag{2.7}$$

The target absorbs and re-radiates some of the energy isotropically, with a small amount of the energy being scattered back towards the receiver. The power received at the receiver, P_r (in W), must take into account the isotropic re-radiation and the effective aperture of the receiving antenna, A_e (in m^2):

$$P_r = P_\sigma \cdot \frac{1}{4\pi r^2} \cdot A_e = \frac{P_t g_t \sigma}{(4\pi)^2 r^4} \cdot A_e \tag{2.8}$$

where A_e is equivalent to:

$$A_e = \frac{g_r \lambda^2}{4\pi} \tag{2.9}$$

Putting Eqs. (2.8) and (2.9) together and assuming a monostatic system with equal gains, g, a simple radar equation for a point target can be represented as:

$$P_r = \frac{P_t g^2 \lambda^2 \sigma}{(4\pi)^3 r^4 l} \tag{2.10}$$

where l represents additional attenuation and losses, often due to the medium the electromagnetic waves travel through. For volumetric targets, the target

cross-section σ must be broken down in depth. For a volumetric target, σ can be represented as:

$$\sigma = V \sum \sigma_i \tag{2.11}$$

where the resolution volume, V, consists of:

$$V \cong \pi \frac{r\theta}{2} \frac{r\phi}{2} \frac{h}{2} \tag{2.12}$$

where θ is the beamwidth in the azimuthal dimension (in rad), ϕ is the beamwidth in the elevation dimension (in rad), and h is the length of the resolution volume along the radial dimension (in m). Assuming a Gaussian transmit and receive beam, Probert-Jones (1962) showed that V can be represented as:

$$V = \frac{\pi r^2 \theta \phi h}{16 \ln(2)} \tag{2.13}$$

Referring back to Eq. (2.11), the cross-section of a spherical target in the Rayleigh regime, σ_i, was shown by Battan (1973) to be:

$$\sigma_i = \frac{\pi^5 |K_w|^2 D^6}{\lambda^4} \tag{2.14}$$

where K_w is the complex dielectric factor (changeable based on the observation of water or ice; unitless) and D is the diameter of an individual target (in m). Since a volumetric target sums all of the targets in a resolution volume cell, V, the summation in Eq. (2.11) must be applied to Eq. (2.14). All of the

variables are constants except diameter across the resolution volume, so only D must stay within the summation. Combining this with Eqs. 2.11, 2.12, and 2.14, a representation of a volumetric target backscatter cross-section can be shown as:

$$\sigma = \frac{\pi^6 r^2 \theta \phi h |K_w|^2 \sum D^6}{16 \ln(2) \lambda^4} \tag{2.15}$$

The summation of target sizes raised to the sixth power is referred to as radar reflectivity factor, Z, in meteorology. Making this substitution and adding in attenuation and losses, Eq. (2.10) can be expanded for a distributed target as:

$$P_r = \frac{P_t g^2 \pi^3 \sigma \phi h |K_w|^2 Z l}{1024 \ln(2) \lambda^2 r^2} \tag{2.16}$$

A final substitution is made for the radial length of the volume size, h. This size is typically represented by the speed of light, c and the pulse length, τ. This final relation is referred to as the weather radar equation:

$$P_r = \frac{P_t g^2 \pi^3 \sigma \phi c \tau |K_w|^2 Z l}{1024 \ln(2) \lambda^2 r^2} \tag{2.17}$$

2.2 Introduction to Waveforms

2.2.1 Resolution Differences

The principal issue for low-power transmitters such as SSPAs is a lack of sensitivity. According to Eq. (2.17), a limited number of variables can be changed in a system that will provide an increase in sensitivity. If peak transmit power is low, one of these other variables must compensate for the lower sensitivity. The available variables in the radar equation that can be changed are wavelength, antenna gain, and pulse length. Other variables, such as range and target diameter and density, are mission-specific, meaning that for weather, are out of the control of radar designers. Additionally, a change in wavelength is not desirable due to the favorable properties of hydrometeors in X, C, and S bands (especially S band due to the lack of significant attenuation). Gain can always be increased, but at a very high cost due to major antenna design changes. This leaves pulse length as a possible variable to change; however, referring back to Eq. (2.4), increasing pulse length increases the range gate size, drastically decreasing along-radial resolution.

It turns out that Eq. (2.4) is a simplification of the range resolution equation for single-frequency pulsed radar systems, which is by far the most common type of radar system used around the world for weather. This simplification stems from the approximate bandwidth that a short pulse utilizes at a constant modulus. In general, as a pulse becomes shorter/sharper (in the time domain),

its bandwidth increases (in the frequency domain). This is a inverse relationship, meaning that a more appropriate equation for range resolution is:

$$\Delta r = \frac{c}{2B} \tag{2.18}$$

where B is the bandwidth of the pulse (in Hz). The relation described in Eq. (2.4) assumes a constant bandwidth cutoff level, but Eq. (2.18) generally assumes that bandwidth is determined by the change in frequency across the pulse. This is different than is typical in weather radars, which usually use constant modulus, short pulses of high power. In many other types of radars, the frequency changes along the length of the pulse. This frequency change covers some amount of bandwidth that is used in the determination of range resolution in Eq. (2.18), effectively decoupling range resolution from pulse length. In standard short-pulse weather radars, it can be seen from Eqs. 2.4 and 2.18 that time and bandwidth are inversely proportional, or in other words, have a 1:1 ratio. When a frequency modulation is used across the pulse, time and bandwidth no longer require a 1:1 ratio. In this case, a new measure of the pulse is called the time-bandwidth product, or TB product. While TB products of 1 are the norm in most weather radars, TB products larger than one are commonly referred to as “pulse compression” waveforms (Cook 1960).

2.2.2 Pulse Compression and the Matched Filter

Pulse compression is a powerful tool for radar engineers, allowing for longer pulse lengths (for greater sensitivity) and higher range resolution (for higher detail), simultaneously. Although there are tradeoffs that will be discussed later in this section, the relative gain versus loss of using pulse compression is exceptionally high, leading to its use nearly ubiquitously across most military radar platforms. The general premise behind pulse compression is that a frequency change, or "chirp," is performed throughout the length of the pulse. This frequency change can be of any type; linear, nonlinear, stepped, etc. As the pulse encounters targets, the different frequency components glean different information along the pulse. When the pulse returns to the receiver, the frequency components can be compared against each other in order to separate multiple targets within the pulse, subject to the bandwidth restriction in Eq. (2.18). An illustration of different pulse chirp bandwidths with the same pulse length is shown in Fig. 2.3.

Pulse compression works by comparing the received pulse (and hence frequency components) to what was transmitted. This can be thought of as taking a long pulse and "compressing" it into the resolution gleaned from a shorter pulse by comparing frequency components. A critical analysis tool that allows for the study of pulse compression is the matched filter.

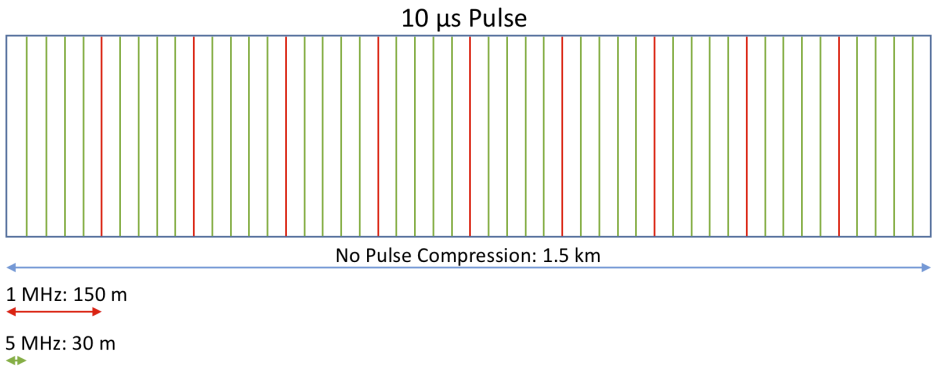

Figure 2.3: *Range resolution illustration for three different long pulses; one with no pulse compression (constant modulus) in blue, resulting in 1.5 km range gate size. The second, in red, uses a 1 MHz chirp, and has a 150 m range gate size. The third, in green, uses a 5 MHz chirp, and has a 30 m range gate size. All use a 10 µs pulse.*

The matched filter allows the radar to compare the reflected energy to a known signal, providing information on the change between the known signal and the target. In essence, the detection of a target is dependent on the signal level from the target relative to the environmental noise. This relation is known as signal-to-noise ratio, or SNR, and is a critical consideration in any radar system. The SNR is desired to be the absolute maximum possible value at all times. Luckily, it can be shown that the matched filter provides the maximum theoretical SNR. This proof (Levanon and Mozeson 2004) begins with a definition for SNR:

$$\left(\frac{S}{N}\right)_{\text{out}} = \frac{|s_o(t_0)|^2}{\overline{n_o^2(t)}} \tag{2.19}$$

where S is signal power, N is noise power, $s_o(t_0)$ is signal output from the matched filter at time zero, and $n_o(t)$ is the noise output from the matched filter. We can define the signal and noise outputs as Fourier transforms between the signal and the frequency response of the matched filter, $H(\omega)$:

$$s_o(t_0) = \frac{1}{2\pi}\int_{-\infty}^{\infty} H(\omega)S(\omega)\exp(j\omega t_0)\mathrm{d}\omega \tag{2.20}$$

$$\overline{n_o^2(t)} = \frac{N_0}{4\pi}\int_{-\infty}^{\infty} |H(\omega)|^2\mathrm{d}\omega \tag{2.21}$$

where $N_0/2$ is a two-sided power spectral density of additive white Gaussian noise. Eqs. 2.20 and 2.21 can be substituted into Eq. (2.19) to yield:

$$\left(\frac{S}{N}\right)_{\text{out}} = \frac{\left|\int_{-\infty}^{\infty} H(\omega)S(\omega)\exp(j\omega t_0)\mathrm{d}\omega\right|^2}{\pi N_0 \int_{-\infty}^{\infty}|H(\omega)|^2\mathrm{d}\omega} \tag{2.22}$$

The Cauchy-Schwarz inequality states that for any two complex signals $A(\omega)$ and $B(\omega)$, the following inequality holds:

$$\left|\int_{-\infty}^{\infty} A(\omega)B(\omega)\mathrm{d}\omega\right| \leq \int_{\infty}^{\infty}|A(\omega)|^2\,\mathrm{d}\omega\int_{\infty}^{\infty}|B(\omega)|^2\,\mathrm{d}\omega \tag{2.23}$$

but only if:

$$A(\omega) = KB^*(\omega) \tag{2.24}$$

where K is an arbitrary constant. $A(\omega)$ can be chosen as:

$$A(\omega) = H(\omega) \tag{2.25}$$

and $B(\omega)$ can be chosen as:

$$B(\omega) = S(\omega)\exp(j\omega t_0) \tag{2.26}$$

Substituting Eqs. 2.25 and 2.26 into Eqs. 2.23 and 2.22:

$$\left(\frac{S}{N}\right)_{\text{out}} \leq \frac{1}{\pi N_0}\int_{\infty}^{\infty} |S(\omega)|^2 \mathrm{d}\omega = \frac{2E}{N_0} \tag{2.27}$$

where E is equal to:

$$E = \int_{-\infty}^{\infty} s^2(t)\mathrm{d}t = \frac{1}{2\pi}\int_{-\infty}^{\infty} S^2(\omega)\mathrm{d}\omega \tag{2.28}$$

Equality of the Cauchy-Schwarz equation in this proof states that:

$$H(\omega) = KS^*(\omega)\exp(-j\omega t_0) \tag{2.29}$$

Taking the inverse Fourier transform of Eq. (2.30) results in the impulse response of the matched filter, or:

$$h(t) = Ks^*(t_0 - t) \tag{2.30}$$

meaning that the impulse response of the matched filter is a time-delayed mirror image of the conjugate of the signal. This says that when the filter is

"matched" to the signal, SNR is maximized. This result is important because not only does the matched filter provide maximum SNR, it also provides an ideal comparison between the transmitted and received energy. While this is optimal for a real-world system, it makes theoretical testing of a pulse compression waveform relatively simple. It can be shown that the convolution between the signal and the matched filter is equal to the signal out of the matched filter (i.e., the definition of convolution is used to obtain filter output):

$$s_o(t) = s(t) \otimes h(t) = \int_{-\infty}^{\infty} s(\tau) s^*(\tau - t) \mathrm{d}t \tag{2.31}$$

where τ and t represent a time-delayed signal. This relation is referred to as the autocorrelation function, or ACF, of a waveform. In theoretical derivations and analysis, a potential waveform signal can be compared directly with itself through autocorrelation to determine performance. This represents the compressed response of the matched filter and greatly simplifies the design process for pulse compression waveforms, as will be seen in Chapter 3.

The ACF provides extremely useful information for waveform design and analysis. Because the autocorrelation of two windowed non-constant-modulus signals results in a sinc function, the ACF readily shows sidelobes in the along-radial dimension. An example of an ACF for a linear frequency modulated (LFM) pulse is shown in Fig. 2.4. Note that the ACF is symmetric, a property that will be discussed during presentation of the ambiguity function later in

this section. The mainlobe (marked in green) is normalized to a peak power of 0 dB, while every lobe beyond the first null is considered a sidelobe. Three key areas that will be discussed in-depth in Chapter 3 are highlighted. The peak sidelobe level is the level of the highest sidelobe, which in this case is the first sidelobe (marked in blue). The integrated sidelobes includes the integration of all sidelobes relative to the mainlobe. The integrated sidelobe power is normalized by the power in the mainlobe. This integration is represented by red markings, but also includes the peak sidelobe in blue. Finally, the mainlobe width, which is the width from null to null marked by the circled arrow, is a critical metric that will be used throughout this research. A more common metric that is rarely used in this research (and is hence not marked) is the 3-dB mainlobe width, which is roughly equivalent to the value described in Eq. (2.18).

A good pulse compression waveform for weather maintains low peak and integrated sidelobes, as well as a thin mainlobe at both null-to-null and 3-dB levels. Another aspect of the pulse compression waveform that has yet to be discussed is the amplitude modulation, or "windowing" of the pulse. While frequency modulation, even relatively simple LFM or stepped frequency changes, provides the ability to drastically improve range resolution in a long pulse, sidelobe levels are generally unacceptably high in these waveforms. This phenomenon can be seen in Fig. 2.4, where the peak sidelobe level of a LFM

pulse is -13.3 dB. As will be shown with volumetric weather data in Chapter 3, sidelobes will artificially "stretch" the target in range, in essence lowering the usable increase in range resolution afforded by frequency modulation. In order to combat this issue, amplitude modulation is used to lower sidelobe levels (note the lower sidelobes in a windowed LFM pulse shown in Fig. 2.5). It is important to note that in Fig. 2.5a and all following figures of waveform I/Q signals, the signals are generated at baseband for aesthetic purposes.

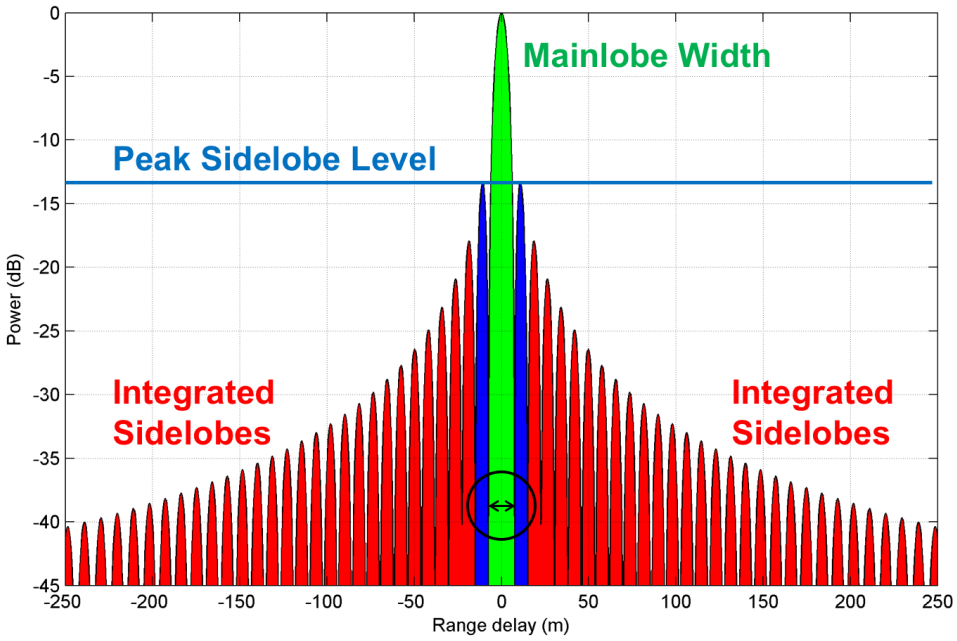

Figure 2.4: *Sample autocorrelation function (ACF). Range (in m) is marked on the abscissa, while power (in dB relative to the peak) is marked on the ordinate. The mainlobe is highlighted in green, the first/peak sidelobe is highlighted in blue, and the integrated sidelobes are highlighted in red (but also include the first "blue" sidelobe). Mainlobe width for the purpose of this research is from null to null.*

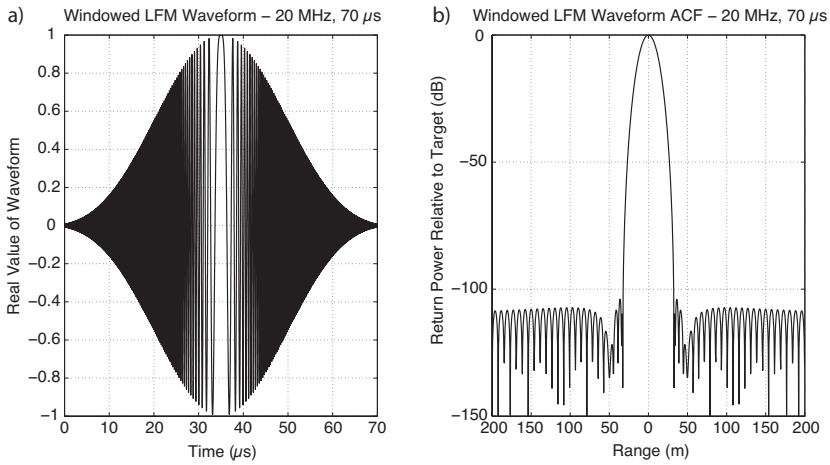

Figure 2.5: *An example of (a) a heavily windowed transmit pulse and (b) its associated compressed result. Note the much lower sidelobes compared with Fig. 2.4. Because of the heavy windowing, however, significant power loss results.*

Unfortunately, the windowing from amplitude modulation causes a loss in sensitivity. As illustrated in Fig. 2.6, a windowed pulse has less integration of power, especially on the edges. Because of this, less power is transmitted and therefore less power is incident on the target, lowering the effective dynamic range of the receiver due to a raised noise floor. However, with lower sidelobes, this tradeoff of up to 6 dB in sensitivity loss is often tolerated in waveform design.

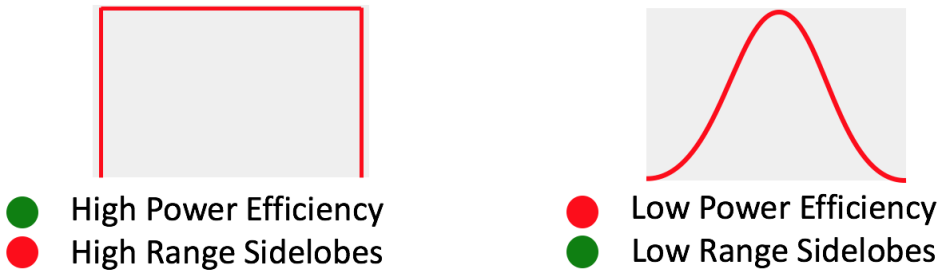

Figure 2.6: *Illustration of amplitude modulation and its effect on pulse energy. The left side demonstrates a non-windowed pulse, which allows high power efficiency due to the integration over the entirety of the pulse; however, sidelobes are generally high. The right side shows a windowed pulse that does not utilize the full integration of pulse power, but generally achieves lower sidelobes.*

2.2.3 The Ambiguity Function

While the ACF provides valuable information in the range/time dimension, additional information is needed in order to properly assess the performance of a waveform. Frequency modulated pulse compression waveforms utilize a matched filter, but that filter assumes a Doppler shift of zero. Once the target is moving in the along-radial dimension, a Doppler shift is added to the return signal, causing distortions in the matched filter. This Doppler dimension of performance is called Doppler tolerance of a waveform, and can be assessed using the ambiguity function, or AF. The AF consists of the range/time and power dimensions from the ACF, as well as a Doppler dimension, making it a three-dimensional function. Each "slice" of the AF at a given Doppler shift is

an ACF at the given Doppler shift; although, this is a bit of a misnomer, since "autocorrelation" in the ACF assumes identical signals, but the Doppler shift is only applied to the return signal (not the filter).

The AF represents the fact that the matched filter is mismatched when the target has any Doppler shift, since knowledge of this shift is not possessed by the filter. The AF can be derived by assuming that the Doppler-shifted signal complex envelope is represented by:

$$s_D(t) = s(t)\exp(j2\pi\nu t) \tag{2.32}$$

where ν is the frequency shift in Hz. Utilizing the matched filter output in Eq. (2.31) and replacing the first s with s_D, it can be shown that the filter output is modified to:

$$s_o(t,\nu) = \int_{-\infty}^{\infty} s(\tau)\exp(j2\pi\nu\tau)s^*(\tau - t)\mathrm{d}\tau \tag{2.33}$$

The definition of the AF was standardized for reversed roles of t and τ, as well as positivity by Wang (1974), and is represented in final form by:

$$|\chi(t,\nu)|^2 = \left|\int_{-\infty}^{\infty} s(t)s^*(t+\tau)\exp(j2\pi\nu t)\mathrm{d}t\right|^2 \tag{2.34}$$

The AF has four main properties:

1. Maximum at $(t,\nu) = (0,0)$

2. Constant volume across the function

3. Symmetry with respect to the origin

4. Adding LFM modulation shears the AF

The first four properties are relatively self-explanatory, however the fourth property deserves explanation. Adding frequency modulation to a pulse, as stated previously, adds Doppler mismatch when Doppler shift is applied to the target. This "shearing" effect is manifested in the AF as a symmetric off-axis ridge of peaks, causing the apparent target center to be shifted away from zero time/range with increasing Doppler shift. This phenomenon essentially *moves* the target in range when filtering is complete. While this is a difficult problem to overcome and is beyond the scope of this research, techniques such as Doppler frequency binning have been utilized in a bank of matched filters to correct for Doppler tolerance issues (Evans 1969; Evans et al. 1970; Wen et al. 2004). Doppler tolerance of weather-related waveforms is explored in Chapter 3.

Finally, the AF is an opportunity to discuss periodic signals, or in the case of weather radar, pulsed signals. The AF, as a three-dimensional function, can represent multiple pulses/peaks in time and space. Because of this fact, it is important to realize that the term "waveform" is not simply limited to a single pulse shape or design; it encompasses the entirety of the pulse design, the pulse structure (i.e., the PRT/PRF), the duty cycle, and the scanning strategy.

While the majority of this research focuses on pulse design for pulse compression waveforms, a significant amount of attention is paid to holistic waveform design for the Atmospheric Imaging Radar in Chapter 5.

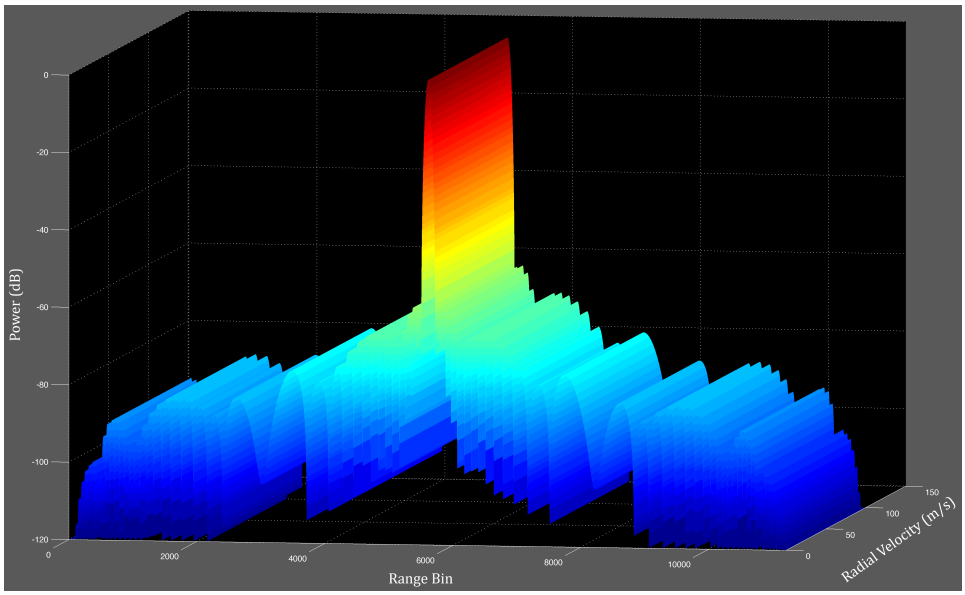

Figure 2.7: *An example of an ambiguity function (AF). The abscissa is marked as range bins (range/time), the ordinate represents relative power from peak (in dB), and the third dimension is Doppler velocity (for an X-band signal). Note how the ACFs shift to the right with increasing Doppler shift.*

2.3 Benefits of Pulse Compression

The next generation of weather radar is anticipated to consist of a fully digital array architecture, meaning that every individual element will act as a transmitter and receiver. The fully digital architecture, shown in Fig. 2.8, provides innumerable benefits, including advanced waveform flexibility, graceful

degradation, and opportunities for beam multiplexing and digital beamforming. This section discusses the benefits of using pulse compression in such a design, as well as some aspects that can be beneficial for a dish-based system. These benefits are broken down into four sections:

1. Element cost
2. Reliability, heat dissipation, and charge levels
3. Physical size and tiling
4. Waveform Flexibility

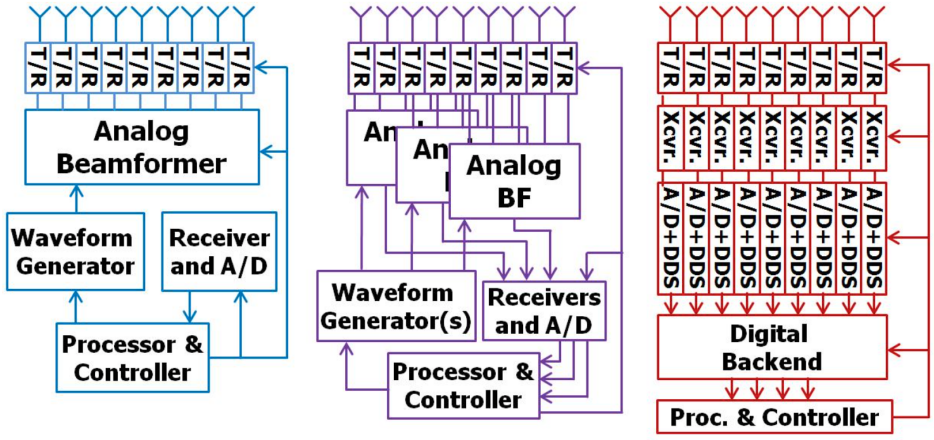

Figure 2.8: *Traditional (left), digitized subarray (center), and fully digital (right) phased array architectures. Figure courtesy of Caleb Fulton.*

2.3.1 Element Cost

Potentially the most critical aspect of using pulse compression is the cost savings afforded by using low-cost, highly reliable solid state transmitters. The

use of SSPAs is all but a foregone conclusion for the MPAR project (FAA 2012) due to their extreme flexibility in an array configuration. Given this concept, the sum of the powers of the elements must be considered before determining the necessary power and associated pulse length for the sensitivity requirements in the NFR specifications. With the goal of achieving no worse than a 1-deg beamwidth at all angles between $\pm$45 deg, an array size of at least 6.75 m (but likely more) is a reasonable expectation for an MPAR system. With half-wavelength spacing, this results in 135 S-band elements in each dimension, resulting in a minimum of 18,225 elements, although some estimates have exceed 20,000 elements (FAA 2012).

At 100 W per element, largely considered to be a high-cost solution at the current time, the resulting total peak transmit power would be over 1.8 MW, which is well beyond the necessary power level. As a reference, the current WSR-88D has a peak transmit power of 750 kW using a single klystron transmitter. Of course, the use of 100-W per-element peak transmit power comes at a potentially extreme cost, so lower power levels should be explored. If the element power is reduced by an order of magnitude to 10 W, the total peak transmit power decreases to 182 kW, a value that is significantly below the necessary value for acceptable sensitivity. In order to meet the NFR specification, a pulse length of approximately 4.1 μs would be necessary, limiting the

blind range to 615 m and potentially resulting in significant cost savings. However, to achieve a range resolution of 150 m, only 1-2 MHz of chirp bandwidth would be necessary, severely limiting the TB product and potential sidelobe performance.

Finally, assuming peak element powers of 1 W, a total peak power of 18.2 kW would be available on each face of the array, a marked differenced from the 1.8 MW with 100-W elements. In this configuration, a pulse length of approximately 41 μs would be necessary, along with an associated blind range of 6.15 km. With 2 MHz of chirp bandwidth, a TB product over 80 would have the potential for much better sidelobe performance. The blind range would need to be filled with a short pulse with little-to-no frequency modulation, resulting in increased spectrum usage.

The cost effects of these three scenarios are striking. Of course, the only possible current comparison of costs would need to be made from current-day prices, but in 10-20 years, these prices may be different. Regardless of the actual cost, it goes without saying that 1-W transmitters will likely remain significantly less expensive than their 100-W counterparts, resulting in cost savings at any given time. At current-day prices, the cost of SSPAs is roughly \$4 per peak transmitting W (when purchased in bulk), resulting in a cost of roughly \$400 for a 100-W element and \$4 for a 1-W element (via the MACOM product brochure, as of September 2015). Despite changing costs, it

is generally anticipated that this order-of-magnitude cost structure will continue in the future; meaning that if 1-W transmitters become $0.50, 100-W transmitters may still approach the $50 range.

With these assumptions stated, it is interesting to compare the possible dollar cost savings between the different transmitter types. With the previously stated estimate of 20,000 elements per array, a four-array platform might consist of approximately 80,000 elements. At $400 per element, this comes out to a T/R element cost in the range of $32M, a relatively staggering number for a single set of components. This would easily result in MPAR systems costing many tens of millions of dollars, and with over 500 possible individual systems, the cost is enormous. At 10 W per element, this cost comes down to $3.2M per system for T/R elements, a drastic improvement. Finally, at 1-W peak transmit power per element, the T/R costs come down to $320k per system. Assuming 500 individual MPAR systems, the national cost breakdown for T/R elements comes out to $16B, $1.6B, and $160M for 100-, 10-, and 1-W element peak powers. Even assuming a 70% reduction in costs over the next 10-20 years, these numbers come out to $4.8B, $448M, and $44.8M, respectively. At current prices, even when purchased in bulk, the network-wide savings between 100 W and 1 W could approach $15B, with the improvement between 10 W and 1 W valued at over $1.5B. Even assuming a 70 % reduction in costs, the difference between using pulse compression and not using

pulse compression could result in billions of dollars of savings across the entire MPAR network.

2.3.2 Reliability, Heat Dissipation, and Charge Levels

Heat production of nearly 73,000 T/R elements is a major concern that has implications in cost, reliability, and performance. A 100-W SSPA must use multiple gain stages to achieve such a high power, meaning that multiple amplifiers are used to transmit the specified power. This amplifier chain can consist of as many as 3-4 gain stages, each with their own losses. By the time each of these gain stages is passed through, the efficiency of the element may have decreased significantly, possibly approaching 40-50% loss. A 1-W SSPA, however, is likely to be able to achieve its maximum transmit power with only one gain stage. Assuming the same ambient noise floor as a starting point, the efficiency of the 1-W element compared to the 100-W element can be strikingly different, with efficiencies greater than 70-80% (via the MACOM product brochure, as of September 2015).

This difference in efficiency leads to multiple effects. First, the total transmit and sensitivity values stated in the previous sub-section will be lower than expected, resulting in the need to make up for lost power with even higher transmit powers, a practice that rapidly approaches diminishing returns. Second, for the same expected total transmit power (for example, a 1-W peak

transmit power with a 100 μs pulse versus a 100-W peak transmit power with a 1 μs pulse), greater heat production will result from the 100-W element due to efficiency losses. This is counterintuitive in the sense that despite identical average powers, the efficiency losses due to hardware design cause more heat to be generated by the high-power transmitter. As heat increases, two major issues arise: the necessity for increased cooling (resulting in higher costs and power usage) and decreased reliability. It is well known that solid-state electronics, and for that matter all electronics, operating at a consistently higher temperature tend to fail faster and more often. This could lead to additional maintenance and operation costs in the future, as well as considerations for relatively expensive liquid cooling solutions.

Finally, the necessary capacitor load for a four-faced array consisting of a total of 4-8 MW peak transmit power for approximate 1 μs approximately every 1 ms (or faster) is enormous. This amount of power discharge is significantly higher than the current WSR-88D platform, due mostly to the fact that four simultaneously operating arrays may be present. Such a high discharge requires extremely large capacitors that take up space, generate heat, and are likely failure points. Of particular concern with this type of failure is that it negates the offset of graceful degradation from individual T/R elements; if a capacitor failure occurs, depending on the architecture, it could mean that a single failure point could be responsible for bringing down the entire system.

2.3.3 Physical Size and Tiling

At S band, which equates to an approximately 10-cm wavelength, elements spaced at half-wavelength distances would need to be 5 cm or smaller in each dimension. Additionally, a substrate edge would likely limit this size to 4-4.5 cm. Currently, a 100-W element takes up roughly 5.6 cm, making it impossible to use in a brick pattern array architecture with the desired spacing. While some improvements in size are likely, physical limitations will keep 100-W T/R elements much larger than 1- or 10-W elements.

The spacing of elements has multiple effects on an array design. If spacing is close, added issues with heat generation and how to dissipate additional heat can occur. Different tiling techniques may alleviate concerns about horizontal spacing via plug-in cards for the back-end. An example of a brick pattern architecture is shown in Fig. 2.9, demonstrating the horizontal and vertical size restrictions. A tiled array could leverage the third dimension for closer spacing, but has not been used extensively to date.

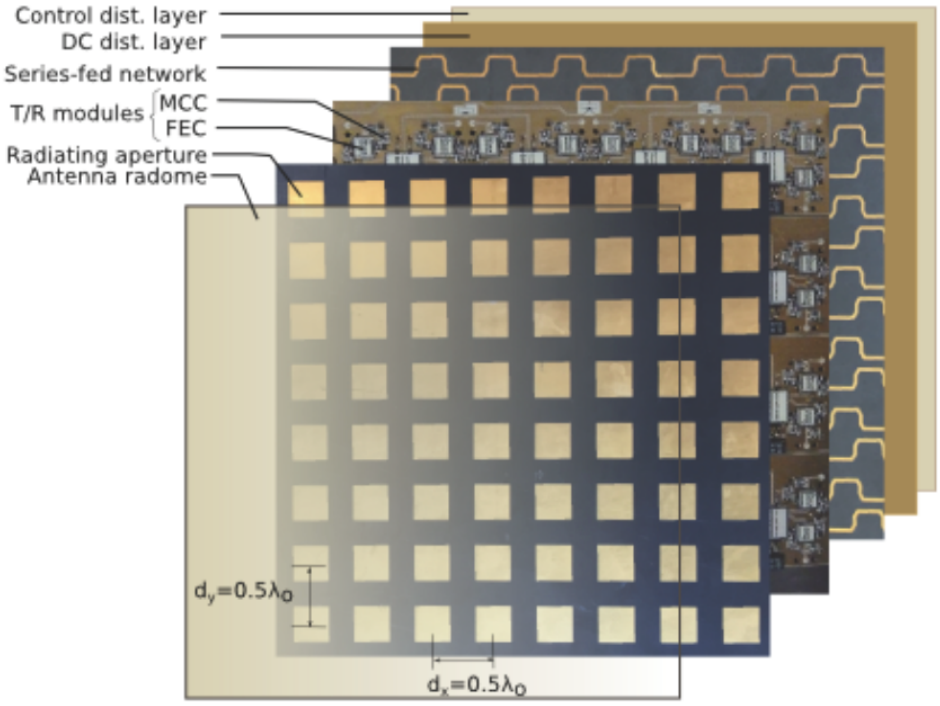

Figure 2.9: *Example RF front-end architecture in an 8x8 element subarray, depicting the horizontal and vertical size restrictions in a brick pattern layout. Figure courtesy of Jorge Salazar.*

2.3.4 Waveform Flexibility

The final focus area for pulse compression advantages is the immense flexibility for multiple-mission strategies. By allowing flexible pulse lengths and bandwidths, the blind range, sensitivity, resolution, and other aspects of the mission can be changed on the fly or as part of different pre-programmed scanning strategies (e.g., clear-air observations, severe storm tracking, uncooperative targets, etc.). Increased sensitivity may be desired for observing clear-air

targets, or a shorter pulse may be desired for vertical velocity estimates. Increased bandwidth may be useful for scanning high-turbulence storms such as tornadoes, allowing for range oversampling and more independent samples. High resolution may also be desired for determining the precise location of a single target or for ATC operations.

The use of a library of transmit waveforms that are pre-optimized for use in a specific system and situation could make these changes nearly seamless for the operator. A broad overview of advanced waveform techniques with a series of specific examples is presented in Chapter 4. These uses range from isolation maximization to clear-air and tornado observations, to cognitive radar concepts. Waveform flexibility can also allow for dynamic spectrum sharing and radio frequency interference mitigation, as well as the capability to use adaptive range oversampling and other advanced scanning techniques.

2.3.5 Dish-Based Platform Advantages

All of the advantages that apply to array architectures can have similar impacts on their dish-based counterparts. The transmitter is often one of the most expensive aspects of a radar system, and without the ability to combine the power of thousands of elements, a dish-based radar is often limited to a single transmitter in each polarization. In this case, it is more appropriate to compare the power gained from pulse compression with a SSPA compared

with a high-powered transmitter such as a TWT, klystron, or magnetron. Generally, a SSPA can be orders of magnitude less expensive than its equivalent high-power alternatives, potentially resulting in significant overall system savings for a dish-based system.

The reliability aspect is particularly intriguing for any radar system that is expected to have near-100% up time. High-powered transmitters are a common failure point for single-transmitter radar systems such as dish-based platforms, and due to their size and cost, can be non-trivial to replace, often expanding down time. SSPAs, for reasons explained earlier in this section, tend to have much higher reliability than higher power transmitters. Much of this improvement is due to the lack of a rapid "on-off" sequence at each pulse, similar to the previous description of capacitor loads for short pulses of high power rather than long pulses of lower power.

In small systems, specifically mobile platforms, size can also have a major impact on radar performance. TWTs, and especially klystrons, can be excessively large for certain applications, leading to the need for platform modifications. Magnetrons can often be constructed in a relatively small form factor, but issues regarding spectral leakage and non-constant phase can lead to additional problems. SSPAs are exceptionally small while providing excellent spectral performance, making them an ideal candidate for smaller systems. Finally, the issues regarding waveform flexibility are generally the same for

dish-based platforms. Arbitrary waveform generators and advanced hardware can utilize SSPAs to design mission-tailored waveforms and signal processing techniques.

2.4 Introduction to Optimization

Optimization is a technique for finding the best solution set to a problem based upon a set of criteria (Boyd and Vandenberghe 2004). Optimization problems involve an equation, known as the fitness function, that contains variables that can be altered by a computer-based algorithm in a sequential basis. Multiple "solutions" to the function are computed, and the set of variables that corresponds to an optimal fitness function value represent the ideal solution. The solutions to the fitness function are called fitness scores, and the general solution of the fitness function is referred to as "fitness."

A variety of optimization techniques are available for use in various types of problem solving. The simplest optimization method involves searching a two-dimensional space for a maximum or minimum value. This is typically completed by taking the derivative of a function and testing all of the zeros for their fitness scores. In a quadratic equation, for example, two "zeros" may be found by taking the derivative of the function. Each zero represents a change in concavity of the function and a possible maximum or minimum of the curve. Each zero is tested for a fitness score, and the most optimal value is selected.

In many cases, a polynomial equation may have two or more "local" maximum values, which may be far apart but have very similar fitness scores. For this reason, simply taking the first zero in a derivative approach may not yield the truly optimum value. This approach can be thought of as starting from one end of a number line and taking the first concavity change as an optimal value without searching the entire number line. While this may seem simplistic, imagine a solution set with trillions of possible solutions; a full search may be too computationally expensive, so finding a local optimum value from a starting point may suffice as an approximation.

Ideally, however, a *global* (or near-global) optimum is desired. Even though a solution curve may contain a series of "local" maxima or minima, a global optimization technique will attempt to find the highest possible fitness score. Different global optimization techniques have different properties, with various advantages and disadvantages for the goal at hand. While the best solution is usually preferred, items such as computational complexity become important as well.

2.4.1 Optimization Techniques

Each optimization problem is different, possessing different goals, constraints, and hence ideal techniques for solving. For many problems, a variety of possible optimization algorithms can yield acceptable results. A common area of

research in mathematics is optimization algorithm comparisons. Since each problem is different, strengths and weaknesses of different algorithms may change depending on the goal. Since global optimization is preferred, this section explores a handful of global techniques available, including some of the most recent advances in optimization techniques. A brief overview of selected optimization techniques is provided in the following subsections.

2.4.1.1 Exhaustive Search

Exhaustive search algorithms, also known as the brute force technique, search every possible variable combination for fitness testing. After a fitness score calculation for every combination, the variables with the best fitness are selected as the optimal value. An exhaustive search is the only way to guarantee that a truly global optimum has been found. This type of search is the most basic optimization algorithm and is clearly only feasible for small combinations of variables. Once the number of possible solutions becomes computationally unfeasible for an exhaustive search, the technique quickly loses its appeal. Regardless of solution set size, this method always leads to extensive computation time, and is often impractical for most modern optimization problems. A subset of exhaustive search is directed search, where the algorithm analyzes which direction to change a variable based on trends in the fitness. Tabu search is an example of directed search, where potential optimal solutions are marked

so as to not allow the algorithm to revisit the solution repeatedly (Glover 1989, 1990).

2.4.1.2 Multistart Algorithms

Multistart algorithms, which ideally attempt to locate a global optimum, actually utilize local maxima search techniques. Instead of searching continuously along a line, these algorithms attempt to start searches at a large number of points along the solution curve of the objective function (Oh et al. 2004). These searches ideally find a large number of local maxima, often with a derivative-based technique, which are compared to each other in order to estimate the global optimum. While individual calculations may be less complex than a full, exhaustive search algorithm, the number of calculations occurring simultaneously increases significantly, leading to a tax on the computational power available. However, for sufficiently small search domains, the multistart technique can often lead to the global optimum more rapidly than exhaustive search algorithms (Boender et al. 1982).

It is worth noting that with recent increases in multi-core central processing units (CPUs) and graphics processing units (GPUs), multistart methods are becoming more popular. GPUs, for example, can posses many thousands of individual cores that can be used in parallel processing for relatively simple tasks. Depending on the type of optimization problem, marked increases in

processing capability can be realized with multistart algorithms and parallel processing. Another variation of multistart is described later in this chapter in the evolutionary computing section. Certain types of optimization contain a "population" of possible variables that run in parallel on a multi-core machine, and since these population members do not depend on each other and consist of identical processing architectures, they can be run at the same time, saving computation time and complexity.

2.4.1.3 Linear Programming

Linear programming represents a category of optimization techniques that attain optimal results via a linear relationship of constraints (Gass 2003). These constraints may include variables in a cost function, linear equalities, and any other combination of linear constraints. Many simple optimization problems can be represented linearly, making linear programming a popular form of optimization. Compared to an exhaustive search, linear optimization techniques can converge on a global optimum in a linear problem set extremely rapidly. Although some of these problems may be simplistic, many applications require multiple problems solved in succession (or simultaneously), sometimes in real time. These needs highlight the importance of any computation time that can be saved with advanced algorithms.

One form of linear programming, the simplex algorithm, forms linear constraints based upon user input, and finds a "feasible region" of possible solutions that fall within each of the constraints. The algorithm forms a type of solution curve which lies along the edge of the feasible region, and steps along until the optimal state is found. While this can be a very fast, efficient method of optimization for simple cases, more complicated cases can lead to less than desirable results (Dantzig and Thapa 1997).

Interior point algorithms work in a similar way to the simplex algorithm. However, they explore the entire depth of the feasible region, as opposed to simply following the edge. While this increases computational complexity, and still requires a near-complete "search" of the solution space, it is commonly believed to offer a higher probability of global optimum (Karmarkar 1984). However, both simplex and interior point methods offer different advantages to varied problems, and can either one may be considered more appropriate given the situation.

2.4.1.4 Nonlinear Programming

Nonlinear programming works in the same general fashion as linear programming. However, the constraints may be represented as nonlinear equalities or inequalities. This type of optimization represents an increasing portion of real-world problems. Examples of nonlinear programming include cell site

optimization, optimal power generation in a wind farm, and virtually any type of solution set that cannot be generalized as a simple polynomial.

The Quasi-Newton approach is very similar to a standard Newton method, which finds zero derivatives in a function. However, Quasi-Newton methods assume a quadratic form of the function around potential optimal areas, and do not need to calculate second derivatives, resulting in less computational complexity. Instead, gradient vectors are used to determine local maxima/minima (Shanno 1970).

The Nelder-Mead method is a form of simplex optimization used in non-linear programming. It is often used in multi-dimensional space optimization problems, where feasible planes and shapes can be defined for potential solution areas. The algorithm attempts to guess new optimal solutions based on the observed behavior of the objective function in order to converge relatively quickly on global optimum (Nelder and Mead 1965).

Trust-region techniques are similar to the Quasi-Netwon approach, in that they only search a portion of the objective function. These methods model the function in the form of a quadratic equation to create the trust region, and expand/contract the region based on the results of the model. The forecasted change in improvement is compared to the actual improvement of the objective function (Celis et al. 1984).

2.4.1.5 Multi-Objective Optimization

While each of the previously mentioned methods for optimization all depend on solving for a maximum in a fitness function, some optimization problems involve multiple goals that cannot be well-represented in a single fitness function. For example, two (or more) variables may counteract each other in a fitness function, causing them to cancel out if represented as a single equation. In these cases, a broad approach known as multi-objective optimization may be applied. Multi-objective methods can be applied to many different nonlinear optimization techniques and consist of solving for multiple fitness functions simultaneously.

Because these fitness functions may counteract each other, a series of equally optimal solutions are determined through the algorithm of choice. These solutions define a Pareto front (Fudenberg 1991), with each solution being referred to as Pareto optimal; a sample Pareto front is shown in Fig. 2.10. After a Pareto front is solved for, a decision maker (typically a human, or possibly some other type of algorithm) will choose the ideal solution for the problem at hand. In this respect, multi-objective optimization does not attempt to find a single solution, but offers a series of candidate solutions.

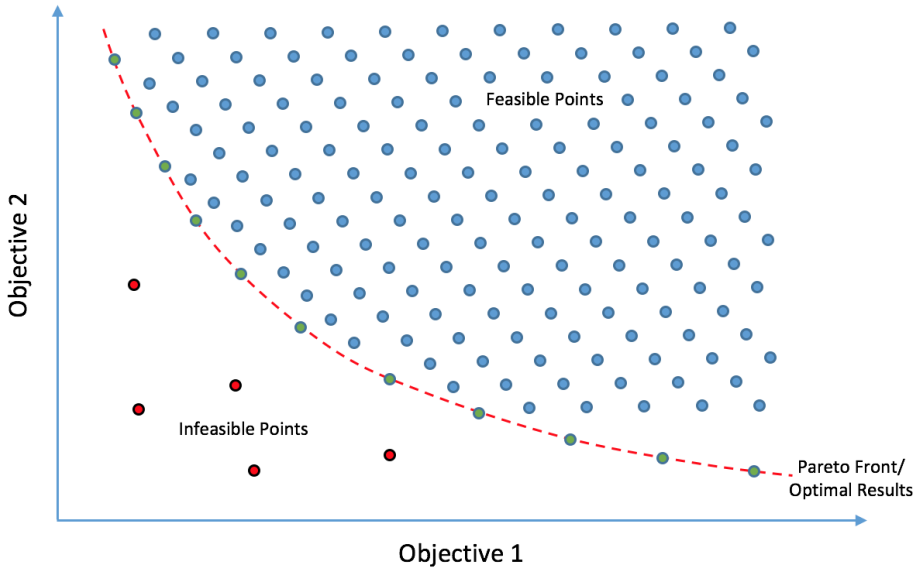

Figure 2.10: *Example of a Pareto front in a multi-objective optimization problem. A series of feasible points and infeasible points make up the majority of solutions, but a function of equally optimal solutions makes up the Pareto front.*

Multi-objective optimization is an excellent illustration of the difficulty in choosing fitness functions for optimization. As will be discussed in future sections and chapters, fitness function choices such as scaling can significantly alter results of an algorithm, and can even alter the type of optimization algorithm that will perform best (both from a pure fitness standpoint as well as a computation time perspective). When a single fitness function cannot be determined for the problem at hand, multi-objective optimization can help mitigate the problem. However, a Pareto front will span as many dimensions as the number of fitness functions, making the results exponentially more difficult to analyze with linearly added complexity.

2.4.1.6 Metaheuristics

Metaheuristics represent a group of algorithmic techniques that are used to search extremely large solution spaces to optimization problems. Similar to a nonlinear global optimization method, these algorithms are designed to solve massively complex problems that are highly nonlinear and often not easily representable mathematically. In these cases, it is often computationally unfeasible to guarantee a true global optimum over such a large search space. Metaheuristics can be thought of as partial search algorithms that use a strategy or heuristic to *guide* the search in the proper direction. They can often combine multi-start, multi-objective, and evolution-based methods to produce acceptable results in highly nonlinear problems.

Metaheuristics are designed to find mathematically *acceptable* solutions to large problems, not necessarily a global optimum. They come in many shapes and forms, but typically employ a search algorithm based on a process observed either in nature or in the human brain as a method of machine-based learning. Some of the naturally inspired forms of metaheuristics that are rapidly gaining popularity in science and engineering are simulated annealing (SA), particle swarm optimization (PSO), ant colony optimization, and the firefly algorithm (FA), among others.

SA is a technique that is naturally inspired by the heating and cooling of materials, representing a thermodynamic process (Metropolis et al. 1953;

Kirkpatrick et al. 1983). It "cools" slower than it "warms," theoretically preventing the loss of acceptable solutions and focusing the search space. PSO, another naturally inspired metaheuristic, is based on simple equations dictating the position and velocity (the first and second moment) of a population of "particles" (Kennedy and Eberhart 1995). These particles represent common social and mating behaviors in various species, making it a subset of evolutionary computing (to be described later in this section). Ant colony optimization (Colorni et al. 1991) and FA (Yang 2008) are both similar to PSO in that they mimic simplified equation-based motions of ants and fireflies in their mating and food-gathering characteristics. While many of these techniques utilize slightly different methodologies and/or equations, they have all shown to be relatively successful for various types of optimization problems in the literature (e.g., Youhua et al. 1996; Dorigo and Gambardella 1997; Clerc and Kennedy 2002; Robinson and Rahmat-Samii 2004; Bryan et al. 2006; Dorigo et al. 2006; Babaoglu et al. 2007). However, it is exceedingly difficult to directly compare their performance levels without choosing specific fitness functions, making it challenging to determine the best solution for a given problem.

Another subset of metaheuristics is evolutionary computing, a generalized concept which encompasses numerous types of optimization algorithms. Originally, the term evolutionary programming was used to describe optimization

techniques which utilized the theory of Darwinian evolution for processing of problems (Fogel et al. 1966). Around the same time, genetic algorithms (GAs) were developed by Holland (1975), while evolution strategies were under development by Rechenberg (1973) (Eiben and Smith 2007). GAs work to progressively improve the functionally defined fitness based on pairing, offspring, and stochastic mutation. GAs are capable of quickly finding feasible solutions to both simple and complicated nonlinear problems, offering of the most consistent methods to achieve near-global optimum in a computational feasible fashion (Holland 1975). More information on GAs is provided in the following section, as this is the method of focus for this research.

2.4.2 Genetic Algorithms

GAs are among the most popular methods that fall under the evolutionary computing category (Eiben and Smith 2007). They are designed to be capable of finding global optimum solutions to complicated, non-linear, real-world problems. Additionally, GAs have the ability to remain computationally inexpensive for simple problems, or to be developed into sophisticated algorithms capable of solving advanced problems. GAs offer one of the most consistent methods to achieve global optimum, while also being flexible enough to accommodate real-world boundary conditions.

2.4.2.1 Genetic Algorithm Process

A GA, as the name suggests, works on the basis of genetics, which stems from the theory of evolution. Since exhaustive search methods have been shown to be inefficient, an advanced optimization technique such as a GA should be considered for searching a fraction of the potential search space while also achieving near-global optimum. In a GA, this is accomplished by combining potential solutions over a series of "generations" in order to develop new, possibly better solutions.

GAs operate by first developing an initial population. This set of possible solutions contains many members of the population. The number of members is defined by the "population size." In a simple GA, each member is represented by a series of bits (zeros and ones). If, for example, an 8-bit representation is chosen, members will be represented by a series of eight 0's and 1's, which can represent any number between 0 and 255. As an example, assume that the population size is 10.

This first generation, with 10 members, is tested based on the user-supplied fitness function. This function can be as simple or as complicated as the problem warrants, and it is made up by variables which are defined within the members of the population. After each of the 10 members are entered into the fitness function, the resulting values are called fitness scores. For this case, we will assume that the optimum value is the *highest* possible fitness score.

Of the 10 population members, some may be chosen as "elite." These elite members, represented by those with the highest fitness scores, are passed on to the next generation of the algorithm unchanged. By doing so, it is guaranteed that the overall fitness will not decrease from generation to generation. Typically, only two elite children are passed along with each generation. The number does not usually deviate throughout the run of the algorithm.

Remaining population members are then randomly paired to form "parents." The pairing is completed by weighting members based on fitness score, with a higher probability of selection if their fitness score is higher. Once parents are selected, a "crossover" is completed. Crossover involves randomly choosing a crossover point (the same for each parent), and replacing all of the bits on one side of the point with all of the bits from that side of the other parent's bit string. Fig. 2.11 shows the crossover point of two parents, and the resulting children. This process is meant to randomly attempt to combine the best genes from the best parents in the newly formed "children". It can be done randomly, or can be weighted based upon the fitness score for each parent.

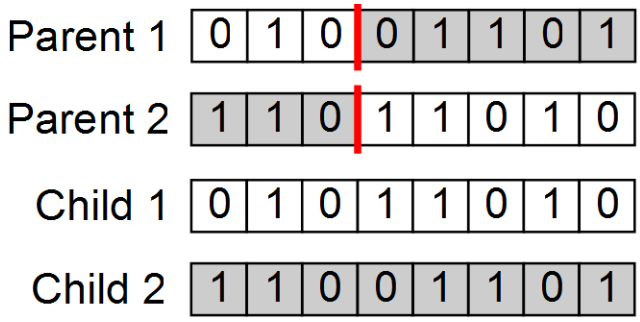

Figure 2.11: *Illustration of crossover in a genetic algorithm. Bit strings for each parent are combined to form two new children (Eiben and Smith 2007).*

After crossover is completed, "mutation" may occur, which is a key component to a GA, as it aids against the possibility of converging to a local maximum. This process occurs based upon the "mutation rate," which represents the *probability* of mutation. After each set of parents produces two children, each bit of the new children has equal probability to undergo mutation. A random number generator chooses a number, and if it falls within the probability range, the bit in question is flipped (i.e., a zero becomes a one and vice versa). By allowing for a small chance of mutation, the algorithm will not become locked to a local optimum. Fig. 2.12 illustrates the mutation of one random bit from two children.

The resulting generation is populated by elite, crossover, and mutant children. By advancing the highest fitness scores, combining the genes of the best parents, and occasionally allowing for slight mutations, there is a high probability of rapid increase in fitness score, even for relatively complicated

problems. Generations are continued in the same fashion until one of many possible stopping criteria are met:

1. Fitness does not improve over a set number of generations ("stall" generations)
2. The average change in fitness reaches a set level ("function tolerance")
3. A set amount of time has passed
4. A set number of generations have been completed
5. A set fitness limit has been reached

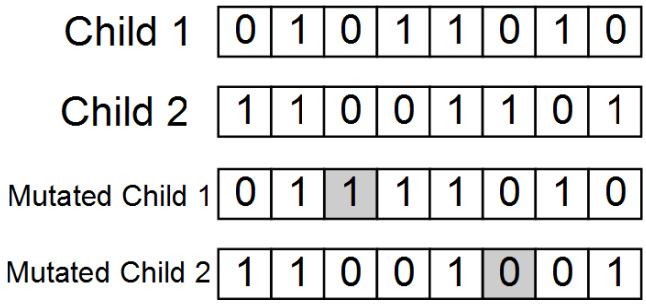

Figure 2.12: *Illustration of mutation in a genetic algorithm. Bit strings are probabilistically flipped in order to encourage diversity amongst children (Eiben and Smith 2007).*

2.4.2.2 Variations of Genetic Algorithms

GAs can be applied in a variety of problems. First and foremost, most of the variables mentioned can be changed to suit the needs of the problem. Population size, elite count, mutation rate, stopping criteria, and the flexibility

of the fitness function expression all lead to a highly customizable algorithm. Boundary conditions and constraints are also adaptable to the situation, and can range from the very simple to more complicated.

Additionally, *representation* of population members is an important aspect of any GA. In the example shown previously, an eight-bit string of binary numbers was used to represent each member of the population. The number of bits is easily customizable for the needs of the user, but additional options are also available. Integer and floating point representations use random number generation to perform crossover and mutation, and can allow the user to easily apply a GA to complex, real-world problems. In the case of this research, floating point representation and random number generation are used instead of binary representation.

2.5 Meteorological Considerations

A number of important considerations for weather radar must be taken into account based on the meteorological goals of the platform. For example, the goals of a holistic observing weather radar will be different than a radar that is designed to only scan tornadoes or hurricanes. The two most fundamental considerations for weather radars are resolution (temporal and spatial) and data quality. This section describes these issues and how they apply to phased arrays, scanning strategies, and waveform design for meteorological targets.

2.5.1 Resolution

Temporal resolution is the main consideration for the upgrade to phased array systems for weather observations. NWS forecasters desire higher temporal resolution in a future weather radar network in order to provide more timely information in rapidly changing weather conditions (Zrnić et al. 2007). The advent of phased array radar technology in the weather community has sparked numerous studies regarding the feasibility for a future phased array radar network in the USA and how such a network would impact weather forecasting, warnings, and research. Phased arrays offer the opportunity for rapid volumetric updates due to the use of electronic steering and digital beamforming.

This distinction for phased arrays is important compared with the WSR-88D network due to the fact that a volumetric update on a WSR-88D takes 4.2 min in the fastest volume coverage patter (VCP; Brown et al. 2000). A number of meteorological phenomena change on the order of seconds rather than minutes, and even those that do not change significantly over the span of seconds can hide elusive clues to their development over the span of minutes. These types of phenomena include supercells, tornadoes, microbursts, mesoscale rain/snow bands, and short-lived phenomena in tropical cyclone bands.

A classic convective scenario that commands high temporal resolution volumetrically is a microburst. Microbursts present a significant challenge to

aviation due to rapid changes in lift presented to a pilot. As detailed in Fig. 2.13, an aircraft on final approach will typically be in a descent-oriented angle (nose toward the ground). As the outflow approaches the aircraft as the head of a density current, extra lift is supplied to the aircraft, causing the pilot to point the noise further toward the ground. Shortly afterwards, the outflow moves past the aircraft and the vehicle encounters the convective downdraft. With the nose already pointed significantly downward toward the ground at relatively low elevation above ground level, the pilot may not be able to recover in time before making contact with the ground. Numerous instances of airline disasters due to microbursts have been documented, causing hundreds of fatalities in the USA alone (Wilson et al. 1984; Wolfson et al. 1994). Microbursts occur on the order of 30-90 s, and volumetric updates multiple times in that period can provide excellent estimates of downward vertical motion and an impending microburst (Irwin and Smith 2009).

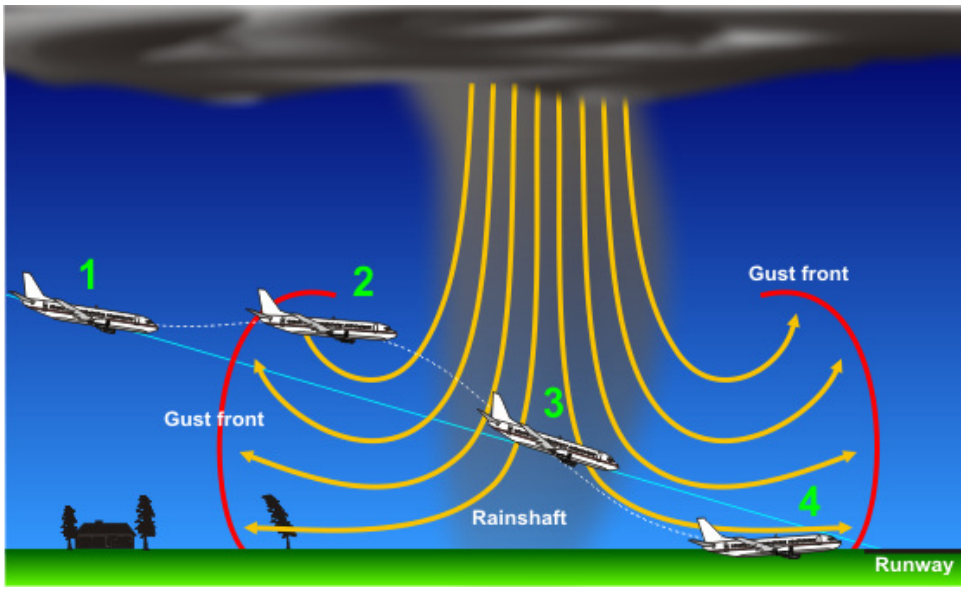

Figure 2.13: *How an aircraft on final approach reacts when encountering a microburst. The initial lift on the edge of the density current causes the pilot to angle the nose toward the ground. The downburst is then encountered with little or no time to recover with the lack of available lift remaining. Image courtesy of NOAA.*

Tornadoes are another meteorological phenomenon that can form, change, shift, and dissipate volumetrically on the order of seconds. Supercellular tornadoes are generally spawned from a parent mesocyclone, and tornadogenesis can occur extremely rapidly and via multiple forcing mechanisms. Limited-resolution observations have left meteorologists and researchers with a number of theories regarding tornadogenesis and tornadic dissipation. These theories include the role of the rear-flank downdraft (RFD; Markowski 2002), top-down/bottom-up vortex formation (French et al. 2013b), and numerous studies regarding the transition from mesocyclone to tornadic vortex (e.g., Dowell and

Bluestein 2002a; Bluestein et al. 2003, 2007a; Kosiba et al. 2013; Wurman and Kosiba 2013; Houser et al. 2015). Many of these changes are theorized to occur on time scales that are too short for traditional radar observations, leading to interpolation with models (e.g., Marquis et al. 2012) and "cartoon" theories (Markowski and Richardson 2014). Additionally, the three-dimensional nature of these phenomena makes scanning with a pencil beam that much more difficult for acceptable temporal updates.

In addition to temporal resolution restrictions, spatial resolution (in the azimuthal, elevation, and radial dimensions) is a critical consideration for a weather radar. A fan beam, for example, has been used to cover multiple elevations in applications such as air traffic control (e.g., the ASR series of radars), using aircraft transponders for specific elevation information. With volumetric targets, however, resolution in the vertical/elevation dimension is just as critical as that in the azimuthal/range dimensions, leading to the widespread use of pencil beams for weather observations. Pencil beam resolution is typically determined by the 3-dB beamwidth equation (Eq. (2.5)), leading to the desire for either large apertures or short wavelengths. This is an issue particularly for mobile platforms where a large dish is not possible on a portable vehicle, resulting in a tradeoff between frequency and aperture size. For this reason, many mobile platforms are at C band or shorter wavelengths, with a common "sweet spot" at X band, resulting in considerable attenuation issues.

Spatial resolution is a constant whenever pointing at broadside of an antenna, which is how dish and fan antennas work at all times. For an array, however, phase shifters can point the beam off broadside for steering with no moving parts. This steering causes an effective shrinking of the antenna aperture off of broadside, causing the beam to widen. The beam widens by a factor of the cosine of the angle, meaning that for an array that points to $\pm$45 deg, the beam will widen to $\sigma/\cos(45\,\text{deg})$ at the edges. For a 1-deg 3 dB beamwidth at broadside, this equates to a 1.4-deg beamwidth at $\pm$45 deg. This maximum beamwidth must be considered during the array design stage, and if a narrower beam is needed on the edges of the scan range, a larger aperture must be implemented.

Temporal and spatial resolutions have a direct relation known as effective beam-width that can become a limiting factor in extremely rapid scanning strategies. When a dish platform is moving rapidly (usually in the azimuthal dimension), beam smearing causes an effective widening of the beamwidth, causing a degradation in azimuthal resolution. This relation is expressed in Eq. (2.35) (Doviak and Zrnić 1993), and can become a significant problem in rapid-scanning mobile tornado radars.

$$\text{erf}\left(2\sqrt{\ln 4}\phi/\theta_1\right) - \text{erf}\left[2\sqrt{\ln 4}(\phi - \alpha M T_s)/\theta_1\right] - \frac{1}{2}\text{erf}\left(\sqrt{\ln 4}\alpha M T_s/\theta_1\right) = 0 \tag{2.35}$$

In Eq. (2.35), θ_1 is the standard 3-dB beamwidth, M is the number of samples, and α is the antenna rotation rate in rad s^{-1}. The equation has two solutions, σ_1 and σ_2, whose difference determine the effective beam pattern width.

These radars typically have relatively wide native beamwidths due to the necessity to balance aperture size and attenuation due to high frequencies, meaning that any additional effective widening of the beam can be significant. The most relevant example is the Rapid X-band polarimetric (RaXPol) radar at the University of Oklahoma. RaXPol maintains a 1-deg 3-db beamwidth, but scans at a rate of 180 deg s^{-1}, resulting in the possibility for significant beam smearing in azimuth. Specific transmit waveforms and advanced signal processing allow for mitigation of these issues, but at a cost of higher bandwidths.

2.5.2 Data Quality

The pinnacle of any radar, especially a radar with stochastic volumetric targets, is data quality. Data quality is a holistic topic that considers estimate errors/noise, resolution, independent samples, and general usability for the end user. Data quality standards for the WSR-88D network are relatively high, as are the requirements for the planned MPAR network, as detailed in the notional functional requirements (NFR; FAA 2012). All of these requirements

must also satisfy requirements regarding maximum transmit power, spectral containment requirements, and of course, cost concerns. Some of the standard requirements in the NFR include maximum spectrum width and radial velocity errors of 1 m s^{-1}, Z_{DR} bias equal to or less than 0.1 dB, very high sensitivity, and resolution values of 150 m in the along-radial dimension and 1 deg in the azimuthal/elevation dimensions.

Achieving all of these specifications requires careful planning of hardware, signal processing, and scanning strategies for a radar. Sensitivity requirements are satisfied mainly through transmitter peak power, pulse length, number of elements and beam weighting (for an array), integration time, and antenna gain. Resolution requirements can be satisfied based on aperture size and pulse length, or by using a frequency modulated waveform. Radial velocity and spectrum width requirements, along with the data quality for virtually all other moment estimates, are directly related to the number of independent samples.

To put this in perspective, consider a pencil beam pulsed Doppler radar that is scanning in azimuth at a constant elevation with a convective storm in range. A typical PRF of 1 kHz results in a pulse being sent/received every 1 ms, or 1,000 pulses per second. While a radar transmits many pulses in a short amount of time, the amount the target/storm of interest changes from pulse to pulse is often minimal, especially if the storm lacks high values of

turbulence. This means that the information that is gleaned pulse-to-pulse is not necessarily very useful to the radar estimate, since little value has been added. The radar must wait for the storm to decorrelate in order to gain new useful information.

The number of independent samples relative to the number of samples actually collected is a function of the variance of the target, and can be derived using an estimate-variance reduction factor as described by Papoulis and Pillai (2002). Doviak and Zrnić (1993) simplified this factor for a square law receiver-detector and determined that a relevant relation could be shown as:

$$M_I = \frac{4M\sigma_v T_s \pi^{1/2}}{\lambda} \tag{2.36}$$

where M_I is the number of independent samples and σ_v is the variance of the velocity field in a resolution volume (i.e., the spectrum width). For reflectivity factor estimates, a standard deviation of the estimate can be represented as:

$$\sigma_z = 10\log\left[1 + \frac{\sigma_{\hat{S}}}{\overline{S}}\right] \tag{2.37}$$

where σ_z is the standard deviation of reflectivity factor, $\sigma_{\hat{S}}$ is the standard deviation of the signal power estimate, and $\overline{S}$ is the mean signal power. Eqs. 2.36 2.37 indicate that, in general, the higher the number of samples, the lower the error in estimates. In order to achieve more *significant* samples, more independent samples must be collected. This is possible either by increasing the total

number of samples or by scanning a target with high variance/turbulence. A final method to increase the number of independent samples is to "artificially" increase T_s. This is possible via range undersampling, as well as through the use of different frequencies (known as frequency hopping). For a given frequency, T_s is increased, and new information can be gained from each pulse pair at a different frequency.

The majority of Doppler weather radars utilize autocovariance processing to generate velocity and spectrum width moment estimates; this technique is also known as pulse pair processing. Using this method, a pair of pulses are used to measure Doppler shift from pulse to pulse. Simplified versions of the pulse pair estimator for radial velocity and the variance of the radial velocity estimate, respectively, can be represented as (Doviak and Zrnić 1993):

$$\hat{v} = -(\lambda/4\pi T_{\mathrm{l}})\arg\left[\hat{R}(T_{\mathrm{l}})\right] \tag{2.38}$$

$$\mathrm{var}(\hat{v}) = \frac{\sigma_v \lambda}{8MT_{\mathrm{l}}\pi^{1/2}} \tag{2.39}$$

where arg represents the argument in radians and $\hat{R}(T_l)$ is the autocorrelation at a sample time lag of T_l. The pulse pair variance of the spectrum width estimate can be represented as (Doviak and Zrnić 1993):

$$\mathrm{var}(\hat{\sigma}_v) = \frac{3\lambda\sigma_v}{64MT_{\mathrm{s}}\pi^{1/2}} \tag{2.40}$$

Finally, polarimetric variance is largely dependent on cross-polar isolation between horizontal and vertical pulses. This can be mitigated in many ways, including spatial isolation, alternating pulses, a "slant-45" method, or through waveform design. The issue of polarimetric isolation will be examined in Chapter 4.

All of these considerations combine to force the radar engineer to be extremely aware of the end goals for a system. In a platform like a future MPAR, an extremely wide range of missions is possible, including aircraft tracking, stratiform precipitation, clear air observations, convective storms, and more. In a similar fashion to the WSR-88D, MPAR will need to make use of different VCPs for different situations and mission goals (Brown et al. 2000). For example, with the inherently low-turbulence and low-reflectivity nature of stratiform precipitation, slow rotation/scanning rates are necessary in order to generate an acceptable number of independent samples to meet the system requirements. This is important to remember for MPAR, because even with the ability to rapidly scan without effective beamwidth changes due to mechanical steering, the appropriate number of independent samples will still be necessary.

2.6 ARRC Radar Platforms

Across the remainder of this research, two primary radar systems will be used for demonstration and analysis. Both systems are maintained by the ARRC at the University of Oklahoma and each has a different core design and purpose. Pulse compression has major effects on both of these radars and is a necessity for their proper operation and data collection. The systems are the PX-1000 and the AIR.

2.6.1 PX-1000

The PX-1000 is a polarimetric, X-band, transportable radar designed, built, and maintained by the ARRC (Cheong et al. 2013a). Mounted on a trailer-based platform, the system consists of a processing computer, pedestal controller, and RAID storage unit mounted on the base of the trailer, with the entirety of the transmit/receive chain mounted behind the antenna above the floor as part of the pedestal turntable, which is contained by a spherical radome. The upper portion of the radar, behind the antenna, consists of dual SSPAs, an arbitrary waveform generator, and a server capable of realtime pulse compression. The SSPAs are currently rated at 200-W peak power, but for the majority of this research, 100-W SSPAs were used in the transmit chain. Additionally, both the horizontal and vertical chains collect a "leak through" copy of the transmitted pulse that is superimposed on the time-series data for analysis and

Table 2.2: *PX-1000 system characteristics.*

Transmitter Type	Dual SSPA
Operating Frequency	9550 MHz
PRF	1–2000 Hz
Radiating Center	2.5 m AGL
Sensitivity	$<$20 dBZ @ 50 km
Observable Range	60 km
Antenna Gain	38.5 dBi
Antenna Diameter	1.8 m
3-dB Beamwidth	1.8 deg
Polarization	Dual Linear, SHV
polarimetric Isolation	26 dB
Maximum Rotation Rate	50 deg s^{-1}
Peak Power	100 W
Pulse Width	1–69 μs
Chirp Bandwidth	5 MHz
Maximum Duty Cycle	20%
Minimum Gate Spacing	30 m

testing purposes. This combination of hardware and software makes PX-1000 an ideal platform for waveform research and development. A table depicting PX-1000 system characteristics is provided in Table 2.2, and a picture of PX-1000 is shown in Fig. 2.14.

Although the specifics of waveform design for PX-1000 are discussed in depth in the following chapter, it is important to note the general characteristics of the platform here. Due to the maximum transmit power of 200 W, pulse compression is an absolute necessity for the operation of PX-1000 for weather

observations. The system can transmit up to a 69 μs pulse at up to 5 MHz of total bandwidth, resulting in the capability for up to 14 dBZ of sensitivity at 50 km range with 100 W, and 11 dBZ with 200 W, along with range resolution as high as 30 m. However, the long transmit pulse causes a rather substantial blind range >10 km, and with the range gate writing capability only at 60 km, a significant portion of the usable range cannot be used due to transmitting the long pulse. For this reason, only 57 μs of the available long pules is transmitted, along with only 2.2 MHz of the available bandwidth. Directly after the long pulse, a "fill pulse" of 2 μs length and 2.4 MHz of bandwidth is transmitted as a filler for approximately the first 10 km. While the sensitivity is much lower with the short pulse, the maximum range of 10 km significantly increases its effectiveness.

Figure 2.14: *The PX-1000 completing system tests during the PECAN project in 2015.*

PX-1000 has participated in numerous field campaigns and collected multiple notable datasets that have been featured in the literature (Kurdzo et al. 2015a). Among the campaigns it has taken part in are a winter precipitation field campaign in South Korea in 2014, (Cheong et al. 2014), a flash-flooding campaign in Colorado in 2014 and 2015, and the Plains Elevated Convection at Night (PECAN) project in 2015. With only 200 W of peak transmit power, PX-1000 represents an inexpensive alternative to most mobile radar platforms. Additionally, with concerns regarding waveform development for volumetric targets for use with MPAR, PX-1000 serves as a testbed for candidate MPAR waveforms in a variety of realistic weather scenarios. Due to the in-house design of the system, characterization of the transmit/receive chains is also readily possible, allowing for deep understanding of distortion and processing effects.

2.6.2 Atmospheric Imaging Radar

The AIR is a mobile X-band imaging radar platform designed for extremely high spatial and temporal resolution observations of tornadoes and supercellular thunderstorms (Isom et al. 2013). A feed-horn mounted on top of an antenna array transmits a 20-deg (vertical) by 1-deg (horizontal) beam, oriented as a range-height indicator (RHI). A 36-channel receiver array at half-wavelength spacing below the feed-horn utilizes digital beamforming to form

an arbitrary number of 1-deg beams in the vertical dimension, forming an RHI with every pulse. The entire assembly is rotated in the azimuthal dimension, and can be pointed between -80 deg and +100 deg relative to the rear of the vehicle, covering a total of 180 deg by 20 deg. With a rotation rate of up to 20 deg s^{-1}, volumetric scans can be completed in 9 s, and with a T_s of 314 μs, up to 160 samples can be used for moment estimation. Smaller sectors and/or slower scan rates can be chosen on the fly for customized operation depending on the meteorological phenomena being observed. A listing of AIR system characteristics is provided in Table 2.3, while a picture of the system is shown in Fig. 5.21. A depiction of its operating methodology is shown in Fig. 2.16.

Figure 2.15: *The AIR scanning a supercell near Great Bend, KS in 2014.*

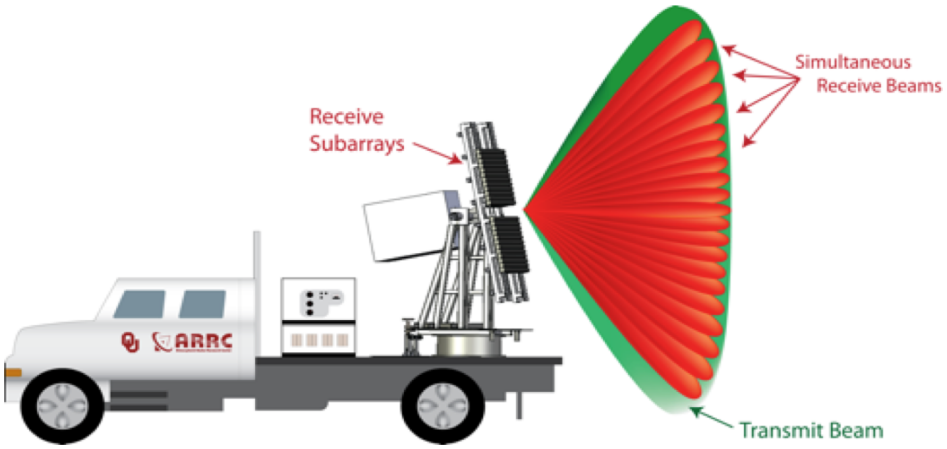

Figure 2.16: *Illustration of the AIR design methodology. A wide transmit fan beam (in the vertical dimension) illuminates an instantaneous RHI, while a receive array uses digital beamforming to form pencil beams on receive. Adapted from Isom et al. (2013)*

Table 2.3: *AIR system characteristics.*

Transmitter Type	Traveling Wave Tube
Peak Power	3.5 kW
Operating Frequency	9550 MHz
Sensitivity	$<$10 dBZ @ 10 km
Observable Range	40 km
Polarization	Horizontal
Transmit Beamwidth (V)	20.0 deg
Transmit Beamwidth (H)	1.0 deg
Transmit Gain	28.5 dBi
Array Aperture	1.2 $\times$ 1.8 m
Number of Elements	36
Array Gain	27 dBi
Receive Beamwidth	1.0 deg $\times$ 1.0 deg
Rotation Rate	Up to 20.0 deg s^{-1}
Rotation Angle	-80.0 deg to +100 deg
Pulse Length	1-15 μs
Pulse Repetition Frequency	1-2000 Hz
Maximum Duty Cycle	2%
Maximum Pulse Bandwidth	5 MHz
Waveform Type	NLFM
Range Resolution	37.5 m (oversampled to 30 m)

Due to the relatively low power, wide transmit beam, and attenuation concerns at X band, sensitivity is a major consideration for the AIR. To mitigate this issue, pulse compression is critical, providing nearly 7 dB in gain over

a 1 μs pulse. Additionally, the AIR has served as a developmental testbed for beamforming techniques. Since all 36 receive channels independently store I/Q data, numerous beamforming methods have been tested on collected datasets (Nai et al. 2013). While Capon and Robust Capon methods have shown promise for weather radar, the data presented in this paper are processed using Fourier beamforming.

Chapter 3

Waveform Design Techniques

3.1 The Need for Advanced Waveforms

The advent of phased array radar (PAR) technology in the weather community has sparked numerous studies regarding the feasibility for a future PAR network in the USA (Weber et al. 2007; Heinselman et al. 2008; Bluestein et al. 2009; McLaughlin et al. 2009; Weadon et al. 2009; Brown and Wood 2012). PAR offers not only rapid volumetric updates, due to the use of electronic steering, but also a number of additional benefits. Active phased array systems use low-power, solid-state transmit/receive elements, resulting in lower overall cost. In fact, low-power transmitters are not a new idea in the weather radar community. The use of solid-state radar transmitters is becoming a popular alternative to high-power klystron, magnetron, and TWT transmitters due to their relatively low cost and improved reliability. The potential benefits of inexpensive, low-power transmitters are wide and varied, however there are drawbacks associated with their use. Low sensitivity, the principal issue with utilizing low peak power, can be mitigated using a longer pulse with some variant of frequency modulation (i.e., pulse compression).

Pulse compression allows for the use of significantly lower power transmitters while achieving similar performance. Unfortunately, side effects are introduced when using a pulse-compressed waveform. Range sidelobes, for example, can become detrimental to radar system performance. A LFM results in peak sidelobes of -13.3 dB, effectively elongating the target in range, causing a distributed target to appear to the user. In order to combat this problem, target tracking applications have long used an amplitude-tapered transmit pulse (or "window") in order to identify individual targets. Windowing is known to significantly decrease range sidelobe intensity, alleviating the dilemma caused by using pulse compression. However, windowing could significantly prevent the transmitter from sending a full-power pulse, since the beginning and end of the pulse are cut significantly in power in order to create the windowed shape. Since many detection-only applications do not require a high level of sensitivity, this method has served as a viable option for inexpensive radar systems using pulse compression. In windowed waveforms, the loss in sensitivity can be as high as 5-6 dB. This loss can be quantified via:

$$\mathrm{SNR}_{\mathrm{loss}} = 10\log\left\{\frac{\left(\sum_{n=1}^{N} w_t w_r\right)^2}{N\left[\sum_{n=1}^{N}(w_t w_r)^2\right]}\right\} \tag{3.1}$$

where w_t and w_r represent the amplitude weighting function of the transmit waveform and receive window, respectively, and N is the length of the pulse

in samples. The loss is represented in dB below optimum, which would be achieved with no windowing on transmit and receive. Eq. (3.1) represents a normalized two-way SNR loss that can be formed via a generalization of processing gain methods described in Harris (1978) and Bharadwaj and Chandrasekar (2012) for either matched or mismatched filters.

As interest has grown in using pulse compression for weather radar systems, the method of windowing has come into question. Instead of point targets, weather radar systems deal with distributed targets over a high dynamic range (anywhere from -10 to 75 dBZ). With many windowing methods cutting power efficiency by greater than 3 dB, and as high as 6 dB, weak distributed weather targets suffer greatly from the drop in sensitivity associated with a window, resulting in a lowered SNR and lower overall observability for reflectivity measurements. The loss in SNR leads to the desire to improve sensitivity for a weather radar scenario, meaning a method other than windowing must be used in order to suppress range sidelobes.

This chapter describes a method for designing optimized frequency modulated (OFM) pulse compression waveforms designed using a genetic algorithm. The framework takes into account individual system characteristics and performance measures in order to design a low SNR loss (high power efficiency) waveform for use with an atmospheric weather radar utilizing pulse

compression. In a general sense, the technique presented in this chapter significantly improves not only theoretical sidelobe performance, but also significantly closes the gap between theory and practice in the actual system by tailoring the design to the hardware being used. This method has the potential to be utilized within all types of hardware, ranging from weather radar to military solutions such as airborne and satellite-based radar systems.

3.2 Pulse Compression Waveform Background

While pulse compression has been utilized in military radar applications for many decades, the idea of using pulse compression with weather radar systems is not as well developed, and has changed considerably over the past 30 years. The first methods used for weather radar pulse compression appeared in the 1970s, and were based on Barker codes (Ackroyd and Ghani 1973; Austin 1974). While this produced sidelobes lower than a linear frequency chirp, results were quite limited, and the sidelobes were less desirable for the high sensitivity needs of a weather radar system. After a lull in advancement in the field, a number of new techniques arose in the 1990s and 2000s. Keeler and Hwang (1995) presented one of the first holistic studies involving what was known about pulse compression for weather radar at the time. This was the first mention of the possibility of higher spatial and temporal resolution using phased array antennas for weather observations, and helped define many of

the parameters still used to analyze waveform performance. Also of concern to weather radar specifically was how tolerant pulse compression waveforms would be to Doppler shifts. Bucci and Urkowitz (1993) showed successful simulations indicating a lack of significant degradation using certain types of waveforms.

A number of simulations using Barker codes were performed (Baden and Cohen 1990; Bucci et al. 1997; Mudukutore et al. 1998; Duh et al. 2004), showing limited usefulness for weather radar. Around the same time, Griffiths and Vinagre (1994) presented a study involving the use of a piecewise LFM, also known as nonlinear frequency modulation (NLFM), for use with satellite-based weather radar systems (shown in Fig. 3.1). This was based on original work by Cook and Paolillo (1964), but adapted for use in an actual radar system. By introducing slightly different LFM rates at the edges of the waveform, and keeping LFM throughout the center of the waveform, lower sidelobes were made possible. In order to achieve the desired sidelobes of -62 dB, however, significant windowing was still used in conjunction with the NLFM technique.

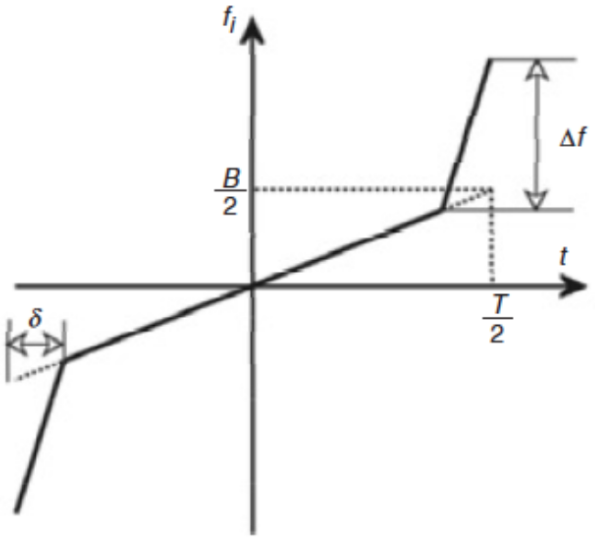

Figure 3.1: *A model of the earliest form of nonlinear frequency modulation for pulse compression. Three distinct areas of different linear chirp rates are apparent, with the two ends being equal in rate. This is known as a "stepped nonlinear waveform," and has been adapted from Cook and Paolillo (1964) and Griffiths and Vinagre (1994).*

De Witte and Griffiths (2004) presented a "continuous NLFM" waveform which improved upon the piecewise NLFM waveform from Griffiths and Vinagre (1994). An amplitude taper was used on receive only, leading to the use of a mismatched filter (shown in Fig. 3.2). While -70 dB sidelobes were achieved in theory, it was not clear how significantly the mismatched filter affected SNR. Further investigation shows the use of a Nuttall window on receive, resulting in expected two-way SNR loss as high as 2.96 dB. Also of significance was their discussion regarding NLFM Doppler tolerance. In cases where the NLFM is symmetric, it was shown that shifts in the ambiguity function with

higher Doppler velocities were not as significant as other pulse compression waveform design methods. This was shown again by George et al. (2008), a study which also discussed elements of system calibration and blind range mitigation (which will be covered in later sections of this chapter).

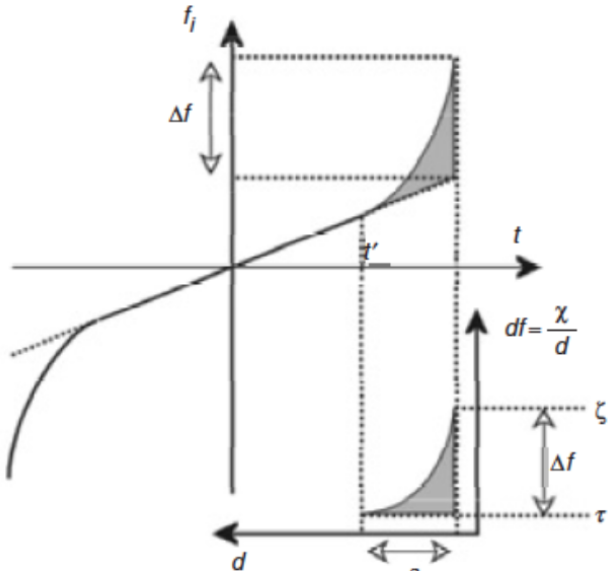

Figure 3.2: *An example of the first type of continuous nonlinear frequency modulated waveform, from De Witte and Griffiths (2004). Additional flexibility allowed for lower sidelobes, but some type of windowing was still needed in order to achieve desired sidelobe levels.*

Few examples of actual weather data collection using pulse compression exist in the literature. One of the first weather datasets collected using pulse compression was presented in O'Hora and Bech (2007). Despite relatively few examples of weather data collected using pulse compression in the literature, there have been a number of systems developed that utilize pulse compression for weather observations. Weighted NLFM methods have been used

recently with low-power, high-frequency radar systems. Carswell et al. (2008) described a solid-state, dual-polarized, dual-wavelength precipitation Doppler radar which operates at Ka band. Additionally, Hirth et al. (2012) presented initial data collected using Ka-band research weather radar systems.

There have also been a limited number of optimization studies regarding pulse compression with weather radar systems, with most focusing on only small details of the waveform, as opposed to a holistic approach that would optimize a waveform from the beginning of the design phase to actual deployment in a system. Among such optimization studies, topics varied from coded waveforms (Ackroyd and Ghani 1973; Baden and Cohen 1990), to window design (Yichun et al. 2005), to mismatch filter design (Cilliers and Smit 2007). Wang et al. (2008) proposed the use of a genetic algorithm to optimize the inter-pulse frequency step in a stepped LFM, however did not explore the possibility of optimizing the entire waveform and minimizing window usage. More recently, Bharadwaj and Chandrasekar (2012) presented a study regarding waveform design for solid-state weather radar systems. While a similar NLFM waveform to De Witte and Griffiths (2004) was used with a mismatched filter, many new elements were presented. Discussions regarding characterization of the SNR loss, as well as the important issue of "blind range" mitigation offered a refreshed look at the reality of using pulse compression with weather radar.

In the past decade, nearly all forms of pulse compression used methods either derived from De Witte and Griffiths (2004), or from the stationary phase principle, with various types of windowing (Ge et al. 2008). Very recently, methods using minimum mean square error (MMSE; Li et al. 2015) and adaptive pulse compression (Wang et al. 2015) have been prevalent in the literature. Additionally, Pang et al. (2015) presented a NLFM method for minimal windowing using simulated annealing, and Blunt et al. (2014a,b) explored polyphase-coded frequency modulation. Of particular interest was a recent set of studies exploring the use of spectral shaping (Jakabosky et al. 2015) and over-coded orthogonal frequency division multiplexing (Jakabosky et al. 2013, 2014) for transmitter-in-the-loop optimization. By shaping the pulse in the spectral domain rather than the time/space domain, significantly lowered sidelobes with minimal windowing was possible by drastically increasing the degrees of freedom.

The best solutions prior to Kurdzo et al. (2014) and Jakabosky et al. (2015) have lacked flexibility to provide low sidelobes without significant windowing. Additionally, while waveforms could be designed with somewhat acceptable power efficiency and theoretically low sidelobes, the implementation through actual systems often results in significantly degraded performance.

3.3 Waveform Design Methodology

3.3.1 Frequency Function and Bézier Curves

The key element to any NLFM waveform is the frequency function. By allowing for a sharper change in frequency along the edges of the frequency function, an effective windowing can be applied to a rectangular waveform. This is due to the fact that less emphasis is placed on the highest "edge" frequencies. De Witte and Griffiths (2004) proposed a commonly used method to design a NLFM waveform, however the flexibility of the function was limited, resulting in a relatively small solution set. The goal for the described method is to utilize global optimization techniques in order to match a frequency function to hardware specifications.

While numerous iterations of polynomial-based frequency function representations were attempted, it was found that a more flexible function method was necessary. In order to provide this flexibility, Bézier curves were employed, which are commonly used in vector graphics applications (Farin 1996). These curves can be implemented in software by defining a straight line and a series of "anchor points." The anchor points can be "pulled" using a vector stemming from the line (defined by an X and Y coordinate in a two-dimensional plane). Fig. 3.3 demonstrates the application of Bézier curves

to frequency function design. When the anchor points are pulled in various directions, unique shapes can be made from an originally straight line. This significantly increases the overall solution set (and therefore search space within an optimization framework) due to the much higher flexibility for line shapes.

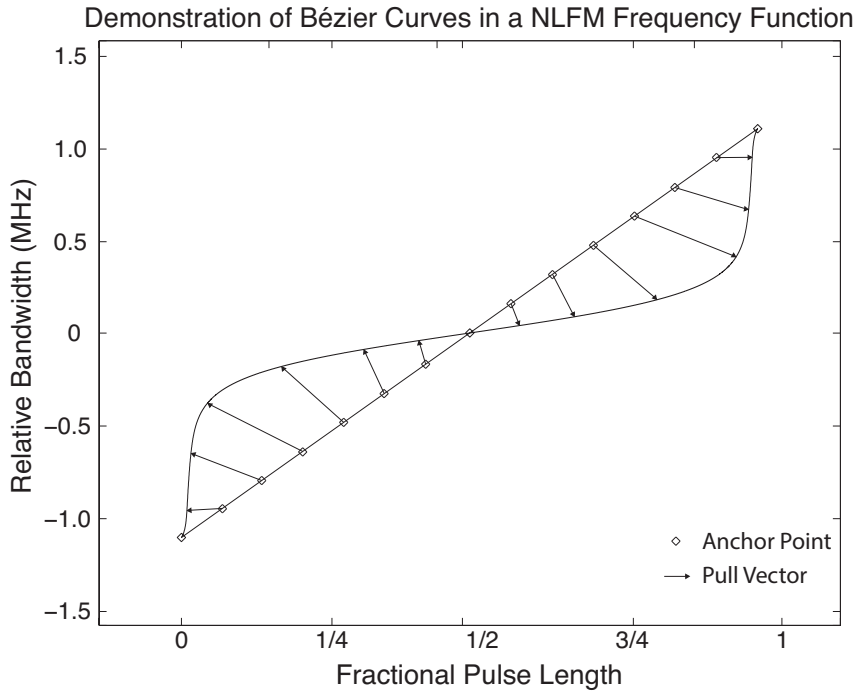

Figure 3.3: *Demonstration of how a straight line with fixed anchor points can be bent into a complex function using the method of Bézier curves. The anchor points are pulled using a series of vectors. These vectors can be used as variables within an optimization framework in order to design flexible frequency functions.*

By making use of a Bézier curve for the design of the frequency function, an optimization framework can be developed. For this study, 15 evenly-spaced anchor points were utilized along a line spanning the pulse length (along the

abscissa) and available bandwidth (along the ordinate). This example is illustrated in Fig. 3.3. Of the 15 anchor points, the ends and the middle point were locked to the bounds of the design, leaving 12 total changeable anchor points. Due to the desire for symmetry for Doppler tolerance (Bucci and Urkowitz 1993; Griffiths and Vinagre 1994; Levanon and Mozeson 2004; George et al. 2008), the anchor points are mirror images, meaning only six are optimizable. Given that each anchor point contains both an X and Y coordinate, a total of 12 degrees of freedom remain for optimization. Within the optimization, the axes are normalized to the pulse length and available bandwidth, and are sampled at a user-defined resolution which is based on computational availability. For the examples in this chapter, a resolution of 2,001 points was used in both dimensions, resulting in 2,001 possible values for each of the 12 variables. This equates to 4.12×10^{39} possible solutions for the frequency function. It should be noted that depending on desired performance, as well as the availability of additional computational power, the search space can be much larger. The division of the normalized frequency function into 2,001 possible values in each dimension was the feasible resolution for the presented cases.

3.3.2 Optimization Technique

Due to the large search space, genetic algorithms were chosen based on their simplicity, flexibility, and speed. Genetic algorithms, specifically, are capable

of quickly finding near-global optimum solutions to both simple and complicated non-linear problems. Genetic algorithms offer one of the most consistent methods to achieve global optimum in a computationally feasible fashion (Holland 1975). While it is possible that other methods could result in slightly more accurate or timely computations, it was found that genetic algorithms provided successful results in a reasonable amount of time.

The genetic algorithm progresses by changing the values of the 12 parameters, which represent the pull vectors of the Bézier anchor points. The predetermined boundary conditions for the optimization are simply the normalized values of pulse length and available bandwidth, which are divided into resolution segments based on the available computational power. Since the actual values of pulse length and bandwidth are not used in the optimization due to normalization, it is the ratio between time and bandwidth which is important in determining the final shape of the frequency function. Each of the 12 parameters contributes to a vectorized "pull" of the originally linear frequency function into a non-linear shape, and can be represented in numerical form for operation within the genetic algorithm framework.

While the genetic algorithm uses the 12 degrees of freedom and their predetermined bounds for optimization, there must still be a fitness function, which defines the goal for optimization. Two main factors were determined as being critical in optimization performance: peak side lobe level (PSL) and

mainlobe width (MLW). Both indices can be calculated using a theoretical matched filter response. PSL is defined as the highest point in the compressed result outside of the mainlobe. It is important to note that this may not always be the first sidelobe. MLW is defined as the null-to-null width of the mainlobe, and is a proxy both for range resolution and general waveform performance.

The use of MLW within the frequency function, specifically, goes beyond the scope of simply defining waveform performance based on the 3-dB range resolution convention. By focusing on null-to-null MLW, the algorithm performs much more efficiently than using the more-common 3-dB main lobe resolution. In this manner, the 3-db range resolution is governed by the bandwidth of the chirp. However, in order to maintain an acceptable mainlobe shape, the MLW is constrained within the algorithm. In the examples provided in this chapter, a null-to-null MLW of 600 m was set as a constraint so that the mainlobe did not become too wide for a weather radar purpose. The fitness function used in the optimization framework is:

$$F = \frac{PSL}{MLW} \tag{3.2}$$

where the units of PSL are in dB and the units of MLW are in meters.

The genetic algorithm attempts to minimize the fitness function by decreasing PSL and/or decreasing MLW. The algorithm can change these parameters by altering the original 12 degrees of freedom which define the frequency

function, then compressing the pulse and checking the indices on a successive generation. This process repeats, following standard genetic algorithm procedures, until a stopping criterion is met. Typically, stopping criteria are defined as a minimum change in average fitness, and/or a significant number of generations without an improvement in fitness. Fig. 3.4 offers a visual representation of the genetic algorithm optimization procedure.

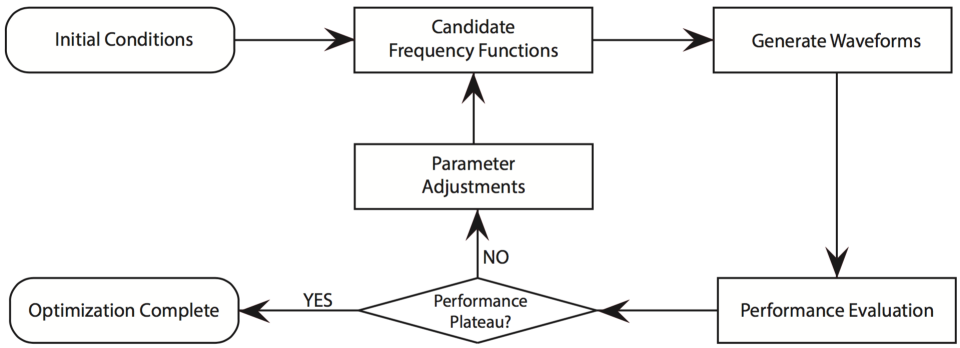

Figure 3.4: *Flowchart for the genetic algorithm. Potential frequency functions are converted into waveforms based on system specifications, and their theoretical matched filter responses are tested for performance. If sufficient time has passed without an improvement in performance, based on the specified fitness function, the optimization ends.*

3.4 PX-1000 as a Testing Platform

The platform being used for testing waveform design at the University of Oklahoma is the PX-1000 transportable polarimetric X-band radar system (Cheong et al. 2013a). For the results described in this chapter, PX-1000 operated via two independent solid-state transmitters (one for each polarization), each

operating at 100 W peak power. In order to achieve the desired sensitivity for weather observations despite such low transmit power, pulse compression must be used. A chirp bandwidth of 4 MHz is available for waveform design, and the maximum pulse length is 69 μs, yielding a maximum time-bandwidth product of 276. Additionally, a coupled transmit waveform is recorded on each channel for use as a matched filter. This feature is critical for determining waveform performance and the application of pre-distortion.

The system is transportable, and is equipped with mobile internet for operation from remote locations. An in-house-developed software platform is capable of fully operating the system, ranging from waveform selection, to scanning strategy, to data management. Raw time series data are available for experimental advanced signal processing, however moment data are automatically generated and available for simple viewing.

3.4.1 Blind Range Mitigation

While pulse compression greatly improves the range resolution from such a long pulse (up to 69 μs), we are left with an undesirable side effect: the blind range. While the system is transmitting, no receive data can be collected, meaning that a large unobservable area exists around the radar. For a 69 μs pulse, this equates to a circle of radius 10.35 km, or about one-sixth of the total observable range of the system.

In order to combat this issue, the method described in Cheong et al. (2013a) is used. Instead of utilizing the full 69 μs and 4 MHz bandwidth available for a long pulse, only 67 μs and 2.2 MHz is used for the long pulse. The remaining time and bandwidth are used for an adjacent short pulse, which is called the "fill pulse." These two sub-waveforms are combined into one time-frequency multiplexed transmit waveform which utilizes all available pulse length and bandwidth, and are separated in processing using different matched filters for different ranges (see Fig. 3.5). The area within the blind range from the long pulse is filled with data from the short pulse. While sensitivity is low with a short pulse and low transmit power, the distance covered in the blind range is sufficiently small for acceptable sensitivity.

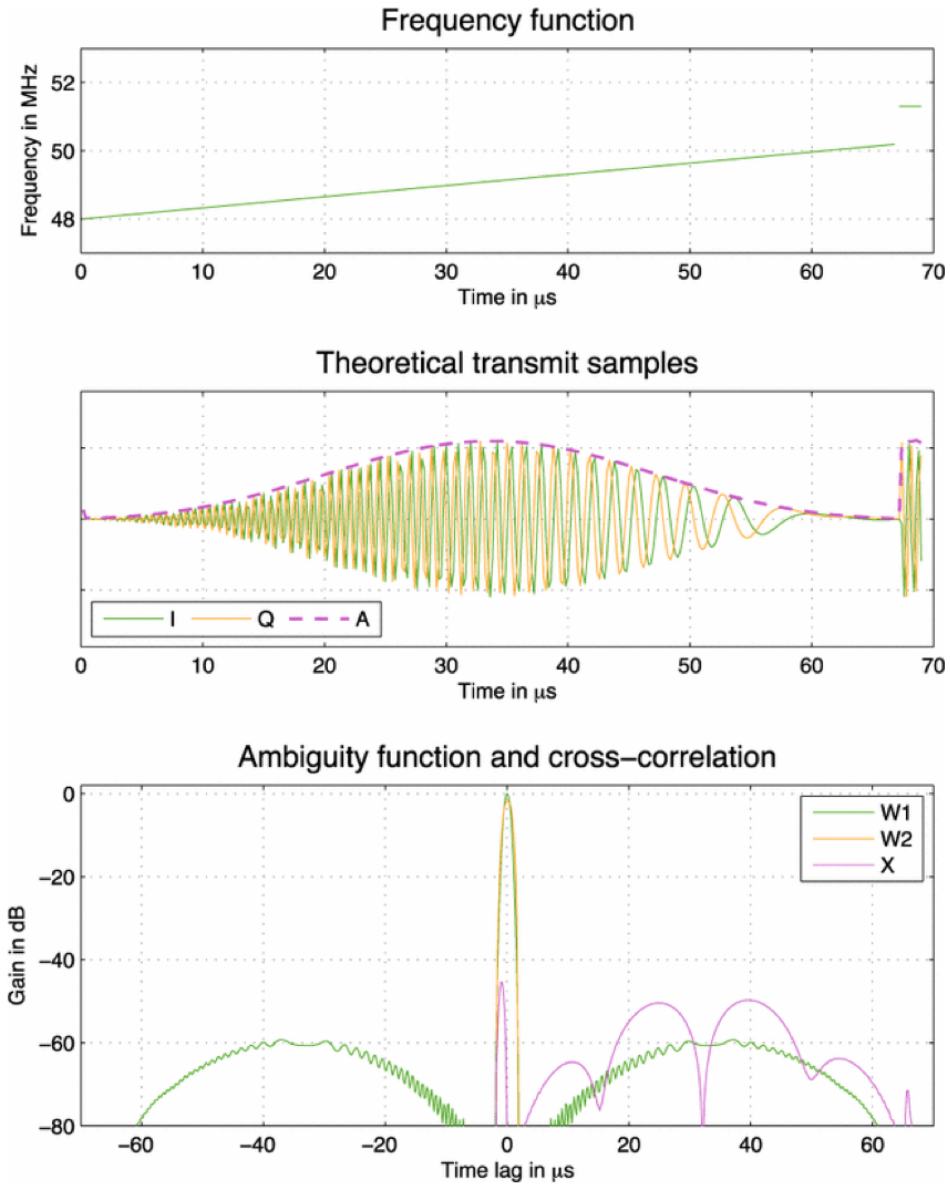

Figure 3.5: *Time-frequency multiplexing used for blind range mitigation on PX-1000. The frequency steps (at intermediate frequency), time domain amplitudes and I/Q, and compressed result are shown in the top, middle, and bottom insets, respectively. Figure provided by Boon Leng Cheong.*

3.5 Waveform Optimization Results

While the technique described previously is capable of designing high performance waveforms in theory, even for low time-bandwidth product radar systems, there are a number of additional steps that must be taken in order to design a waveform for use in a real-world system. The following three sections describe the waveform design from a purely theoretical standpoint, the changes applied in order to account for transmitter and system distortions, and comparisons with other methods.

3.5.1 Theoretical Waveform Design

In theory, a high-performance waveform for the PX-1000 system with two-way SNR loss of 0.05 dB can be designed, which represents a large increase over the windowed waveform in Fig. 2.5a, for example. In a real system, however, there are typically undesired edge characteristics in the transmitter. This means that large spikes of distortion typically occur at the extreme edges of the pulse, which must be mitigated. These major distortions occur most often at both the rising and falling edges of the pulse, however, additional "droop" often occurs with long-pulse waveforms in a solid-state transmitter. In the next section, accounting for most of the distortion in the system will be explored, however these sharp edge distortions are particularly difficult to model. For this reason, the first step to designing a real-world waveform is

to start with a slightly windowed pulse in the optimization. Drastically decreased edge distortions are observed by using a theoretical design window with a 0.24 dB SNR loss. This window is defined as a raised cosine taper on both ends of the waveform with a roll-off factor of 0.1, and assists with the implementation through a real-world solid-state transmitter that contains inherent imperfections.

After the window is applied, the parameters of the system are input into the optimization framework. As noted previously, the specifications of this system include 4 MHz bandwidth and a pulse length of up to 69 μs. However, since the long-pulse will be designed separate from the fill-pulse, the input to the optimization framework must only utilize the available bandwidth and pulse length for the long pulse. Therefore, the specifications input to the framework for waveform design in this case are 2.2 MHz bandwidth and 67 μs pulse length, since the fill-pulse utilizes the remaining bandwidth and pulse length specifications. The optimized frequency function for PX-1000 is shown in Fig. 3.6. Fig. 3.7 shows the theoretical matched filter response of the designed waveform for PX-1000 system specifications. A window with two-way SNR loss of 0.24 dB is used, with resulting peak sidelobes of -59 dB, integrated sidelobes of -37 dB, and 3 dB range resolution of 120 m. While similar sidelobes could be achieved using amplitude modulation with the same system

characteristics, the lack of aggressive windowing results in significantly lower power loss as well as high 3-dB range resolution.

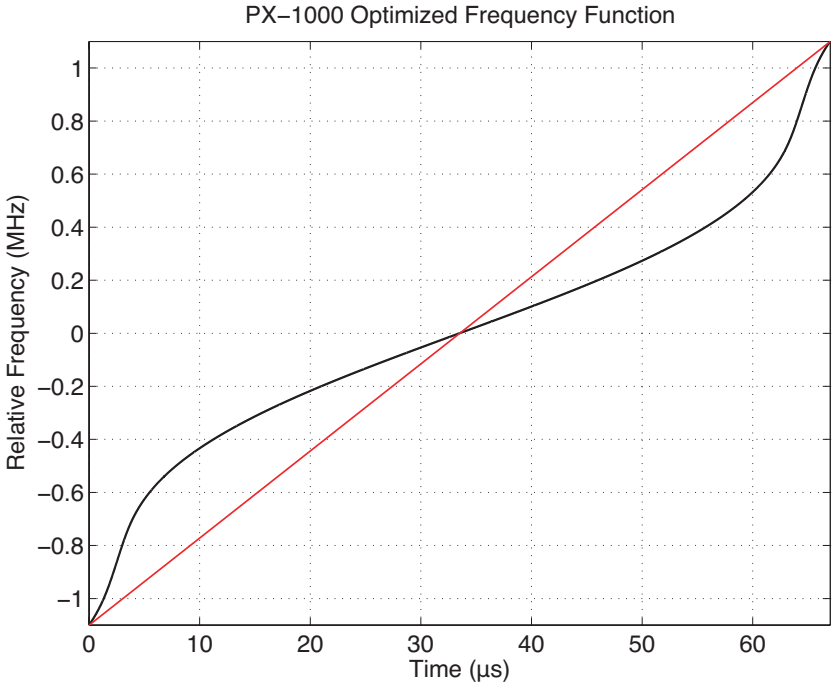

Figure 3.6: *PX-1000 frequency function (black line), with time on the abscissa and frequency on the ordinate. The chirp spans 2.2 MHz, with 1.1 MHz on either side of the carrier frequency, and chirps nonlinearly over 67 µs. A reference LFM chirp is shown in red.*

A number of other positive aspects of the theoretical waveform are also apparent. In addition to relatively low integrated sidelobes, there is also a consistent drop in peak sidelobe level. Additionally, as predicted by Bucci and Urkowitz (1993), Griffiths and Vinagre (1994), and George et al. (2008), the Doppler tolerance of the optimized waveform is within acceptable range for weather targets. Due to the forcing of a symmetric frequency function, Fig. 3.8 shows little shift of the mainlobe in the ambiguity function with increasing

Doppler velocities. The only noticeable side effect at 50 m s^{-1} is an increased peak sidelobe level of -40 dB on one side of the mainlobe. For velocities of 25 m s^{-1}, the peak sidelobe level raises to only -46 dB. In each case, the integrated sidelobes remain nearly constant outside of the peak sidelobe, leading to acceptable overall performance in extreme conditions. While this distortion effect at high Doppler velocities may be unavoidable, the symmetric nature of the NLFM design leads to a minimization of error compared with other methods.

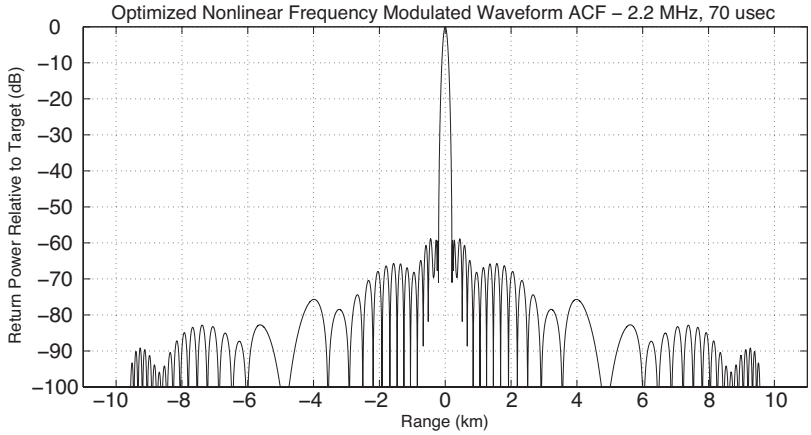

Figure 3.7: *Theoretical autocorrelation function for a waveform optimized using 2.2 MHz of bandwidth and a 67 µsec pulse length (the specifications for PX-1000). Peak sidelobe level is -59 dB, integrated sidelobes are -37 dB, and 3 dB range resolution is 120 meters, with a power efficiency of 95%, resulting in only 0.24 dB of SNR loss.*

In terms of sensitivity gains over more traditional, heavily-windowed methods, the optimized waveform displays significant improvements. Fig. 3.9

shows an increase in sensitivity of approximately 2.95 dB throughout the entire range of operation. At 50 km, for example, the optimized NLFM waveform displays a sensitivity under 14 dBZ, while the WLFM lacks observation of echoes below 17 dBZ. This improvement in sensitivity is a critical component in any weather radar platform. It is important to note that there is an abrupt change in sensitivity near the 10 km mark. This is due to the switch between use of the short-pulse and the chirped long-pulse (the edge of the blind range). For comparison, the popular waveform technique described in De Witte and Griffiths (2004) is also included in Fig. 3.9. De Witte and Griffiths (2004) utilize a mismatched Nuttall window on receive.

The Nuttall window is extremely aggressive, resulting in an example where even a mismatched filter can have significant two-way SNR loss (in this case 2.96 dB compared to 3.19 dB with the 70 dB Kaiser window matched filter LFM). The theoretical sensitivities in Fig. 3.9 are based on the weather radar equation, from which reflectivity factor can be calculated (Doviak and Zrnić 1993):

$$Z = \frac{r^2 l^2 (4\pi)^3 16 \ln 2 P_r \lambda^2}{P_t g^2 c \tau \pi^6 \theta^2 |k_w|^2} \tag{3.3}$$

P_r is set to the noise floor of the system, which is equal to -110 dBm for the PX-1000 platform.

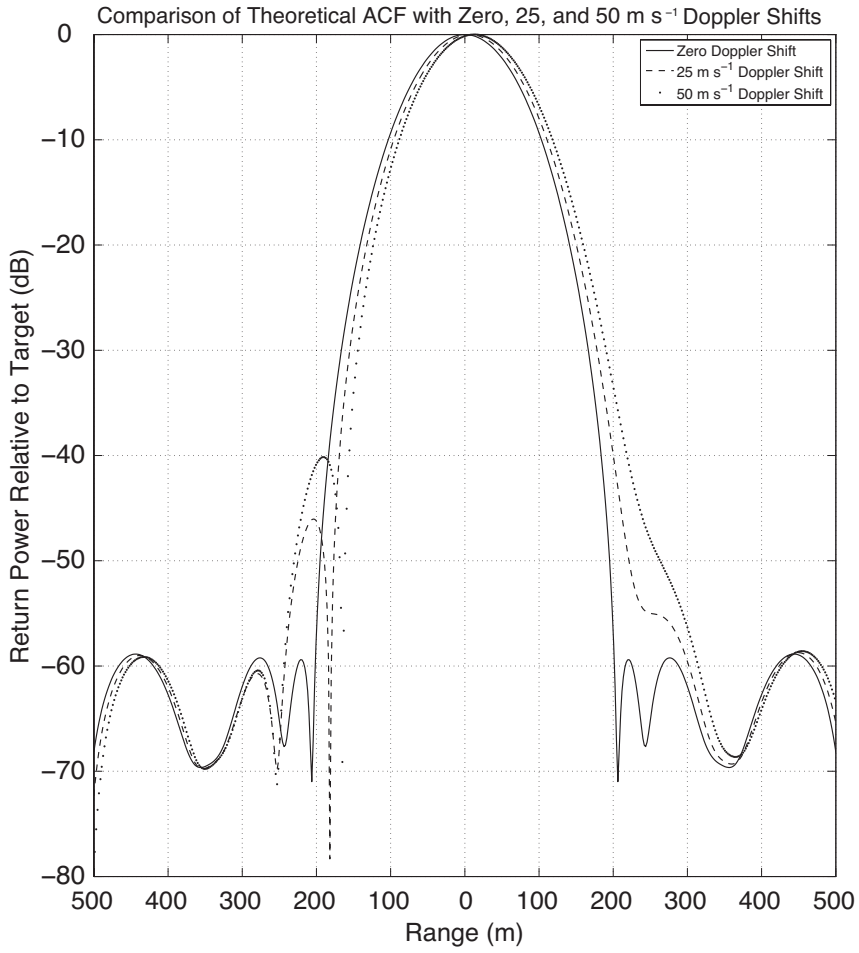

Figure 3.8: *Cuts through the ambiguity function for a theoretically optimized waveform for the PX-1000 system at 0 m s^{-1}, 25 m s^{-1}, and 50 m s^{-1} Doppler shifts. SNR loss of 0.24 dB yielding from a slight raised cosine window is achieved, with peak sidelobes of -59 dB in the compressed result at zero Doppler shift. An increase to 50 m s^{-1} in Doppler shift shows little distortion in the mainlobe, and an increase in peak sidelobe level on one side of the mainlobe. Even at higher Doppler shifts, integrated sidelobes outside of the peak sidelobes remain nearly constant, resulting in acceptable overall performance.*

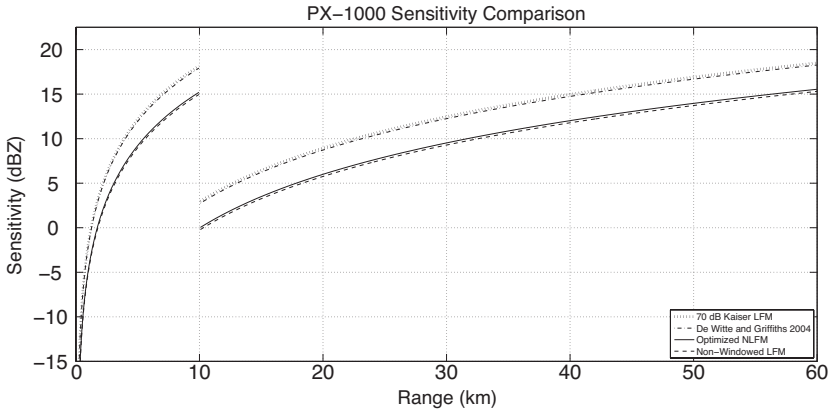

Figure 3.9: *Theoretical sensitivity comparison between a 70 dB Kaiser window LFM (3.19 dB SNR loss), the Nuttall window mismatched waveform described in De Witte and Griffiths (2004) (2.96 dB SNR loss), the optimized NLFM (0.24 dB SNR loss), and a rectangular LFM (0.00 dB SNR loss). A sensitivity increase of 2.95 dB from the WLFM to the optimized NLFM is observed throughout the operating range. Additionally, the optimized NLFM theoretical sensitivity is within 0.24 dB of the rectangular LFM, indicating very high power efficiency. Note, lower values indicate higher sensitivity, and the first 10 km display poor sensitivity due to the short pulse used to fill the blind range.*

The use of a matched filter in waveform design and processing is supported by various results in the literature, most notably those contained within Harris (1978). While a mismatched filter, even with lower bandwidth on receive, would result in a lower noise floor due to lower receiver noise, Harris (1978) showed that no combination of mismatched filters can overcome the gain in sensitivity afforded by using a matched filter. While there is no separate theorem for distributed targets such as hydrometeors, system tests with PX-1000 consistently verify this concept for weather observations.

A comparison of the theoretical power spectrum between a non-windowed LFM, a 70 dB Kaiser window LFM, and the optimized NLFM, all at 2.2 MHz chirp bandwidth, is provided in Fig. 3.10. The optimized waveform, due to the lack of windowing, shows a slight broadening in the spectrum above -75 dB compared with the heavily windowed waveform. However, the optimized waveform utilizes distinctively less spectrum than the non-windowed LFM. It is important to note that from a spectral efficiency standpoint, the use of a slightly windowed, matched filter waveform will use less overall spectrum than a rectangular transmit waveform with a mismatched receive filter, despite the slight increase in receiver noise.

Finally, in order to measure the effects of system phase noise on the waveform technique, a series of 100 phase noise simulations was averaged in Fig. 3.11. As expected, an increase in phase noise results in decreased sidelobe performance, similar to the results shown in Bharadwaj and Chandrasekar (2012). The estimated phase noise of PX-1000, however, is only approximately 0.05 deg, which is marked with a black diamond in Fig. 3.11. At this level, the effect on waveform PSL performance is approximately 0.08 dB. Systems with higher phase noise will show decreased performance as phase noise increases.

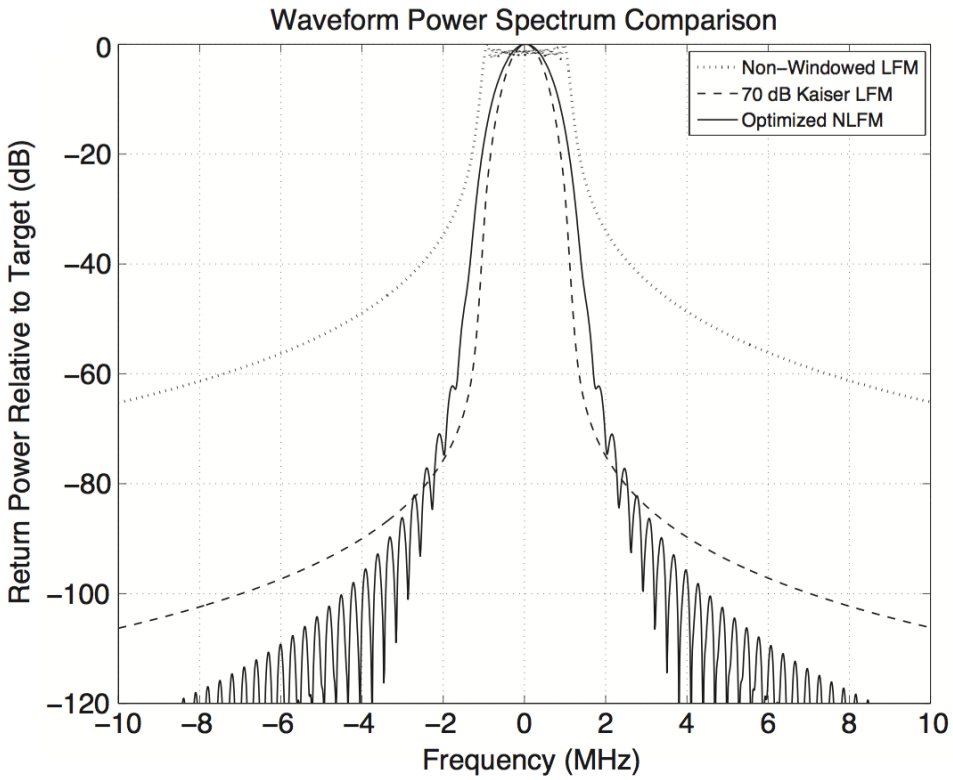

Figure 3.10: *Theoretical power spectrum comparison between a rectangular LFM, 70 dB Kaiser window LFM, and the optimized NLFM, all with 2.2 MHz chirp bandwidth. The lack of windowing on the optimized waveform causes a slight broadening compared with the windowed LFM in the spectrum above -75 dB.*

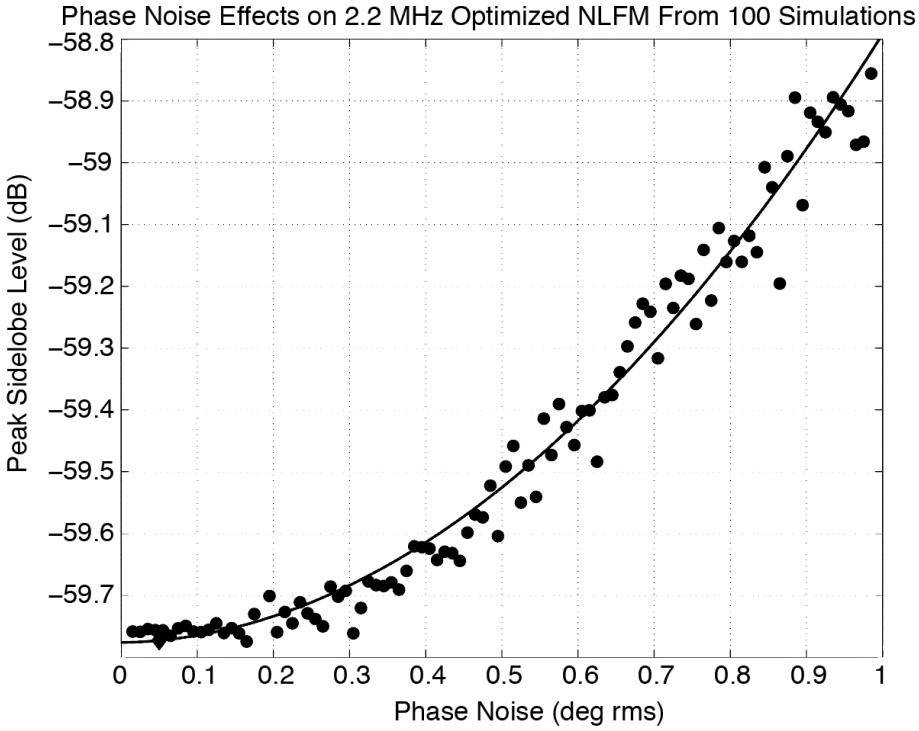

Figure 3.11: *Estimate of phase noise effects on the 2.2 MHz theoretical OFM waveform using an average of 100 simulations. A polynomial fit is shown via the thick black line, and the system phase noise estimate of PX-1000 is marked with a black diamond (0.05 deg), showing no appreciable detrimental effects in the system.*

3.5.2 Accounting for Transmitter Distortion

A significant advantage to using an optimization technique for waveform design is the ability to build "pre-distortion" into the design. Unlike techniques such as the stationary phase principle and other amplitude-modulated waveform design methods, which often produce a single result, optimization allows

for an adjustment within the design process, which can account for transmitter imperfections. This is achieved by first transmitting a non-optimized LFM waveform through the system in question, and measuring the coupled pulse. The coupled pulse is recorded in the time series data of each channel for precise matched filtering in processing. The measured pulse, which is affected by transmitter distortions, is then compared with the intended transmit pulse in the frequency domain, allowing for the generation of an effective transfer function of the system. The transfer function is then inserted into every calculation of the matched filter response in the optimization, effectively modeling the expected distortion by the transmitter. Fig. 3.12 shows the added step in the optimization procedure in order to account for the transmitter distortion.

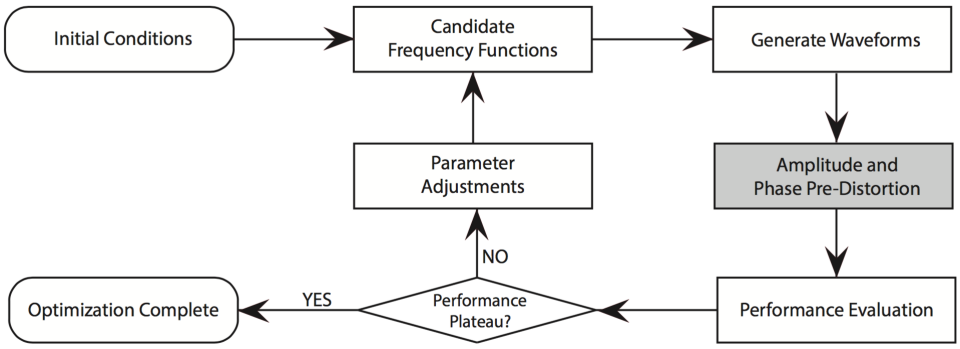

Figure 3.12: *Same as Fig. 3.4, but with amplitude and phase pre-distortion taken into account. The pre-distortion takes measured transmitter and system fluctuations into consideration before testing waveform performance.*

This technique, which has been used in various other system implementations, is an attempt at predicting what will happen to the waveform when

it is passed through the non-ideal transmitter, and can be incorporated into any iterative waveform optimization process. The resulting optimized waveform, when autocorrelated, does not appear to be optimal. However, when it is sent through the actual system, the resulting transmit pulse displays significantly improved performance. This additional method can only be used in an optimization design technique in which the waveform can be dynamically changed from generation to generation. By accounting for expected transmitter distortions, the actual performance in the system becomes much closer to theory.

When combining pre-distortion with the flexibility of the method used in the optimization algorithm, the resulting observed waveform through the real-world system achieves significantly better performance than previous methods. This method can be used with any system capable of using pulse compression, and routinely achieves better PSL sidelobe performance than heavily-windowed methods while utilizing high power efficiencies with SNR loss as low as 0.05 dB. The resulting sensitivity gain in our system tests is as high as 2.95 dB compared with methods which utilize heavy windowing. Additionally, with the built-in pre-distortion, sidelobes are generally much closer to theoretical designs.

Despite the ideal theoretical waveform response shown in Fig. 3.7, the waveform actually transmitted by PX-1000 results in a much less desirable

pulse (Fig. 3.13a). Fig. 3.14 shows the compressed result of the coupled pulse after sending the theoretically optimal waveform through the transmitter. It is clear that performance has been significantly degraded, and the transmitter results in a number of undesirable effects.

The measured coupled pulse results in peak sidelobes of -42 dB, integrated sidelobes of -26 dB, and 3 dB range resolution of 120 meters. The SNR loss has remained at 0.24 dB. With a theoretical waveform design resulting in -59 dB and -37 dB peak and integrated sidelobes, respectively, the distortion clearly leads to a waveform that is not acceptable. In order to mitigate this issue, a measured inverse transfer function is used in the optimization process (see Fig. 3.12) to account for transmitter distortion.

While a slightly more aggressive window with 0.24 dB SNR loss, rather than a window with SNR loss of 0.05 dB, was used in the original theoretical design in order to lessen noisy transmitter edge effects, there are still distortions which occur away from the edges of the pulse. Both frequency and amplitude distortions occur, with the most obvious being a "droop" in amplitude from the beginning of the pulse to the end. This is where the inverse transfer function accounts for distortions accurately, and can drastically improve performance.

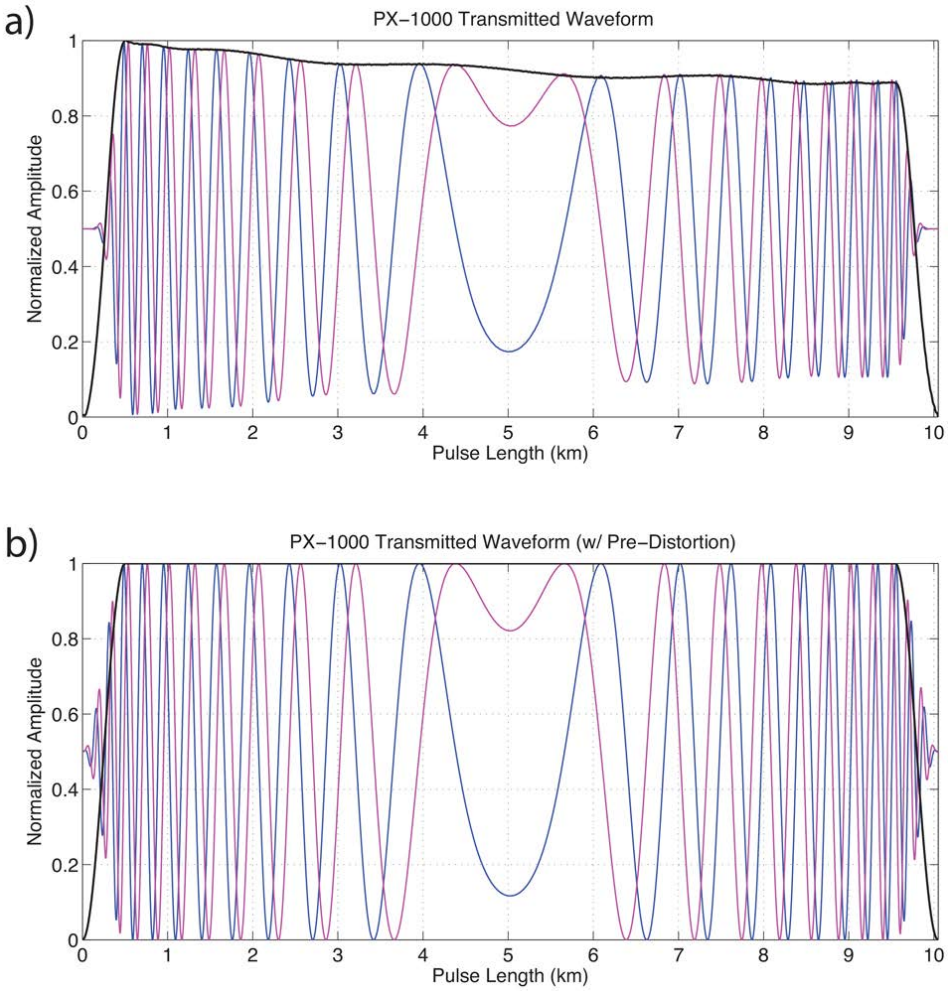

Figure 3.13: *PX-1000 pass-through measurements of optimized waveform. (a) With no pre-distortion. (b) With pre-distortion applied.*

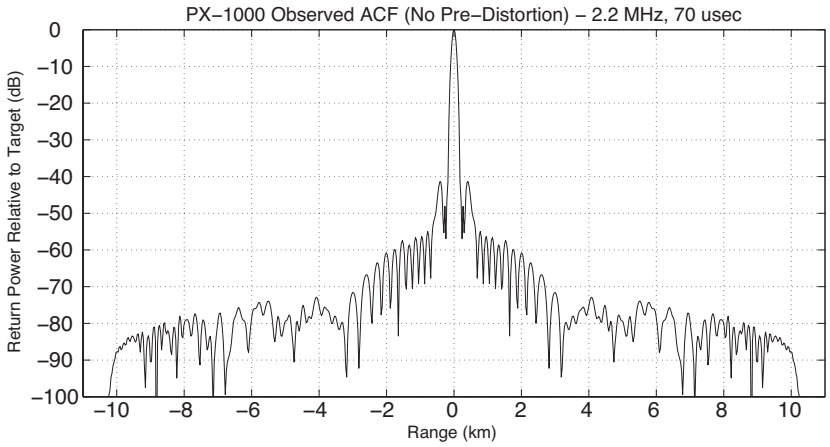

Figure 3.14: *Observed compressed pulse for a waveform optimized using 2.2 MHz of bandwidth and a 67 μsec pulse length (the specifications for PX-1000) without accounting for transmitter distortion. Peak sidelobe level is -42 dB, integrated sidelobes are -26 dB, and 3 dB range resolution is 120 meters, with a power efficiency of 95%.*

Fig. 3.15 shows the coupled result of the compressed waveform from Fig. 3.7 optimized with pre-distortion taken into account, while Fig. 3.13b shows the corrected pulse in the time domain. Fig. 3.15 can be directly compared to Fig. 3.14 to see improvement of the compressed waveform through the actual system. Actual observed sidelobes have decreased from -42 dB to -52 dB, and integrated sidelobes have decreased from -26 dB to -33 dB. Two-way SNR loss has remained at 0.24 dB, and 3 dB range resolution has remained at 120 m. The results are significantly closer to theoretical values.

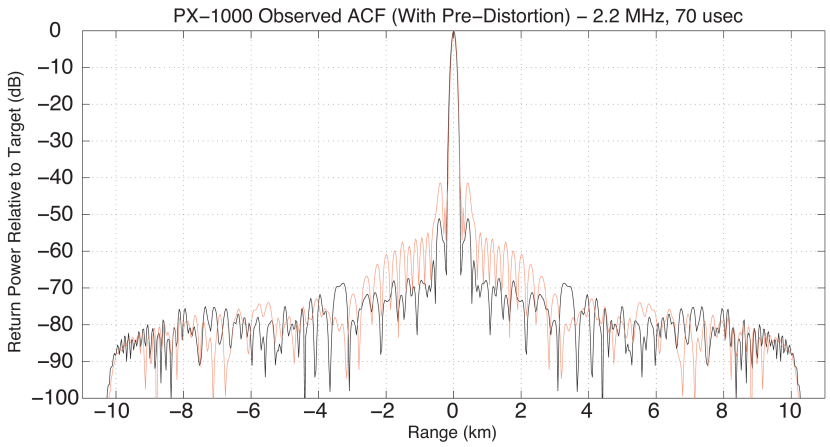

Figure 3.15: *Observed compressed pulse for a waveform optimized using 2.2 MHz of bandwidth and a 67 µsec pulse length (the specifications for PX-1000) and accounting for transmitter distortion. Peak sidelobe level has improved to -52 dB, integrated sidelobes are -33 dB, and 3 dB range resolution is 120 meters, with a power efficiency of 95% and two-way SNR loss of 0.24 dB. An underlay of the compressed pulse without taking transmitter distortions into account (from Fig. 3.14) is shown in red.*

The pre-distortion is completed using an inverse transfer function method that corrects exceedingly well for amplitude distortions, but does not account very well for phase distortions. Although this method is simplistic, its results are clear in Fig. 3.16 where the amplitudes of the original, the distorted signal, and the corrected signal are shown. It should also be noted that due to effects from the Gibbs phenomenon (Wilbraham 1848; Hewitt and Hewitt 1979), this method will not be capable of correcting high-amplitude distortion on pulse

edges. These situations have been seen in certain types of transmitters, specifically TWTs, and often require a heavier window than SSPAs. Example systems that use TWTs are the AIR and RaXPol at the OU ARRC.

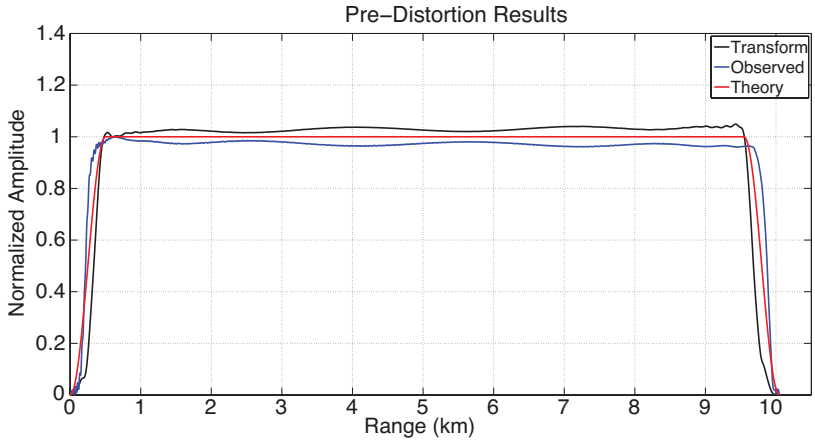

Figure 3.16: *Output amplitudes from the pre-distortion step. The original observed signal, in blue, droops with time. An inverse transfer function, shown in black, corrects the pulse amplitude to theory, in red.*

3.5.3 Comparisons with Other Methods

The method described can be applied to any combination of bandwidth, pulse lengths, and amplitude modulation specifications. As a primer for comparison between this method and previous pulse compression techniques, some of the most commonly-utilized and prevalent methods in the literature have been chosen as methods for comparison. Across these chosen waveforms, a common analysis point of TB equal to 270 was chosen due to the its prevalence in previous literature. This TB was achieved via a 200 μs, 1.35 MHz bandwidth pulse for each waveform. The comparison waveforms all utilized mismatched

filtering with amplitude modulation applied on receive only. The values of two-way processing gain for these waveforms were 0.50 (Klauder et al. 1960), 0.73 (Cook and Paolillo 1964), 0.73 (Griffiths and Vinagre 1994), and 0.51 (De Witte and Griffiths 2004). These four waveforms were compared with four equal TB (and equal mainlobe width/resolution) OFM waveforms using the proposed technique, with a raised cosine matched filter with roll-off factors (ROF) of 0.10, 0.02, 0.01, and 0.00 (no windowing). The two-way processing gain values for the designed waveforms were 0.950, 0.990, 0.995, and 1.000, respectively.

While the comparison list is hardly exhaustive, Table 4.1 shows significant differences between previous methods and the OFM waveforms. The best peak sidelobe level achieved in the comparison studies was -71.5 dB (De Witte and Griffiths 2004), however, such performance came with a heavy cost of 2.96 dB loss. The best peak sidelobe level achieved via the proposed technique was -65.0 dB, but with a much more reasonable loss of 0.24 dB due to the 0.10 ROF raised cosine matched filter. A nearly identical result of -64.8 dB was achievable with a 0.02 ROF filter, which yields a processing gain of 0.99 and a loss of 0.05 dB. For many radar systems, range sidelobe levels of -64.8 dB are considered quite reasonable, especially given typical antenna sidelobe levels of both dish and array platforms. The critical difference becomes a sensitivity gain of 2.72 dB, enough to vastly alter the cost of a radar system. As an

Table 3.1: *Comparison of common waveform techniques*

Waveform	**FM Type**	**AM Type**	**TB**	**Loss**	**PSL**
Klauder et al. 1960 (Klauder et al. 1960)	LFM	Blackman-Harris Mismatch	270	3.00 dB	-50.4 dB
Cook and Paolillo 1964 (Cook and Paolillo 1964)	Stepped LFM	Hamming Mismatch	270	1.35 dB	-58.2 dB
Griffiths and Vinagre 1994 (Griffiths and Vinagre 1994)	Stepped LFM	Hamming Mismatch	270	1.35 dB	-62.8 dB
De Witte and Griffiths 2004 (De Witte and Griffiths 2004)	NLFM	Nuttall Mismatch	270	2.96 dB	-71.5 dB
0.00 ROF OFM	NLFM	Raised Cosine (0.00 ROF) Match	270	0.00 dB	-56.0 dB
0.01 ROF OFM	NLFM	Raised Cosine (0.01 ROF) Match	270	0.03 dB	-59.9 dB
0.02 ROF OFM	NLFM	Raised Cosine (0.02 ROF) Match	270	0.05 dB	-64.8 dB
0.10 ROF OFM	NLFM	Raised Cosine (0.10 ROF) Match	270	0.24 dB	-65.0 dB

example, the 0.02 ROF raised cosine matched filter response is shown in Fig. 3.17.

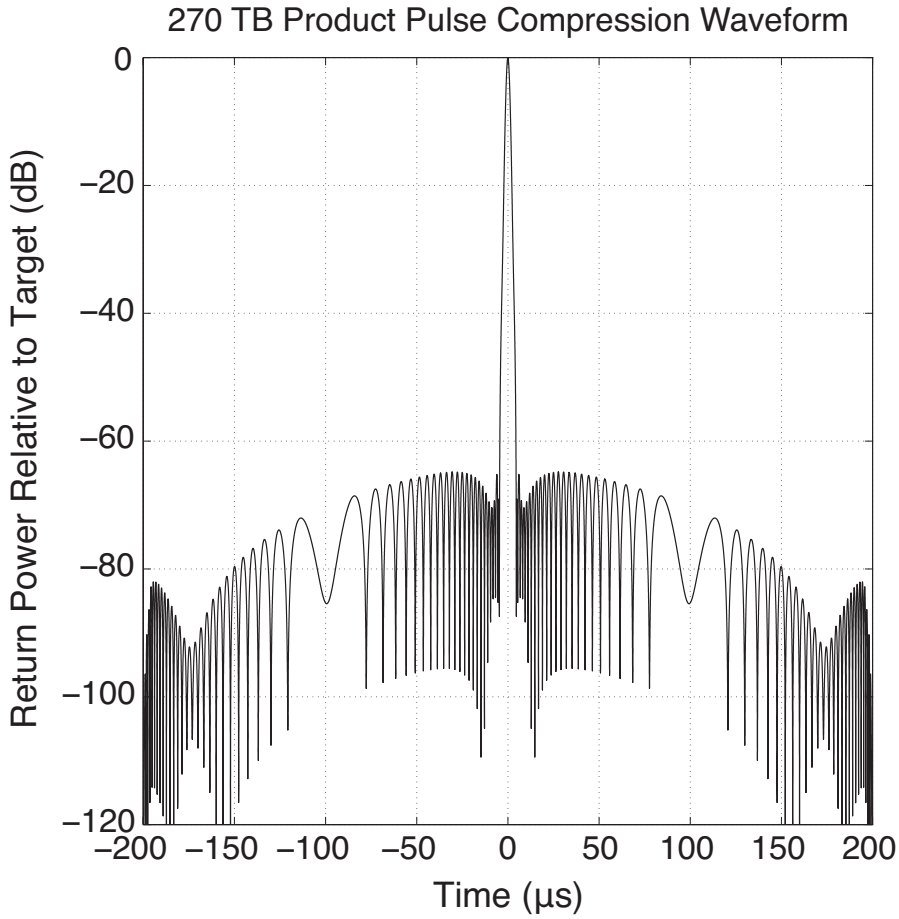

Figure 3.17: *Example 0.02 ROF comparison compressed waveform at 270 TB.*

3.6 Weather Observations

In order to demonstrate the increase in sensitivity afforded over heavy windowing methods, this section presents three weather cases observed with the PX-1000 system. The key aspects to waveform performance, specifically for weather observations, are low sidelobes and high sensitivity. In each of the

following cases, the OFM excels in both of these aspects. It is capable of retaining nearly identical sensitivity to a non-windowed LFM waveform, but displays no increase in sidelobes over a more traditional WLFM. It is important to note that this is a small collection of cases that demonstrate high waveform performance for the OFM. Marked increases in performance of all weather radar moments and parameters have been observed in all cases that have been collected. In each case, a comparison of results using a non-windowed LFM waveform, WLFM waveform, and the OFM waveform, all with PX-1000, are compared with the estimated moments from a WSR-88D radar (either KTLX or KOUN). In case 3, specifically, the OFM also includes the use of a time-frequency multiplexed fill-pulse in order to assist in blind-range mitigation (Cheong et al. 2013a).

3.6.1 Case 1: High Reflectivity Gradient, 9 July 2012

Fig. 3.18 shows a classic situation where a strong reflectivity gradient can result in undesirable sidelobes. In Fig. 3.18a, an LFM waveform used to observe a strong reflectivity gradient results in an extension of reflectivity towards the radar. Not only does this distort weather targets, but the artificial observations are not corrected in derived estimates. This means that rainfall estimations, for example, will appear to be anomalously high. In addition to strong reflectivity

gradients, sidelobes can contaminate clustered areas of cells without knowledge of the user. Fig. 3.18b shows a range profile through the area of highest reflectivity, with the left side pointing towards the radar (to the northeast), and the right side pointing away from the radar (to the southwest). It is clear that high sidelobes are contaminating the signal to the northeast of the convection.

Fig. 3.18c shows the same convective cell approximately 20 s later. This time, a WLFM waveform is used with a SNR loss of 3.19 dB. While the artificial extension in reflectivity has disappeared due to high sidelobe suppression, a marked loss in sensitivity is observed. All reflectivity values below approximately 15 dBZ are no longer observable due to the reduced sensitivty caused by heavy windowing of the waveform. This alters the shape and structure of the cell as it appears to the user, with similar negative impacts to those discussed in the LFM case. Fig. 3.18d shows that the high sidelobes from Fig. 3.18b have been suppressed, but at a cost to sensitivity. It is also important to note that data with a SNR value below 0 are filtered out in all of the PX-1000 cases shown.

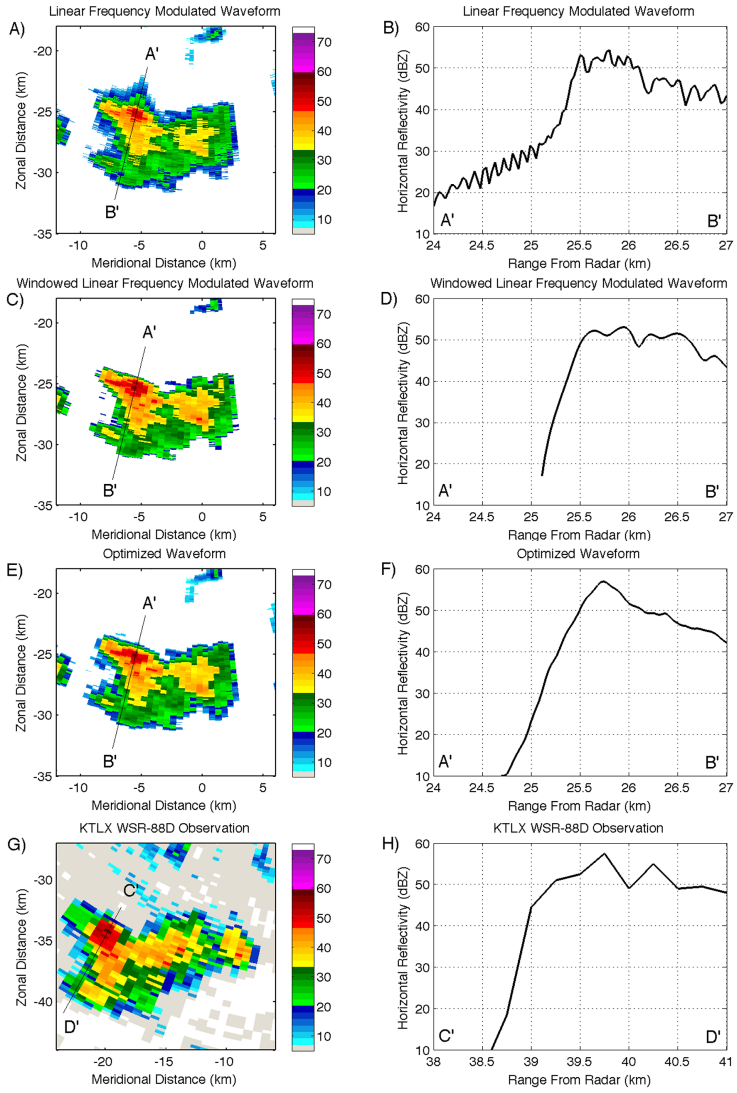

Figure 3.18: *Observations of a convective cell with a strong reflectivity gradient on 9 July 2012 at 20:28 UTC in Norman, Oklahoma. The left hand side shows reflectivity (dBZ), and the right hand side shows a normalized range profile view through the highest area of reflectivity, simulating an the response of the matched filter. In the range profile plots, the left hand side indicates range towards the northeast (towards the radar), while the right hand side indicates range towards the southwest (away from the radar). (a-b) were collected with a LFM waveform, (c-d) were collected with a WLFM waveform, (e-f) were collected with an OFM waveform, and (g-h) were collected with the KTLX WSR-88D at approximately the same time.*

Fig. 3.18e shows the same cell approximately 20 s after Fig. 3.18c. In this case, an OFM waveform is used, with a SNR loss of 0.24 dB. In addition to no artificial sidelobes, the sensitivities observed in the LFM case have been recovered, showing accurate edge characteristics for the cell in question. Fig. 3.18f shows that no sidelobes are being observed, and that we have an accurate representation of the cell.

Finally, Figs. 3.18g-h show the same cell observed at approximately the same time by the KTLX WSR-88D at Twin Lakes, Oklahoma. Despite being further away from the storm, the same sharp reflectivity gradient is seen. Due to the significantly higher power of the WSR-88D system, additional sensitivity below 10 dBZ is possible, however these values are below those capable of being observed with a 100-W radar platform, even with a long pulse. Regardless of the power difference, the same general storm shape is seen, including the important outer edges seen in both the LFM and OFM waveforms. Table 3.2 shows the relevant system characteristics of the WSR-88D platform for comparison to PX-1000.

3.6.2 Case 2: Stratiform/Convective Multicells, 18 August 2012

Waveform performance is critical in all weather situations, not just those which involve sharp reflectivity gradients. Additionally, it is important to be sure that

Table 3.2: *System characteristics of WSR-88D (Doviak et al. 2000).*

Transmitter Type	Klystron
Operating Frequency	2700-3000 MHz
Sensitivity	-27 dBZ @ 50 km
Observable Range	460 km
Antenna Gain	45.5 dBi
Antenna Diameter	8.5 m
3-dB Beamwidth	0.95 deg
Polarization	Simultaneous Linear
polarimetric Isolation	37 dB
Maximum Angular Velocity	36 deg s^{-1}
Peak Power	750 kW (Total)
Pulse Width	1.57-4.5 μs
System Bandwidth	0.63 MHz
Maximum Duty Cycle	2%
Minimum Gate Spacing	250 m (in super resolution mode)

other estimates aside from reflectivity agree with those from nearby radar systems. Fig. 3.19 shows a case involving a mix of stratiform and convective precipitation in the summer months. Despite the lack of clear reflectivity gradients, changes in sensitivity are apparent between different waveforms. The WLFM waveform lacks returns below 20 dBZ at ranges greater than 25 km from the radar. This is most apparent at the hole in reflectivity in the northwest quadrant of each plot. While the LFM waveform partially fills the hole with

lower reflectivity values, these values are not observable with the WLFM. Because no return is detected, which is indicated by low SNR and low spectrum width in the low reflectivity area, other estimations are not possible. Velocity estimates and dual-polarimetric estimates are non-existent in this area using the WLFM compared with the LFM.

The third column in Fig. 3.19 shows the same scenario approximately 20 s later, but observed with the OFM waveform. The gap in low signal return has been mostly filled in around the edges with lower reflectivity values. The fourth column was collected at approximately the same time by the co-located KOUN WSR-88D. It is clear that the area of low SNR should be mostly filled with low reflectivity values, indicating that the OFM has retained significantly more sensitivity than the WLFM. While sidelobes are not readily apparent in the LFM waveform in this case, it should be noted that without sharp reflectivity gradients it is difficult to observe sidelobes. Simply via the nature of non-windowed LFM waveforms, however, it must be assumed that the data are corrupted by sidelobes.

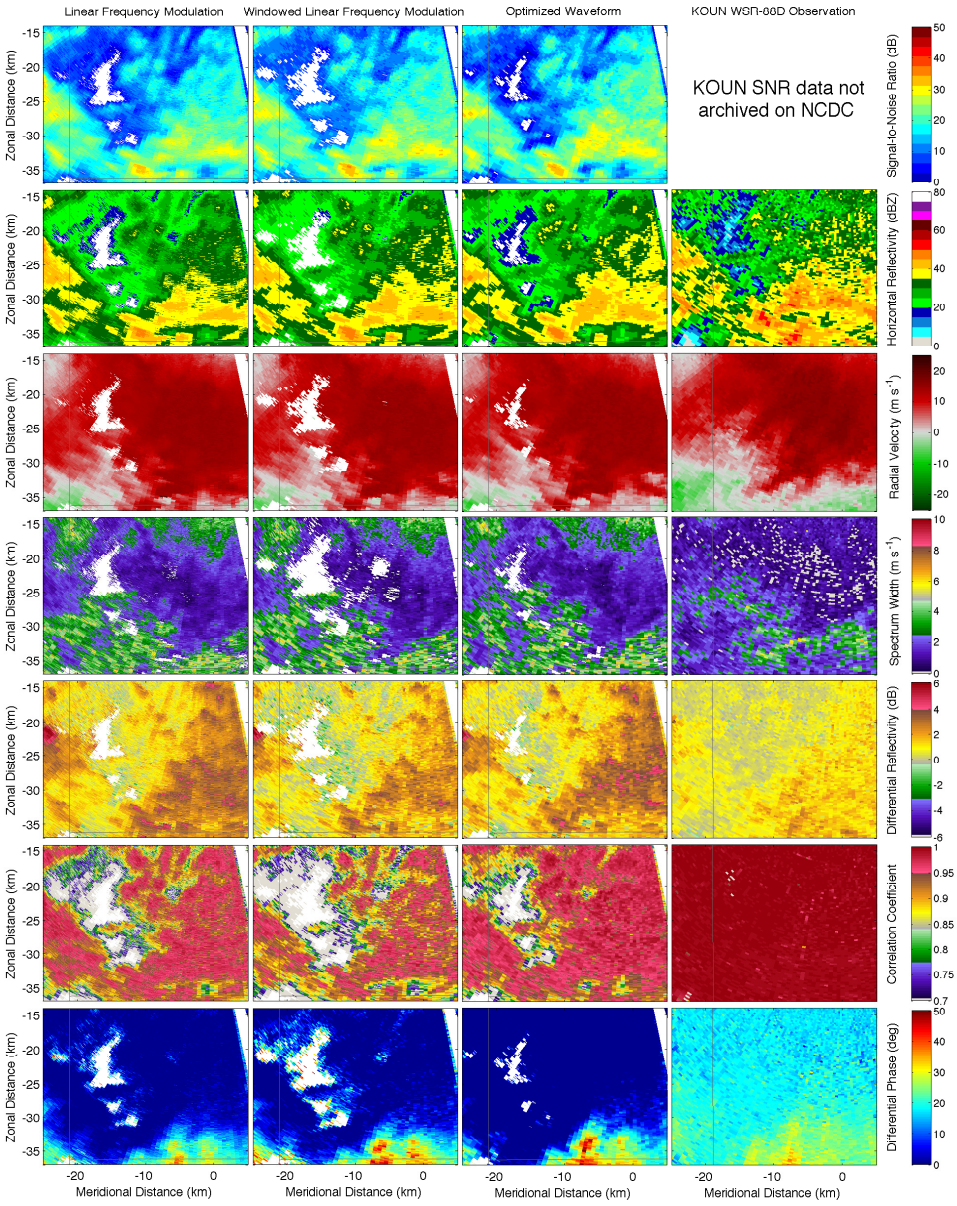

Figure 3.19: *Observations of a mixed stratiform/convective multicellular cluster on 18 August 2012 at 19:14 UTC in Norman, Oklahoma. From left to right, the columns represent collection with a LFM waveform, WLFM waveform, OFM waveform, and the co-located KOUN WSR-88D, respectively, at approximately the same time. From top to bottom, the rows show SNR (dB), horizontal reflectivity (dBZ), radial velocity ($m\,s^{-1}$), spectrum width ($m\,s^{-1}$), differential reflectivity (dB), correlation coefficient, and differential phase (deg), respectively.*

In this case, where sufficient sensitivity is retained, velocity estimates are not affected by the use of pulse compression waveforms. As long as a signal is received, velocity estimates appear to closely match the WSR-88D estimates. In order to cover 60 km, PX-1000's configuration had an an aliasing velocity of 15 $\mathrm{m\,s^{-1}}$. To correct for this, a simple de-aliasing algorithm was applied to the PX-1000 observations.

The bottom three rows in Fig. 3.19 show dual-polarization estimates, which are an important aspect of any weather radar platform. It is important for pulse compression waveforms to deliver similar polarization performance as their short pulse counterparts. A key aspect to dual-polarization moment estimation with pulse compression is the retainment of sensitivity. As sensitivity falls off, error in dual-polarization moment estimations rises considerably (Lei et al. 2012). This is apparent primarily in large areas of non-natural correlation coefficient values observed with the WLFM waveform in areas with low SNR. Due to the loss in sensitivity from windowing, relatively few areas in the precipitation display expected correlation coefficient values higher than 0.95. While the OFM certainly does not match KOUN's observations, a significant recovery is evident over the WLFM waveform. Low-powered radars, even with high power efficiency pulse compression waveforms, are an example where the multilag method described by Lei et al. (2012) could be used for

more accurate correlation coefficient values. Such an approach would only be strengthened by using an OFM waveform compared to a WLFM waveform.

Similar performance can be seen in differential reflectivity. It is important to note that differences in wavelength can lead to different polarimetric estimates (Ryzhkov and Zrnić 2005; Ryzhkov 2007; Kumjian and Ryzhkov 2008). In this case, we see similar spatial patterns in all radar moment estimates, and the differences we would expect between S-band and X-band are apparent. The only estimates that do not necessarily match KOUN observations are the reflectivity estimates. Due to the use of a low-power X-band transmitter, even a long pulse cannot avoid attenuation in convective precipitation. As the transmitted signal travels further through precipitation, signal loss becomes increasingly apparent. As long as some signal is returned, however, attenuation correction methods can be applied, given that differential phase estimates are accurate (Bringi et al. 1990; Gorgucci and Chandrasekar 2005; Park et al. 2005; Snyder et al. 2010). The bottom row in Fig. 3.19 shows reasonable differential phase values at X-band, leading to attenuation-corrected values which come close to KOUN estimates.

3.6.3 Case 3: Convective Line Segments, 26 August 2012

One of the primary concerns for long-pulse radar systems is the blind range. While multiple studies have attempted to mitigate the blind range (most notably Bharadwaj and Chandrasekar 2012; Cheong et al. 2013a), the method described in Cheong et al. (2013a) is being tested on PX-1000. Fig. 3.20 presents a situation with two convective line segments; one to the west of the radar, and one directly over and to the east of the radar. It is clear that in this situation, seen in full detail in the fourth column as observed by the co-located KOUN WSR-88D radar, a solution must be developed in order to see both convective lines.

While Fig. 3.20 shows the same method for collecting pulse compression data with the LFM and WLFM as before, the third column shows an example of a time-frequency multiplexed OFM waveform. After a long pulse of 67 μs is transmitted, a short pulse of 2 μs is transmitted at the end of the waveform. Areas outside of the blind range are match-filtered with the long pulse for maximum sensitivity, while areas within the blind range are match-filtered with the short pulse in order to fill in the area which was invisible to the radar while transmitting the long pulse. Using this method combined with an OFM waveform, the third column in Fig. 3.20 shows estimates both outside and inside the blind range. While not fully resolved due to the inherent lack of sensitivity with a short pulse and 100 W peak transmit power within the blind

range, the leading convective line which passes over the radar is observed. As with Case 2, an application of attenuation correction can be useful in situations where reflectivity bias correction is needed.

In the other moment estimates, similar results to those noted in Case 2 are observed. The OFM waveform shows considerable increase in sensitivity over the WLFM, as is evident by increased SNR, especially to the east of the radar. This is a particularly critical area for power efficiency and radar sensitivity in this example, since an area of heavy convection is directly over and to the east of the radar. We see a significant increase in sensitivity in the OFM waveform to the east, as returns between 10-15 dBZ are observable. As with Case 2, the increased sensitivity afforded by the OFM waveform allows for more accurate estimates of all moments, and estimates of moments that were not observable with traditional pulse compression methods.

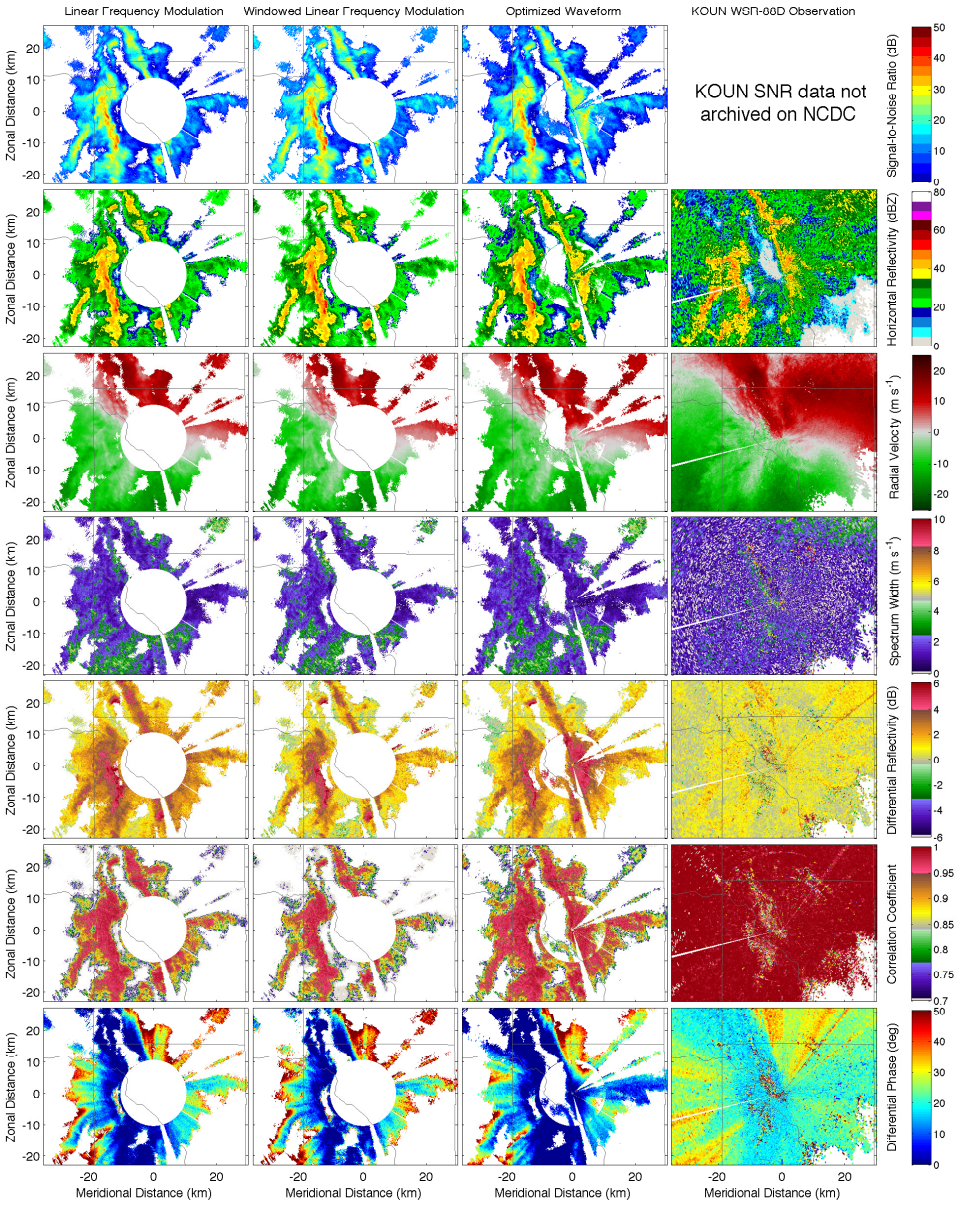

Figure 3.20: *Observations of two convective line segments on 26 August 2012 at 04:53 UTC in Norman, Oklahoma. From left to right, the columns represent collection with a LFM waveform, WLFM waveform, OFM waveform, and the co-located KOUN WSR-88D, respectively, at approximately the same time. From top to bottom, the rows show SNR (dB), horizontal reflectivity (dBZ), radial velocity ($m\,s^{-1}$), spectrum width ($m\,s^{-1}$), differential reflectivity (dB), correlation coefficient, and differential phase (deg), respectively.*

Chapter 4

Advanced Waveforms: Specific Design Methods

4.1 Waveforms for Signal Isolation

4.1.1 Background

Signal isolation is an important aspect for many radar applications, including array isolation, polarimetric isolation, and passive radar applications. In these cases, multiple transmit/receive signals are present in an operational setting, and each must be isolated from the other signals. In most of the situations, the signals are in similar (or the same) frequency ranges and bands, making isolation a particular challenge. For traditional, dish-based weather radar, the most common situation where high isolation is required is simultaneous transmit/receive of dual-polarized signals. Polarimetric isolation is important due to the desire for pure horizontal and vertical returns for characterization of hydrometeors. If leakage from the horizontal to vertical channel (or vice-versa) exists, polarimetric estimates will contain bias.

Isolation is also critical for the advent of a multi-array MPAR system and network. In order to keep costs low and facilitate maintenance, a quadruple

array in a centralized location has often been assumed in MPAR-related simulations and studies. Such a design is fundamentally different than more-typical designs of multiple arrays that are often distributed spatially across a relatively wide area for maximum array isolation. An example of array spatial isolation is the placement of arrays on different parts of a large ship, as was common for the development and implementation of the Aegis system in the United States Navy (Adam 1988). Without the ability to distribute arrays in separate areas, interference between arrays must be carefully considered in developing pulse waveforms and scanning strategies for a four-array MPAR. While beam patterns can be designed for ideal isolation near broadside, as beams on adjacent arrays come together, spatial isolation of returns from far-field targets decreases to 0 dB (Fig. 4.1).

Additionally, spectral usage is becoming a large concern for the USA. Reducing the total spectrum usage of a multi-array, co-located MPAR array could have major implications for the combination of multiple operating bands (the C-band TDWR, the S-band WSR-88D and ASR, and the L-band ARSR). There is immense pressure by national governments to decrease spectrum usage, especially at S band (Obama 2013). If it is possible to re-use frequencies across MPAR arrays, less of the S band could be used by this new network. By efficiently utilizing spectral resources, the economic impact of spectral savings is large.

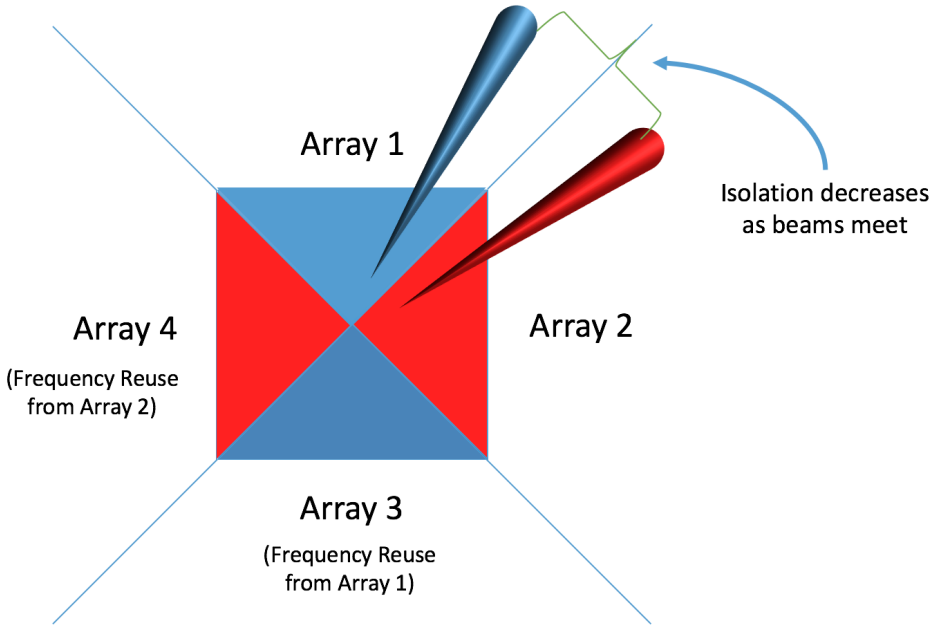

Figure 4.1: *Spatial isolation of returns from far-field targets between adjacent arrays decreases to 0 dB as the beams meet off broadside. Colors indicate that opposite arrays will conceptually operate at the same frequency.*

This section describes efforts to apply single-waveform optimization techniques to an adaptive multi-waveform design, providing maximum isolation for various scenarios. This method has potential to provide polarimetric isolation improvements for pulse compression weather radars, as well as spectrum-use reduction for a multiple arrays. A discussion regarding implications for simultaneous waveform isolation, specifically for polarimetric isolation, is provided and compared with recent studies (Zrnić et al. 2014). Additionally, a detailed look at how this method can help reduce MPAR spectrum usage is provided.

4.1.2 Methodology

In recent years, focus on waveform design (especially for weather radar observations) has centered on maintaining sensitivity (Kurdzo et al. 2014) while keeping sidelobes at an acceptable level (Mudukutore et al. 1998). Additional work has focused on blind range mitigation (Bharadwaj and Chandrasekar 2012; Cheong et al. 2013a). There are no examples in the literature of designing a series of waveforms for spatial isolation purposes, however, there have been studies regarding polarimetric isolation (Zrnić et al. 2014). In order to determine a base design methodology for a series of waveforms, the technique described in Chapter 3 was chosen as a starting point.

4.1.2.1 Spatial Isolation

This section separates isolation into three types: spatial, waveform, and frequency. Spatial isolation for returns from far-field targets is determined by the overlap of beam patterns on two adjacent arrays. The beam pattern for this experiment was determined using the NFR specifications (FAA 2012); an S-band frequency with a maximum 1-deg beamwidth was assumed. Using the NFR specification as a mask and a 135-element (6.75 m) array, a squared Taylor window was adjusted until an appropriate beam pattern was found. The beam pattern at broadside, along with the NFR mask, is shown in Fig. 4.2.

This method treats the two arrays as a bistatic system, with each array serving as a transmitter and receiver. The potential steering angles on each array are aligned on a single axis, ranging from -90 deg to +90 deg. Each array's beam can steer between -45 deg and +45 deg, with the "north" array (array 1) encompassing the first half of the axis, and the "east" array (array 2) encompassing the second half of the axis.

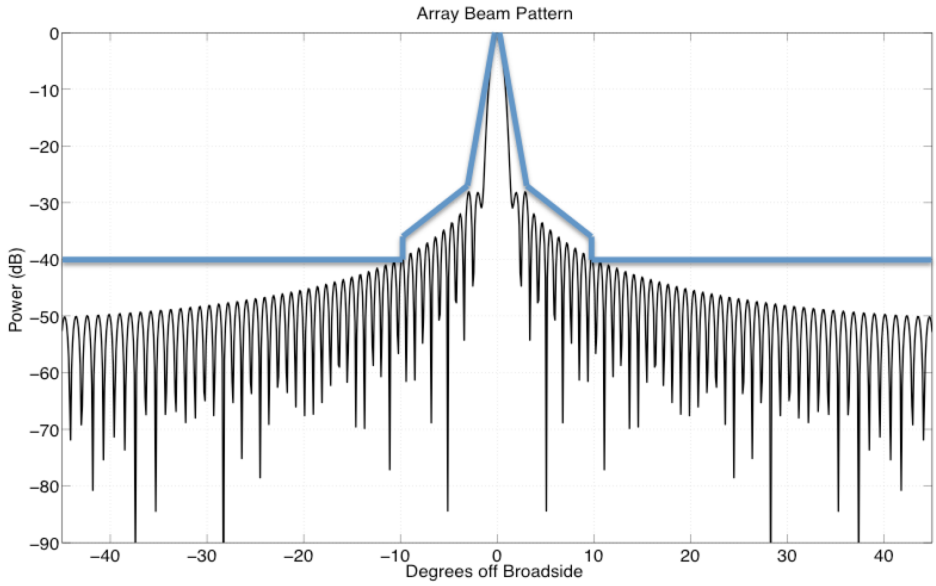

Figure 4.2: *Broadside array beam pattern used for multi-array simulations. The beam pattern is generated using the MPAR NFR 1-way specification (FAA 2012) at S band with a maximum 1-deg beamwidth over all scanning angles. The beam pattern was designed using a squared Taylor window to achieve the specification, shown as a blue mask.*

The beam pattern changes (widens) as it is "steered" off broadside. The beams are steered within 45 deg of broadside on each array, and isolation due to the overlapping/steered beam patterns is determined using Eq. (4.1):

$$I = 10\log\left(\frac{\sum|p_1|^2|p_2|^2}{\sum|p_b|^4}\right) \tag{4.1}$$

where p_1 is the steered pattern for array 1, p_2 is the steered pattern for array 2, and p_b is the broadside pattern. An example of two beams on this axis, referred to as a principal plane, is shown in Fig. 4.3. Each beam is pointed 5 deg away from 45 deg, making for 10 deg of total separation on the principal plane. The isolation between the beams is 36.98 dB. This is pure spatial isolation, and does not include any considerations from waveform or frequency isolation.

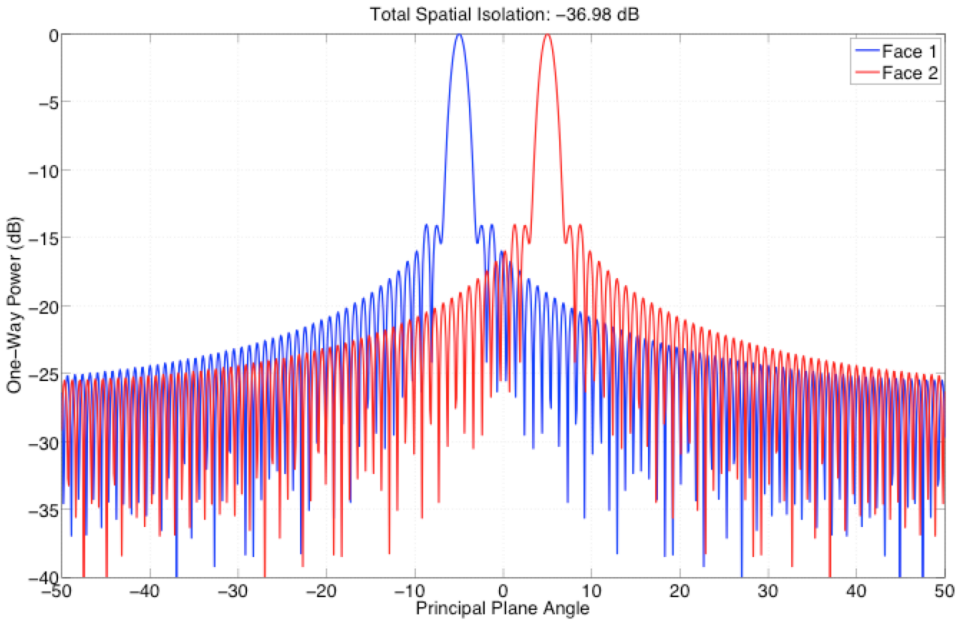

Figure 4.3: *Example isolation calculation using two beams, each pointed 5 deg from the maximum steering angle (45 deg). Each array is represented by a different beam. In this example, the calculated spatial isolation is 36.98 dB.*

Considering a constant offset of beams in a coordinated scan strategy, Fig. 4.4 shows the spatial isolation in a single steering "dimension." Clearly, at

± 45 deg, the beams are pointing in the same far-field direction, resulting in zero spatial isolation. In short, this means that any isolation at these angles must come entirely from waveform design. Polarimetric isolation in a simultaneous transmit/receive dish-based system is an analogy for this "worst-case" scenario.

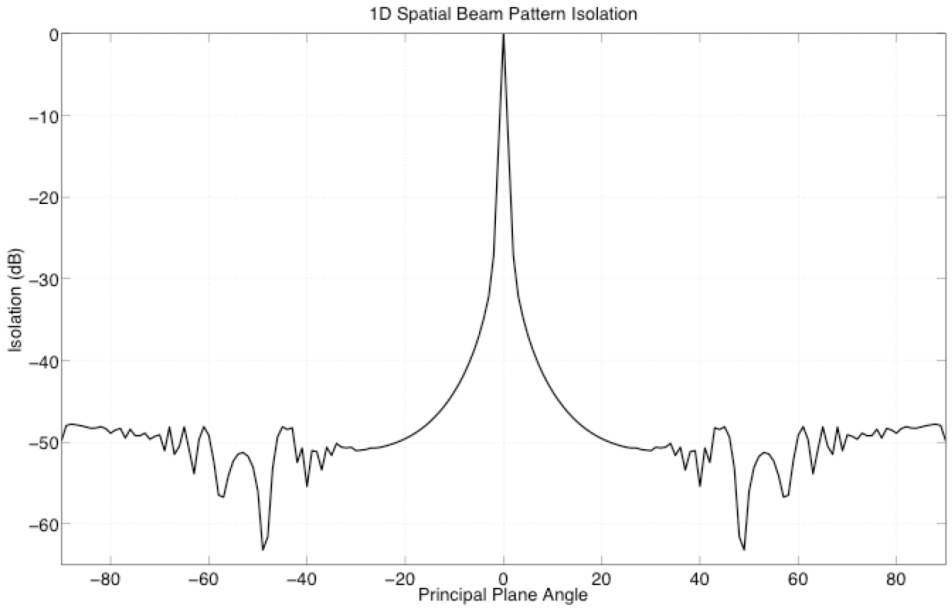

Figure 4.4: *Spatial isolation in a single steering dimension along a principal plane. As the beams approach the same angle, 0 dB of spatial isolation is observed. A rapid drop off to below 40 dB is apparent beyond 10 deg, or 20 deg of total separation.*

A two-dimensional plot of spatial isolation between two arrays with the chosen beam pattern is presented in Fig. 4.5. Although isolation decreases to 0 dB when the beams are steered in the same direction (0 deg on the principal plane axis shown in Fig. 4.4), the increase in isolation is relatively rapid as the

beams move apart, with values of 30 dB at ±40 deg, 40 dB at ±30 deg, and widespread 45 dB or better beyond.

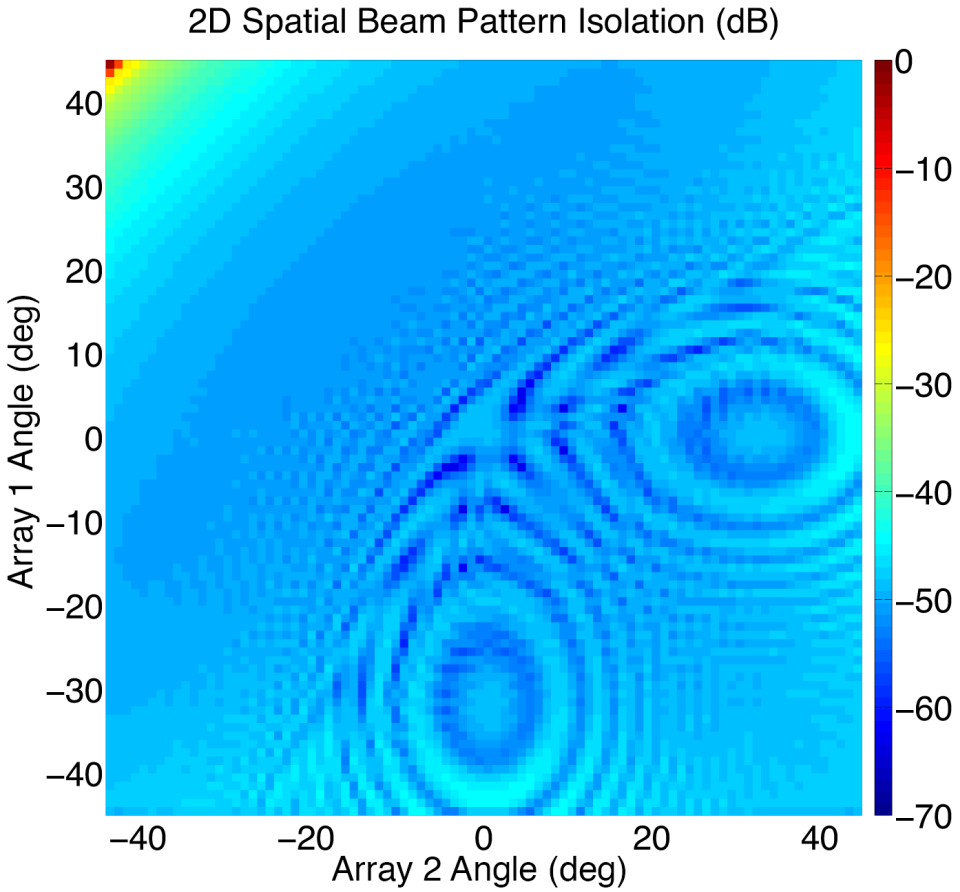

Figure 4.5: *Spatial isolation values for all possible steering angles. Two perpendicular arrays are assumed, and only far-field isolation effects are considered.*

4.1.2.2 Waveform Isolation

The NFR specifications state that 80 dB of two-way isolation is necessary, meaning that even for the widely separated angles, 30-40 dB of additional isolation is needed. In a constant-modulus waveform, as is typical with weather radar, this would require fully frequency-separated short pulses. With short

pulses taking up considerable bandwidth on their own, the total bandwidth of a four-faced MPAR, for example, could be higher than a current WSR-88D, which is not possible at S band with spectral requirements. With frequency-modulated waveforms, however, slight variations in the frequency functions can lead to added isolation. Additionally, the use of similar (or identical) frequencies on opposite-side faces may be possible, especially if there are no creeping waves (i.e., spatially-separated planar arrays). The waveform isolation is determined using Eq. (4.2) where s_1 is the complex waveform for array 1 and s_2 is the complex waveform for array 2.

$$I = 10\log\left|\frac{\sum s_1 s_2^*}{(\sum |s_1|^2 \sum |s_2|^2)^{\frac{1}{2}}}\right| \tag{4.2}$$

In order to adapt the single-waveform optimization technique in Chapter 3 to a multiple-waveform method, the number of variables was extended to 24 (12 for each waveform). Each waveform is optimized iteratively, with a cost function that accounts for individual waveform performance (i.e., using peak sidelobe level and null-to-null mainlobe width) as well as total isolation. A genetic algorithm attempts to maximize this fitness function, resulting in ideal sidelobe levels and range resolution, as well as the maximum possible isolation due solely to waveform design. The fitness function can be represented as:

$$F = \alpha \left(\frac{PSL_1}{MLW_1} + \frac{PSL_2}{MLW_2} \right) - \beta I_w \tag{4.3}$$

where α and β are fitness scalars that can be chosen to evenly weight the fitness values between the left term of the function (the combined individual waveform fitness functions labeled with a 1 for array 1 and a 2 for array 2) and the right term of the function (waveform isolation, I_w). Multi-objective genetical algorithm techniques were experimented with for this purpose, but the Pareto front did not yield acceptable options without exceedingly tedious tweaking of the fitness scalars, a task that essentially negates the use of multi-objective methods. Instead, rough scalars based on order of magnitude yielded better results with a standard genetic algorithm.

As in Chapter 3, minimal windowing is used on transmit and receive, leading to two-way SNR losses on the order of 0.2 dB. Each chirp is 5 MHz, and each pulse is 100 μs long. These values were chosen as representative examples of a likely MPAR waveform, but are easily changeable; they are used throughout the remainder of this section. A sampling of the waveform design output is shown in Fig. 4.6. The top panels show the compressed result for each waveform. The bottom panels show the DFT of each waveform, as well as the chirp functions for each waveform (respectively, from left to right). In this case, more emphasis was placed on the individual waveform performance

metrics than the isolation, leading to 10.3 dB of waveform isolation. It is important to note that slightly altered approaches have yielded results as high as 27 dB, but for the purposes of this section, the more conservative value of 10.3 dB will be used as an example.

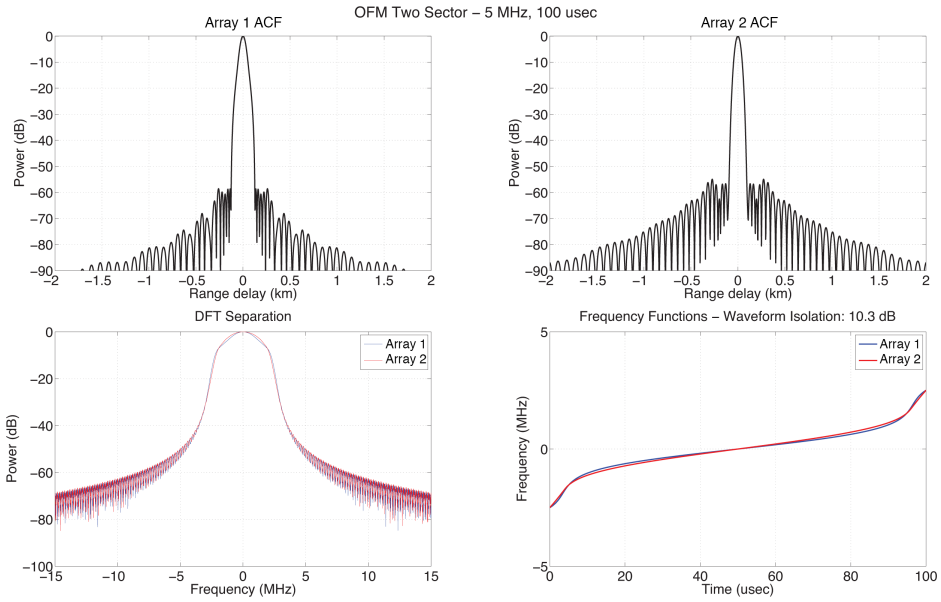

Figure 4.6: *Example waveform optimization result. Clockwise, from top left: compressed waveform from array 1, compressed waveform from array 2, frequency chirp functions, and spectra (for both arrays).*

It is prudent to discuss the difference between Fig. 4.6 and the common choice for polarimetric isolation, the up-down chirp. An up-down chirp typically assumes the same waveform on two channels, but one chirps through the frequencies in a positive sense, while one chirps through the frequencies in a negative sense. Theoretically, this provides the maximum waveform-based isolation that can be nearly double the isolation assumed in this section. However,

if a minimal amount of total frequency use is desired, up-down chirps will always have a crossing point, meaning that at some point during the chirps, the two chirps will be at the same frequency at the same time. This necessary overlap, while often better than a up-up waveform at first sight, is vastly limited by the crossing point. The crossing point is discussed in further detail in the frequency isolation section of this chapter.

4.1.2.3 Frequency Isolation

The frequency isolation is determined by the remaining isolation possible by offsetting the chirp functions by a constant frequency along the entire pulse. Since the NFR states a goal of 80 dB of total isolation for each array, the *minimum* amount of frequency offset necessary to achieve a combined isolation, waveform, and frequency isolation of 80 dB is applied. It is important to minimize the frequency offset of the waveforms because of the added spectral usage. With pure isolation and waveform isolation, before any frequency isolation is applied, the two waveforms have the same center frequency and the same chirp bandwidth, meaning that no additional bandwidth is needed. Since the use of solely isolation and waveform isolation is not generally sufficient to achieve a full 80 dB of isolation, some frequency offset is necessary. Fortunately, for most of the pointing angles described for a multiple-array MPAR,

the necessary amount of isolation can be achieved via relatively small amounts of frequency offset, as depicted in Fig. 4.7

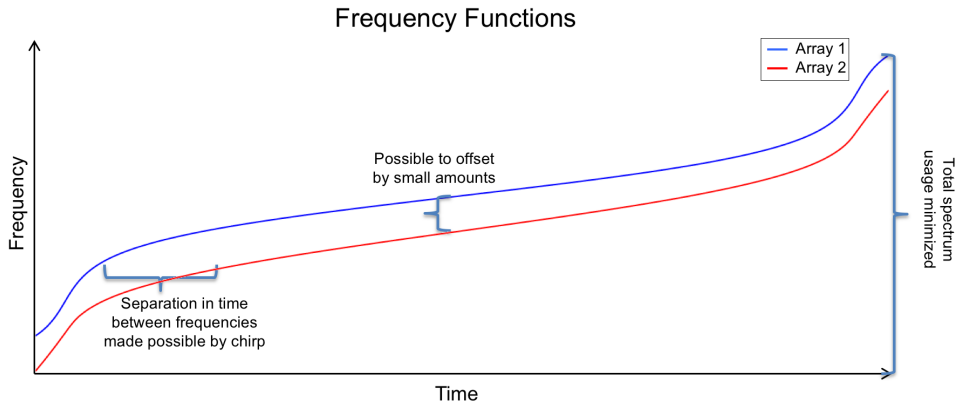

Figure 4.7: *Illustration of frequency isolation via offsets of the frequency functions. Two arrays are shown, one in blue and one in red. By separating the functions slightly in frequency, a large separation in time between frequencies is made possible by the nonlinear chirp shape. The total spectrum usage is minimized in this way due to the small frequency offset.*

There are a few important assumptions that must be considered with this methodology. First, as previously stated, a tradeoff between waveform performance and isolation exists. This tradeoff has been considered to be a conservative value of 10.3 dB, but over 20 dB of isolation has been observed with more-relaxed sidelobe constraints. This is an area where additional work is necessary. Second, *no* near-field effects are being accounted for; this analysis considers only two-way far-field beam patterns. While near-field effects are important in a real-world system, these have not been included in the analysis. Near-field effects and other complexities must be considered in future work, especially for the cylindrical array problem.

A critical aspect of generating frequency isolation is the previously mentioned crossing point. Regardless of waveform and isolation isolation values, by definition, if two waveforms are at the same center frequency and are symmetric (for Doppler tolerance reasons), the frequency functions must be equal at the center of the pulse. Additionally, the waveforms occupy the same frequencies at the beginning and end of the frequency function. Therefore, significant opportunities for additional isolation exist by shifting the waveforms slightly apart from each other. Through isolation and waveform isolation gaining a significant proportion of the total necessary isolation, it is important to note that the necessary frequency offset remains rather small.

By including frequency separation in the optimization process, it may be possible to optimize the frequency functions to not overlap anywhere, while simultaneously building nonlinear phase offsets for additional isolation. This would provide more isolation than simply taking the same waveform and shifting the overall center frequency. Experiments have been carried out with this technique, but have been somewhat unsuccessful due to computational limitations. The fitness functioned used was:

$$F = \alpha \left(\frac{PSL_1}{MLW_1} + \frac{PSL_2}{MLW_2} \right) - \beta I_w - \gamma I_f \tag{4.4}$$

where I_f is frequency isolation and γ is a fitness scaler for the frequency isolation term. Note that isolation isolation is not included in this function, since for a given set of pointing values, it is considered to be a constant.

A final consideration for both waveform and frequency isolation is the stability of the transmit chain and the capabilities of the pre-distortion method. Since the method described in Chapter 3 primarily corrected for amplitude droop, phase distortions must be carefully considered with the method described in this section. Work is currently underway at the ARRC to generate better pre-distortion filters that could make a technique like this implementable in a real-world system (Dunn et al. 2015).

4.1.3 Simulations and Discussion

The design objective in this section is to achieve a total of 80 dB of isolation while utilizing the minimum possible frequency separation between 5 MHz chirps on adjacent arrays. It is noted that a different objective (optimization of MPAR network frequency utilization) could also be considered and this might in fact support wider frequency separation between the arrays of a single radar. For this objective, the ideal case would use zero frequency separation, meaning that for all steering angles, the arrays would be able to operate on separate missions while using the minimum amount of spectrum. However, as discussed in the previous section, frequency separation is necessary.

For each combination of steering angles, the amount of isolation isolation and waveform isolation resulted in the ability to calculate the minimum frequency separation to achieve the necessary isolation, and hence the total spectrum usage for two 5 MHz chirps on adjacent arrays. The results are shown in Fig. 4.8, while some critical steering angle values are summarized in Table 4.1. At $\pm$45 deg, where the beams are steered in the same direction, the total spectrum usage is 8.40 MHz, a savings of 1.60 MHz from using two fully separated 5 MHz chirps (which would necessitate 10 MHz of total bandwidth).

Very quickly after steering away from each other, the total spectrum usage drops to 5.70 MHz at $\pm$40 deg (a total of 10 deg of separation), a savings of 4.30 MHz. After reaching approximately $\pm$30 deg (a total of 60 deg of separation), the total spectrum usage drops to a near-constant value of approximately 5.40 MHz, resulting in 4.60 MHz of spectral savings. Each waveform achieves two-way SNR loss of 0.2 dB, 3-dB range resolution of <40 m, and peak sidelobes better than -55 dB, values that have been found by Kurdzo et al. (2014) and Kurdzo et al. (2015a) to be sufficient for weather observations.

It should be noted that it is assumed that opposite arrays will be able to operate in identical frequency bands due to their isolation isolation. However, an actual system may by subject to different effects not accounted for here, especially near-field effects and emissions affecting electronics inside the radar shelter. Additionally, the effect of fill pulses has not yet been considered. It

is important therefore to recognize that the proposed values are not final values for an MPAR system, but more so an approximate order-of-magnitude estimate for spectral savings.

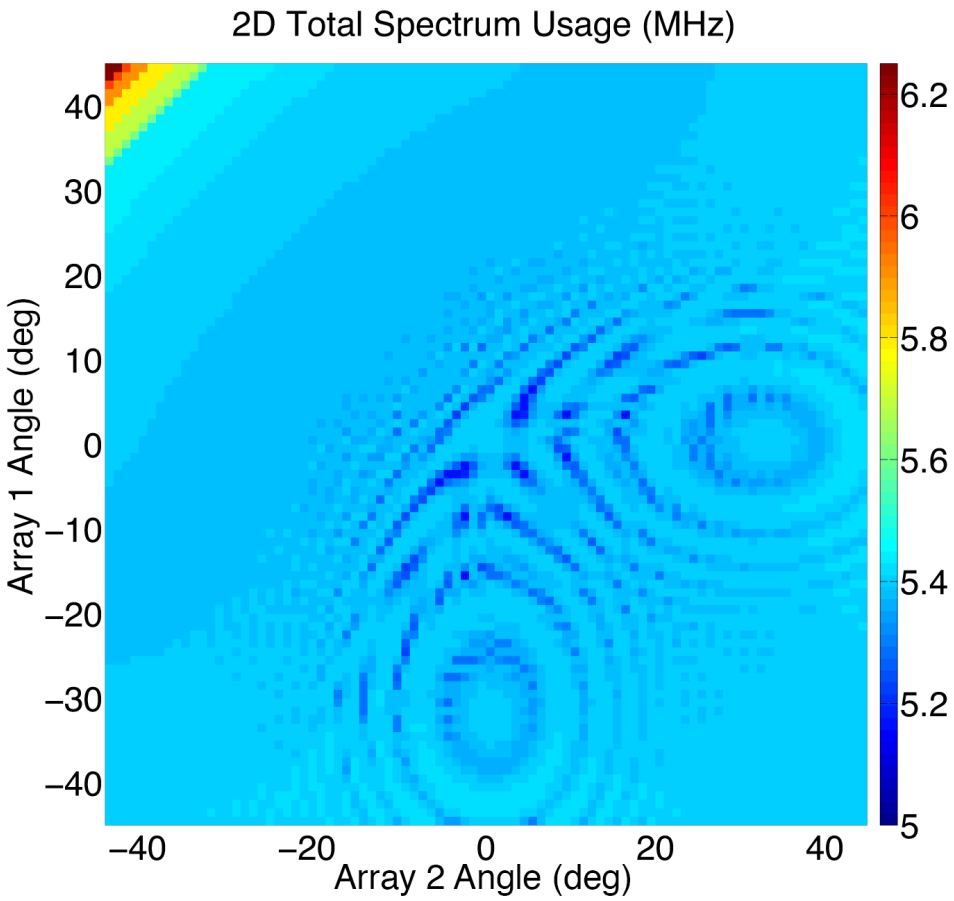

Figure 4.8: *Total spectrum usage for all possible pointing angles, assuming 5 MHz chirps on each face and the minimum amount of frequency offset combined with isolation and waveform isolations to achieve the NFR specification for isolation of 80 dB.*

As mentioned earlier, previous studies have explored the potential for up/down frequency chirps for maximum isolation. While waveform isolation values in this section are not as impressive as up/down chirps, there are a few

Table 4.1: *Total spectrum usage and savings*

Steering Angles	**Total Isolation**	**Total Spectrum (Regular)**	**Total Spectrum (New)**	**Spectrum Savings**
0 deg / 0 deg	80 dB	10 MHz	5.40 MHz	4.60 MHz
15 deg / 15 deg	80 dB	10 MHz	5.40 MHz	4.60 MHz
30 deg / 30 deg	80 dB	10 MHz	5.41 MHz	4.59 MHz
40 deg / 40 deg	80 dB	10 MHz	5.70 MHz	4.30 MHz
45 deg / 45 deg	80 dB	10 MHz	8.40 MHz	1.60 MHz

important considerations that should be mentioned. First, the value used in this example for waveform isolation is quite conservative. Additionally, the up/up chirp methodology provides a critical advantage over up/down chirps: a slight frequency offset can completely prevent overlap of the waveforms in the time domain, resulting in relatively high isolation values using relatively low separation amounts. This is an important advantage that pulse compression waveform design provides, and is an area of research that has been largely unexplored, especially with regard to polarimetric isolation. An up/down chirp can not provide the advantages of frequency offset, and has therefore been discounted in these experiments for achieving 80 dB of total isolation. Finally, the cross-ambiguity function between multiple waveforms is an area for extensive exploration. A Doppler shift difference between two different angles will exist on orthogonal arrays, meaning that the Doppler tolerance will need to be considered in the future.

4.2 Waveforms for Severe Local Storm Observations

In Chapter 2 it was mentioned that the term waveform indicates the holistic design of the pulse, T_s, and the scanning strategy. This is important when considering issues such as duty cycle limitations, the number of independent samples, and the turbulent nature of the mission. As a case study example for holistic waveforms, this section presents the waveform design procedure for the AIR with the goal of observing tornadoes at close range.

4.2.1 AIR Transmitter and Mission Limitations

The AIR uses a TWT transmitter with a peak power of 3.5 kW. This energy is spread out over 20 deg in the vertical, however, making the approximate 1-deg beamwidth peak power roughly 175 W, on par with the transmit capabilities of PX-1000. This makes pulse compression a critical aspect of AIR operations. Ideally, the longest possible pulse would be used to make up this sensitivity, but there are a few considerations that must be taken into account when designing the pulse. First, the mission of the AIR includes scanning tornadoes at ranges as close as 3 km, meaning that the pulse length and associated blind range can not exceed roughly half that distance (for the purpose of observing inflow and boundary-related regimes). This sets a hard limit on pulse length of roughly 10 μs, which limits the potential sensitivity gain over a short pulse to about 10 dB. This is a much shorter pulse length than the PX-1000 (which

can also utilize a fill pulse), however, with the goal of tornado observations being on the order of 3 km, the necessary range for observations is considerably shorter than PX-1000.

Second, the AIR transmitter is limited to a 2% duty cycle, a considerably smaller value than typically available with SSPAs. Additionally, due to the need to send a trigger that is slightly larger than the pulse length, the effective duty cycle is limited to 1.85%. This limitation is critical when combining a long pulse with Nyquist concerns, since a shorter T_s is desired for higher Nyquist values. The highest possible Nyquist is strongly desired in a tornado-scale radar to aid in future dealiasing of the data. Tornadoes can have winds in excess of 140 ms^{-1} (Burgess et al. 2002), but even relatively weak tornadoes (EF1 on the Enhanced Fujita Scale, McDonald and Mehta 2006) can approach 50 ms^{-1}. With low peak transmit power and the desire to observe storms at close range, the maximum unambiguous range is not of high concern for the AIR, meaning T_s is desired to be as low as possible. With a maximum duty cycle of 1.85%, this places a direct restriction between T_s, Nyquist, pulse length, and associated sensitivity.

Third, the Nyquist interval must be considered in terms of the expected spectral shape of the tornadic winds. Staggered PRTs (Zrnić and Mahapatra

1985) are a popular method to achieve higher Nyquist values to make unfolding Doppler velocities easier. Staggered PRTs are in use on the WSR-88D network (Torres et al. 2004) and numerous research radars (e.g., Pazmany et al. 2013). RaXPol, for example, utilizes staggered PRTs, but does not have the same limitations on duty cycle due to the short pulse in use. The AIR, however, must consider the pulse length, as well as writing limitations due to the 36 channels of raw I/Q data being written after each pulse. The chosen pulse length can not exceed 1.85% duty cycle for the shortest T_s. Additionally, certain T_s ratios are necessary for unfolding, limiting options for selection. For these reasons, the only option for staggered PRT data collection with the AIR involves a relatively short pulse with relatively small *individual* Nyquist intervals. In a tornado, turbulence values can be extremely high, causing the spectral shape to be nearly flat, especially in small Nyquist intervals. As will be seen in early AIR data in Chapter 5, this leads to unusable Doppler velocities.

Fourth, the number of independent samples necessary for the desired data quality must be considered. As shown in Chapter 2, the number of independent samples is related to the number of total samples and the turbulence (spectrum width) in the storm of interest. Of course, with high turbulence values, a tornado will lead to a greater number of independent samples for the same number of total samples. However, away from the core vortex, areas such

as the forward flank and inflow/boundary regions will generally have much lower turbulence values, leading to fewer effective independent samples in those areas. Therefore, the overall scene must be considered, and this limitation largely impacts the scan rate that can be achieved. Scan rate also impacts two other important areas; effective beamwidth and sensitivity. Slower scanning with a mechanically scanning antenna will lower the effective beamwidth, raising azimuthal resolution via reduced beam smearing. Additionally, slower scanning will allow for more pulses to be averaged, causing higher sensitivity values. T_s is also tied into these considerations due to the number of total samples over a given period of time.

Finally, bandwidth considerations are important for severe storm observations. There is obviously the desire to scan weather (and severe local storms) at the highest possible resolution. The AIR TWT can support up to 5 MHz of total chirp bandwidth. While it is clear that all possible bandwidth should be used, it is worth noting that the desire for high-resolution observations outweighs the desire to use bandwidth for a fill pulse, especially when the pulse length is under 1-1.5 km in length. This is considerably different than PX-1000, which has a blind range that is greater than 10 km. Additionally, bandwidth considerations for resolution can become more complicated depending on the signal processing methods used for tornadic observations. RaXPol, for

example, utilizes frequency hopping in order to gain more independent samples while scanning extremely rapidly (180 deg s^{-1}; Pazmany et al. 2013). Due to the necessity to hop between up to 11 frequencies and only having 20 MHz of available bandwidth, the total bandwidth available for each hop is reduced, making for complicated decisions regarding tradeoffs between scan rate, resolution, and data quality.

4.2.2 AIR Waveform Design for Tornado Observations

The waveform design for the AIR had to take into account pulse length, duty cycle, Nyquist interval, independent samples, and resolution in order to achieve the desire data quality. The first step was determining an acceptable Nyquist interval. Through discussions with other scientists and observations in the literature, it was determined that 25 m s^{-1} was the minimum Doppler aliasing velocity that could be tolerated. This served as a starting point, since it provided the necessary T_s of 314 μs. Backing out the maximum duty cycle considerations, a pulse length of 5.25 μs was decided upon, providing a 7.2 dB improvement in SNR from a 1 μs pulse. Without a fill pulse, the maximum bandwidth of 5 MHz was used, making for a TB product of 26.25, a relatively low value for waveform design. Finally, with a desired number of total pulses of 160 and a T_s of 314 μs, an azimuthal scan rate of 20 deg s^{-1} was decided on. With the ability to scan between -110 deg and +70 deg relative to the rear

of the vehicle, and accounting for slowed edges in sector scans, this strategy allows for 180-deg by 20-deg volumetric scans in less than 12 s.

The AIR strategy presents two problems to the aforementioned waveform design method. First, with a short pulse length, the TB product is low, making decent waveform performance a challenge. Additionally, with 36 individual elements and no transmit leak through, there are limited options for pre-distortion. Due to the low TB product and poor pre-distortion options, a slightly more aggressive window with a 0.20 roll off factor was used. This causes slightly lower sensitivity (under 7 dB instead of the 7.2 dB maximum), as well as a wider mainlobe and associated 3-dB range resolution. The optimized waveform, not considering pre-distortion, is shown (in theory) in Fig. 4.9. Despite a TB product of 26.25, peak sidelobes of -44 dB are achieved, with a 3-dB range resolution of 37.5 m, plenty high enough for tornado-scale estimates.

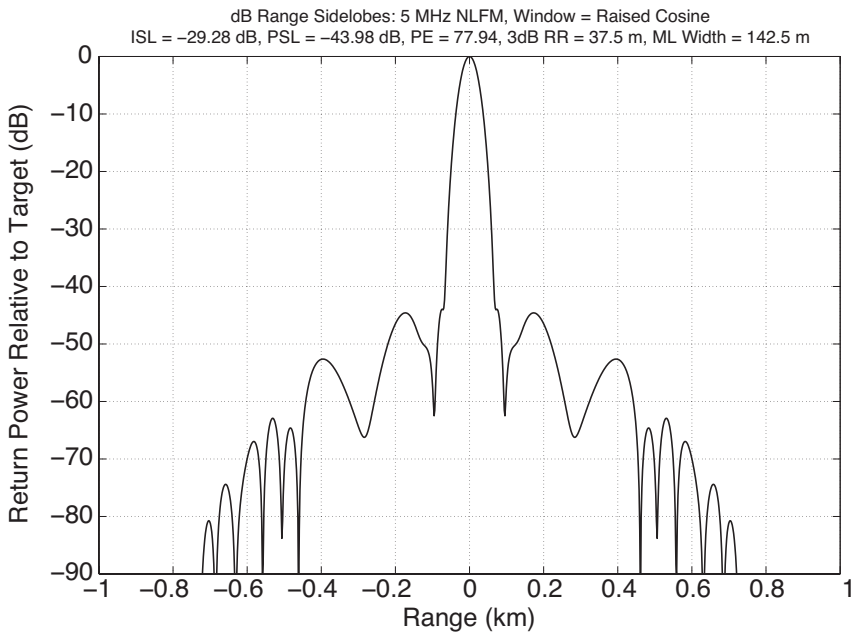

Figure 4.9: *Theoretical AIR tornado-scale compressed waveform. With a 5.25 μs pulse and 5 MHz of bandwidth, PSL of -44 dB, ISL of -29 dB, and 3-dB range resolution of 37.5 m are achieved.*

An example of the gain afforded by higher sensitivity is shown in Fig. 4.10. In this case, a convective case was located to the west of the radar moving toward the northeast. On the left, poor sensitivity from the short pulse does not provide sufficient sensitivity of the storm cluster. The noise floor is exceedingly high (roughly 32 dBZ) and attenuation is extensive behind the convection. In the center, using pulse compression and a 5 MHz/5.25 μs pulse a few minutes later, a much lower noise floor of approximately 20 dBZ and SNR is evident. The right inset in Fig. 4.10 is a longer waveform for clear air observations that is described in the next section.

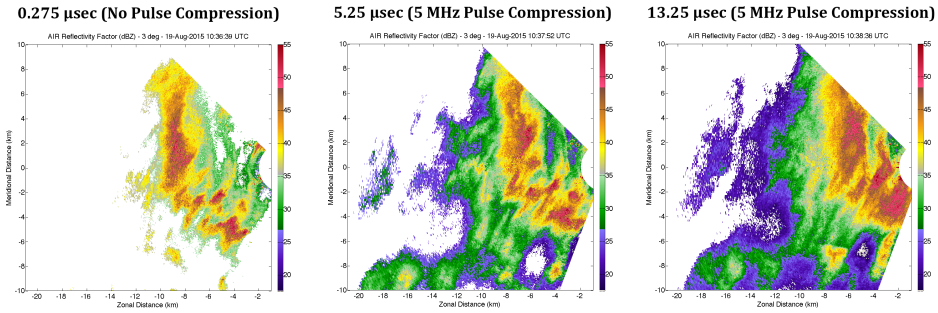

Figure 4.10: *Comparison of reflectivity factor of a convective cluster without (left) and with (center/right) pulse compression with the AIR. Each waveform has roughly 40 m of range resolution and is oversampled to 30 m. The noise floor is very high without pulse compression and attenuation is extreme through heavy precipitation. Significantly increased sensitivity and lowered noise floors are evident with both a 5.25 µs and 13.25 µs pulse. The 13.25 µs pulse is the same waveform described in the next section.*

Due to the lack of a leak through on transmit, the AIR has limited potential for pre-distortion. However, with the transmit feed horn located at the top of the array, the bottom elements of the array are less saturated than those at the top and sample a useful characteristic waveform during transmission. In order to achieve some pre-distortion, a sampling of the bottom four elements was averaged to obtain a transmit sample. This was used to complete pre-distortion, although the quality of the filter was not expected to be as high as PX-1000. In order to test the sidelobe performance, the radial power near the point target to the northwest of the radar on the right side if Fig. 4.10 was analyzed in Fig. 4.11. The peak power is at -35.9 dB, with the first sidelobes

as -66.8 dB, making the PSL roughly -31 dB. This is a substantial decrease from theory, but is sufficient for most weather observations with the AIR.

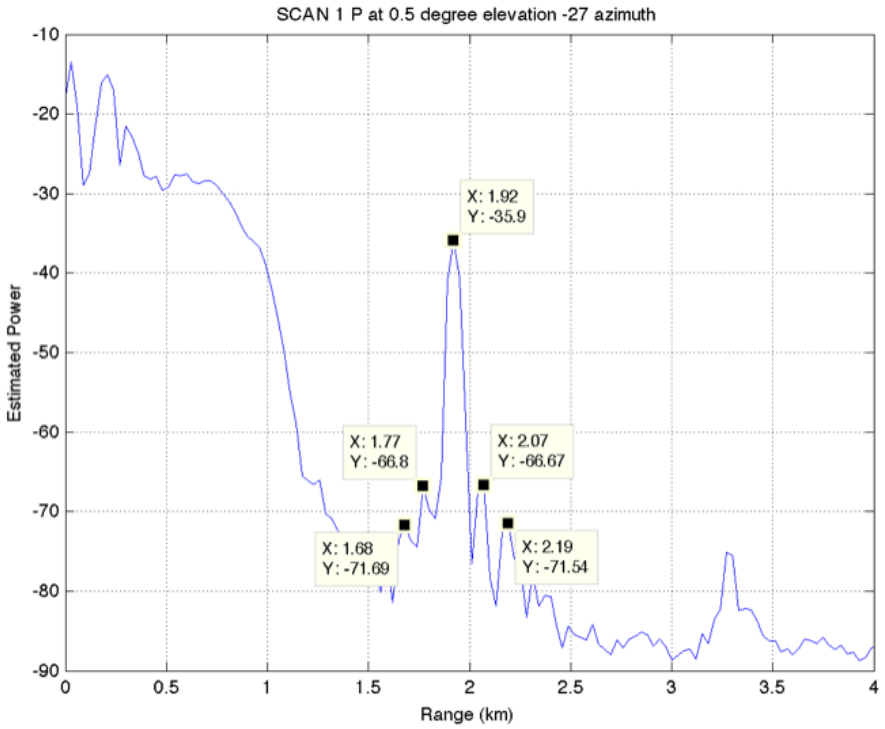

Figure 4.11: *Sample of a point target power return from the AIR to test sidelobe performance. PSL of approximately -31 dB are observed on each side of a point target.*

4.3 Clear Air and High Sensitivity Waveforms

A final case study for mission-specific waveforms is the observation of clear air and weak-return boundaries with low-power radar systems. While radars like the PX-1000 and AIR can achieve their primary goals quite well with the use of pulse compression, low-reflectivity phenomena, even close to the radar, present a unique challenge. This issue can be compared to the scanning modes

on the WSR-88D; in order to achieve acceptable sensitivity and data quality in clear air conditions, the WSR-88D scan strategies and waveforms are quite different than they are for severe thunderstorms. Therefore, it is prudent to explore different waveform solutions with low-powered radars as well.

4.3.1 PX-1000 Waveforms for High Sensitivity

The primary waveform for PX-1000 has three main goals: high sensitivity, long range, and low sidelobes. This is possible through the use of the maximum pulse length (for sensitivity and range) and the optimization procedure from Chapter 3 to minimize sidelobes while limiting windowing. The primary waveform provides excellent performance out to roughly 60 km, but at one major cost: the blind range. This is mitigated with the fill pulse, but even out to only 10.3 km, a 2 μs is not sufficiently sensitive at 100 W peak power. This means that if the feature of interest has low reflectivity and is close to the radar, the region inside the blind range can suffer enough in sensitivity to make the radar unusable for the desired mission.

These types of phenomena are wide and varied, but two specific cases will be investigated in this section: gust front passages and clear air wind observations. Both of these cases involve the necessity to shorten the blind range as much as possible while still achieving significant sensitivity increases from

pulse compression. Of course, a short pulse length results in lower overall sensitivity, but it increases the sensitivity in the original blind range and shortens the range necessary for a fill pulse. With the dependence on r^2 in Eq. (3.3), ranges very close to the radar do not need as long of a pulse length to achieve high sensitivity; this is the same principle that the fill pulse operates on, but it is shortened here to observe weak targets within the original blind range.

For the examples presented in this section, a target pulse length was roughly 5 km, or 33.5 μs (half the original pulse length of PX-1000). Using the same 2.2 MHz of bandwidth for the long pulse, this results in a TB product of 73.7. However, since the absolute maximum sensitivity is desired, *absolutely no windowing* was applied to this design. The resulting matched filter response is shown in Fig. 4.12, with one notable difference from earlier PX-1000 designs; very high sidelobes. With a peak sidelobe level of -44 dB in theory, and worse in practice, these sidelobes are not ideal for a weather radar. However, it is important to realize that the phenomena being observed are *low-reflectivity* targets, meaning they are likely to be just above the noise floor. This means that any sidelobes below 20-25 dB are likely to be sufficient for these examples. In addition, the transmitters were driven entirely into saturation with this waveform, causing higher distortion rates but gaining 1-2 dB of additional sensitivity. This would not normally be done if sidelobes were a concern with little windowing.

The primary use for this waveform was the PECAN project in 2015. This campaign aimed to gain a better understanding of elevated nocturnal convection, a historically difficult process for meteorologists to model and predict. As part of PECAN, there were four main mission goals: observations of mesoscale convective systems (MCSs), bores, pristine convective initiation (CI), and the low level jet (LLJ). PX-1000 was deployed for all four types of missions in June and July of 2015.

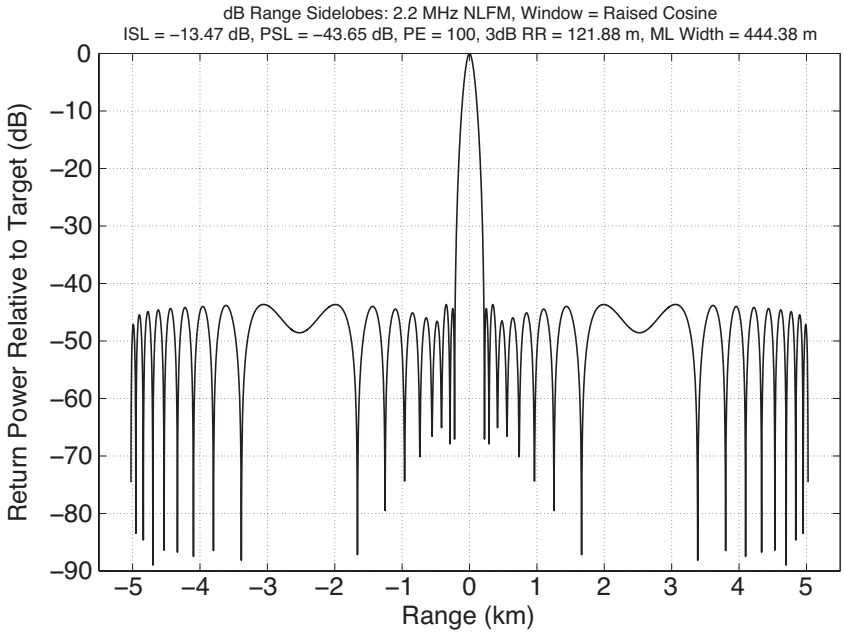

Figure 4.12: *PX-1000 compressed waveform for high-sensitivity observations and clear air operation. PSL is -44 dB, ISL is -13 dB, and 3-dB range resolution is 122 m. No amplitude modulation is applied.*

MCSs and bores generally involve one or more "fine lines" of outflow or oscillatory waves. These phenomena typically pick up small amounts of insects,

bugs, and dirt, lofting them into the radar beam at the head of a density current. A high-powered radar can receive enough scattered energy off of these relatively low densities of targets due to their size (the D^6 ratio in Eq. (2.14)). Part of the PECAN mission goals was to observe the dynamics of these outflow boundaries and bores and how new convection initiates off of them. Since density currents associated with outflow are generally low-level phenomena, they are best observed within 10-15 km of a radar. An example from PECAN of an outflow boundary ahead of a bowing MCS that later became a bore is shown in Fig. 4.13 just before encountering the blind range.

Unfortunately, with a 10.3-km blind range and a short fill pulse, this often leads to a ring of sensitivity that is too low to observe outflow boundaries between approximately 5-10 km. This is shown in Fig. 4.14, where the outflow boundary is crossing through the 5-10 km range within the fill pulse. The short pulse is not able to see the outflow boundary, causing a significant discontinuity.

Since the focus of this case is the outflow boundary, sidelobes are not a critical issue due to its low reflectivity. Therefore, in Fig. 4.15, PX-1000 was switched to the 5 km pulse. The outflow boundary was crossing into the 5-km range, but a significant proportion was still in the 5-10 km range. The entirety of the boundary was observable in this mode, essentially culling the issue seen in Fig. 4.14. There are some radial spikes of energy apparent near the radar

from clutter sidelobes, but this is largely due a limitation of the existing ground clutter filter and the blind range transition. In future operational instances, these issues would be corrected.

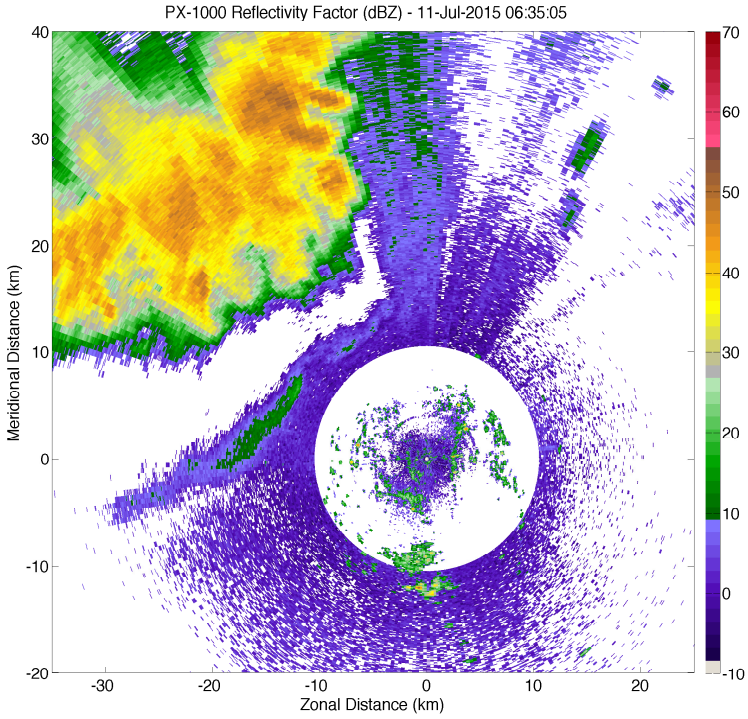

Figure 4.13: *PX-1000 reflectivity factor (in dBZ) showing an outflow boundary ahead of an MCS approaching the blind range.*

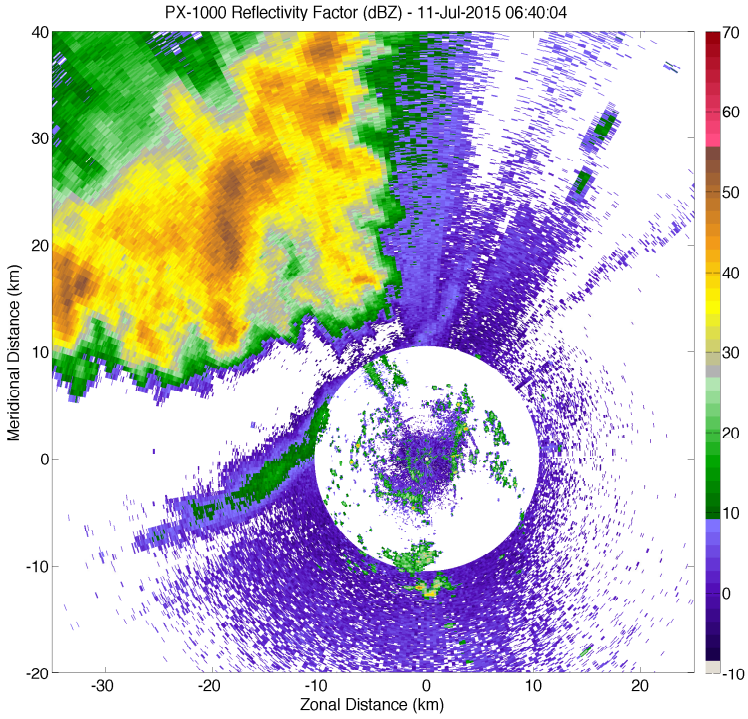

Figure 4.14: *PX-1000 reflectivity factor (in dBZ) showing an outflow boundary ahead of an MCS partially inside the blind range. The outflow boundary can not be resolved, even with the fill pulse due to its low reflectivity and the short pulse length.*

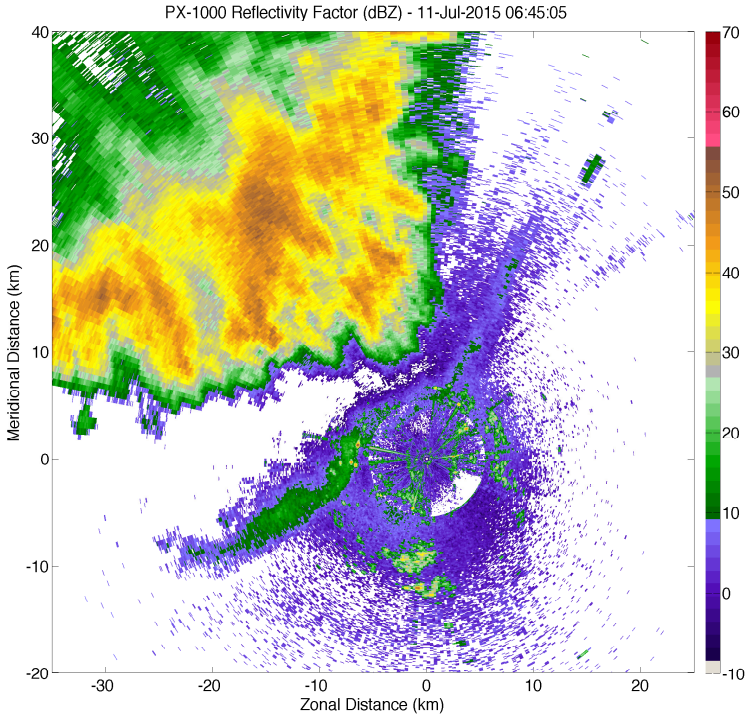

Figure 4.15: *PX-1000 reflectivity factor (in dBZ) showing an outflow boundary ahead of an MCS inside the original blind range (10.3 km) and crossing into the new blind range (with a 5 km pulse). The vast majority of the outflow boundary is observable, especially in the 5-10 km ranges.*

An additional mission of PECAN was observation of the LLJ. The LLJ is a strengthening of the horizontal wind field at the top of the decoupled nocturnal boundary layer that is often responsible for isentropic lift over frontal boundaries resulting in thunderstorm development at night. The LLJ was observed by in-situ methods (radiosondes and tethered balloons) and remote methods (lidar, sodar, and radar). The technique used for radar observations of the LLJ

is called a velocity azimuth display (VAD) wind profile (VWP), which provides horizontal wind estimates using a volumetric scanning strategy (Browning and Wexler 1968). A VWP utilizes the fact that different range gates are associated with different heights. As the radar rotates, the radial wind direction and velocity creates a sine wave with the phase indicating the direction and the amplitude relating to the velocity. As the radar scans in elevation, higher heights can be recorded, similar to a Skew-T Log-P diagram used in radiosonde soundings.

In clear air modes, especially during LLJ missions as part of the PECAN project, the primary scattering mechanism was insects trapped in the boundary layer transition zone. With very low densities but large sizes, the reflectivity factor of these insects was in the 5-10 dBZ range. This was an acceptable level of sensitivity out to approximately 5 km and beyond the edge of the fill pulse, but the range between 5-10 km was left with only the short fill pulse and not enough sensitivity to get any returns above the noise floor. An example of the result is shown in Fig. 4.16. Note the large gap in radial velocity returns, preventing a continuous VWP in range and height. The echo to the west-northwest of the radar is a second trip return from a distant thunderstorm.

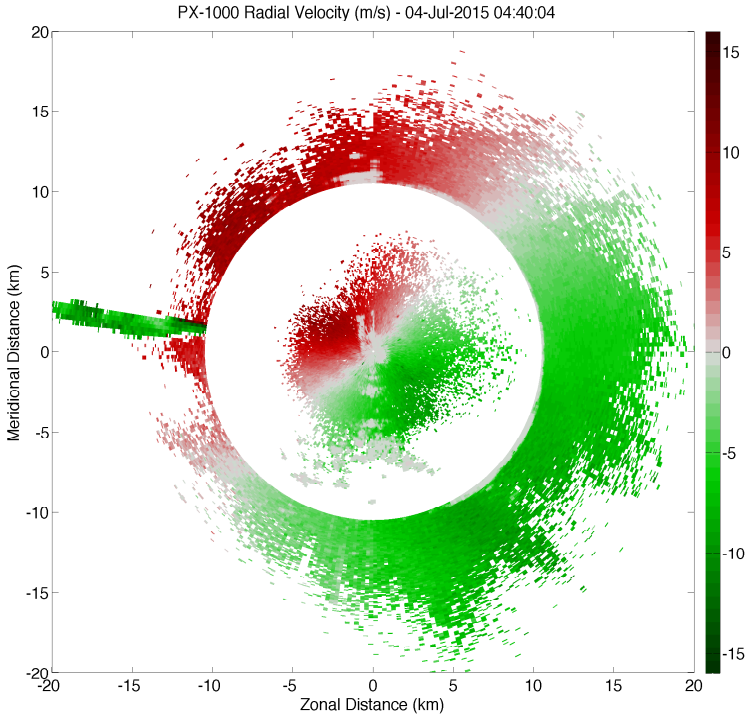

Figure 4.16: *PX-1000 radial velocity (in ms^{-1}) during a LLJ mission as part of the PECAN project using a 10.3-km pulse. The low sensitivity from 5-10 km is due to the use of a short fill pulse not capable of seeing insects at these ranges in the original blind range, making it impossible to form consistent VWPs in range and height. Note that the echo to the WNW of the radar is a second trip return.*

Using the 5-km pulse described previously, a substantially improved picture of the wind field can be seen in Fig. 4.17. By using a 5-km pulse, the fill pulse only needs to be used out to 5 km, which is an acceptable range for scattering off insects with a short pulse. There remains a small ring of low sensitivity which could have been solved with a slightly shorter pulse, but such

a pulse was not readily available during PECAN. The scan in Fig. 4.17 was approximately 10 min after Fig. 4.16. Using this method, consistent scans of the LLJ in range, height, and time were possible throughout the duration of PECAN.

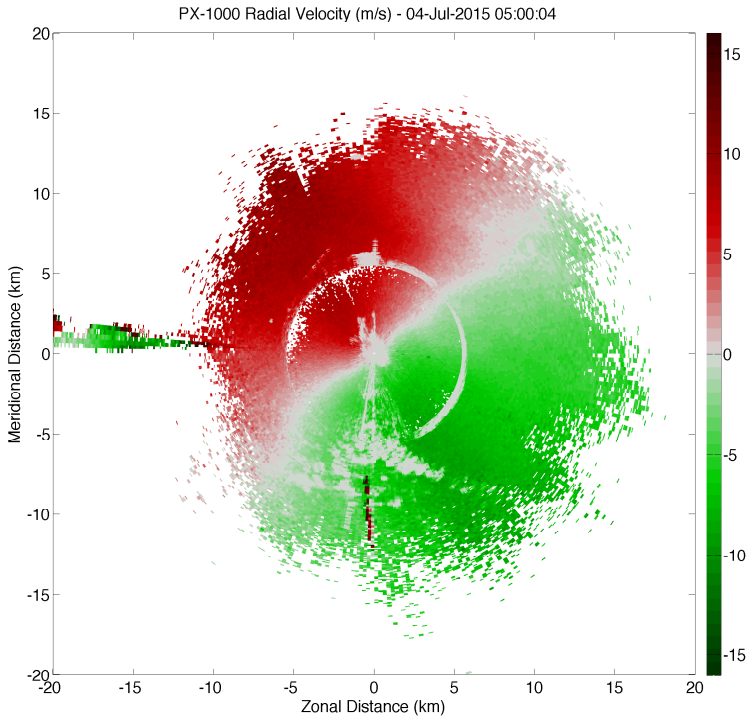

Figure 4.17: *PX-1000 radial velocity (in ms^{-1}) during a LLJ mission as part of the PECAN project using a 5-km pulse. The area of low sensitivity seen in Fig. 4.16 is mitigated by the use of a short pulse (and hence shorter fill pulse). Note that the echo to the WNW of the radar is a second trip return.*

4.3.2 AIR Waveforms for Gust Front Observations

The AIR has also been used for low-reflectivity observations, with the most prominent mission surrounding gust fronts. During supercell and tornado operations it was noticed that the AIR was able to pick up gust fronts ahead of forward flank downdrafts, but the sensitivity was poor. The idea of looking at gust fronts in depth with the AIR has been proposed by Mahre et al. (2016). Due to the nature of gust fronts to act as a density current with a "curling" head at the cusp of the current, RHIs were proposed as a method for observing their dynamics. Typically, scanning radars, even when completing an RHI, must scan in elevation, which takes time to complete. With the AIR, an instantaneous RHI can be completed with every pulse, leading to the ability to combine many pulses for higher sensitivity at extremely high temporal resolutions.

However, even with the combination of multiple pulses, the 5.25 μs pulse is not sensitive enough to obtain the amount of detail desired in a gust front. The observations of gust fronts during supercells with the 5.25 μs pulse were barely above the noise floor at very close range, leading to the need for a longer pulse. Unfortunately, as discussed previously, this leads to the need to re-consider T_s and other waveform aspects due to duty cycle limitations. For this waveform, the maximum pulse length was desired with a Nyquist velocity of 11 ms^{-1}. This leads to a 713 μs T_s, but with advances in processing in

recent years, the duty cycle was able to be pushed to 1.96% instead of 1.85%. This allowed for a 13.25 μs pulse. With a 0.25 rolloff factor, a 4.3 dB increase in sensitivity was observed over the original 5.25 μs pulse (and approximately 10.5 dB over a 1 μs with no pulse compression). The compressed waveform is shown in Fig. 4.18 with peak sidelobes of -47 dB, integrated sidelobes of -29 dB, and 3-db range resolution of 45 m due to added windowing (all in theory). Unlike the PX-1000 clear air waveform, the AIR waveform used windowing due to the desire to also scan an accompanying MCS behind the gust front with acceptable sidelobes. An example of the sensitivity afforded by this waveform is shown on the right side of Fig. 4.10 in the previous section.

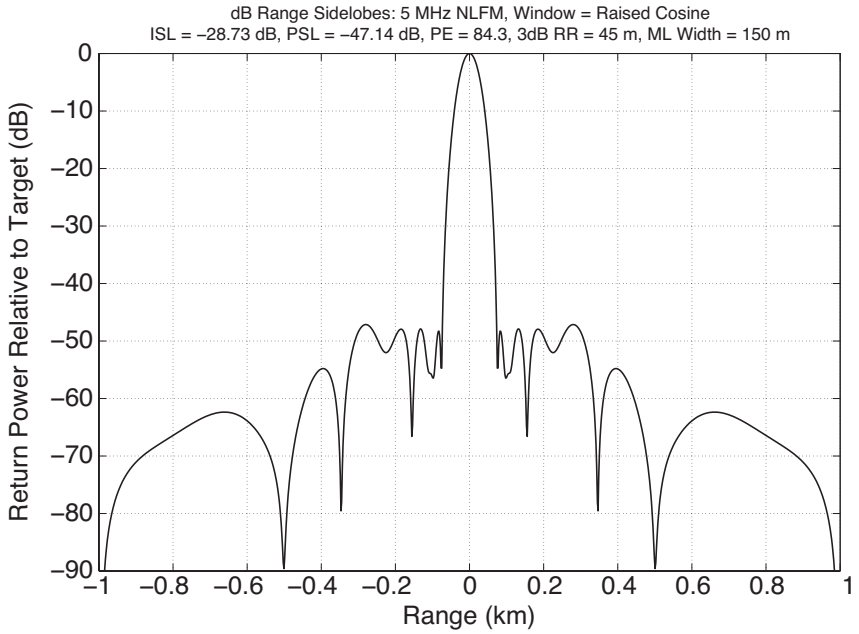

Figure 4.18: *Theoretical AIR clear air compressed waveform. With a 13.25 μs pulse and 5 MHz of bandwidth, PSL of -47 dB, ISL of -29 dB, and 3-dB range resolution of 45 m are achieved. The rolloff factor is 0.25.*

4.3.3 Cognitive Radar Applications

While these examples demonstrate the possibility for waveforms that depend on the observation target, it should be noted that there is the potential for cognitive applications to weather radar. Cognitive radar is an area of study that is undergoing rapid research and development (Haykin 2012a,b). Cognitive radar was introduced by Haykin (2006) as a potential solution to many of the problems that remain unsolved in radar technology. Specifically, Guerci (2010, 2011) develop a series of potential applications to future radar systems, ranging from target detection and tracking to networked and collaborative sensing. Among these applications is active selection of transmit waveforms for weather radar based on the mission. Cognitive radar uses information gleaned from received and processed signals to intelligently select the next transmit waveform.

There are a number of applicable examples mentioned in this chapter that could benefit from cognitive radar techniques. For example, changes to shorter waveforms during the passage of a gust front or during VAD scans could be coordinated. One of the more interesting possible applications is the spectral usage issue mentioned earlier in this chapter. With finite spectral allocations for the total MPAR system, as well as the entire MPAR network, the usage of these spectral resources is a critical operational consideration. One option

is to dynamically change the spectral resources between sectors based on recent observations. This falls under the category of cognitive radar due to the changing of a transmit waveform based on what was observed and processed.

A standard waveform space is shown on the left side of Fig. 4.19. Each sector would be allocated an equal amount of spectral resources, both for the long pulse and the fill pulse. This would be the standard operating mode. However, if a storm of interest moved into one sector, deemed the "active" sector, spectrum from the other sectors could be borrowed while the active sector is scanning the storm. This could involve scanning higher elevations on the other sectors while the active sector is scanning the storm at low elevations to save temporal resources. With the extra spectrum, the active sector could potentially scan the storm of interest at higher isolation resolution and then average range gates to achieve more independent samples (or, alternatively, use frequency hopping, which could change across the entire waveform space from pulse to pulse). This could allow more-rapid scanning and more-rapid update rates of the storm. This modified waveform space is shown on the right side of Fig. 4.19 as an example. This may be a future aspect of advanced dynamic scanning strategies in an MPAR network that could benefit from numerous optimized transmit waveforms of different lengths and bandwidths.

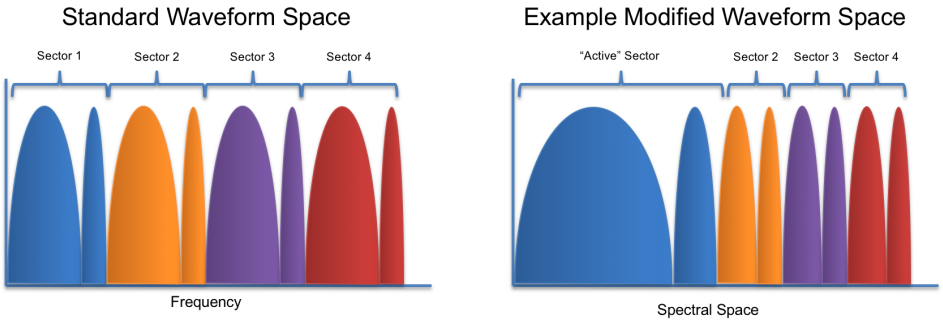

Figure 4.19: *An example of cognitive radar applied to the MPAR issue of spectrum management. On the left, each sector is allocated an equal amount of spectral resources for the long pulse and short pulse. On the right, the "active" sector (theoretically with severe weather or some other area of importance) is allocated more resources while the other sectors are allocated fewer resources. This methodology can be used when a storm of interest is being scanned at low levels on the active sector.*

Chapter 5

Applications of Waveforms for Weather Observations

5.1 The 20 May 2013 Moore Tornado: Analysis with PX-1000

The PX-1000 was designed, in part, as a testbed for meteorological waveform design. However, its home location in central Oklahoma has allowed for the observation of numerous severe storms while utilizing pulse compression waveforms. These datasets are relatively rare in the meteorological community and provide excellent validation for pulse compression weather radar. One dataset in particular, the 20 May 2013 Moore, Oklahoma tornado, is a resounding example of the quality of data that can be achieved with a solid state weather radar. This section provides a rigorous scientific analysis of this case using PX-1000 data. This analysis provides a convincing argument for the use of pulse compression in weather radar.

5.1.1 Meteorological Background

The 20 May 2013 EF5 tornado that affected the cities of Newcastle, Oklahoma City, and Moore, Oklahoma was observed by at least 11 radar systems in and around the metropolitan area of Oklahoma City with varying update

rates, spatial resolutions, distances/angles to the storm, and capabilities (e.g., polarimetric moments; Fig. 5.1). The PX-1000 combined temporal resolution of 20 s and spatial resolution of 112 m in range (oversampled to 30 m) with high-quality polarimetric estimates and a serendipitously close range to form a distinct perspective regarding fine-scale phenomena in the storm.

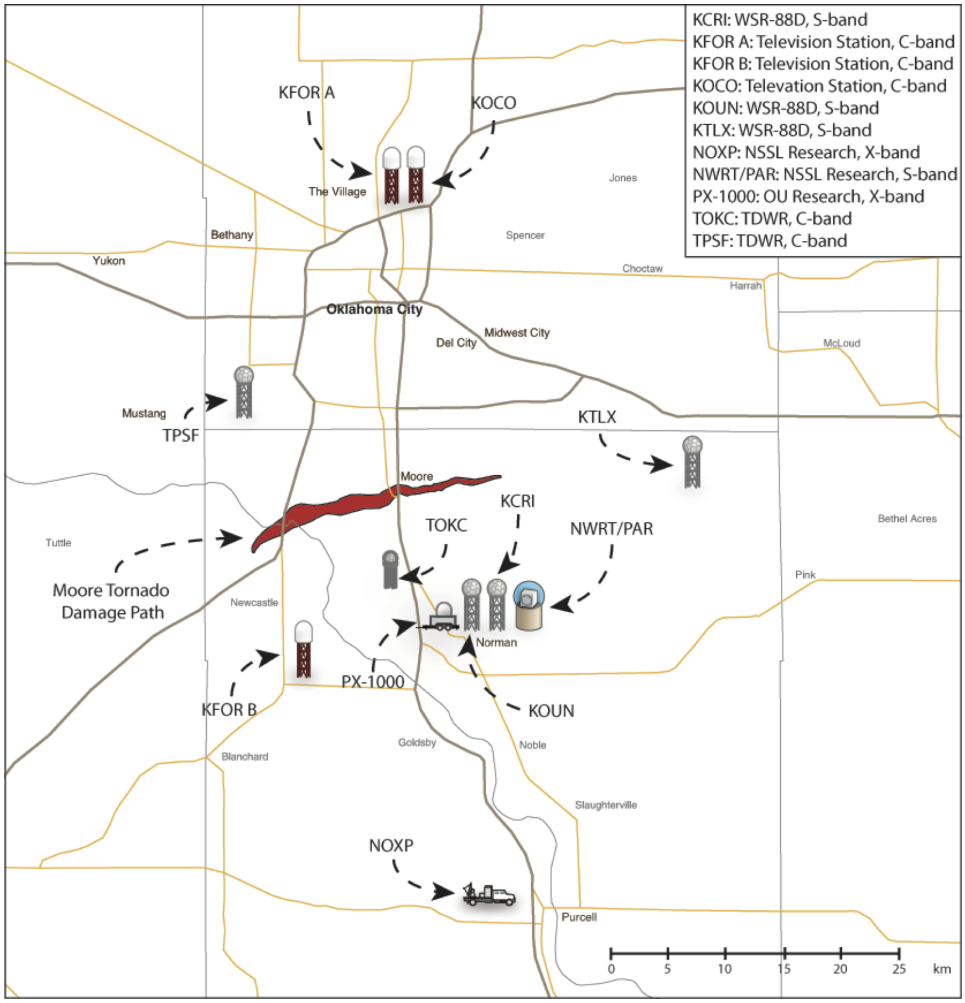

Figure 5.1: *Locations of known radars scanning the 20 May 2013 Moore tornado . Theses radars represent operational weather radars, research radars, and television station weather radars. In total, at least 11 radars scanned the storm for its duration at varying update rates, spatial resolutions, distances/angles to the storm, and capabilities.*

The Moore storm is particularly suited for this type of analysis due to its strength, location, and high-profile nature. These factors combined to result in the most detailed storm survey in NWS history, consisting of more than 4,200 damage indicators (Atkins et al. 2014a; Burgess et al. 2014). Of particular interest in the damage survey results was the path of the tornado in the vicinity of the Moore Medical Center (MMC), where a distinct shift in direction and a loop were observed. During analysis of PX-1000 data, a number of fine-scale shifts in the track of the tornado were discovered that were not readily apparent in the damage survey. This section analyzes these track shifts, forward speed changes, debris ejections, and polarimetric tornadic debris signatures (TDSs; Ryzhkov et al. 2002, 2005b) in order to differentiate/compare each of the observed shift instances with the observed loop at the MMC. Such shifts in track are not easily observable without extremely rapid update rates commonly associated with tornado-scale mobile research radars.

Cyclic supercells (Darkow and Roos 1970; Fujita et al. 1970) have been of key interest to many tornado-related research thrusts due to the relation between their rarity and impact. Cyclic mesocyclogenesis, specifically, was first conceptualized by Burgess et al. (1982), while a later detailed case study by Beck et al. (2006) added to the conceptual theory behind mesocyclone occlusions and new mesocyclogenesis. Finer-scale studies regarding cyclic tornadogenesis through the use of higher temporal and spatial resolutions have also

been carried out, and it has been shown that cyclic supercells can be prolific tornado producers and are often the type of supercell associated with tornado outbreaks (Dowell and Bluestein 2002a,b; Tanamachi et al. 2012). These studies have also shown it is not uncommon for brief, weak tornadoes to precede longer-lived, stronger tornadoes.

Furthermore, recent high-resolution mobile radar observations of tornadoes during convective field experiments have provided numerous other areas of insight into supercell and tornado dynamics (e.g., Bluestein et al. 2004; Wurman and Alexander 2005; Bluestein et al. 2007b; Kosiba and Wurman 2010; Wurman et al. 2012; Kosiba and Wurman 2013; Wurman and Kosiba 2013; Kurdzo et al. 2015c,b), as well as storm-scale microphysics and thermodynamics (e.g., Markowski et al. 2002, 2012; Kosiba et al. 2013; Marquis et al. 2012). Specifically, polarimetric observations have driven entirely new studies of mesoscale and storm-scale phenomena, particularly studies of storm microphysics. TDSs, for example, have provided remote tornado detection capabilities (Ryzhkov et al. 2005b; Bluestein et al. 2007a; Kumjian and Ryzhkov 2008; Palmer et al. 2011; Snyder and Ryzhkov 2014) and the potential for new conceptual formulation exists such as the use of TDS observations for tornado strength and debris type determination (Schultz et al. 2012; Bodine et al. 2013, 2014). Ryzhkov et al. (2005b) defined the TDS as an area of high reflectivity,

low differential reflectivity (Z_{DR}), and low co-polar cross-correlation coefficient (ρ_{HV}) co-located with a tornadic vortex signature in radial velocity (v_r). Kumjian and Ryzhkov (2008) identified high Z_{DR} values along the inflow side of the forward-flank precipitation echo, which they termed the Z_{DR} arc. Later studies have shown that the Z_{DR} arc results from size sorting (Kumjian and Ryzhkov 2009; Dawson et al. 2013), and in cyclic supercell cases, formation and dissipation of the Z_{DR} arc is associated with mesocyclogenesis (Kumjian et al. 2010).

A number of important questions remain unanswered regarding our understanding of the relationship between mesocyclo-/tornado-genesis, dissipation, and cyclic evolution. While this is due in large part to the wide range of possible scenarios in severe local storms and their environments, an added caveat is the lack of extremely rapid update rates combined with high-quality data (Heinselman et al. 2008; Heinselman and Torres 2011). When the combination of a cyclic storm with rapid radar updates and high data quality is available, the potential for new conceptual formulations exists. Recently, a series of mobile radar platforms (e.g., Wurman and Randall 2001; Biggerstaff et al. 2005; Weiss et al. 2009; Bluestein et al. 2010; Isom et al. 2013; Pazmany et al. 2013) have provided new insight into the dynamic and cyclic nature of mesocyclogenesis (Ziegler et al. 2001; Beck et al. 2006; French et al. 2008) and

tornado structures and life cycles (Wurman et al. 2010; French et al. 2013b; Wurman and Kosiba 2013; Houser et al. 2015; Snyder and Bluestein 2014).

Rear flank downdrafts (RFDs), specifically, have been a focus of numerous supercell and tornado studies (summarized in Markowski 2002). While in-situ thermodynamic/kinematic observations and studies of RFDs have become quite common since VORTEX and VORTEX2 (e.g., Markowski et al. 2002; Grzych et al. 2007; Finley and Lee 2008; Hirth et al. 2008; Lee et al. 2012; Markowski et al. 2012; Atkins et al. 2014b; Skinner et al. 2014, 2015), rapid-scanning polarimetric datasets of complex RFD evolutions are scarce in the literature. Additionally, the relationship between cyclic mesocyclogenesis, cyclic tornadogenesis, and ongoing RFD/rear-flank gust front surges (RFGFS) can vary considerably from storm to storm.

The comparison between RFGFSs and mesocyclone structure has been a common research theme in recent years (Adlerman et al. 1999; Finley and Lee 2004; Adlerman and Droegemeier 2005; Skinner et al. 2014), as has the comparison between RFGFSs and ongoing tornadic debris (Houser 2013). The Moore storm displayed numerous instances of RFGFSs and subsequent debris ejections; however these surges occurred on extremely rapid time scales and did not result in tornadogenesis or tornadic dissipation, nor did they result in a new mesocyclone in the conventional sense. Adlerman et al. (1999) described the conventional (or "classic") occlusion process as the development

of an evaporatively driven RFD wrapping cyclonically around the mesocyclone, causing a gust front surge and updraft development at midlevels. As the new, two-celled structure of updrafts progresses, the upshear updraft weakens as it is cut off from storm-relative inflow. The single instance of near-occlusion in the Moore storm, herein called a "failed" occlusion, is of particular interest among the RFGFSs.

5.1.2 Event Overview and Tornado Track

During the early afternoon hours of 20 May, 2013, a 500-hPa trough extended from southeastern South Dakota through western Nebraska and Kansas and into northeastern New Mexico, while the right entrance region of a 31 m s^{-1} mid-level jet streak and 15 m s^{-1} of 850-mb flow out of the south-southwest were situated over central Oklahoma. A sharp dryline was located in a north-northeast/south-southwest orientation west of the Interstate 35 (I-35) corridor in central Oklahoma, and the 1800 UTC KOUN sounding in Norman indicated mixed-layer (ML) CAPE of 3120 J kg^{-1}, MLCIN (convective inhibition) of 33 J kg^{-1}, a MLLCL of 890 m, 0-6 km AGL bulk shear of 27 m s^{-1}, and 0-1 km storm relative helicity of 131 m^2 s^{-2} (Fig. 5.2). A stationary surface boundary was co-existent with the dryline, which by 1800 UTC, had begun to bulge into central Oklahoma with surface winds directly to the east turning out of the south-southeast.

The first radar returns of the Moore storm appeared around 1900 UTC, west of Bridge Creek (via PX-1000, the KTLX WSR-88D, and the TOKC TDWR; not shown). By 1934 UTC, three distinct cells and associated mesocyclones were evident, with one near Mustang, a second east of Tuttle, and a third just north of Bridge Creek. By 1946 UTC, the northern cells had dissipated, and the southern cell had rapidly strengthened and organized, with a defined hook structure in reflectivity factor at horizontal polarization (Z_{HH}) and a $\sim$60 m s^{-1} inbound/outbound radial velocity differential (Δv_r) across the mesocyclone (which was $\sim$2 km in horizontal diameter at the sampled elevation). Between 1946-1956 UTC, a surge of precipitation occurred around the southern edge of the hook, with tornadogenesis estimated at 1956 UTC according to the NWS damage survey (Burgess et al. 2014) and gate-to-gate PX-1000 Δv_r of $\sim$35 m s^{-1}. A low-Z_{HH} region in the hook and a polarimetric debris signature quickly became evident in low-level radar scans.

The tornado rapidly strengthened, producing EF3-EF4 damage within four minutes of tornadogenesis. A series of Z_{HH} and v_r examples from key times during the tornado are shown in Fig. 5.3, as well as a hand-analysis of the PX-1000-indicated tornado track (using the location of maximum Δv_r) and the contoured maximum EF-scale damage ratings from Burgess et al. (2014). The track is interpolated using a periodic interpolating cubic spline curve (Lee 1989), which is necessary due to the wide native beamwidth of PX-1000 (1.8

deg). A photograph of the tornado is shown in Fig. 5.4, taken at approximately 2018 UTC (just after impacting Briarwood Elementary School).

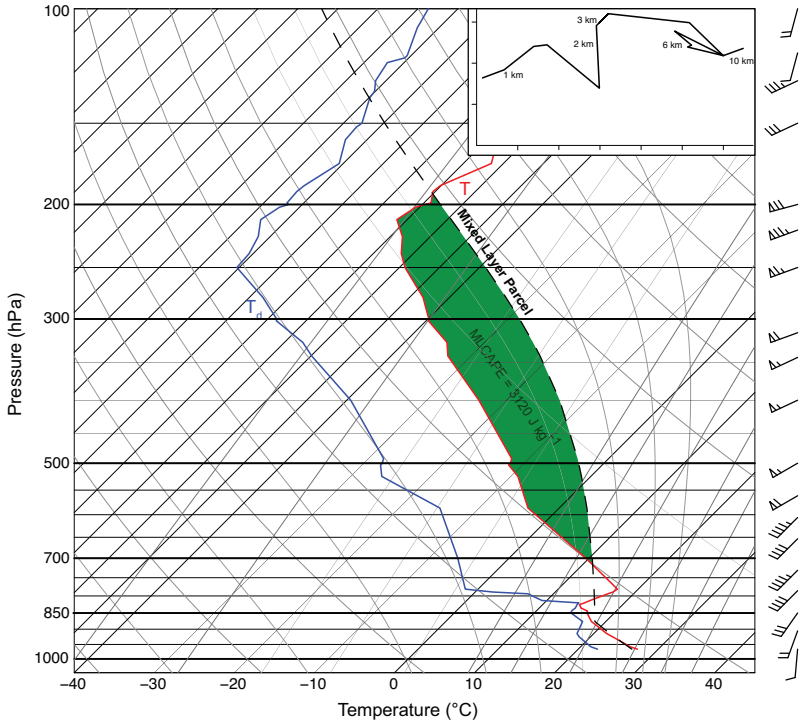

Figure 5.2: *Sounding released by NWS Norman at 1800 UTC 20 May 2013. Thermodynamic sounding consists of temperature T in deg C (red), dew point temperature T_d in deg C (blue), mixed layer parcel path (dashed black), and unstable region shaded in green. Top-right inset shows the hodograph, with winds plotted in m s^{-1} (axis tick marks are in 5 m s^{-1} steps), and critical heights labeled along the hodograph. On the right side of the figure, flags, wind barbs, and half wind barbs denote 50, 10, and 5 kt, respectively.*

While EF3 damage was apparent throughout the majority of the tornado's lifetime, EF4 damage did not occur again until approximately 2010 UTC, although this may be attributable to the sparse density of structures in northern Newcastle. From 2014-2023 UTC, a constant swath of EF4 damage, with occasional EF5 damage, was evident in the damage survey. As seen in the PX-1000 data, the tornado shifted east and north multiple times before turning sharply to the north and looping just west of the MMC at I-35 between 2023-2024 UTC. After this loop, Δv_r decreased and forward ground speed increased, but consistent EF3 (and common EF4) damage continued through approximately 2030 UTC, with dissipation occurring around 2035 UTC. The NWS survey indicated that the tornado lasted 39 minutes and had a path length of 23 km and a maximum damage width of 1.7 km. Of the 4,531 damaged structures, over 3,500 were residential buildings (Atkins et al. 2014a), and more than 300 structures experienced EF4/EF5 damage (Burgess et al. 2014).

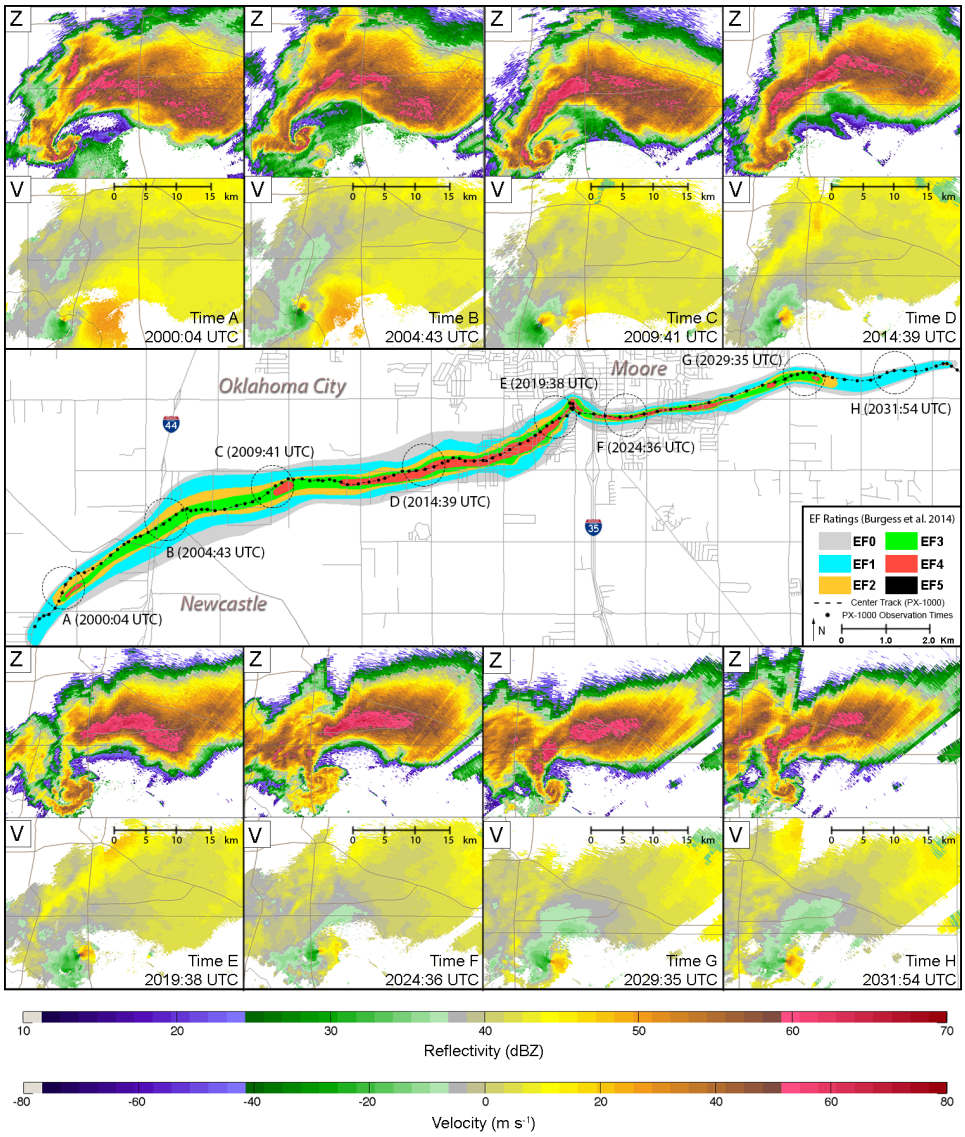

Figure 5.3: *EF-scale damage ratings (colored shading, from Burgess et al. 2014), vortex center track from PX-1000 Δv_r data (dotted black line), PX-1000 observation times (black dots), and sample Z_{HH} and v_r data from different times/locations along the tornado track shown in top/bottom frames (denoted by circles and times A-H).*

Figure 5.4: *The tornado in Moore, Oklahoma at approximately 2018 UTC. View is from just east of Indian Hills Road and 48th Avenue NW, looking to the NNW. Photograph provided by Gabriel Garfield.*

5.1.3 Data Collection and Processing Methods

Operating at 100-W peak power on each channel (for simultaneous independent H/V transmit/receive), the pulse compression scheme described in Chapter 3 was used in order to achieve the necessary sensitivity for meteorological data collection. The resulting sensitivity is approximately 14 dBZ at 50 km range, and the native range resolution is 112 m. The 1.8-m diameter parabolic dish results in a 1.8-deg azimuthal resolution at 9.55 GHz, and the scanning

technique used on 20 May resulted in an effective beamwidth of 2.0 deg (utilizing the effective beamwidth formulation in Doviak and Zrnić 1993). The range gates and azimuths were oversampled to 30 m and 1.0 deg, respectively.

The time-frequency multiplexing (TFM) method described in Cheong et al. (2013a) was utilized to fill the blind range with a short pulse (2 μs). The resulting sensitivity is lower in the 10.3 km surrounding the radar, however, strong echoes such as those associated with the tornado/parent supercell are sufficiently resolved and do not hinder the analysis presented in this study. This discrepancy is more apparent in weaker echoes, as seen in Fig. 5.5 where a circular area of lower sensitivity is apparent. The Moore tornado skirted the edge of the blind range, but for the majority of its lifetime was just beyond this range.

In order to achieve high quality estimates, the multilag method detailed in Lei et al. (2012) is used for moment estimation. The multilag method is especially valuable for ρ_{HV} estimation in low-signal-to-noise (SNR) situations. This method, when combined with the TFM technique, allows for ρ_{HV} estimates that are less susceptible to low SNRs, resulting in significantly increased accuracy and smooth transitions across the blind range (Cheong et al. 2013b). In areas of high spectrum width, however, the multilag Gaussian fit does not hold. Therefore, gates with lag-2 spectrum widths greater than 5 m s^{-1} as well as SNR greater than 10 dB were processed with standard pulse-pair moment

estimates. An example of this masking is shown in Fig. 5.6, where the area inside the white dashed circle (the TDS) does not have the multilag method applied.

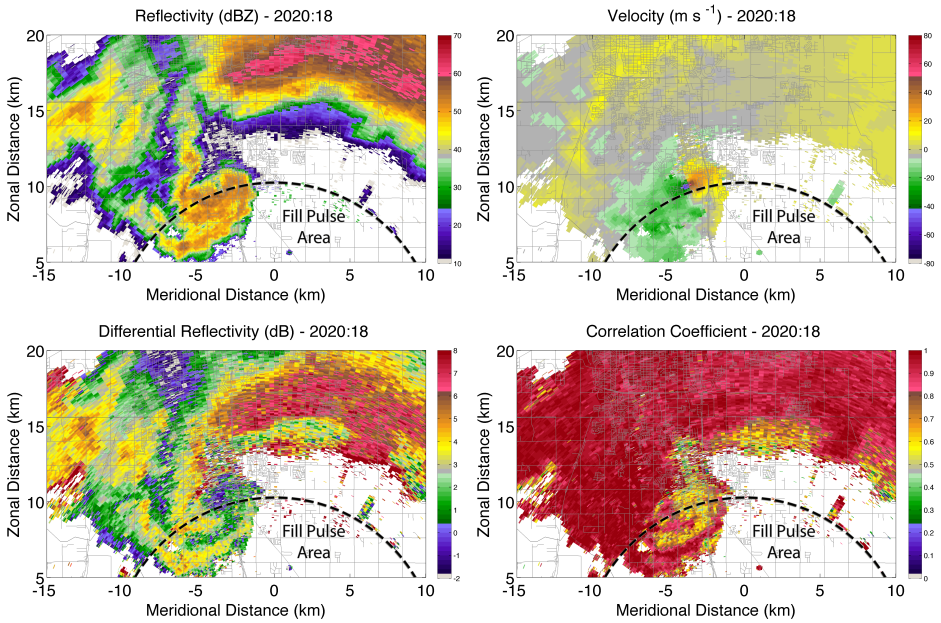

Figure 5.5: *From top left, clockwise:* Z_{HH}*, dealiased* v_r*,* ρ_{HV}*, and* Z_{DR} *at 2020:18 UTC. Dashed semi-circle represents the northern half of the PX-1000 fill pulse edge, approximately 10.3 km from the radar. Distances labeled are from the radar location, which is to the south of the frame.*

PX-1000 is capable of custom scanning strategies, ranging from volumetric scans to PPI scans and RHI scans. Before the onset of severe weather on 20 May, PX-1000 was set to run at a constant 2.6-deg elevation (PPI) scan at a rotation rate of 18 deg s^{-1}, resulting in an update rate of 20 s. Although other scanning strategies would have been useful for various types of analysis (e.g., volumetric analysis), the 20-s update rate, even at a single elevation, resulted

in a polarimetric dataset capable of detecting rapidly evolving areas of the storm that a volumetric scanning strategy would have missed.

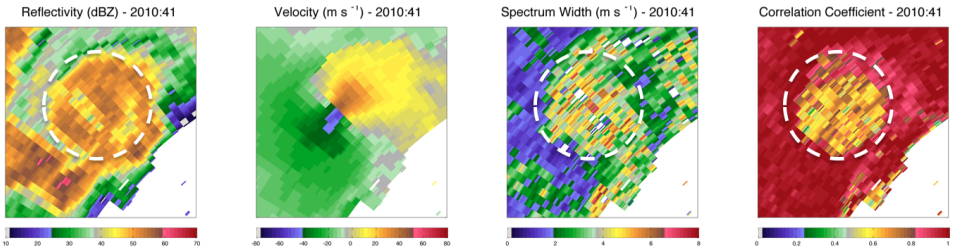

Figure 5.6: *Example of where the multilag method is not applied to data from PX-1000. A simple test for a tornadic debris signature (TDS) is performed (roughly inside the white dashed circle), and multilag is not applied in this mask due to the breakdown of the Gaussian ACF assumption.*

PX-1000 I/Q data were processed with a TFM matched filter to generate moment data. 100 pulses were used for moment estimates. Velocity dealiasing was completed manually using standard unfolding techniques. With availability of high quality polarimetric estimates, attenuation correction was applied to the data using differential attenuation parameterizations (Bringi et al. 1990; Jameson 1992; Park et al. 2005). The values suggested by Snyder et al. (2010) at X-band were used for correction of Z_{HH} and Z_{DR}. The dual-Doppler example shown in future sections was completed using a 14 km x 14 km grid with spacing of 300 m in both dimensions, centered on the tornado. A Barnes analysis (Barnes 1964) with smoothing lengths of 100 m in both dimensions and three passes (Majcen et al. 2008) was used along with a two-dimensional variant of the dual-Doppler method described in Shapiro and Mewes (1999):

$$u = \frac{[(y-y_1)R_2v_{r2} - (y-y_2)R_1v_{r1}]}{[(x-x_2)(y-y_1) - (x-x_1)(y-y_2)]} \tag{5.1}$$

$$v = \frac{[(x-x_2)R_1v_{r1} - (x-x_1)R_2v_{r2}]}{[(x-x_2)(y-y_1) - (x-x_1)(y-y_2)]} \tag{5.2}$$

where x and y are meridional and zonal positions (respectively) to an analysis point with respect to a radar, R is the range to the analysis point from a radar, and v_r is the radial velocity measured by a radar. The subscripts 1 and 2 refer to radar 1 (PX-1000) and radar 2 (KTLX), respectively.

The maximum radial velocity increase (v_i) calculations were formulated using a sliding window along each radial of the single-Doppler v_r field from PX-1000. In order to compare with the values seen in Lee et al. (2012) at a fair resolution difference, the window size was set to approximately 1 km, or 34 range gates. The maximum absolute value of radial velocity differential was determined for each gate based on this sliding window.

Finally, the horizontal vorticity (ζ) calculations were generated via a single-Doppler v_r field from PX-1000. ζ, for a range gate g and azimuth a is computed using the Δv_r between two range gates spaced n_r radials from the range gate at (g,a):

$$\zeta(g,a) = 2\frac{v(g,a+n_r) - v(g,a-n_r)}{(2n_r+1)\Delta\theta} \tag{5.3}$$

5.1.4 PX-1000 Radar Observations

5.1.4.1 Early Tornado Track

Throughout the period of 1900-1956 UTC (pre-tornadogenesis), the general storm motion of the main supercell was northeasterly, with a relatively constant maximum cyclonic vorticity (ζ_{max}) of approximately 0.1 s^{-1}. After the distinction of the main supercell (dissipation of the northern two cells), a fourth cell with a weakly-rotating updraft consisting of generally cyclonic ζ rapidly approached the main supercell from the south. This southern cell began to merge with the main supercell at nearly the exact time of tornadogenesis ($\sim$1956 UTC; Fig. 5.3a) and was not fully ingested into the main supercell until approximately 2012 UTC (Fig. 5.3c). During this period of ingest, the predominantly cyclonic ζ of the main supercell was influenced by the predominantly cyclonic ζ associated with the cell being ingested, and ζ_{max} of the main supercell rose from $\sim$0.2 s^{-1} to $\sim$0.4 s^{-1} over 15 min (Fig. 5.7). While the lack of three-dimensional dual-Doppler data prevents the ability to analyze this cell merger in depth (and data assimilation is beyond the scope of this paper), various studies regarding cell mergers via both simulations and observations have suggested a potential role in tornadogenesis (Bluestein and Weisman 2000; Lee et al. 2006; Wurman et al. 2007b; Hastings et al. 2014).

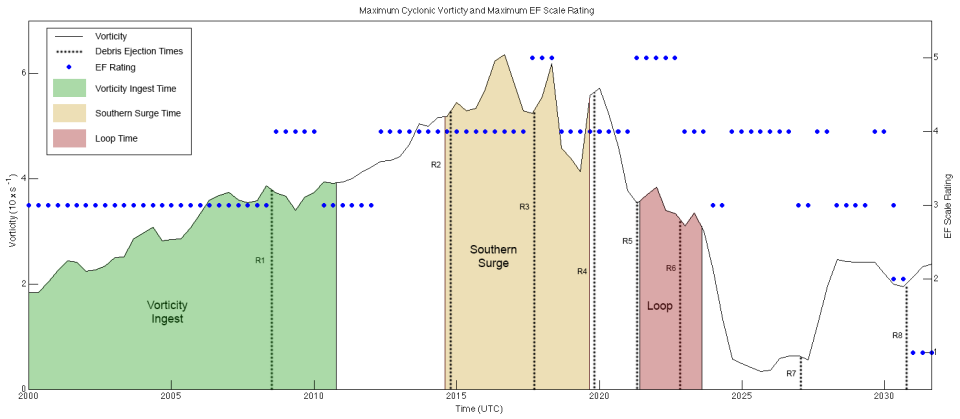

Figure 5.7: *Vorticity time-series (solid black line), instantaneous maximum EF-scale ratings interpreted from Burgess et al. (2014) (blue dots), RFGFS times (dotted black vertical lines and labels R1-R8), and key times referenced throughout the study (shaded; ζ ingest, southern surge, and loop). Left ordinate axis is labeled for $\zeta_{\max}$ plots (10 x s^{-1}), and right ordinate axis is labeled for EF-scale plots.*

Before and during the cell merger, the mesocyclone displayed distinctly different RFGF characteristics compared with the latter part of the storm's life, highlighted by the lack of RFGFSs (to be discussed in depth in upcoming sections). By completion of the merger with the southern cell, a distinct tornadic vortex signature (Brown et al. 1978), quasi-circular TDS (Ryzhkov et al. 2002, 2005b), and Z_{DR} arc (Kumjian and Ryzhkov 2008) were all apparent, along with classic supercellular Z_{HH} and v_r structures (Fig. 5.5; Lemon and Doswell 1979). Additionally, a possible low-reflectivity ribbon (LRR; Snyder et al. 2013) is apparent in some of the early Z_{HH} data.

Fig. 5.8 provides a time-series of maximum EF-scale damage rating (interpreted in time from the NWS damage survey), maximum Δv_r, forward ground speed of the tornado, the direction of vortex movement, and an event timeline highlighting numerous key events. The middle three plots are smoothed using a 5-point sliding window on account of the wide native PX-1000 beamwidth. The timeline depicts start times of RFGFSs and temporary track shifts, the loop at MMC, the existence of a Z_{DR} arc breakdown, and a southern surge of precipitation discussed in later sub-sections.

A gradual increase in maximum Δv_r to values greater than 100 m s^{-1} (and occasionally over 120 m s^{-1}) was apparent, coinciding with a large swath of EF4 and EF5 damage indicators seen in the NWS damage survey (Burgess et al. 2014). During the early stages of the tornado, ground speed was maintained between 8-11 m s^{-1}, with occasionally slower movements during apparent "track shifts."

These track shifts are marked on the timeline and can also be seen in the directional time-series plot, where the vortex center occasionally turned slightly to the right temporarily before recovering to the same general northeasterly motion. These track shifts can be seen in the center panel of Fig. 5.3. The second of these shifts, occurring around 2008-2010 UTC, was associated with a slowed forward ground speed ($\sim$4 m s^{-1} slower than previously), as well as an area of EF4 damage indicators.

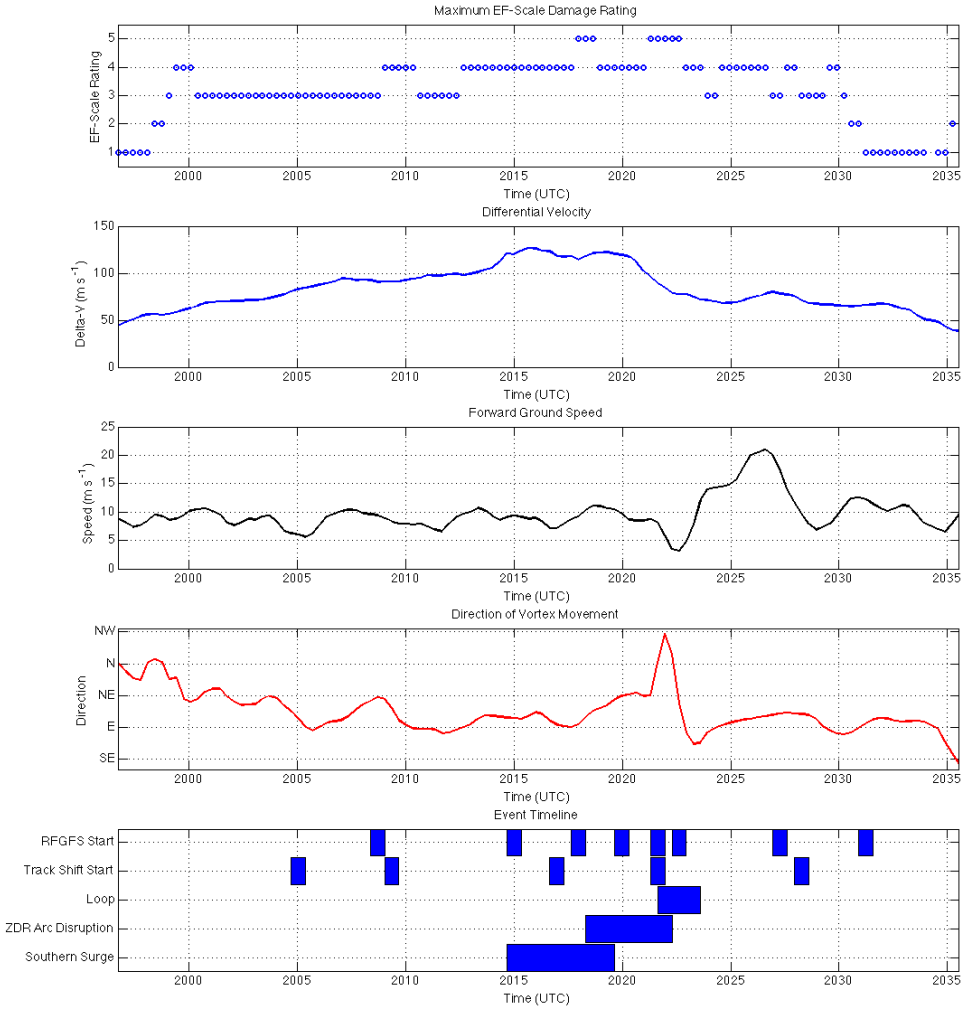

Figure 5.8: *Top four panels: Instantaneous maximum EF-scale ratings interpreted from Burgess et al. (2014), time-series of maximum Δv_r in m s^{-1}, vortex forward ground speed in m s^{-1}, and direction of vortex movement, from top to bottom. Bottom panel: Timeline of various observed characteristics of the tornado/supercell, including (from top to bottom) RFGFSs, track shifts, the loop at the MMC, the existence of a Z_{DR} arc disruption, and a strong southern surge of hydrometeors just before the beginning of the occlusion process.*

5.1.4.2 RFGF Surges and Debris Ejections

Throughout the lifetime of the Moore tornado, a series of track shifts and debris ejections were observed in the PX-1000 data. Debris ejections in this context are defined as an area of debris ejected from the core tornado vortex along a line typically to the south of the tornado and have been referred to as debris "tails" or debris deformation events in previous studies (Houser 2013; Houser et al. 2015). For the purposes of this study, debris ejections/tails are differentiated from the TDS by an asymmetry in the TDS with a non-debris separation between the TDS and the tail necessary for identification. A conceptual diagram of debris ejections/tails is provided in Fig. 5.9, and a series of examples from the Moore case, discussed further in the following sections, can be seen in Fig. 5.10.

As with debris in a TDS, polarimetric radar can be used to identify debris in one of these ejections/tails via relatively low values in ρ_{HV} and Z_{DR}, and relatively high values in Z_{HH}. Bodine et al. (2013) suggest that debris at S-band can be differentiated using Z_{HH} values greater than 42.5 dBZ co-located with ρ_{HV} values below 0.825. These thresholds have been applied to the PX-1000 data at X band in order to locate debris inside and outside the tornadic circulation with the expectation that the values will yield viable results at X band. Since the only debris thresholding studies have taken place

at S band, the scattering differences between S and X band are poorly understood, so it is assumed that S-band values can be applied with reasonable confidence at X band. For the purposes of this study, the S-band values should be close enough for proper discrimination of debris from meteorological scatterers, which typically have considerably higher ρ_{HV} (Dolan and Rutledge 2009; Snyder et al. 2010).

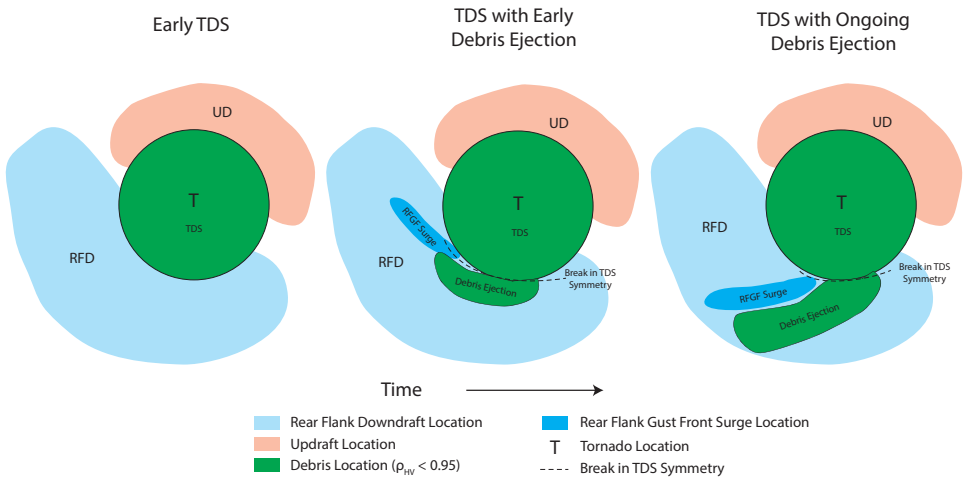

Figure 5.9: *Conceptual diagram of the debris ejection process. The early stages of the tornado (left) display a typical ρ_{HV} minimum within the TDS. As the tornado matures (center), the RFD develops a concentrated area of high low-level winds marking a RFGFS and a debris ejection. The debris ejection/RFGFS is qualitatively defined as a debris "tail" that protrudes beyond the usually symmetric TDS. Later in the debris ejection process (right), the concentrated RFGFS moves around the TDS, pushing debris further from the TDS, characterized by an extended "tail" of low ρ_{HV}.*

Furthermore, it is contended that debris tails have a direct association with RFGFSs, since a surge of high winds would be likely to carry debris from

the tornadic circulation, especially in strong tornadoes in populated areas that contain a significant amount of debris (Fig. 5.9). Additionally, a RFGFS implies an intensification of the downdraft, which would likely enhance debris fallout into the RFD. While the analysis of RFGFSs with high-temporal and high-spatial resolution dual-Doppler observations would be ideal, the lack of radar datasets in the Oklahoma City metropolitan area on 20 May with the temporal resolution of PX-1000 makes this type of analysis in the Moore tornado impossible, especially due to the fact that many of the debris ejections observed existed on time scales less than 1-2 min. Therefore, for the Moore case, it is argued that the PX-1000 observations of debris ejections can be used as a proxy to analyze RFGFSs at high temporal resolution. In order to support this assumption, an overlay of single-Doppler maximum radial velocity increase (v_i) contours at 13 m s^{-1} with a ρ_{HV} underlay for each of the first six debris ejections is shown in Fig. 5.10. Only the first six debris ejections are chosen for this analysis since the final two ejections were primarily in the cross-beam direction, leading to a suboptimal radar viewing angle. The first two cases also consisted of significant cross-beam components, making their appearance much less obvious in Fig. 5.10. The 13 m s^{-1} threshold was chosen based on observations from Lee et al. (2012) in RFGFSs.

It can be argued, as shown in Fig. 5.10, that each of the debris ejections was associated with a v_i maxima in either a co-located or slightly lagged sense,

suggesting that near-surface convergent flow along RFGFSs caused debris lofting and therefore, a manifestation of each RFGFS in the ρ_{HV} field. In some of the cases, especially the first three RFGFSs, a distinct area of convergence directly behind the debris ejection is not apparent; however, a non-symmetry in the convergence field to the south of the TDS is apparent near the observed debris. Although dual-Doppler observations are not available for the majority of RFGFS cases during the Moore tornado, a suitable baseline between PX-1000 and the KTLX WSR-88D was available for three scans, one of which was during a debris ejection. A dual-Doppler analysis with KTLX was performed at 2022:17 UTC, shown in Fig. 5.11. Convergence values higher than 0.1 s^{-1} are contoured in dashed lines. Along the southern debris ejection, pockets of high convergence co-exist with the lowest areas of ρ_{HV}. Given the observation height of roughly 470 m, debris is likely being lofted by updrafts along the RFGFS, as implied by low level convergence and the continuity equation.

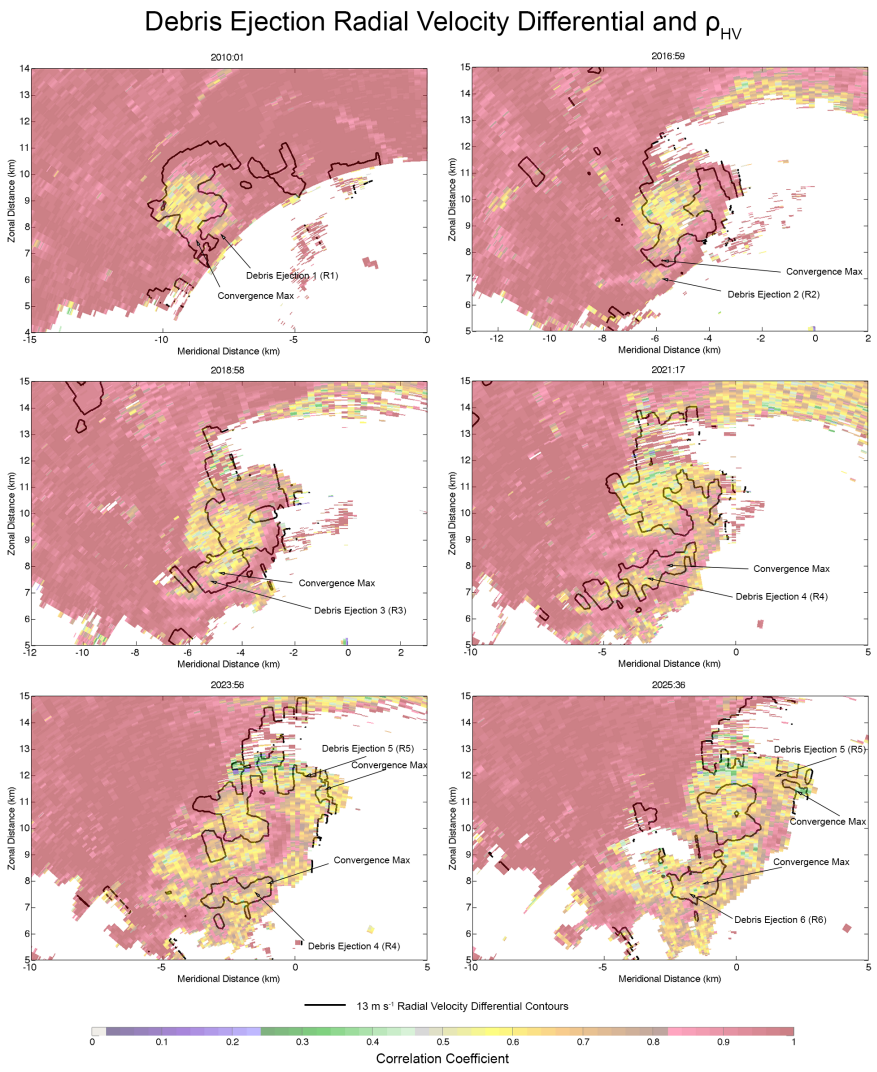

Figure 5.10: *Comparison of the first six debris ejections with single-Doppler PX-1000 maximum radial velocity increase field (v_i). Shading is PX-1000 ρ_{HV} and solid lines are 13 m s^{-1} v_i contours. Areas of convergence maxima corresponding with each debris ejection are marked by arrow and text. Distances labeled are from the radar location, which is to the south of the frame. Note that the first two ejections have significant cross-beam components, making them less obvious in the v_i field.*

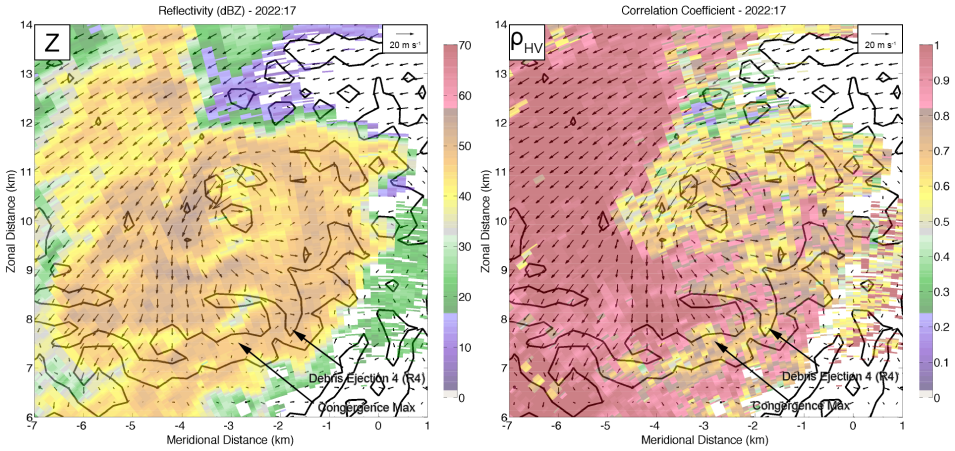

Figure 5.11: *Sample dual-Doppler analysis from PX-1000 and the KTLX WSR-88D. Overlays are two-dimensional ground-relative wind vectors and 0.1 s^{-1} horizontal convergence contours. Underlays are PX-1000 Z_{HH}, left, and PX-1000 ρ_{HV}, right. Time of the analysis is 2022:17 UTC, and the axes are labeled with respect to the PX-1000 location, which is to the south of the frame. KTLX is located to the right of the frame.*

Assuming this is true for all observed debris ejections throughout the lifetime of the Moore tornado, a series of RFGFSs can be analyzed using the high-resolution PX-1000 polarimetric data. The debris ejections (referred to uniformly as RFGFSs from this point forward) occurred regularly along the track of the tornado and often preceded track shifts (Fig. 5.12). The eight RFGFSs, labeled R1-R8, are detailed in Table 5.1, and their beginning stages are labeled in the event timeline in Fig. 5.8. With the lack of high-temporal resolution dual-Doppler observations, the existence of debris in "tail" shapes can be used to analyze characteristics of the RFGFSs. By manually tracing the RFGFS signatures and thresholding for Z_{HH} and ρ_{HV} values consistent with

debris, radar gates associated with RFGFS debris can be compared in direction from the tornado location in a moving reference frame. These locations are shown in polar coordinate histograms in Fig. 5.13. Each gate (i.e., oversampled volume size; roughly 30 x 117 x 117 m in dimension at a range of 10.5 km) is counted as one value for a direction in each plot; however, each plot is normalized in the radial dimension (the number of total gates) to allow the plot to be used primarily for directivity.

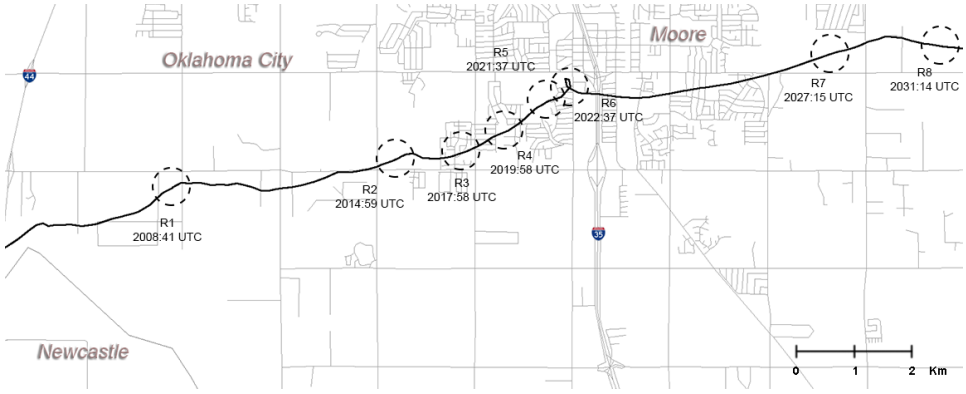

Figure 5.12: *PX-1000 tornado center track (solid black line) and the timing and location of eight RFGFSs (labeled R1-R8 with dashed circles denoting location along track). Noted times and locations are the beginning of each surge.*

Table 5.1: *Rear flank gust front surge characteristics.*

RFGFS	Time Begin	Time End	Max. Velocity	Primary Direction
R1	2008:41 UTC	2010:01 UTC	18.1 m s^{-1}	116 deg (ESE)
R2	2014:59 UTC	2018:38 UTC	13.4 m s^{-1}	206 deg (SSW)
R3	2017:58 UTC	2020:18 UTC	13.6 m s^{-1}	206 deg (SSW)
R4	2019:58 UTC	2023:36 UTC	11.6 m s^{-1}	223 deg (SW)
R5	2021:37 UTC	2026:55 UTC	18.7 m s^{-1}	75 deg (E)
R6	2022:37 UTC	2026:55 UTC	26.4 m s^{-1}	184 deg (S)
R7	2027:15 UTC	2028:55 UTC	20.1 m s^{-1}	152 deg (SSE)
R8	2031:14 UTC	2032:54 UTC	19.0 m s^{-1}	137 deg (SE)

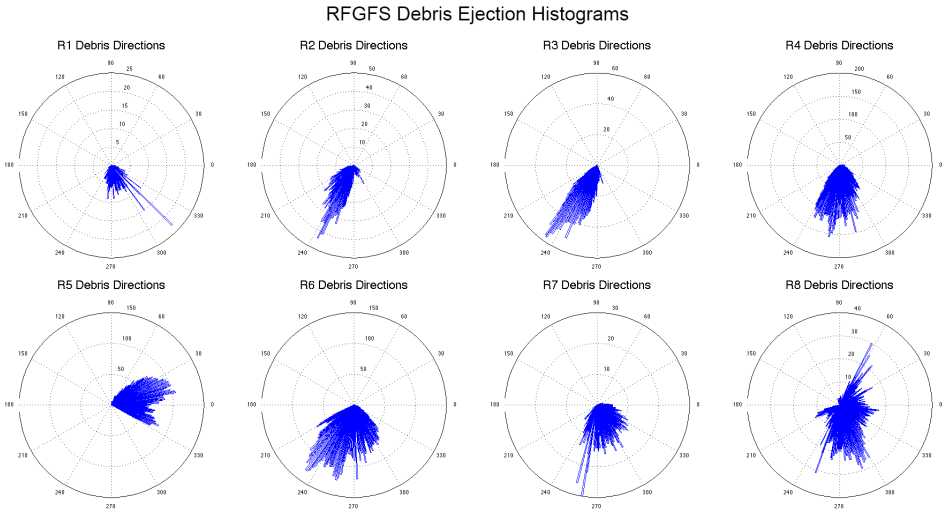

Figure 5.13: *Polar coordinate histograms of radar gates containing debris and their location relative to the center of the tornado (in a moving reference frame) for RFGFSs R1-R8. Magnitude is marked radially outward by number of gates, and direction (360 1-deg bins) indicates relative debris trajectory direction from the tornado. Each ejection plot is normalized by the number of gates, meaning the radial dimension changes from plot to plot.*

It is important to note that this method serves only to indicate gates that contain debris; the debris density is not known. Additionally, it is likely that the amount of debris available for fallout is proportional to tornado intensity and size relative to available damage indicators, meaning that the debris ejections likely contain more debris as the tornado moved through central Moore; therefore, the exact magnitude of each plot in the radial dimension should not be used as a proxy for strength. Instead, the speed values in Table 5.1 are likely more appropriate. The speed values in Table 5.1 were determined using centroid tracking of debris, and the directivity characteristics were derived from the histograms in Fig. 5.13, making them relative to the tornado's location.

As shown in Fig. 5.13, it is apparent that R4, R5, and R6 contain nearly an order of magnitude more radar gates with debris than did the the other RFGFSs. This may be due to stronger surges, but it may also be due to more debris available for lofting/fallout. These particular RFGFSs are discussed in depth in the subsequent sub-section, but it is worth noting that R4-R6 occur with starting points occurring approximately every 1.6 min. The starting time difference of all the RFGFSs, however, ranges from 6.3 min (R1-R2) to 1.0 min (R5-R6). During times other than the occlusion/loop period, described in the next sub-section, this disparity is much smaller, with times ranging from 6.3 min (R1-R2) to 3.0 min (R2-R3), and an average of 4.5 min. Despite the lack of direct correlation between the RFGFSs and the track shifts in Figs. 5.8

and 5.12, a number of the track shifts did occur during or just after a RFGFS. This is visible after R1, R2, the loop after/during R5 (described in the next sub-section), and shortly after R7. R8 also preceded a final occlusion.

5.1.4.3 Loop at Moore Medical Center and Late Track

Shortly after the damage survey presented in Burgess et al. (2014) was completed, there were questions regarding whether a loop or a cusp had occurred near the MMC, approximately 450-500 m west of I-35 (Stumpf 2013; Atkins et al. 2014a). PX-1000 data were used to confirm that the tornado had in fact moved in a circular path just west of the MMC. However, the exact path of the circulation in the PX-1000 data was offset slightly from the damage path (Fig. 5.14). The difference is on the order of 30 m in each direction and is possibly due to a combination of the wide native beamwidth of PX-1000, the potential for vortex tilting (French et al. 2013a), and the effects of combined translational/rotational wind components. Between the time of 2021:37 and 2023:17 UTC, the tornado completed a counter-clockwise loop that spanned a total length of approximately 0.5 km with little forward progress. This event can be seen in the time-series data of forward ground speed and direction in Fig. 5.8 as the tornado moved in a northeast to north to southeast direction at a speed as low as 3 m s^{-1}. At the same time, Δv_r values dipped from a previous high of nearly 125 m s^{-1} to 75 m s^{-1} in the span of less than 150 s.

Shortly after the looping motion in the track, an increase in forward ground speed was observed, from 3 m s^{-1} to 21 m s^{-1} in 4 min. During this time, despite the still heavily populated area, damage indicators generally lessened, with the maximum damage observations dropping to EF3 for the first time in 12 min.

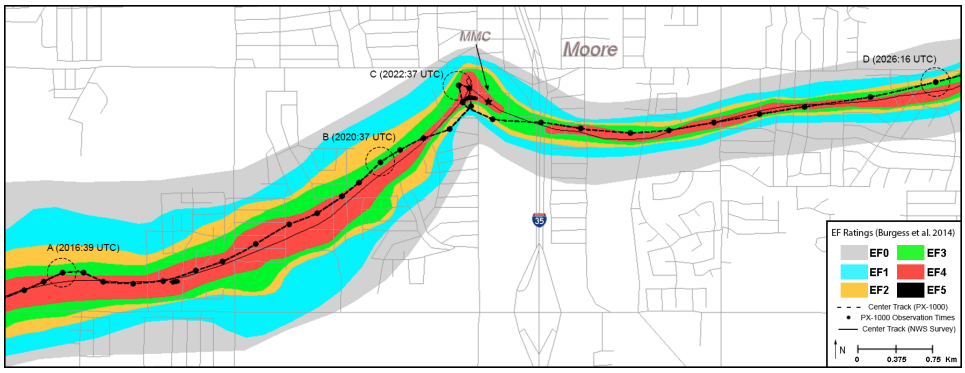

Figure 5.14: *EF-scale damage ratings (colored shading, from Burgess et al. 2014), vortex center track from PX-1000 Δv_r data (dotted black line), and NWS damage survey center track (thin solid black line) for the loop area near the MMC (black star). Circled and labeled times A-D refer to the data presented in Fig. 5.15.*

Although the loop at MMC is apparent in the PX-1000 data, there were a number of potentially related changes in storm structure observed in the minutes beforehand. In order to detail these changes, four sampling times have been selected for annotated presentation in Fig. 5.15, spanning from 2016:39-2026:16 UTC. These times are marked in Fig. 5.14 for reference along the track. Prior to 2016 UTC, a relatively mature tornado in a pseudo-steady state had been ongoing for approximately 20 min (Fig. 5.3), aside

from two minor RFGFS and track shift events (Fig. 5.8). Additionally, a distinctive Z_{DR} arc was evident from the forward flank, all the way to the base of the hook and around the TDS. Between 2014-2017 UTC, an area of high Z_{HH} ($\sim$60 dBZ), high Z_{DR} ($\sim$5 dB), and low ρ_{HV} ($\sim$.9) broke off from the rear/forward flank downdraft interface north of the tornado and surged southward along the RFGF at a speed of 29 m s^{-1}. This phenomenon will be referred to as a "southern surge" from this point forward, and is similar to observations by Kumjian (2011) and French et al. (2015).

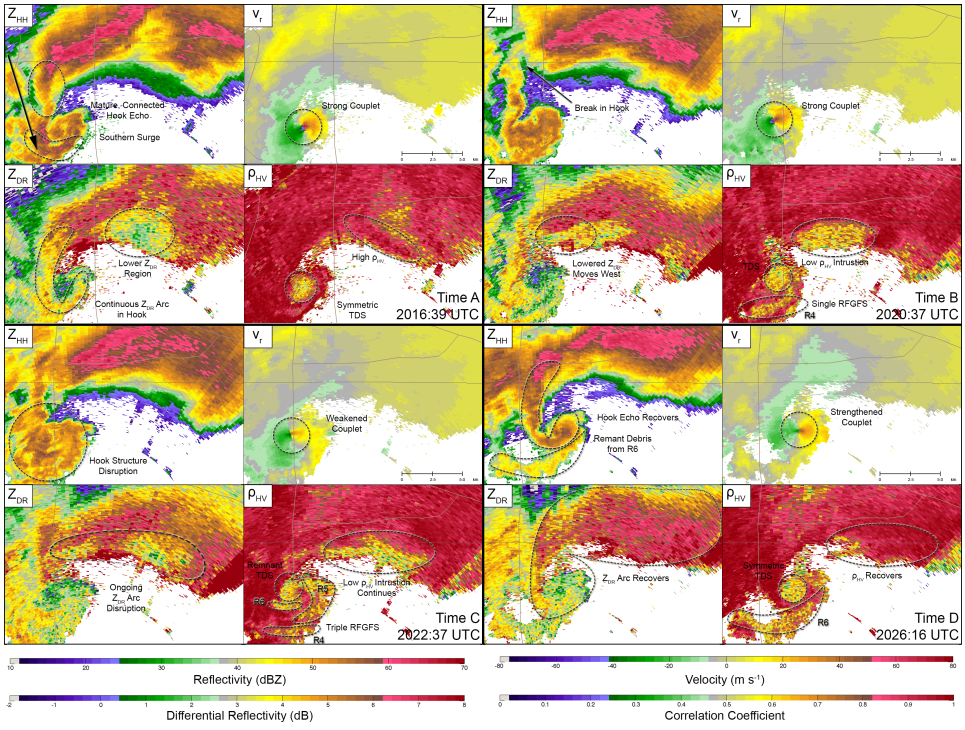

Figure 5.15: *Sample Z_{HH}, v_r, ρ_{HV}, and Z_{DR} data (clockwise from top left in each sub-frame) from different times/locations during the tornado loop period. Times are in reference to circles and times A-D in Fig. 5.14.*

The final stage of this southern surge can be seen in Fig. 5.15a. At this time, 2016:39 UTC, a strong v_r couplet, quasi-circular tornadic debris signature, and Z_{DR} arc were apparent as the mature tornado continued. At nearly the same time as the completing surge, the first area of EF5 damage occurred near Briarwood Elementary School, 2.75 km southwest of MMC. This period marked a distinct turn to the north-northeast, as indicated by the track in Fig. 5.14 and the vortex direction time-series in Fig. 5.8. In the forward flank, ρ_{HV} was relatively high, indicating primarily rain, but an area of lowered Z_{DR} was beginning to break into the Z_{DR} arc along the southern fringe of the forward flank downdraft (FFD).

Shortly afterwards, at 2020:37 UTC, the lowered Z_{DR} values in the forward flank showed a transition to the west (in a storm-relative sense), within the portion of the Z_{DR} arc closest to the updraft (Fig. 5.15b). This has been hypothesized by Kumjian et al. (2010) to indicate a disruption in the updraft and an occlusion process. Additionally, a large area of low ρ_{HV} was becoming evident on the southern flank of the FFD, possibly indicating debris fallout (Magsig and Snow 1998). Subsequently, the southern surge passed through the RFD, and resulted in a RFGFS (R4) and an associated debris ejection, visible in both Z_{HH} and ρ_{HV} in Fig. 5.15b. In the wake of R4, a distinct break in the hook echo to the northwest of the tornado became evident. The high Z_{DR} values in the southern surge had transitioned to lower values as debris was

mixed in with the RFGFS, and the couplet had maintained its high Δv_r over the period (nearly 125 m s^{-1}, among the highest values during the tornado). As can be seen in Fig. 5.13, R4 maintained a predominantly southern motion. Additionally, a strong northerly shift in the track was well underway.

Two minutes later, at 2022:37 UTC, the lowered $Z_{\rm DR}$ values had mostly filled in across the southern forward flank, but an area of lowered $Z_{\rm DR}$ had become apparent to the west of the hook (Fig. 5.15c). In the same area, a seemingly disrupted hook structure is present in $Z_{\rm HH}$. The low $\rho_{\rm HV}$ intrusion in the FFD had shrunk in size but was still evident. A second and third RFGFS (R5 and R6) became evident in both $Z_{\rm HH}$ and $\rho_{\rm HV}$, and the Δv_r had lowered from 125 m s^{-1} to 100 m s^{-1}, indicating a weakened couplet in v_r. RFGFS R5 displayed intensity and directional characteristics of an occluding RFD surge typically seen in occluding cyclic mesocyclogenesis (Fig. 5.13; Adlerman and Droegemeier 2005), with large components of the debris ejection pointing to the northeast, possibly indicating an attempted occlusion of the tornadic circulation as RFD air began to cut off the inflow air to the southeast. R6, on the other hand, was oriented to the south, in a similar fashion to earlier RFGFSs. At this point, the tornado slowed to under 5 m s^{-1} and began to move toward the northwest, also a common characteristic of an occluding mesocyclone/tornado (Burgess et al. 1982; Adlerman et al. 1999; Dowell and Bluestein 2002a).

At 2026:16 UTC (Fig. 5.15d), R6 had surged quickly southward and was arguably the strongest of the RFGFSs (26.4 m s^{-1}; Table 5.1) and had primary debris ejection trajectories toward the south and south-southwest (Fig. 5.13). While the selected time of observation was past the time of the loop, it clearly shows the debris associated with R5 being ejected to the northeast of the tornado while R6 surges to the south. At this time, the forward ground speed had increased to 9 m s^{-1} (Fig. 5.8). Additionally, both the lowered Z_{DR} and ρ_{HV} values had recovered to the values seen during the mature stages before the loop. The Z_{DR} arc, specifically, had recovered to a fully mature state, and the hook echo was once again fully connected in Z_{HH}. A nearly symmetric TDS is evident in ρ_{HV}, and the remnant debris tail from R6 (and presumably previous RFGFSs) is clearly visible in all moments.

Shortly prior to the recovery shown in Fig. 5.15d, at 2024:16 UTC, a fully formed double RFGFS structure was evident. Annotated selections of R5 and R6 are presented in Fig. 5.16, with solid arrows showing mean debris motion along each surge. Forward ground speed rapidly increased to 15 m s^{-1}, even reaching as high as 21 m s^{-1} between 2026-2027 UTC. Afterwards, between 2027-2032 UTC, Δv_r was maintained in the 60-70 m s^{-1} range as forward ground speed recovered to $\sim$10 m s^{-1} and the maximum EF-scale damage ratings fluctuated between EF4 and EF2. A RFGFS (R7) and an associated track shift occurred at 2027:15 UTC, and a final RFGFS (R8) with a predominantly

easterly ejection of debris indicated a final occlusion and tornado dissipation. The tornado moved its final 8 km (post-loop) in 12 min, after it had traversed 15 km in 27 min.

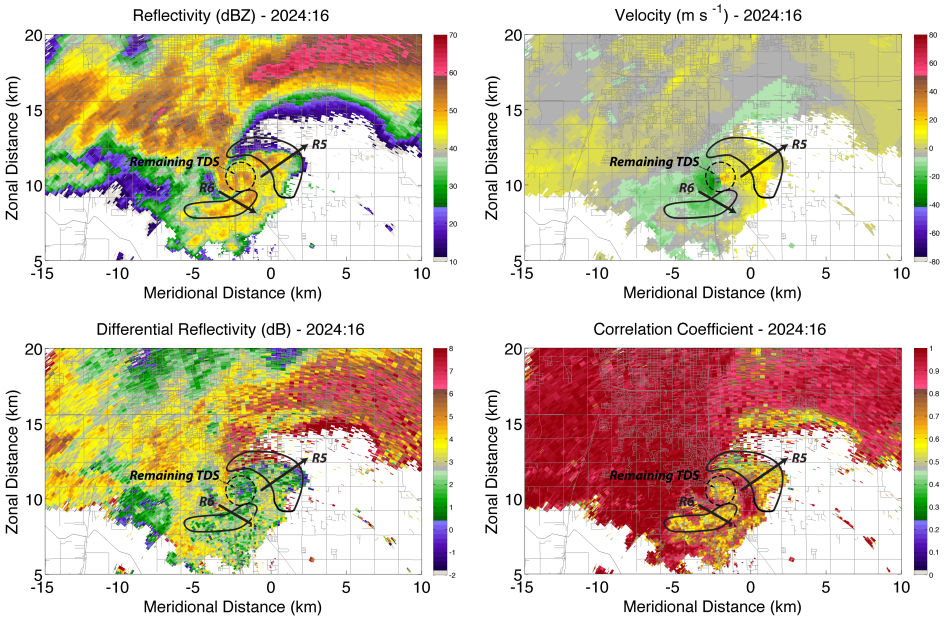

Figure 5.16: *From top left, clockwise:* Z_{HH}*, dealiased* v_r*,* ρ_{HV}*, and* Z_{DR} *at 2024:16 UTC. Annotations and thick lines mark debris ejection 1 (R5), and debris ejection 2 (R6) in the failed occlusion process (Fig. 5.17). Thick arrows depict approximate predominant path of debris ejections/RFGFSs. Dotted circle marks TDS remaining after debris ejections.*

5.1.5 Discussion

The RFD structure in a supercell (Lemon and Doswell 1979) has been hypothesized to be at least partially responsible for both tornado maintenance (Marquis et al. 2008) and eventual tornadic decay through the occlusion process of cold outflow air moving from the south and west sides of the updraft/tornado, around to the north and east sides (Brandes 1978; Lemon and Doswell 1979;

Markowski 2002; Marquis et al. 2012). It has been proposed that the particular RFD surge that results in tornadic occlusion cuts off the source of warm inflow air, disrupting the updraft maintenance process (Klemp and Rotunno 1983; Wicker and Wilhelmson 1995; Adlerman et al. 1999). However, it is important to note that Marquis et al. (2012) show that some tornadoes do not occur until after occlusions.

It can be seen in the PX-1000 data presented that a non-standard mode of cyclic mesocyclone behavior was evident during and around the time of the loop. To date, the majority of cyclic processes observed during similar events revolve around cyclic mesocyclogenesis and/or tornadogenesis. Cyclic mesocyclogenesis can be broken into occluding and non-occluding modes (Adlerman and Droegemeier 2005). In the occluding mode, as each mesocyclone occludes toward the rear side of the storm, a new mesocyclone forms downshear along the trailing RFGF (Ziegler et al. 2001; Beck et al. 2006; French et al. 2008). In the non-occluding mode, the existing mesocyclone propagates away from the main body of the storm along the RFGF as a new mesocyclone forms nearer to the main hook echo. Cyclic tornadogenesis, on the other hand, assumes that in addition to cyclic mesocyclogenesis, new vorticity maxima must form along the RFGF at low levels, increasing in magnitude with height (Dowell and Bluestein 2002a). This concept builds on the Burgess et al. (1982) concept to describe observations of some mesocyclones throughout a

storm's lifetime producing relatively short-lived cyclic tornadoes (Dowell and Bluestein 2002b; Tanamachi et al. 2012).

Furthermore, multiple cyclic tornado cases have observed dissipating tornadoes to move along or near to the occlusion point, resulting in motion toward the "rear" of the updraft (Dowell and Bluestein 2002a; Houser 2013). In some cases, this has led to a nearly full loop of the tornado before eventual occlusion and dissipation occurs (Wurman et al. 2007b; Bluestein et al. 2010; Tanamachi et al. 2012). Houser (2013) and Houser et al. (2015) show a hybrid case from 24 May 2011 in which it is postulated that the RFGFS remained contained without fully wrapping around the updraft, allowing the reorganizing mesocyclone to keep access to warm inflow air. While this did allow the tornado to continue without immediate occlusion, dissipation did occur shortly thereafter.

The Moore case is distinctive in that the occluding RFGFS occurred during a period of rapid, cyclic RFGFS generation, resulting in a well-timed interaction between multiple RFGFSs that caused unusual behavior of the parent mesocyclone and associated tornado. The existence of these observations on such short time scales means that high-temporal resolution observations at high spatial resolution were necessary to observe separation between individual RFGFSs. Although dual-Doppler observations on the same resolution

scales would be ideal, the use of polarimetric radar and associated debris ejections leads to the inference that 8 RFGFSs occurred over a 23-min period. It is important to note that these RFGFSs appear to be manifestations of concentrated RFD flow. There could certainly be dynamic and/or thermodynamic forcing causing multiple areas of focus within the RFD that we are not able to quantify. This has been suggested by Skinner et al. (2014), where dual-Doppler analysis at high-temporal resolution showed multiple areas of concentrated downdrafts within the RFD. However, other than these observations, the existence of such high-resolution surges is lacking in the literature.

While the term "ejection" was chosen for these observations, it should be noted that the predominant forcing resulting in the debris' existence in a tail shape is not necessarily known. Due to the lack of a symmetric ejection of debris, a *purely* lateral ejection caused solely by centrifuging is an unlikely scenario, but some combination of centrifuging, debris fallout, and convergence along the RFGF is a likely culprit. Additionally, observations of RFGFSs at such high frequency is rare, however, recent studies such as Skinner et al. (2014) have seen comparable time scales using relatively rapid-scanning dual-Doppler data. Additionally, the only known observations of debris tails/ejections (Houser 2013; Houser et al. 2015) occurred in another EF-5 storm and were collected at X band. It is possible that such observations will become more prevalent in the near future as rapid-scanning polarimetric

radar (especially at short wavelengths such as X and Ka bands) become more ubiquitous in the field.

It is thought that the high frequency of RFGFSs around the occlusion/loop period may have to do with the weakening/occluding mesocyclone, but it is not clear that there is a direct relation. These relatively quiescent periods display an unmistakably periodic nature of the RFGFSs, although cyclic mesocyclogenesis and/or cyclic tornadogenesis do not occur. It should be noted that in some cases, the debris ejection signatures appear to lead the convergence signatures (or at least line up with each other). Since the observations of PX-1000 are quite high (i.e., hundreds of meters), the position of the gust front is likely further ahead near the surface. The debris lofted into the beam may therefore be associated with the head of a density current that is surging forward below the radar beam. Additionally, a number of causal factors related to the RFGFSs may have affected the tornado track; however, without rapid volumetric scanning capabilities, it is unclear whether these occurrences are due to vortex tilt or other factors. The possible correlation between RFGFSs and track shifts is intriguing, but reasons for these shifts are beyond the scope of this research.

As a potential explanation for what occurred in the Moore tornado, a hybrid conceptual diagram, adapted from the combination of PX-1000 data, Burgess et al. (1982), Dowell and Bluestein (2002a), and the Houser (2013) case, is

presented in Fig. 5.17. As the RFGFS associated with the occlusion (RFGFS 1) wraps RFD air around the updraft and tornado, weakening the mesocyclone and associated vorticity, the tornado begins to move to the north and eventually the northwest in an occlusion-type pattern. Near the apex of the northward turn, a secondary RFGFS, labeled RFGFS 2 in the diagram, pushes a new corridor of RFD air towards the south and southeast, in stark contrast to the predominant direction of RFGFS 1. This process may or may not result in a full loop (a cusp track would also be conceivable), and could take place with more than two RFGFSs. RFGFSs 1 and 2 in the diagram are analogous to R5 and R6 in the Moore case (Fig. 5.16).

The prevailing hypothesis is that initially, an imbalance of inflow and RFD winds causes the tornado to move north, similar to an occlusion process. However, with the strong southerly surge directly afterwards, the inflow and RFD wind balance changes and the vortex migrates southward, restoring the location of the tornado in the updraft and preventing the occlusion of the tornado. This is similar to the tornadic mesocyclone cases described in Adlerman and Droegemeier (2005) and Houser (2013); however, the tornado and mesocyclone recover fully and continue on a path similar to that before the original northerly turn and in a relatively mature state. Additionally, depending on the

strength, timing, and directivity of the secondary RFGFS, as well as any additional RFGFSs throughout the process, abrupt changes in forward ground speed may be observed, as with the Moore case just past I-35.

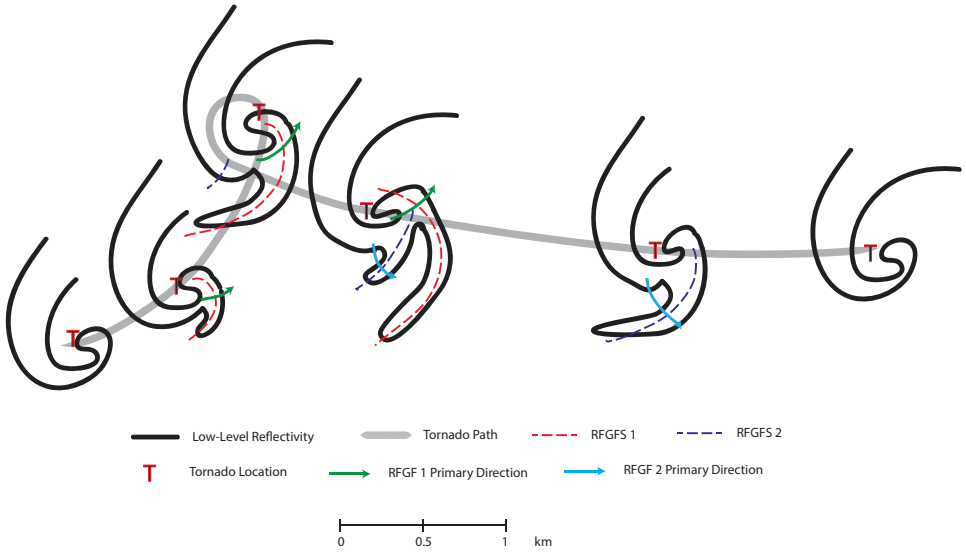

Figure 5.17: *Conceptual diagram of the failed occlusion process. The tornado and mesocyclone are first impacted by an occlusion forcing RFGFS (RFGFS 1), which wraps around the tornado, causing a turn to the north. A second RFGFS (RFGFS 2) impinges upon the tornado near the apex of the loop with a predominantly southern direction relative to RFGFS 1, causing the tornado to move in a circular pattern and re-gain a steady state after a looped track. RFGFSs 1 and 2 are analogous to R5 and R6, respectively, in the Moore case.*

It is important to note that the origins of R5 are not as readily known as the other RFGFSs due to its orientation to the north and east. While it would be a relatively rare occurrence for the RFD to undercut the updraft region of

the storm, the possibility of the RFD wrapping *around* the updraft/tornado regions should be noted (i.e., similar to a synoptic-scale occlusion process; see Fig. 7 in Kumjian 2011). R5 appears to be related to the original source of R4 (the "southern surge"), but a distinct break and difference in debris trajectory is evident. The possibilities for debris sources include RFD wrap around, forward-flank debris fallout, and pure tornadic vortex debris fallout (during a distinct weakening stage), and if more dual-Doppler data were available, the possibility of an occlusion downdraft could also be explored.

This process is being referred to as a "failed occlusion" of the parent mesocyclone and tornado because of the apparent occlusion processes observed prior to the loop. As shown in Fig. 5.15, a number of events indicative of a weakening updraft, debris fallout, and an attempt at occlusion are evident. The southern surge of precipitation that preceded the northerly turn (2016:39 UTC; Fig. 5.15a) was followed by *single-elevation* observations of lowered Z_{HH} and Z_{DR} (2020:37 UTC; Fig. 5.15b), possibly indicating fallout of large drops to heights lower than the radar beam elevation that were then transported rapidly south by the RFD. Such a development in the RFD would likely lead to an enhanced area of RFD winds, resulting in a RFGFS as indicated shortly after in R4. This hypothesis is also supported by the relatively high values of Z_{HH} and Z_{DR} in the southern surge (Fig. 5.15a).

It is hypothesized that the driving force behind the relatively large/strong RFGFS R4 was a combination of more availability of debris (i.e., structure density) and the downward momentum generated in the southern surge via precipitation loading in a wet downdraft. It is important to note that the southern surge is a manifestation of a three-dimensional process, and the polarimetric values associated with the southern surge are likely a result of predominantly large raindrops falling through the RFD, possibly mixed with small debris or non-uniform beam filling (Herzegh and Jameson 1992; Ryzhkov and Zrnić 1995; Kumjian and Ryzhkov 2008; Kumjian et al. 2010). As the large drops fell through the radar beam, it is believed that they were caught in the strong southern surge, transporting them to the southern portion of the RFGF as part of a developing RFGFS.

Eventually, this process appeared to result in a disruption of the hook in Z_{HH} and the Z_{DR} arc. It has been suggested by Kumjian (2011) that the appearance of low values of Z_{DR} to the west of the hook may be indicative of an occlusion downdraft. Additionally, the Z_{DR} arc disruption occurred close to the time that would be expected in an occlusion of the parent mesocyclone and/or tornado (Kumjian et al. 2010; Crowe et al. 2010; Palmer et al. 2011). After the loop, a clear recovery in the Z_{DR} arc is evident by high values of Z_{DR} fully connected around the updraft and hook echo. In order to emphasize the difference between the early mature stages of the tornado, the loop time, and

the later mature stages of the tornado, Fig. 5.18 shows Z_{HH}, ρ_{HV}, Z_{DR}, and differential propagation phase (ϕ_{DP}, in deg) at three times during the tornado. The difference in Z_{DR} arc connection and Z_{DR} values in the forward flank are clear in the middle column compared to the left and right columns.

Despite the attenuation correction applied to the PX-1000 data, and in order to rule out attenuation as a cause for the hook echo break and area of lowered Z_{DR}, KTLX WSR-88D data are presented in Fig. 5.19. KTLX was located 20 km northeast of PX-1000, and was scanning in volume coverage pattern 12 (Brown et al. 2005). The data in Fig. 5.19 are from the 1.4-deg scan in order to closely match the height of the PX-1000 beam. Numerous similar features can be seen, albeit at lower spatial and temporal resolutions. It should be noted that Z_{HH} values in the KTLX data along the southern periphery of the forward flank are low enough to suggest that the low ρ_{HV} values in PX-1000 may not be a result of hail core fallout; rather, that debris fallout is a possible explanation. While sparse, large hail can not be ruled out, the KTLX observations at least suggest that debris fallout is plausible, especially when the amount of debris available for fallout (in a well-developed area) is considered. At no other point in the KTLX data was any indication of a Z_{DR} arc disruption seen.

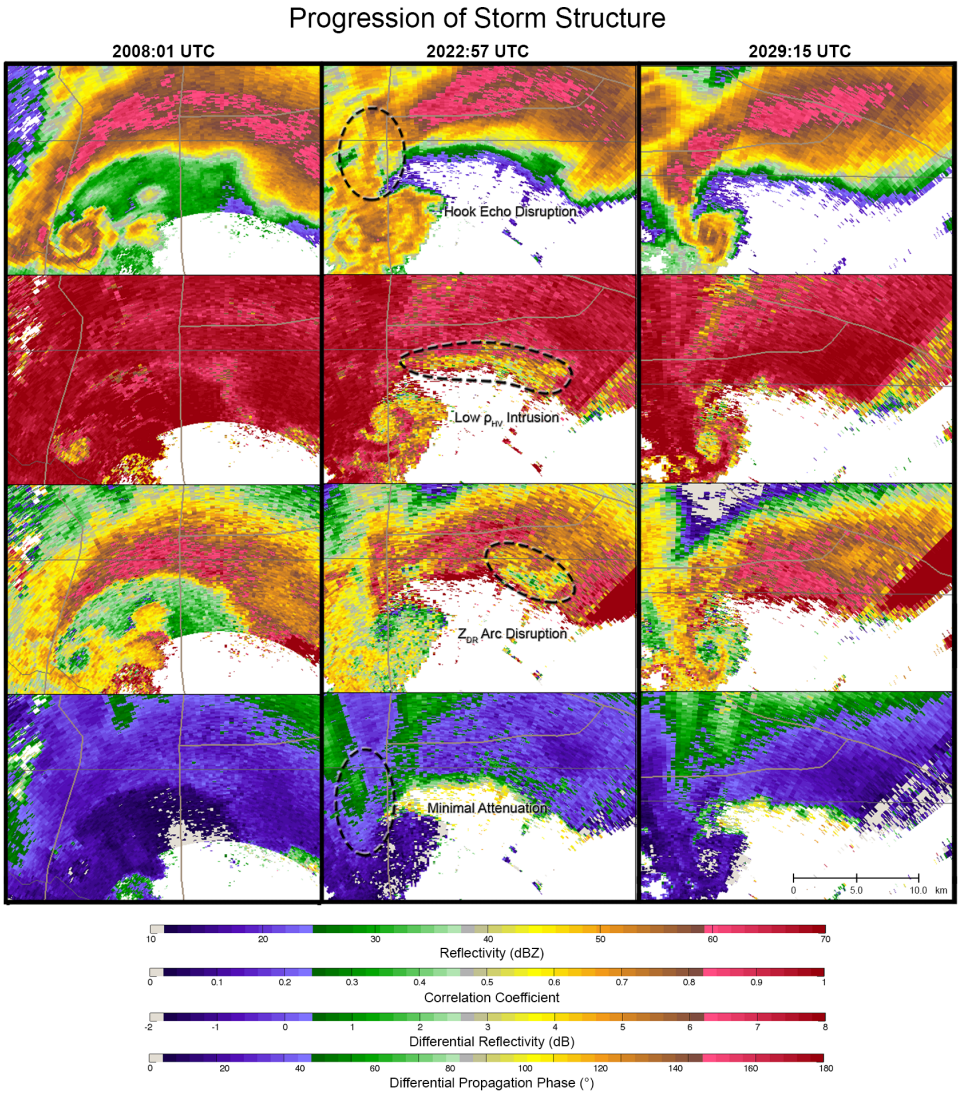

Figure 5.18: *From top to bottom, Z_{HH}, ρ_{HV}, Z_{DR}, and ϕ_{DP} at 2008:01, 2022:57, and 2029:15 UTC, from left to right. Mature reflectivity, TDS, and Z_{DR} arc in the left and right columns are in stark contrast to those in the center column near/during the loop at MMC.*

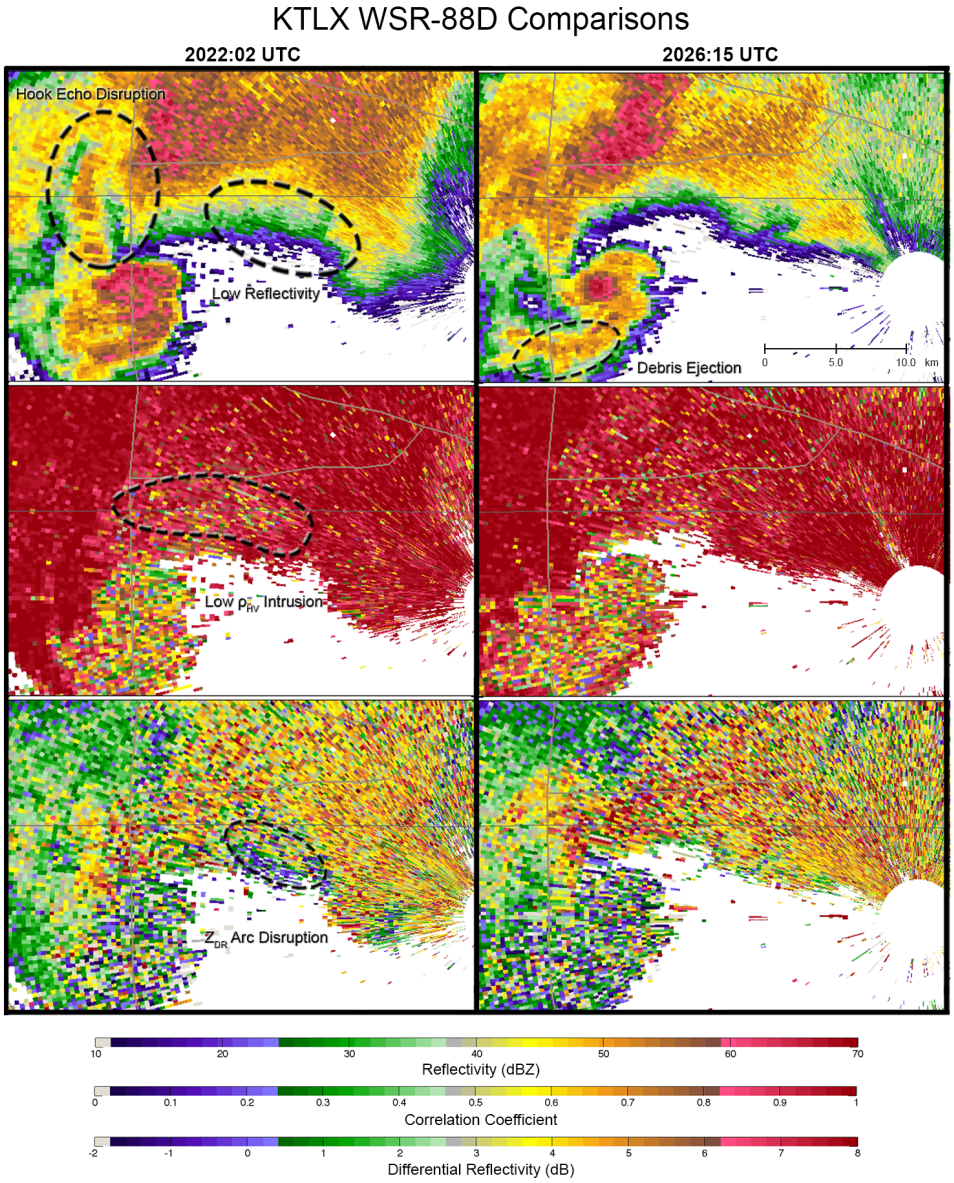

Figure 5.19: *From top to bottom, KTLX Z_{HH}, ρ_{HV}, and Z_{DR} at 2022:02 and 2026:15 UTC, from left to right. Notable similarities with PX-1000 including hook echo and Z_{DR} arc disruption, low ρ_{HV} in the forward flank, and a debris ejection following the loop are marked. KTLX data are from the 1.4-deg elevation.*

Additionally, it can be speculated that the intrusion of low Z_{DR} and ρ_{HV} values into the southern part of the FFD indicate the potential for a weakening

updraft. Magsig and Snow (1998) suggest that rapid weakening of the updraft in a strong tornado could lead to debris fallout in the FFD region. Even small debris mixed with raindrops would be noticeable in both Z_{DR} and ρ_{HV} fields. The difference between low Z_{DR} and ρ_{HV} intrusions in the middle column of Fig. 5.18 is clear compared to the pure rain (and size sorting mechanism of the Z_{DR} arc) in the left and right columns, further indicating a weakened updraft and possible occlusion attempt.

The distinct pattern of debris ejecting to the northeast along the occluding RFGFS, combined with the observations of the tornado moving towards the north in the PX-1000 data, corroborates the hypothesis that an occlusion process was underway. However, visual observations from numerous sources of a continuous condensation funnel and tornado, as well as a continuous damage swath and no indication of a new couplet center in the PX-1000 data suggest that the same tornado was maintained after the loop. The limited number of dual-Doppler analysis points with KTLX, as well as discussions with collaborators looking at other datasets, also suggests that only one mesocyclone existed throughout the failed occlusion process. Due to the highly dynamic and changing situation, even 20 s updates may not be sufficient temporal resolution to determine without a doubt that only one updraft was present throughout the occlusion process. It should be noted that while the failed occlusion is

one hypothesis, other options for mesocyclone/updraft evolution certainly exist with this case (such as extremely rapid cyclic mesocyclogenesis, multiple tornadoes, and/or additional updrafts).

Despite the reduction in apparent strength, the area near MMC was one of only two primary areas where EF5 damage indicators were found in the Atkins et al. (2014a) and Burgess et al. (2014) studies (Fig. 5.14). While this area is highly populated, the slow speed of the tornado over a small spatial area could have had significant impacts on resulting damage (e.g., see Snyder and Bluestein 2014). Although enhanced damage is possible due to extended periods of high wind speeds, this area was also in a more-developed subdivision (Burgess et al. 2014), so no concrete conclusions can be drawn regarding such a correlation.

Finally, the polarimetric variables of the RFGFSs are relatively consistent with each other, as well as those seen in TDSs (Bodine et al. 2013). A summary of the polarimetric variable distributions in the eight RFGFSs is presented in Fig. 5.20. The primary difference between RFGFS observations and those expected in a TDS is the higher median of Z_{DR}. This is likely due to two factors: (1) the existence of more rain drops in the RFGFS where centrifuging is not a primary driving factor of size sorting, and/or (2) debris fallout with a common alignment orientation due to strong, straight-line winds. Additionally, ρ_{HV} median values are slightly higher than those seen in Bodine et al.

(2013). One would assume that the higher frequency of PX-1000 (X-band as opposed to S-band) would tend to lead to lower ρ_{HV} values due to the greater electrical sizes of debris; however, the higher values could be due to the effects of rain and smaller debris being lofted, resulting in less resonance scattering effects. Also of note is an apparent negative mean in Z_{DR} in the TDS (not the debris ejections; not shown), a phenomenon discussed by Ryzhkov et al. (2005b) and Bodine et al. (2014). This phenomenon is a manifestation of Mie scattering and common debris alignment, but could also be caused by differential attenuation; this is an area of ongoing research.

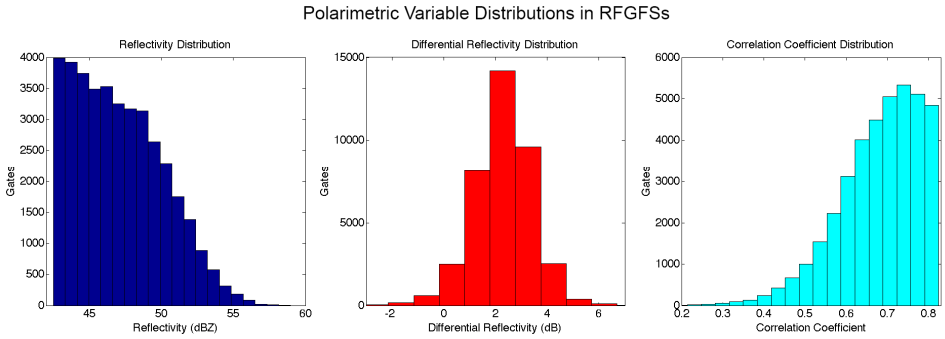

Figure 5.20: *Total distribution of Z_{HH}, Z_{DR}, and ρ_{HV} (from left to right, respectively) moment estimates within the eight RFGFSs, R1-R8.*

A number of different areas for future work exist with the data from this case. Comparisons with other area radars that were scanning volumetrically (e.g., the KTLX WSR-88D and the TOKC TDWR) could be used to piece

together vortex tilt characteristics around the failed occlusion period. Polarimetric comparisons of the debris ejections and the characteristics of the southern surge at multiple frequencies can be made in order to relate the X-band PX-1000 observations with S-band WSR-88D systems that are used operationally and in research modes (e.g., the KOUN WSR-88D). KOUN sector scans are available, which may allow for volumetric characterization of the debris contained in each RFGFS. Such comparisons would also be valuable to the development of the multilag concept, especially its occasional breakdown in areas of high spectrum width. These findings combined with comparisons with other datasets will make for increased accuracy in future low-power pulse compression weather radar systems (Cheong et al. 2013b).

Additionally, despite the lack of extensive dual-Doppler coverage for the Moore tornado, numerical simulations of the failed occlusion processes from this case and future cases could prove instrumental in determining the validity and details of the proposed hypothesis. Polarimetric analysis of the statistical characteristics of debris and hydrometeors at all stages of the storm should be undertaken given the numerous polarimetric datasets from the case, specifically with regard to the apparent negative Z_{DR} mean in the TDS at early stages of the tornado. Finally, further investigation of the cell merger early in the tornado track is an intriguing area for future studies, and may aid in understanding its role in tornadogenesis in the Moore case.

5.2 The Atmospheric Imaging Radar Convective Field Project

As described in the previous section, the evolution of severe convective storms can occur on timescales as fast as seconds. The desire to further understand supercellular and tornadic processes has led to the development of several tornado-scale mobile radar platforms for research and analysis over the past decade (Wurman and Randall 2001; Weiss et al. 2009; Bluestein et al. 2010; Pazmany et al. 2013). Despite volumetric updates as fast as 30 s, our ability to observe extremely rapid storm motions and evolutions has still not reached the combination of spatial and temporal scales that are important for significantly increased conceptual understanding. Eventually, it is expected that such data would be instrumental in data assimilation and storm-scale numerical models.

The majority of operational meteorological radar systems across the world operate using mechanical scanning (i.e., dish antennas, feed-horns, etc.). While phased array radar has been making a strong push for use in the weather radar community, data quality necessities have still prevented volumetric scanning on the order of seconds, precluding the ability to reach desired scan rates for severe storms. In an attempt to offer a significant improvement in temporal resolution, the AIR has been under development and testing at the ARRC over the past 6 years (Fig. 5.21; Isom et al. 2013). After hardware and construction was completed in 2011, a series of spring convective field experiments have been carried out across the Southern Plains between 2012-2014. Numerous

adjustments to scanning strategies, waveform designs, processing methodologies, beamforming techniques, and other configurations were tested during the collection of multiple tornadic, supercellular, and squall line cases at volumetric temporal resolutions as fast as 5 s. The AIR has served as a developmental testbed for beamforming techniques. Since all 36 receive channels independently store I/Q data, numerous beamforming methods have been tested on collected datasets (Nai et al. 2013). While Capon and Robust Capon methods have shown promise for weather radar, the data presented in this section are processed using Fourier beamforming.

Figure 5.21: *The atmospheric imaging radar scanning supercellular outflow south of Great Bend, on 11 May 2014.*

This section presents data from the four years worth of convective field campaigns and discusses the implications on the conceptual understanding of

severe convective storms. Specifically, each case presented focuses on meteorological phenomena that would not have otherwise been seen with conventional scanning radar.

5.2.1 Convective Field Campaigns

The data collection by the AIR thus far has been broken up into four convective field campaigns: the April-June periods of 2012, 2013, 2014, and 2015. Operations are also planned for spring 2016. The operating range for each campaign covered Northern Texas, Western Oklahoma and Kansas, Southern Nebraska, and Eastern Colorado. The primary mission goal was the collection of supercellular tornado data at ranges less than 10 km, and the secondary goals included the collection of non-tornadic supercell, landspout/gustnado, and squall line datasets. During each year, a different primary waveform was used due to the ongoing development of the system and coinciding waveform research at OU. In 2012, no pulse compression was used, and a staggered PRT was utilized in an attempt to dealias high radial velocities. In 2013, a 9 μs pulse with 45 m native range resolution (oversampled to 30 m) was used, again with a staggered PRT. Finally, in 2014, a 5.25 μs pulse with 37.5 m native range resolution (oversampled to 30 m) was used, but it was discovered that the individual aliasing velocities of the staggered PRT's were too low in

high spectrum width situations (i.e., tornadoes), resulting in poor velocity estimates in the previous two campaigns.

Therefore, a single T_s of 314 μs was decided upon in order to balance the pulse length, duty cycle limitations, and the desire for a high Nyquist velocity (see Chapter 4). This configuration is now considered the operational setting, and was also used in 2015. A comparison of data in 2012 without pulse compression, and data in 2013 with pulse compression is shown in Fig. 5.22. Note significantly higher spatial resolution along the radial dimension, as well as increased sensitivity in the hook region in the lower sub-figure. A summary of the three campaigns is shown in Table 5.2.

Table 5.2: *Convective field campaigns*

Year	**Pulse Length**	**Resolution**	T_s
2012	1 μs	150 m	625/938 μs Stagger
2013	9 μs	45 m	625/938 μs Stagger
2014	5.25 μs	37.5 m	314 μs
2015	5.25 μs	37.5 m	314 μs

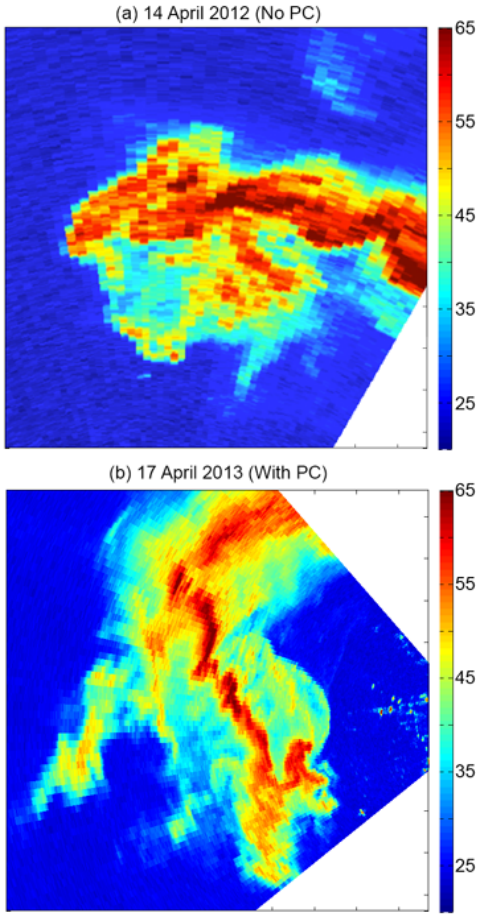

Figure 5.22: *Comparison of data collection with (a) and without (b) pulse compression. (a) contains Z_{HH} estimates (in dBZ) from the 14 April 2012 Carmen, Oklahoma tornado, and (b) contains Z_{HH} estimates from a non-tornadic supercell near Cache, Oklahoma on 17 April 2013. Note the marked increase in spatial resolution and sensitivity with pulse compression.*

Over the four years of field experiments, a total of 12 tornadoes were observed (four of which were "major" tornadoes) and over 30 supercells were scanned at ranges as close as 3 km. A compilation of relevant cases is listed in Table 5.3.

Table 5.3: *Observed cases*

Case Date	Observed Phenomena	Notes
4/14/2012	Cyclic Tornadic Supercell	No Pulse Compression
4/17/2013	Tornadic and Non-Tornadic Supercells	First Use of Staggered PRT
5/19/2013	Tornadic Supercell	Major Tornado/No Velocity
5/29/2013	Non-Tornadic Supercell	Staggered PRT/No Velocity
5/30/2013	Non-Tornadic Supercells	No Velocity
5/31/2013	Cyclic Tornadic Supercell	Major Tornado/No Velocity
5/11/2014	Tornadic and Non-Tornadic Supercells	First Acceptable Velocity
5/21/2014	Tornadic and Non-Tornadic Supercells	Embedded Vortex
3/25/2015	Non-Tornadic Supercell	Dynamic Pipe Effect
4/16/2015	Non-Tornadic Supercell	Embedded Vortex
4/22/2015	Non-Tornadic Supercell	Embedded Vortex
5/8/2015	Cyclic Tornadic Supercell	Attenuated Tornado
5/19/2015	Tornadic Supercell	Weak Tornado
5/16/2015	Tornadic Supercell	Long-Track Major Tornado
5/27/2015	Cyclic Tornadic Supercell	Major Tornado, Close Range

5.2.2 Data Examples

This section presents case examples from eight datasets collected in 2013, 2014, and 2015. These include the 19 May 2013 Shawnee, Oklahoma EF-4 tornado, the 31 May 2013 El Reno, Oklahoma EF-3 tornado, the 11 May 2014 Great Bend, Kansas tornado (unrated), the 21 May 2014 Denver, CO tornadoes (unrated), the 25 March 2015 Gracemont, Oklahoma supercell, the 22 April 2015 Tulia, Texas supercell, the 16 May 2015 Tipton, Oklahoma EF-2 tornado, and the 27 May 2015 Canadian, Texas EF-2 tornado. Each case is

supplemented with information regarding unique observations and their implications on tornado-observing science. It is important to note that many of these examples would be unobservable without the extremely high temporal resolution that the AIR provides, as well as its use of pulse compression for high spatial resolution and acceptable sensitivity with a wide transmit beam.

5.2.2.1 19 May 2013, Shawnee, Oklahoma

The 19 May 2013 Shawnee, Oklahoma EF-4 tornado was part of the 18-21 May 2013 Midwestern/Plains severe weather episode, which also included the 20 May Moore, Oklahoma EF-5 tornado. The Shawnee storm was a long-track tornado that began just north and west of Lake Thunderbird in Norman, and moved northeastward into Bethel Acres and western Shawnee. The AIR deployed in northern Tecumseh and collected 90-deg azimuthal sectors, resulting in volumetric updates every 6 s. Data were being collected during the time of peak damage in northern Bethel Acres, at a range of approximately 8.5 km. A sample low-level Z_{HH} plot at 5-deg elevation is shown in Fig. 5.23a. The height of the beam in the tornado, marked by a dashed white circle, is approximately 750 m AGL, which is likely near the top of the tornadic circulation. The increased sensitivity afforded by pulse compression displays

enough dynamic range to see spiraling rain bands being drawn into the circulation. Co-located with the tornado is a weak echo hole (WEH), which has been hypothesized to indicate debris centrifuging (Dowell et al. 2005).

This case is particularly useful for showing the advantage of RHI scanning with simultaneous beams. When a mechanically steered dish antenna scans volumetrically in a fast-moving tornadic storm, horizontal advection of hydrometeors can become a significant factor when trying to piece together a 30-120 s volume scan. RHI scanning with simultaneous beams, combined with volumetric scanning in 6 s, allows us to assume virtually instantaneous observations, making it much more straightforward to assess storm features such as vortex tilt. While higher elevations are undoubtedly seeing the WEH associated with the broader updraft/mesocyclone, a distinct tilt in the WEH location can be seen across Figs. 5.23a-c. The location of the vortex center at 15 deg (roughly 2.8 km AGL) is 2.3 km north-northwest of the low-level circulation and tornado. This capability can be used to examine vortex tilt during tornadogenesis and dissipation, leading to a greater understanding of how this process affects which storms result in tornadoes and when tornadoes decay in the storm cycle process.

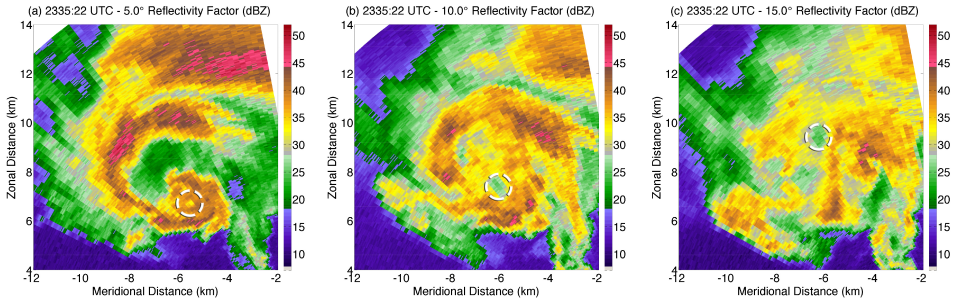

Figure 5.23: Z_{HH} *from the 19 May 2013 Shawnee, Oklahoma EF-4 tornado. From left to right (a-c): 5-deg, 10-deg, and 15-deg elevation scans at 2335:22 UTC, respectively. Dashed white circle indicates location of weak echo hole, determined subjectively.*

5.2.2.2 31 May 2013, El Reno, Oklahoma

The 31 May 2013 El Reno, Oklahoma EF-3 tornado was rated as the widest tornado in recorded history, with a maximum path width of 4.2 km. Additionally, radial velocities from OU's Rapid X-band Polarimetric (RaXPol) mobile radar were observed to be in excess of 130 m s^{-1}, making the El Reno tornado one of the strongest tornadoes ever observed. The rating of EF-3 was due to the limited number of damage indicators during the damage survey (Snyder and Bluestein 2014). Due to an east-west oriented river bed and relatively few bridges available for escape purposes, the AIR remained approximately 25 km southeast of the tornado, but scanned the storm for over 45 min, resulting in excellent volumetric supercell data. The minimum usable beam height (due to beam blockage at elevations below 2 deg) was over 1.2 km. However, the long range of the scans provided data up to 14 km at 40 km range, allowing

for a nearly complete picture of the supercell and rotating updraft. Volumetric scans covered 120 deg in azimuth, and the temporal resolution was 8 s.

A volumetric scan, with an underlay of a single-elevation scan for perspective, is presented in Fig. 5.24. In addition to a very classic supercellular shape and distribution of hydrometeors, a distinctive rotating updraft is evident above the hook echo on the southwest side of the storm. The rotating updraft is clearly visible due to the combination of high spatial and temporal resolution. It is also worth nothing that dish-based weather radars often skip some elevations in order to acquire volumes more often, meaning that interpolation in elevation must be made. The ability of the AIR to form an arbitrary number of 1-deg beams in the vertical dimension allows for equal spatial resolution in elevation and azimuth with no interpolation, resulting in exceptionally smooth volumetric visualizations. In addition to the rotating updraft, areas of high Z_{HH} are observed rotating around the mesocyclone (one such instance is located within the dashed white circle). It is hypothesized that these are examples of debris lofting, with some examples reaching elevations as high as 10 km. Debris has previously been observed at this height by radar (Magsig and Snow 1998; Bodine et al. 2013). Extremely high temporal resolution allows for tracking of these individual areas of debris, resulting in the capability to determine rough estimations of three-dimensional wind patterns around the mesocyclone with single-Doppler observations.

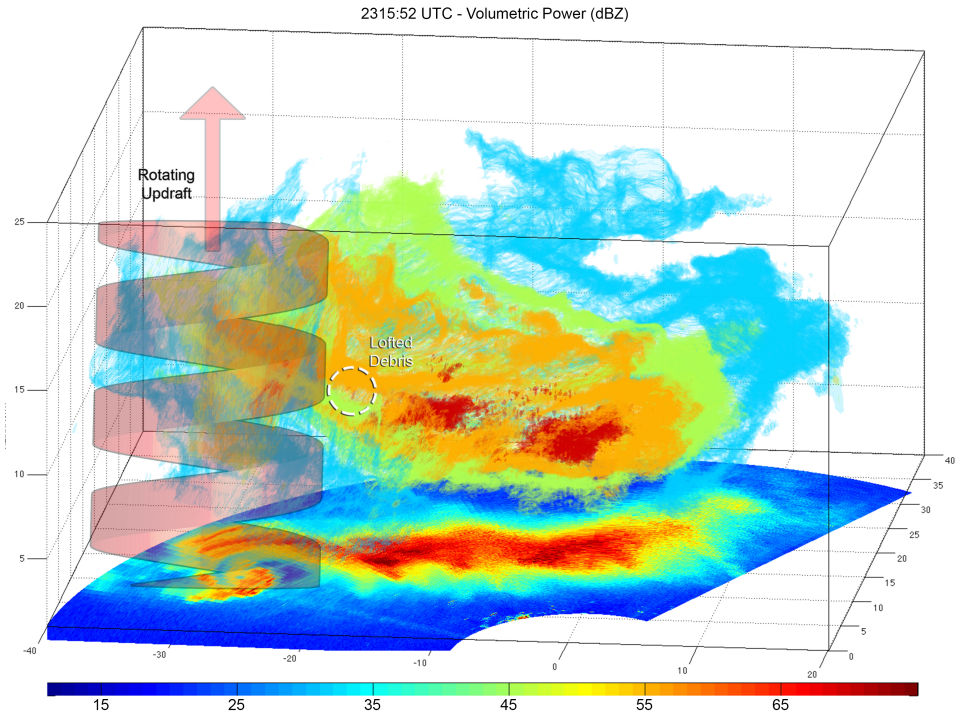

Figure 5.24: *Volumetric Z_{HH} estimate of the 31 May 2013 El Reno, Oklahoma EF-3 tornado at 2315:52 UTC. Underlay is 2-deg elevation scan for perspective. Red spiral indicates cyclonically rotating updraft, which is evident in high-resolution animations. Dashed white circle shows hypothesized debris lofting around the updraft, also notably evident in animations.*

5.2.2.3 11 May 2014, Great Bend, Kansas

The 11 May 2014 Great Bend, Kansas tornado was associated with a Central-Plains trough and dryline severe weather event. Despite occurring near the mesocyclone of a supercell, the tornado took the visual form of a landspout (Fig. 5.25). However, the data showed what looked to be a weak supercellular tornado that lasted less than 1 min. This correlated well with visual observations by the AIR team. A significant proportion of tornadoes last under

1 min, meaning volumetric-scanning weather radars often miss their occurrences. While these tornadoes can pose a threat to people and property, it can be argued that it is more important to understand their decay stages in order to determine why they do not grow into long-track and/or strong tornadoes. These cases, often only captured by mobile radars, may prove instrumental in our ability to understand tornado dynamics in the future, meaning that high temporal resolution is important due to short lifetimes. Additionally, volumetric information is critical in these cases due to the desire to understand interactions between gust fronts and circulation centers. Azimuthal sectors of 120 deg and a slower scanning strategy resulted in volumetric temporal resolution of 12 s.

Figure 5.25: *The atmospheric imaging radar scanning a landspout tornado south of Great Bend, Kansas on 11 May 2014.*

As a prime example regarding the importance of high temporal resolution, visual observations were combined with radar scans at a single elevation (for simplicity) at 7 deg in Fig. 5.26. In Fig. 5.26a, the beginning of an inbound/outbound couplet indicated rotation, but no visual funnel was evident. Only 24 s later, in Fig. 5.26b, a slightly strengthened v_r couplet was visible in the AIR data, but visual observations confirmed a ground circulation and condensing funnel. 50 s later (in Fig. 5.26c), despite a continuing couplet (albeit weakened), the tornado had dissipated visually. The ability to see this phenomenon only exists due to the high temporal resolution of the AIR.

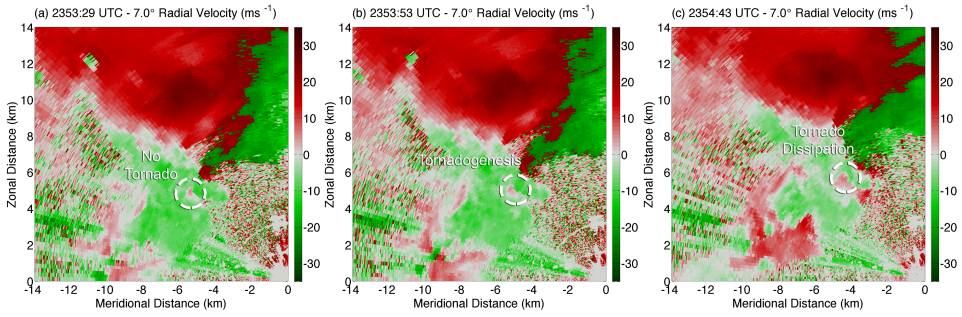

Figure 5.26: *Estimates of v_r from the 11 May 2014 Great Bend, Kansas tornado. From left to right (a-b): 2353:29, 2353:53, and 2354:43 UTC, respectively, at 7-deg elevation. Dashed white circle indicates rotation couplet.*

5.2.2.4 21 May 2014, Denver, CO

The 21 May 2014 Denver, CO tornadoes were part of a multi-day "Denver Cyclone" severe weather outbreak (Crook et al. 1990, 1991). While multiple supercellular storms formed and were maintained over and just east of Denver, one cell served as the primary tornado producer. Although no significant

tornadoes were observed or reported, cyclic tornadogenesis caused by a series of rear flank gust front surges resulted in a number of weak, short-lived tornadoes. The strong rear flank winds in this case required high-quality v_r estimates in order to resolve subtle features that resulted in tornadogenesis. It should be noted that the velocities in this case were manually dealiased in post-processing using standard dealiasing methods. A 110-deg azimuthal sector resulted in 8.5 s volumetric temporal resolution (see Fig. 5.27).

Figure 5.27: *The atmospheric imaging radar scanning a tornadic supercell east of Denver, CO on 21 May 2014.*

A sample of Z_{HH} and v_r estimates is shown in Fig. 5.28. This case had the highest dynamic range of the four convective field experiments due to very large hail in the hook echo. This was evident at later scanning locations to the

south of the hook where the majority of the signal was attenuated before reaching the mesocyclone, resulting in the need to scan from an easterly orientation. The detailed hook structure in Z_{HH} is evident in Fig. 5.28a, with evidence of highly turbulent eddies in hydrometeor motions clear in animations; the documentation of these details necessitates high spatial and temporal resolutions. In v_r (Fig. 5.28b), an area of strong rear flank downdraft winds associated with a rear flank gust front surge is evident in the southern tier of the hook echo. In the dashed white circle, an area of speed shear appears to develop, marked by a rotational couplet between rear flank inbound velocities and weak outbound velocities. The timing of these data match up with storm spotter reports of a tornado east of Denver. Although not shown, a series of four instances similar to this example occurred in a span of 4 min, less than the time it takes for an entire WSR-88D volume scan.

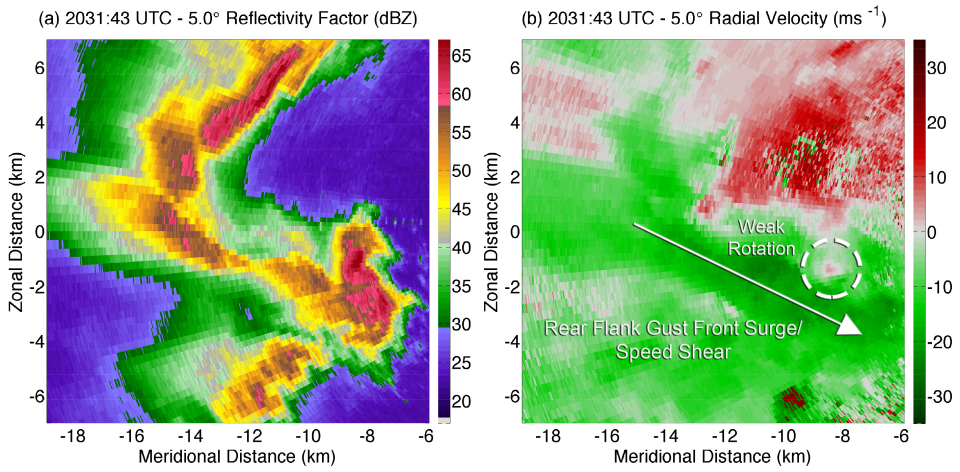

Figure 5.28: Z_{HH} *(left) and* v_r *(right) estimates from a 21 May 2014 Denver, CO tornado. Annotations indicate rotation couplet and surge of the rear flank gust front, hypothesized to have created enough speed shear to assist in the formation of weak tornadoes at the tip of the hook.*

5.2.2.5 25 March 2015, Gracemont, Oklahoma

On 25 March 2015, the AIR was deployed approximately 5 km south of Gracemont, Oklahoma during observations of a non-tornadic supercell. This deployment strategy was chosen due to the intersection of a synoptic cold front and dryline. The AIR completed a 9-min deployment that covered a 120-deg sector at a 9-s update rate during observations of mid-level rotation on the KTLX and KFDR WSR-88D radars (as well as golf ball-sized hail reports). A visual wall cloud was visible behind an outflow-driven shelf cloud (Fig. 5.29) that eventually marked the demise of the cell. The storm was rapidly undercut by the cold front diving southward from northern/central Oklahoma, but a dual

hook echo was evident in AIR data as close as 4 km in range. No tornado was observed visually or at the lowest levels in v_r data.

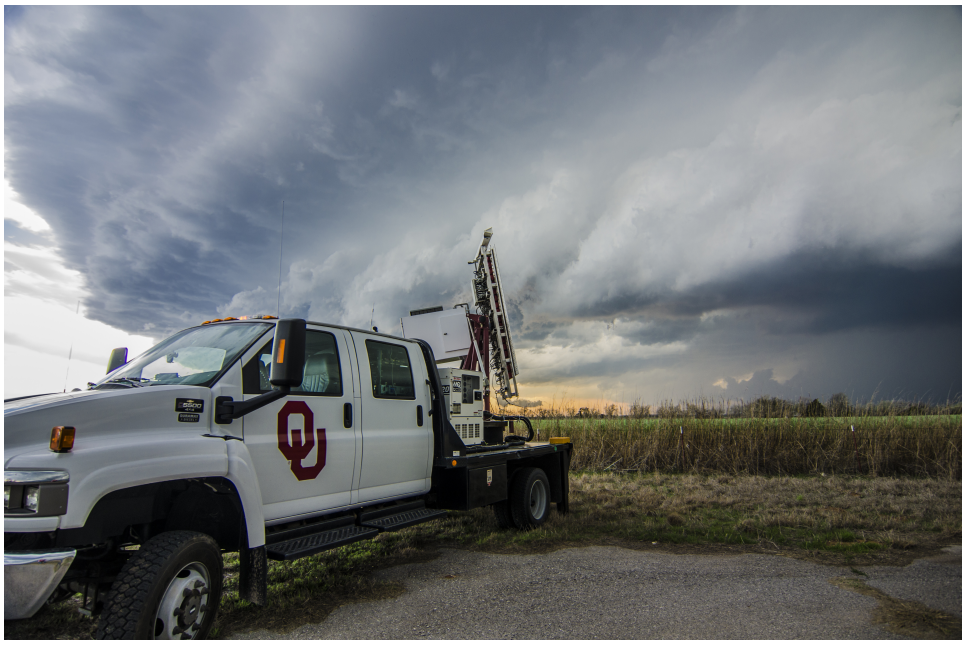

Figure 5.29: *The atmospheric imaging radar scanning a non-tornadic supercell south of Gracemont, Oklahoma on 25 May 2014.*

Among the most interesting features in this case is the observation of an apparent attempt at tornadic development detailed in Fig. 5.30. At approximately 2308 UTC the AIR observed a strong couplet at upper levels (12-deg elevation; Fig. 5.30a). At 13 km range, this corresponded to a beam height of roughly 2.7 km AGL. With Δv_r values approaching 45-50 m s^{-1}, it could be argued that this was a tornado-scale circulation observed at exceptionally high heights. At the same time, at the 4-deg elevation (approximate beam height of 920 m), rotation was evident but it was significantly weaker, with a maximum Δv_r of approximately 20-25 m s^{-1}. It should also be noted that a WEH

is evident at the 12-deg elevation, possibly indicating enough rotation to begin centrifuging hydrometeors at high elevations. No apparent WEH is seen at the same time at the 4-deg elevation.

Just 23 s later, the upper-level circulation had weakened to a Δv_r of approximately 25-30 m s^{-1}, while the lower level circulation had increased to a Δv_r of nearly 40 m s^{-1}. With simultaneous RHI observations and an extremely rapid update rate, it is plausible to assume that this was a manifestation of vertical displacement of a rotational couplet. A previously non-existent low-level circulation was seemingly replaced by a pre-existing circulation that originated nearly 2 km above the the eventual low-level circulation. Tracking this movement of the circulation results in exceptionally high downward vertical motions, but as a caution, the AIR does possess high vertical sidelobes in this dataset due to Fourier beamforming (a discussion and comparison of various beamforming methods can be found in Mucci 1984). Due to this issue, the actual elevation of the circulation in question may be displaced by 1-2 deg in the vertical dimension. Even as a very conservative estimate, downward velocities greater than 40 m s^{-1} are likely in this scenario.

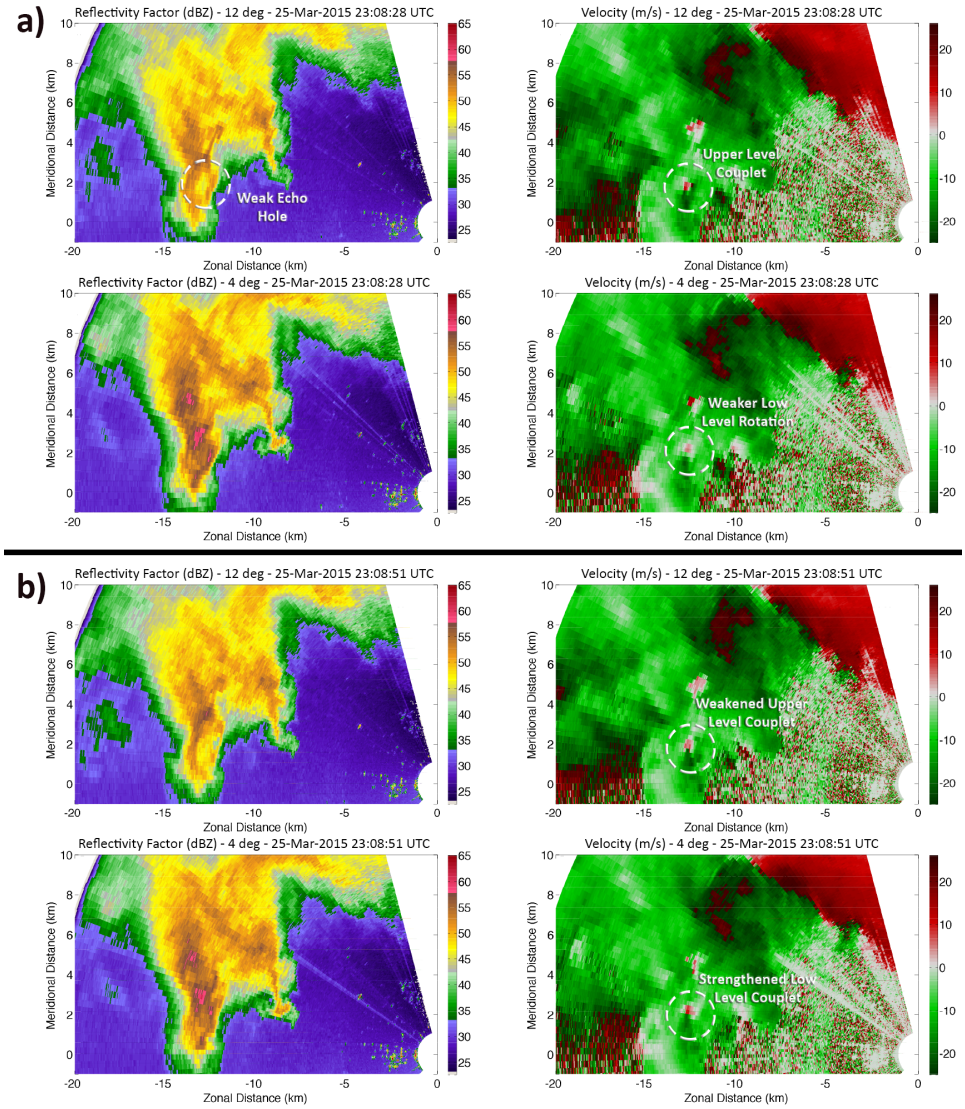

Figure 5.30: *From left to right, Z_{HH} and v_r from the 25 March 2015 supercell south of Gracemont, Oklahoma. (a) 12-deg (top) and 4-deg (bottom) elevations at 2308:28 UTC. (b) 12-deg (top) and 4-deg (bottom) elevations at 2308:51 UTC. A tight rotational couplet is seen descending rapidly in height over a span of only 23 s.*

This observation is similar in nature to the dynamic pipe effect, or DPE. This phenomenon was first described numerically in Leslie (1971) as an area of localized rotation/vorticity with convergence displaced both below and above

its location, causing a pressure gradient force inwards towards the circulation. It was shown by Trapp and Fiedler (1995) (numerically) and Trapp and Davies-Jones (1997) (in terms of tornadogenesis) that the DPE was a theoretical contributor to tornadogenesis (and "vortexgenesis" at different levels, as seen in this AIR case). The Trapp studies suggested that increased convergence *below* the vorticity maximum enhanced vorticity below the original maximum, leading to downward movement (Bluestein 2013). This effect has been observed and simulated on longer time scales in numerous cases (Dowell and Bluestein 2002b; Markowski et al. 2003; Davies-Jones and Wood 2006; Wurman et al. 2007a; Marquis et al. 2012; Houser et al. 2015). Recently, French et al. (2013b) examined vertical development of intense circulation cores using a phased array radar. In these observations, vertical *upward* propagation of vorticity cores was observed, but their motion was considerably slower than the observations on 25 March. It is noted in the French et al. (2013b) study that over the past decade, observations of the DPE by rapid-scanning mobile radars have been roughly half upward-propagating and half downward-propagating.

5.2.2.6 22 April 2015, Tulia, Texas

The AIR collected data on a strongly right-moving supercell 10 km southeast of Tulia, Texas on 22 April 2015 during a warm front deployment in the Texas

panhandle. Storms formed at the triple point near the Texas/New Mexico border and progressed very slowly along the warm front, which was draped from northwest to southeast, eventually becoming very HP (high-precipitation supercell; Burgess et al. 1982; Moller et al. 1994; Markowski and Richardson 2010). During the observation period, a strong RFGFS was underway as the storm transitioned from a classic supercell to HP. Seven minutes of 100-deg sectors and a 7-s update rate were collected with a minimum range of 3 km.

This case is an excellent opportunity to highlight an observation that has been repeatedly observed by the AIR in non-tornadic supercells; low- and mid-level rotational couplets with mature WEH signatures but no evident tornadogenesis. In some of these cases, as with the 22 April case, the WEH can be observed at varying intensities for many minutes at a time. A substantial example of this phenomenon is shown in Fig. 5.31. In the top panel, an area of developing speed shear in v_r is already co-located with an apparent WEH in Z_{HH}. This observation continues at low elevations (this example shows the 2-deg elevation) for many minutes, and is shown at the southern edge of the scan in the bottom panel of Fig. 5.31 nearly 2 min later. At this stage, the couplet has intensified to include outbound velocities (not just speed shear) and a Δv_r of over 35 m s^{-1} and well-defined WEH with Z_{HH} values dipping below 45 dBZ while surrounded by 50-55 dBZ values.

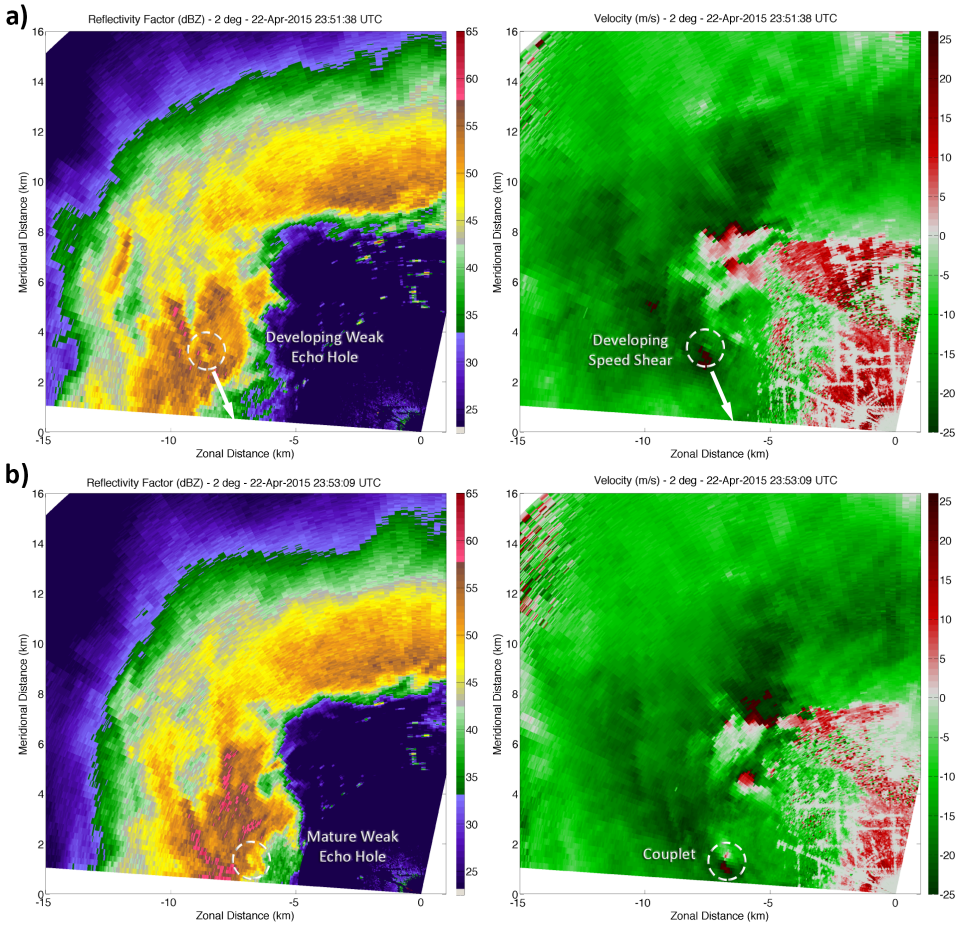

Figure 5.31: *Z_{HH} and v_r from the 22 April 2015 supercell southeast of Tulia, Texas. (a) Development of a weak echo hole in an area of speed shear. (b) Mature weak echo hole co-located with couplet in v_r.*

These observations occur in more than 50% of non-tornadic supercell observations with the AIR and at varying elevations and intensities. It has been hypothesized that the WEH is due to centrifuging of hydrometeors (and/or debris in a tornado) radially outward from the rotation couplet (Snow 1984; Dowell et al. 2005). In particular, Wurman et al. (1996) and Wurman and Gill (2000) hypothesized that this "ring" of high reflectivity is represented by

raindrops (while an inner ring in tornadoes may be indicative of debris). The majority of WEH observations have been linked to tornadic activity, but it has yet to be shown in the literature whether there is a significant link between WEH existence and tornadogenesis. AIR observations suggest that WEH existence may be relatively unrelated to actual tornadogenesis, but does not rule out the possibility that a WEH can sometimes be a tornadic precursor.

5.2.2.7 16 May 2015, Tipton, Oklahoma

On 16 May 2015, the AIR collected data on its first major tornado at close range with usable radial velocity data. Deployed 8 km south of Tipton, Oklahoma, two different sectors were collected. The first sector covered 100 deg with an update rate of 8 s, and lasted for 14 min. At this stage, initial range to the tornado was relatively far (approximately 21 km). By the end of the first sector, the range to the tornado was about 14 km and the tornado was in a mature "wedge" stage. The second sector covered 105 deg, also with update rates of approximately 8 s. The second sector lasted approximately 25 minutes with a minimum range between 10-11 km. A picture of the deployment location and parent supercell is shown in Fig. 5.32.

With such an extended dataset, a number of unique observations can be made. First, a sampling of the 5-deg elevation at approximately 60-s resolution during the mature stages of the tornado are shown in Fig. 5.33. The

tornado moves at a roughly 12 m s^{-1} pace over approximately 11 km with numerous changes in appearance in the Z_{HH} field. An exceptionally large curling hook structure with clearly evident WEH is apparent at 2254 UTC, with this structure breaking down into a two-cell vortex in the 2257 timeframe. By 2300 a more "intense" WEH is apparent (along with high Δv_r estimates; not shown), with a very mature structure. At this stage, numerous observers witnessed a large wedge tornado that appeared to be exceptionally strong and, at times, multi-vortex in nature. Very few structures were struck by the tornado, however, resulting in limited damage indicators and an EF-2 rating. By 2303, the hook structure began to break down, along with the WEH, and visual observations appeared to indicate a weaker tornado; again, very few damage indicators were available. In the later stages of the tornado, a seemingly cyclic nature to the WEH is evident, but the hook structure becomes attenuated by the RFD. Numerous RFGFSs are evident in data animations, including one towards the tail end of observations that appears to be correlated with a looping structure.

The AIR was serendipitously located near the KFDR WSR-88D radar, with less than 10 km of separation and similar radial angles to the tornado. This provides a tremendous opportunity for data comparisons between an experimental, high-resolution research radar and an operational system. A comparison at similar times and elevations is provided in Fig. 5.34. A number of useful

comparisons can be made; aside from the obvious differences in spatial and temporal resolution, as well as the lack of attenuation in the S-band WSR-88D data, the location and detail of the WEH can clearly be compared. The general structure of the FFD and hook is strikingly similar, as is the surging RFD to the south of the tornado. An interesting difference is the echo observed to the northeast of the tornado in the AIR data; this area of higher Z_{HH} outward from the tornado is not apparent in the WSR-88D data. This signature acts as a stream of "smoke" emanating from the outer rings of the WEH and hook echo, and, at times, has it's southwestern portions wrapped back into the inflow region, appearing to be ingested into the updraft.

Figure 5.32: *The atmospheric imaging radar scanning a tornadic supercell south of Tipton, Oklahoma on 16 May 2015.*

An integral part of the AIR is its ability to observe multiple elevations simultaneously, with one of the original goals of the AIR being to observe vortex tilt during tornadogenesis, the mature stages, and tornadic dissipation. Due to the nature of advection correction algorithms, an accurate portrayal of tornado/mesocyclone/ updraft tilt can rarely be drawn. Therefore, it is not

well understood how low-level and deep-layer tilting dynamics may affect tornadogenesis, dissipation, and intensity during maturity. With a long dataset covering multiple stages of the Tipton tornado, this case is ripe for vortex tilt analysis. In order to convey vortex tilt, three elevations were chosen for analysis; the 3, 7, and 11-deg elevations. The 3-deg elevation provides the lowest high-confidence data that is not affected by beam blockage for the entirety of the observation period. The 7-deg elevation is anticipated to roughly indicate the top of the core tornadic vortex. The 11-deg elevation is intended to represent the mesocyclone and updraft position relative to the tornado.

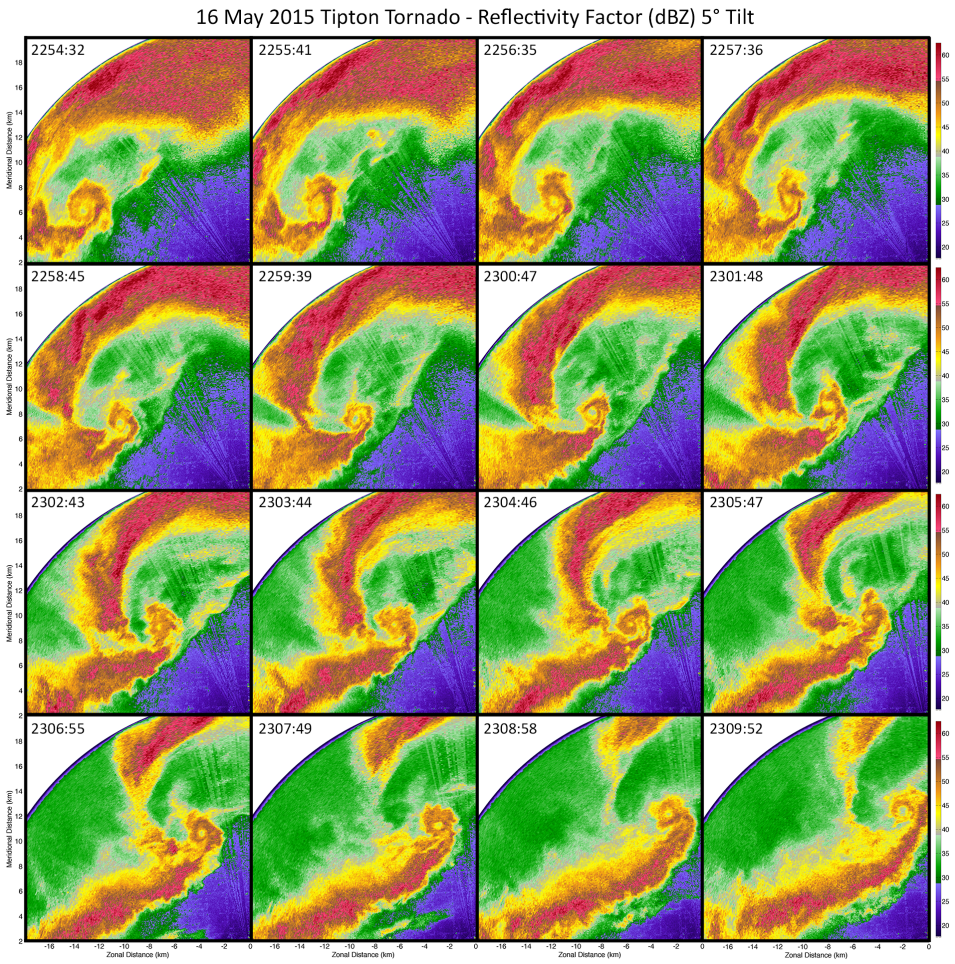

Figure 5.33: Z_{HH} *at roughly 60-s temporal resolution during the mature stages of the 16 May 2015 Tipton, Oklahoma tornado (5-deg elevation). The early times indicate a mature hook echo, while the middle times show a disruption in structure and the final times show a surging RFGF.*

A combination of WEH (using Z_{HH} data) and vortex center location (using v_r data) was utilized to manually track the center of rotation at these three different elevations. At the average distance of 11 km, the 3, 7, and 11-deg elevations correspond to roughly 0.58, 1.35, and 2.11 km in elevation AGL. The result of the manual tracking is shown in the top panel of Fig. 5.35. At

the beginning of the dataset, a significant separation is apparent between the 3- and 11-deg elevations, indicating significant tilt. This tilt is depicted in the middle panel, and corresponds to roughly 30 deg of tilt between the two elevations. The tilt between the 3- and 7-deg elevations is less, but becomes considerably less within the first 1-2 min of observation. By 2300 UTC, the tilt between both elevation sets has reduced to under 10 deg, which is indicated by very close spatial track lines in the top panel of Fig. 5.35. This minimum in tilt corresponded to the time that observers witnessed the wedge stage of the tornado.

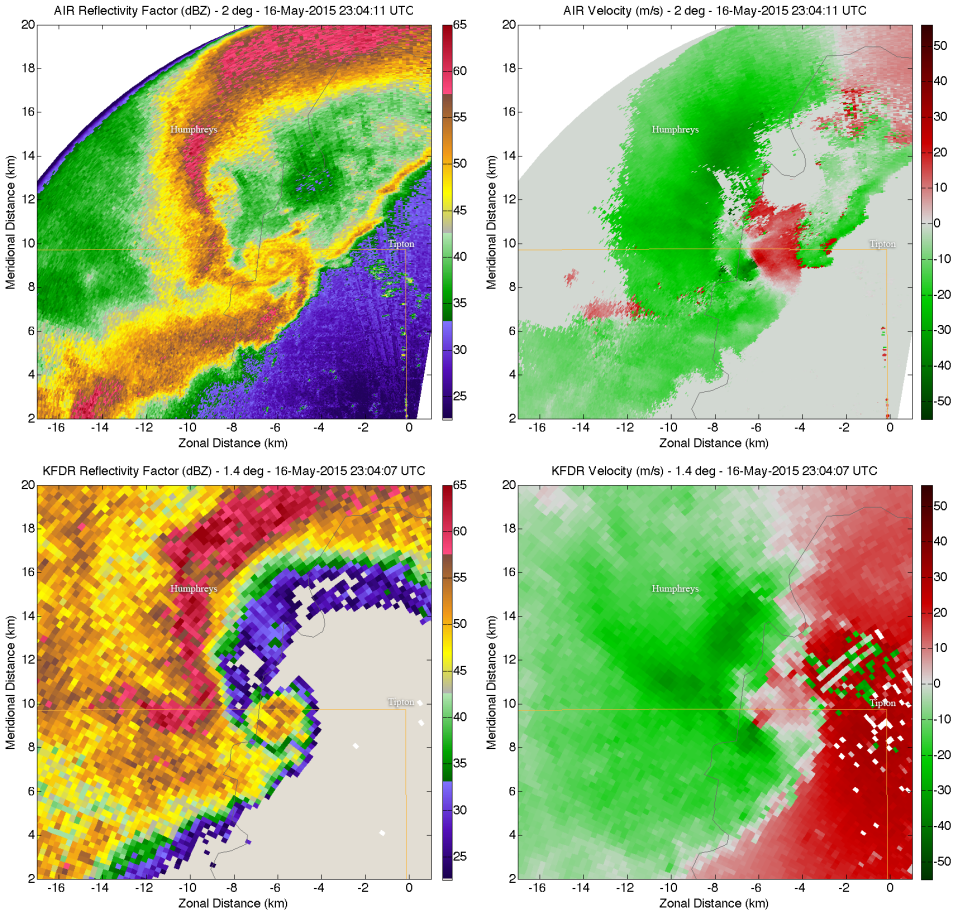

Figure 5.34: *Comparison of Z_{HH} and v_r between the AIR (top panels) and the KFDR WSR-88D (bottom panels). KFDR was approximately 10 km southeast of the AIR. Note the marked increase in spatial resolution in the AIR data.*

Shortly afterwards, the upper levels of the storm broke down considerably, losing much of the hook echo and WEH signature shapes. The low levels remained consistent, but the upper level mesocyclone diverged significantly from the low-level path of the tornado. This is indicated in tilt values once again exceeding 30 deg, but this time with equal tilt at each elevation set. By 2305, another minimum in tilt was observed to the west of Tipton, followed by

increasing tilt and an eventual loop of the upper level WEH despite a relatively consistent low-level tornadic circulation path. The bottom panel of Fig. 5.35 shows the forward propagation speed of the low-level vortex.

While a distinctly periodic "wobble" is apparent in the time series, an interesting observation is apparent around 2303. As the maximum vortex tilt recovers and becomes more erect, the velocity of the low-level vortex slows to a near halt as the upper-level mesocyclone "catches up" to the tornado. This sort of stacking of the mesocyclone and tornado could be related to intensity, damage, or even likelihood of an occlusion (as in a synoptic cyclone).

A final analysis point that is made possible by the AIR's simultaneous RHI scanning strategy is the ability to examine RHIs through the tornado and updraft at each pass by the pedestal. This means that over the 39 min deployment, with an 8-s resolution, nearly 300 RHIs through the tornado were collected. With varying ranges and stages of the tornado, these RHIs paint a unique picture of the vertical structure of the tornado and updraft. Most tornado-scale mobile research radars do not collect RHIs through tornadoes because of the difficulty in tracking and the "lost opportunity" to scan volumetrically. Since most of these pencil beam radars scan azimuthally, scanning in the elevation would be exceptionally difficult to control during a quickly moving tornado.

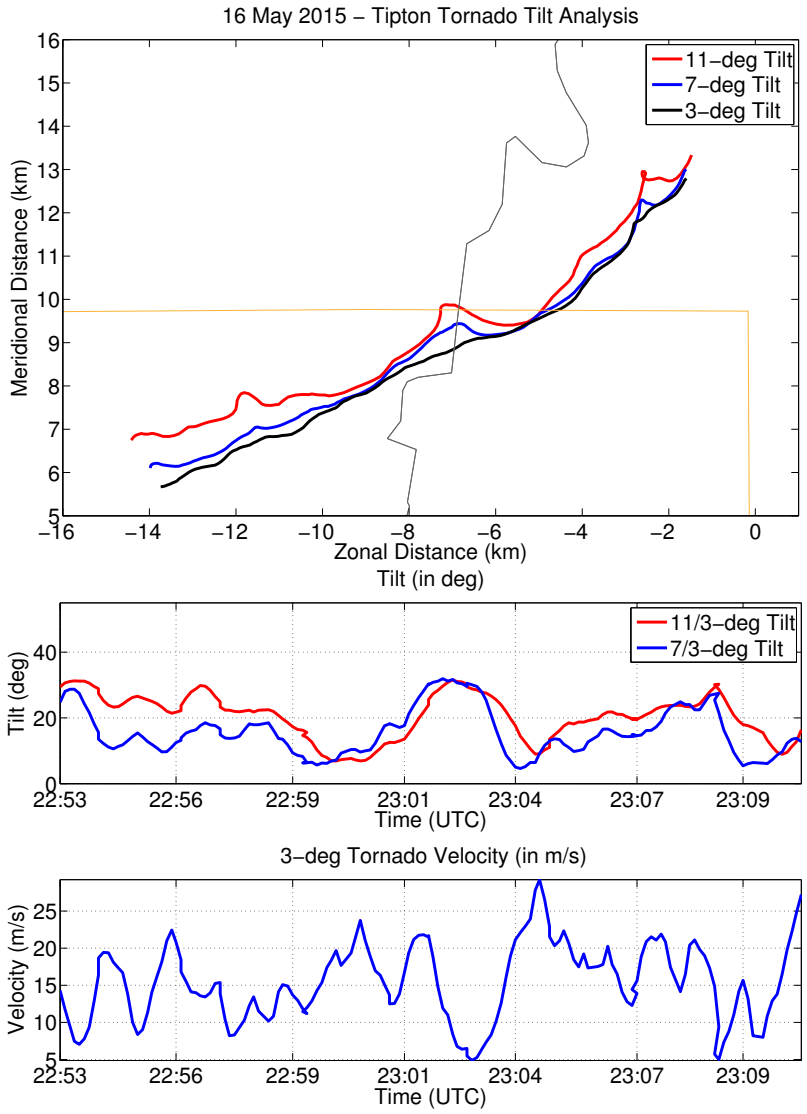

Figure 5.35: *Analysis of the 16 May 2015 Tipton, Oklahoma tornado tilting characteristics. The top panel shows tracks of the 3, 7, and 11-deg elevation WEH. The middle panel shows calculated tilt in degrees between 11/3- and 7/3- deg elevations. The bottom panel presents the 3-deg tornado forward ground-relative velocity.*

A sample RHI is shown in Fig. 5.36 at one of the stronger points during the tornado's lifetime. The left panel shows Z_{HH}, with a clear WEH at low elevations that rapidly tilts toward the radar (to the left of the frame) and becomes more erect and wider in the updraft region. Regardless, tilt is still observed all the way through the updraft. The tornado and mesocyclone are sampled, and are also apparent in v_r, which in this case, has not been dealiased. Either outbounds or inbounds must be chosen for a radial RHI (rather than a "CAPPI" slice that could cut across the radial dimension), and in this case, outbound velocities were chosen. A distinct increase in outbound velocity is visible throughout the depth of the updraft, with significant increases toward 45-50 m s^{-1} in the tornado region.

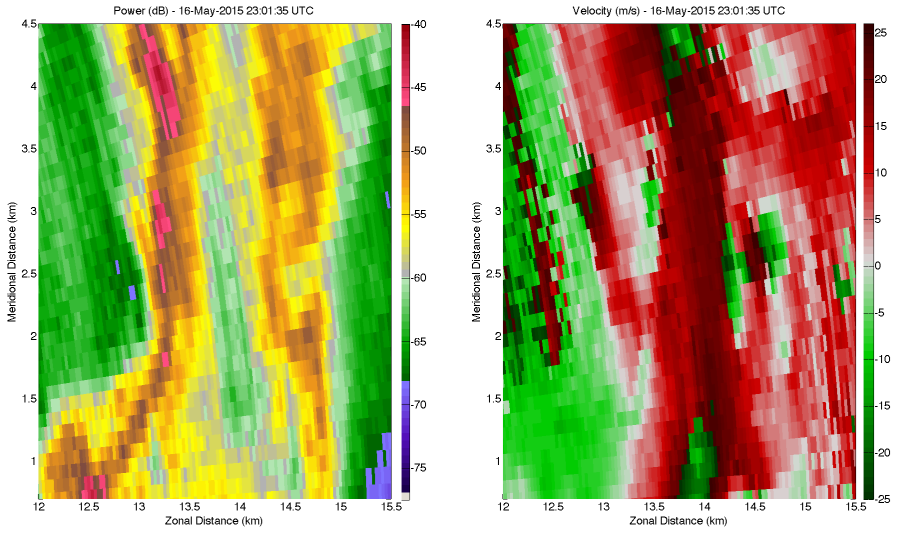

Figure 5.36: *A sample RHI through the 16 May 2015 Tipton, Oklahoma tornado, with* Z_{HH} *on the left and* v_r *on the right. The tornadic vortex and WEH are visible from the tornado through the upper elevations.*

5.2.2.8 27 May 2015, Canadian, Texas

The 27 May 2015 Canadian, Texas tornado occurred along a dryline in a high-CAPE, low-shear environment. The AIR was deployed 4 km north-northeast of Canadian and captured the mature and dissipation stages of a large cone tornado that had very little forward ground motion (and, in fact, progressed in a loop and eventually moved "backwards"). Due to the low-shear nature of the environment, the storm trained over one spot, with cyclic tornadogenesis and extreme flash flooding. The primary AIR deployment was 6 min long and covered an 80-deg sector with a 5.5-s update rate. The closest range to the tornado was 4.5 km (Fig. 5.37). Significant changes in vortex shape and tilt were observed visually as the tornado transitioned from a large cone to a heavily tilted rope stage (discussed later in this section and shown in Fig. 5.39).

A sampling of Z_{HH} and v_r at 0-deg elevation (a beam height of roughly 50 m AGL at the tornado's location) is shown in Fig. 5.38 at approximately 30-s temporal resolution in order to demonstrate the change in tornadic structure during the dissipation stages. Early in the deployment, at 2204 UTC, the tornado was in its mature stage with a WEH over 1 km in diameter (see Fig. 5.39a). Although v_r is not dealiased in these images, it can be clearly seen that the inbound and outbound maxima are separated by nearly 1 km, indicating a large and strong tornado. The total Δv_r spans over 10 radials and equates to

roughly 90 m s^{-1} very close to ground level. Radial velocities in the tornadic core are remarkably low (under 5 m s^{-1} in some areas), but storm motion was slightly toward the radar location, meaning core velocities could be very close to zero.

Figure 5.37: *The atmospheric imaging radar scanning a tornado north of of Canadian, Texas on 27 May 2015.*

Just 32 s later the core vortex has collapsed upon itself in the Z_{HH} field, but a wide vortex continues in the v_r field. The tornado never recovered such a large WEH after the first two scans, which agrees well with the picture in Fig. 5.39b taken approximately one minute after Fig. 5.39a. This rate of weakening continued for over the next 4 min, with maximum Δv_r decreasing by more than 50 m s^{-1} in under 3 min. By 2206, the low-level WEH had mostly disappeared and the tornado had shrunk considerably in size (corresponding roughly to Fig.

5.39c). Additionally, considerable tilt had become visually apparent (a deeper discussion on this phenomenon is provided later in this section). The Δv_r had become gate-to-gate as opposed to the earlier large separation in azimuths. Finally, by 2208, the low-level rotation had mostly dissipated and the tornado was in a highly tilted rope stage (Fig. 5.39d). A WEH was still evident in Z_{HH} but the core rotation had become elevated.

At the strongest stage of the tornado, the beginning of the deployment, an analysis of the vertical structure of the tornado (with dealiased v_r in and near the tornado) is shown in Fig. 5.40. The wide separation of maximum/minimum quickly shrinks by the 3.5-deg elevation (roughly 300 m AGL) and becomes gate-to-gate by the 9.5-deg elevation (825 m AGL). Additionally, a significant tilt is evident in both the WEH and the v_r maxima with height. The top elevation of 13.5 deg corresponds to roughly 1.17 km, meaning 47.8 deg of tilt is present in the lowest portions of the storm and tornado. With estimated cloud bases at only a few hundreds of meters, it is possible that much of the tilting is above the visual cloud base making it difficult to see.

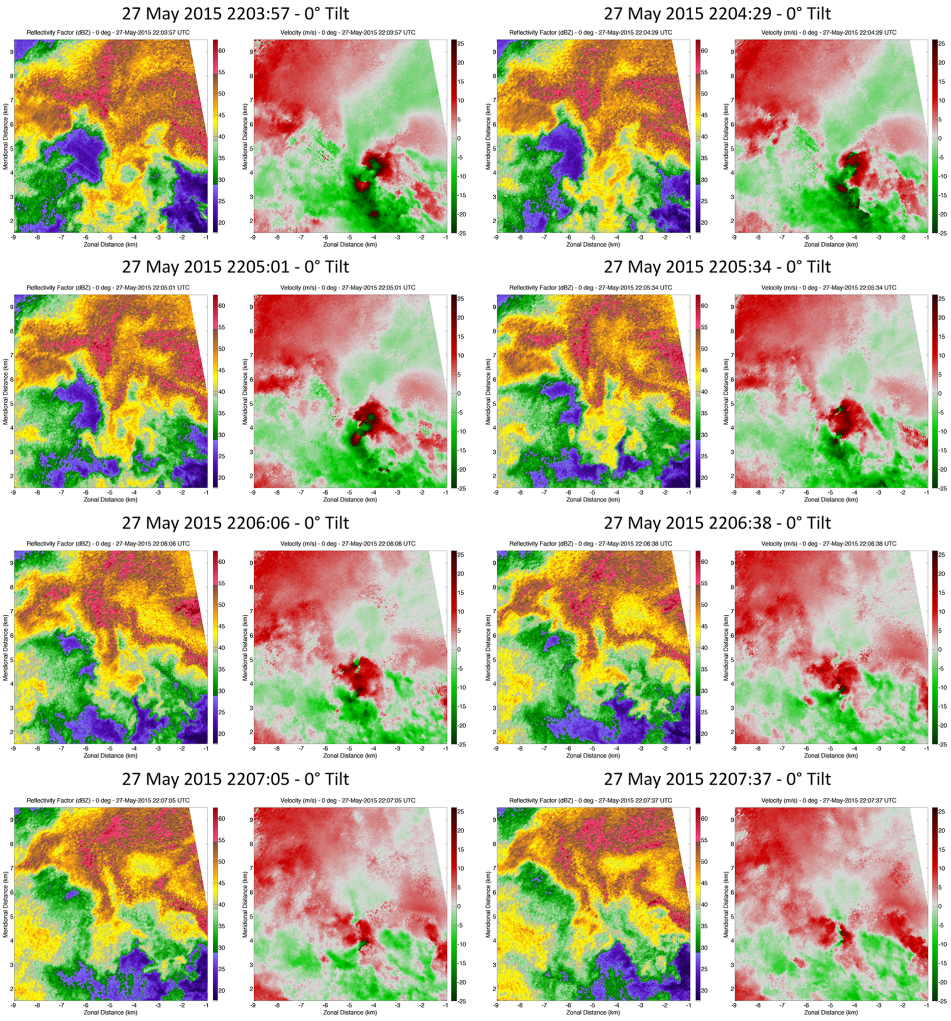

Figure 5.38: Z_{HH} *and* v_r *at roughly 30-s temporal resolution during the mature stages of the 16 May 2015 Tipton, Oklahoma tornado (0-deg elevation). The tornado quickly weakens from a mature vortex with large WEH to a weaker tornado in a rope out stage. Note that* v_r *is not dealiased in this figure.*

Figure 5.39: *Comparison of tornado structure during the AIR deployment on the Canadian, Texas tornado on 27 May 2015. Approximate times for the images are (a) 2204 UTC, (b) 2205 UTC, (c) 2206 UTC, and (d) 2208 UTC.*

In order to further investigate the tilting characteristics, a series of three-dimen-sional spatial analysis points were chosen and analyzed with two differing methodologies. The first technique is shown in Fig. 5.41 and involves a trace of the WEH and the creation of a mask based on its diameter and center point. Once this mask is created a Z_{HH} contour is applied in order to visualize the three-dimensional structure of the WEH. Without thermodynamic, humidity, and pressure/wind fields in three dimensions, a "condensation" funnel can not be visualized, meaning that the WEH is not a true physical representation of the tornado or updraft. However, the centrifuging theory does argue that the

center of the WEH is the center of the vortex, meaning that a tight threshold for contouring does give useful visual information for tilting characteristics.

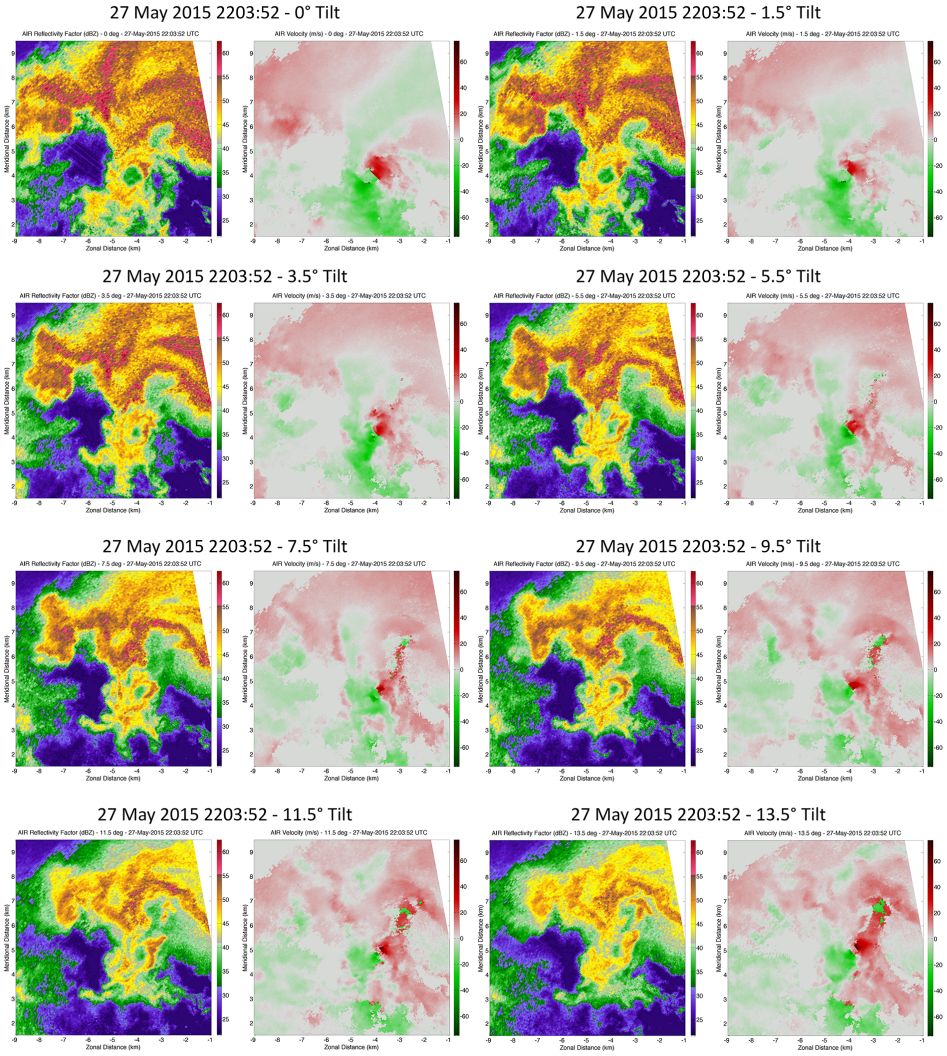

Figure 5.40: *Z_{HH} and v_r at 2203:52 UTC (the strongest stage of the 27 May 2015 Canadian, Texas tornado deployment) at eight different elevations, collected simultaneously with the AIR. The center of the WEH and the vortex tilt to the northeast rapidly with height. Also note that the maximum inbound and outbound radial velocities are separated significantly in space, especially at low levels.*

In Fig. 5.41, two distinctly different times were chosen along with a 40-dBZ contour level. The top panel shows the mature stage of the tornado, while the bottom panel shows the rope out stage. A few observations are immediately apparent; first and foremost, a significantly tilted core vortex is evident, even in the mature stage. Second, an area of significantly widened WEH is seen in the mature stage, but not in the rope stage. As discussed by Wurman et al. (1996) and Wurman and Gill (2000), this outer ring of the WEH may be indicative of large debris being centrifuged at low levels, while the upper levels do not contain nearly as much debris. As the tornado weakened at later stages (and, in fact, roped out above ground level), the lack of significant ground-level winds would preclude the existence of large debris, likely eliminating this area of widened WEH.

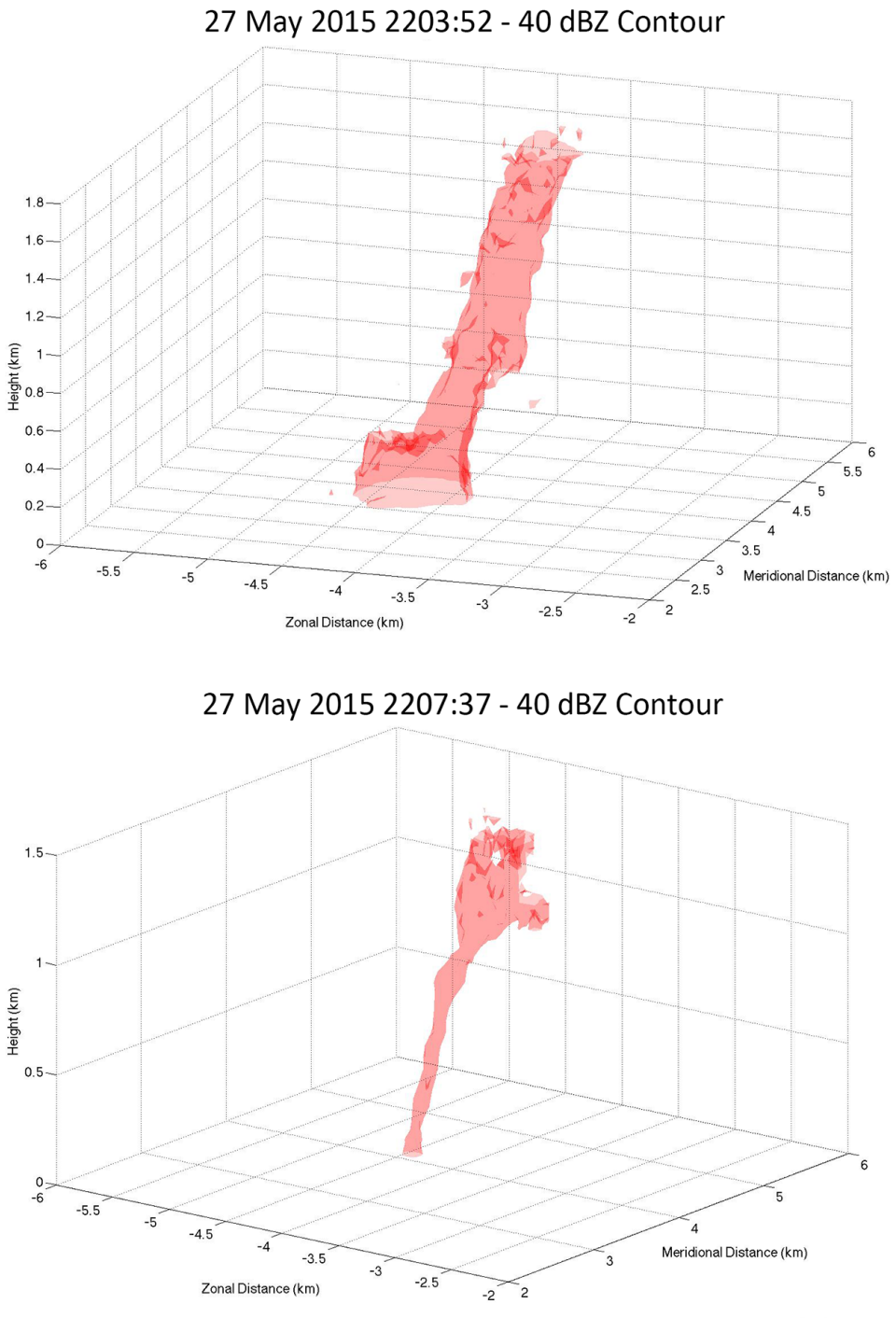

Figure 5.41: *Three-dimensional 40-dBZ Z_{HH} isosurface near the WEH of the 27 May 2015 Canadian, Texas tornado at 2203:52 UTC (top) and 2207:37 UTC (bottom). The tilt direction and angle is nearly identical despite significant changes in width and strength of the tornado between the two times.*

The second technique for three-dimensional analysis of tilting and tornado strength is presented in Fig. 5.42. Due to the lack of physical meaning for the WEH in terms of visualization, a constant diameter was chosen for each plot based on the WEH width at the base scan (0-deg elevation). Each plot is colored based on the maximum Δv_r at each elevation (interpolated through the column). It is important to note that in this case, especially during the mature stages, there is evidence of suction vortices and multi-vortex structure within a two-cell core vortex. This makes it difficult to define the actual "width" of maximum winds, because occasionally a suction vortex will contain a short-duration burst of locally maximized inbound or outbound radial velocities. Therefore, a simple plot of pseudo-vorticity is difficult because of the width considerations, making overall Δv_r a better proxy for intensity.

In Fig. 5.42a, the tilt described previously remains quite apparent, along with a Δv_r of 85-90 m s^{-1} near ground level and as high as 105 m s^{-1} just above ground level (at roughly 250 m AGL). A general weakening trend is apparent near 500 m AGL, before a re-strengthening at the 750 m level. A similar profile is shown in Fig. 5.42b, but with a stronger Δv_r of 100 m s^{-1} near ground level. Fig. 5.42c shows significant weakening throughout the column with a maximum Δv_r of 75 m s^{-1}, while Fig. 5.42d presents the final rope out stage of the vortex (with no distinct TVS in the lowest elevations).

A number of observations are consistent among the four panels in Fig. 5.42. First, all of the times show remarkably similar tilt characteristics and angles. All of the times show tilt to the northeast, despite relatively slow and stochastic movement of the tornado. Additionally, each time that contains a tornadic circulation in contact with the ground (Fig. 5.42a-c) has a slight weakening of Δv_r in the lowest 1-3 elevations before a rapid acceleration in inbound and outbound radial velocities just above ground level. This is likely due to the frictional boundary condition of the ground causing slowed winds discussed by Snow (1982) and Daves-Jones (1986).

While general tilting is expected in the transition from tornado to mesocyclone, observations of significant tilting within the lowest levels of a strong tornado have not been presented previously in the literature. Additionally, based on visual observations, only minimal tilting was apparent during mature stages of the Canadian tornado. It makes some sense that a significantly tilted vortex will eventually weaken with respect to vertically oriented vorticity (due to the eventual horizontal nature of the vortex), and therefore, it can be hypothesized that a tilted tornado is likely to be weaker or weakening. It is worth noting that despite the mature stage of the tornado at the beginning of the dataset, significant weakening occurred immediately afterwards, meaning that the original tilt observations could have been a precursor to weakening stages.

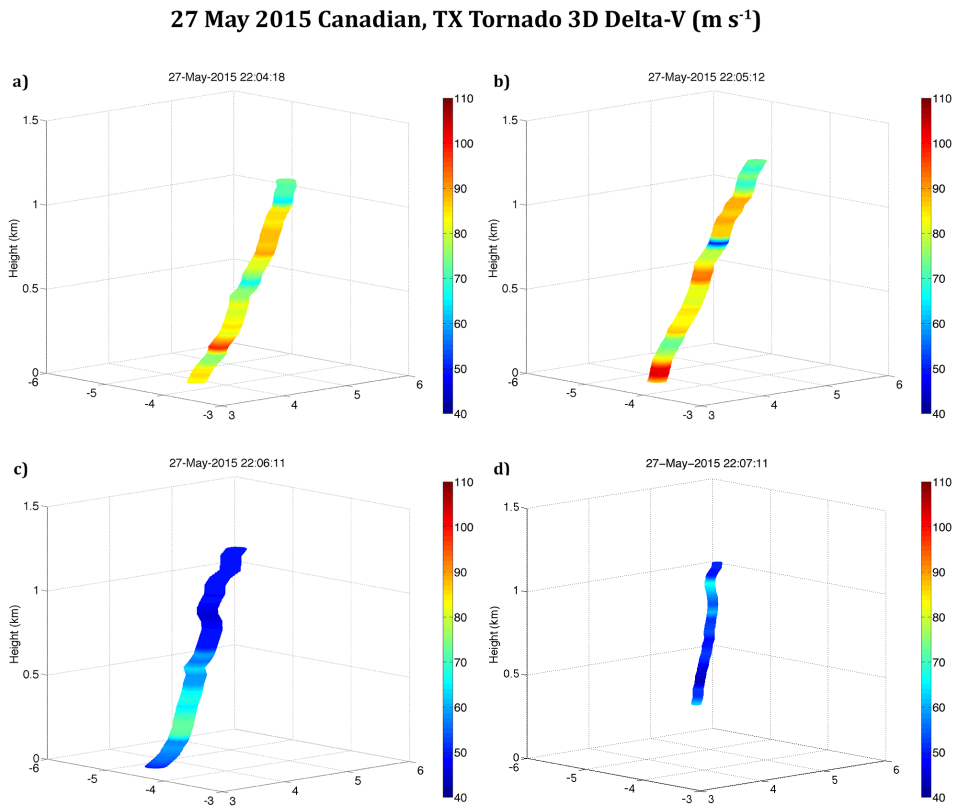

Figure 5.42: *Three-dimensional WEH center plots with maximum* Δv_r *plotted at each elevation, showing tilt and intensity simultaneously. Times from left to right and top to bottom are 2204:18, 2205:12, 2206:11, and 2207:11 UTC, respectively. Note that no TVS is apparent at low levels in the final plot, so the lower levels are not plotted.*

Without earlier observations to verify this theory of a possibly more-erect vortex earlier in the tornado's lifetime, it is impossible to know the answer to this question; however, it should be noted that at least some correlation between tilt and damage/intensity was observed by the AIR in the Tipton, Oklahoma tornado 11 days prior to this case. An example of observations of an extremely tilted vortex core in the 27 May 2015 case is shown in Fig. 5.43.

The tilt in this portion of the rope stage is nearly horizontal, resulting in a vertically oriented couplet when viewed as a RHI.

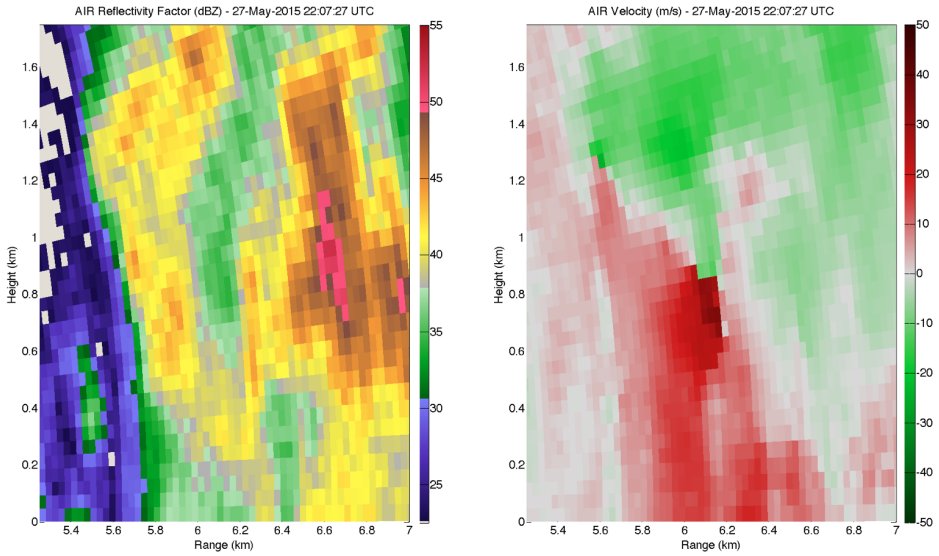

Figure 5.43: Z_{HH} *and* v_r *RHI plots through a highly tilted portion of the rope stage during the 27 May 2015 Canadian, Texas tornado. The horizontal vortex is seen at roughly 900 m AGL, an observation that is made possible only through the use of rapid RHI scans through the tornado.*

As an attempt to explain the tilting nature of the core vortex, especially at low levels during the mature stages of the tornado, a conceptual theory is provided in Fig. 5.44. At least at the mature stages observed by the AIR at the beginning of the dataset, significant tilt was observed by tracing the center of the WEH. However, visual observations indicated a relatively strong tornado in a wedge/cone stage with relatively little tilting. This indicates that a smaller-scale core vortex was likely tilting in the Canadian case. Interestingly, during the weakening stages, the observed rope tilt direction and angle was

remarkably similar to the tilt seen earlier in the tornado's lifetime (i.e., Fig. 5.42).

The theory in Fig. 5.44 indicates that during the "mature" stage of the Canadian tornado, exceptionally high radial velocities yielded a significant pressure drop near the core vortex, lowering the temperature and promoting condensation at a diameter considerably larger than the core vortex. This resulted in a visual "wedge" shape due to the relatively large-scale pressure drop. However, the vortex center was in fact tilted as seen in AIR data, meaning that the core vortex was tilted within the condensation funnel and up through the updraft region. Shortly thereafter, as radial velocities significantly weakened, the pressure drop became weakened, resulting in less condensation around the core vortex. There was still enough vorticity and pressure differential to cause a condensation funnel, but at a narrower width around the core vortex.

This thinner condensation funnel therefore acted as a visual manifestation of the vortex tube, and as the tornado continued to weaken, the rope out stage remained in this general shape (see Fig. 5.39). Despite very little change to the shape and tilt of the core vortex, intensity changes may have yielded a visual of the true tilted vortex after the mature stage of the tornado. This theory could have implications on understanding the difference in scale between a tornado and a condensation funnel. Without the extremely rapid and simultaneous RHI elevations made possible by the AIR, advection correction errors in traditional

scanning pencil beam radars could make such tilt observations and analysis impossible.

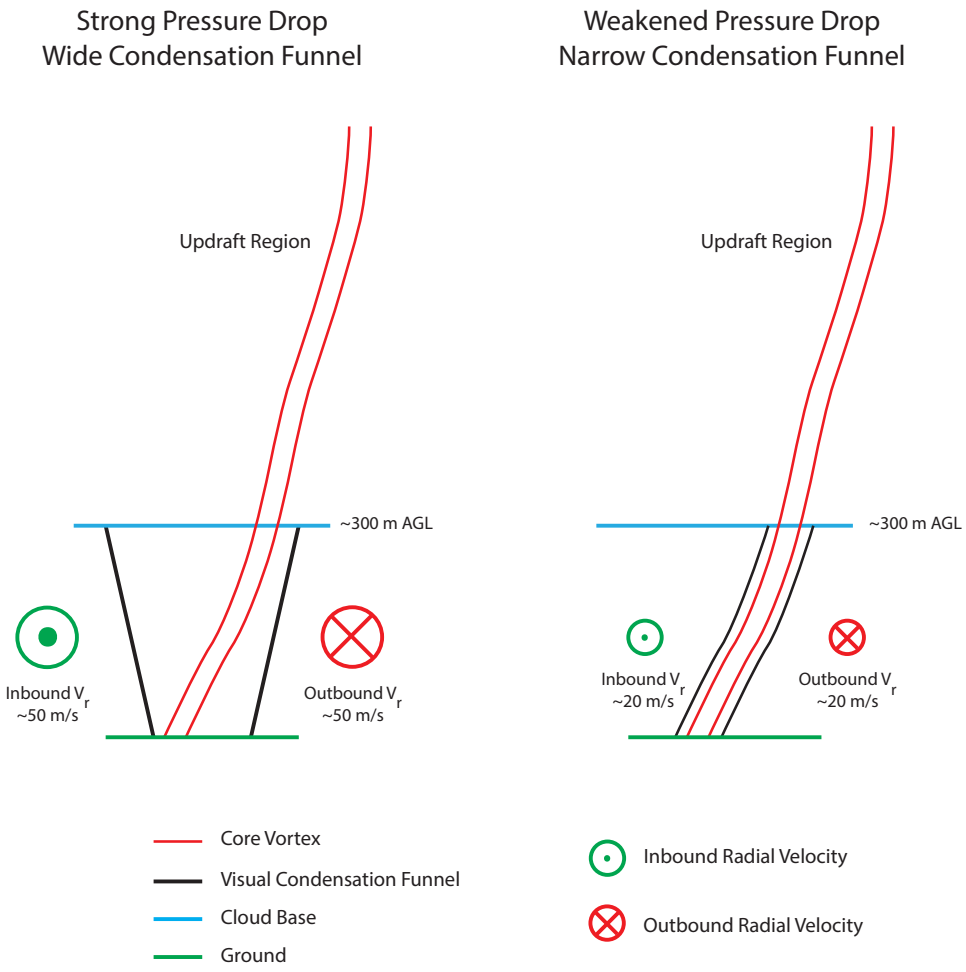

Figure 5.44: *Conceptual diagram for the tilt of the core vortex within the 27 May 2015 Canadian, Texas tornado. A strong pressure drop during mature stages causes a wide "wedge-type" condensation funnel despite a tilted vortex, as indicated by the center of WEHs in the AIR data. As the pressure drop weakens with decreased radial velocities, the condensation funnel decreases in size and width, but the tilt remains nearly the same. This rope out stage therefore represents a manifestation of the original core vortex tilt during mature stages.*

Chapter 6

Conclusions and Future Work

The future of weather radar in the USA and around the world is dependent on rapid-scanning, high-resolution, highly accurate systems capable of observing all types of weather in ways tailored to forecasters and warning meteorologists. It is widely believed that, eventually, these radars will take the form of either phased arrays that will make use of low-power, inexpensive transmitters for large-scale cost savings. Both options require the use of low-powered solid-state power amplifiers, leading to low sensitivity without the use of pulse compression. The MPAR mission in the USA depends on the ability to achieve acceptable data quality within an affordable cost structure, making pulse compression waveforms a critical aspect to MPAR risk mitigation.

This research has presented a new approach to designing weather radar waveforms for pulse compression. As opposed to previous methods, which often relied upon aggressive amplitude modulation with low power efficiencies, this approach yields promising results with theoretical SNR losses as low as 0.05 dB, and actual SNR losses in practice as low as 0.24 dB. By using

a flexible Bézier curve method for the frequency function and an appropriately weighted cost function within a genetic optimization framework, low peak and integrated sidelobes, as well as high range resolution are possible. The waveform implementation results in this research were primarily based on waveform designs for a 2.2 MHz bandwidth, 67 μs pulse length weather radar system with only 100 W of peak transmit power on each channel.

In addition to designing theoretical waveforms that are capable of high performance pulse compression results, this research also utilizes a method to account for transmitter distortions when implementing designed waveforms in real-world systems. By measuring a transfer function of the transmit chain and applying the inverse transfer function within the optimization framework, a significant improvement in performance is observed in implementation. On the PX-1000 system, an improvement from -42 dB to -52 dB was observed for peak sidelobes, and an improvement from -26 dB to -32 dB was observed for integrated sidelobes.

In order to efficiently utilize such a low-power transmitter in a weather radar platform, pulse compression is a necessity. 100 W is not sufficient to observe weak weather targets with a short pulse, and with traditional pulse compression methods, a low power efficiency is also not ideal. Gain in sensitivity as high as 2.95 dB is observed over traditional, aggressively-windowed methods. This is significant in the realm of weather radar due to the nature

of observations which are desired. A higher dynamic range of weather targets are now observable with minimized range sidelobes.

In addition to application in numerous traditional, inexpensive, low-power dish radar systems, pulse compression methods such as this for weather radar have significant potential for future phased array systems. Due to the desire for features such as high temporal resolution, the lack of moving parts, lower maintenance costs, and graceful degradation, low-power transmitters will be important in future phased array radar designs, both for weather and military uses. In order to keep costs reasonable, low-power transmitters and effective pulse compression waveforms will be critical. The methods presented in this research provide a viable option for simple pulse compression implementation in solid-state transmitters, resulting in accurate estimations and low side effects.

Isolation is also a critical aspect to consider for a multi-sector array that has significant spectral restrictions. This research has presented a novel approach for the design of multi-objective, co-optimized pulse compression waveforms. The design goals include obtaining acceptable sidelobes, resolution, and SNR loss, combined with maximizing adjacent-sector isolation while minimizing total spectrum usage of a multi-sector array. Through the use of a genetic algorithm and the simulation of steered beam pattern isolation values, a matrix of spectrum usage for all possible steering angles of a four-sector array has

been presented. For the majority of steering angles, spectral savings as high as 92% are possible, indicating the potential for significant spectrum savings with a future MPAR network.

Mission-specific waveforms are also an important consideration for weather radar. Waveforms for severe convective storms have been presented, considering the limitations of a TWT transmitter with duty cycle restrictions. These waveforms take into account major data quality issues for scanning high-turbulence phenomena with pulse compression, and have been implemented operationally on the atmospheric imaging radar. Waveforms for clear-air observations have also been discussed, especially the ability to dynamically choose different pulse lengths and bandwidths based on range, intensity, and turbulence of the target. These mission-specific waveform selections are a unique application for cognitive radar and could have major impacts on a future MPAR network.

Finally, a detailed discussion and analysis of numerous severe local storm and tornado cases using pulse compression waveforms has been presented. These cases demonstrate research-grade quality data that are possible with pulse compression and low-powered transmitters. Extensive analysis has revealed new storm features and mechanisms that were only possible with extremely rapid scanning and very high temporal resolution. A discussion of a failed occlusion observed during the 20 May 2013 Moore, OK tornado was

only made possible by rapid scanning, and was only possible with PX-1000 by using a high-sensitivity pulse compression waveform. The added spatial resolution greatly assisted in the analysis of small-scale, rapid debris ejections.

A plethora of case studies with the AIR were presented, a system that has been shown to have limited use without pulse compression due to the spreading of transmit power in the vertical dimension. However, it is this spreading of power that allows the AIR to collect extremely high temporal resolution data on supercells and tornadoes, enabling new scientific avenues. This application alone proves incredible worth in the use of pulse compression alone, but the added range resolution allows even more benefits. Multiple cases were shown, but two high-profile major tornadoes were examined in detail based on their vortex tilt characteristics, leading to intriguing new questions for tornado maintenance and dissipation.

Numerous topics exist for future work in the area of pulse compression. Theoretical waveforms have been developed for much higher time-bandwidth systems, but have not been tested with pre-distortion on actual systems. Additionally, only limited work has been completed implementing this technique on TWT transmitters (e.g., the AIR). TWT transmitters tend to have more difficult edge effects to work with, and therefore lead to higher distortion rates. The inverse transfer function method does not work as well in these

situations, and may need refinement. Future work with waveform development for the University of Oklahoma's Cylindrical polarimetric Phased Array Radar (CPPAR) is anticipated in the near-future (Zhang et al. 2011), along with additional optimization applications taking into account spectrum usage and Doppler tolerance. Advanced pre-distortion will be a necessity for future waveform development. Additionally, future work in the area of specific waveform design will involve the ability to achieve higher waveform isolation, further decreasing the total spectrum usage, especially near the edges of arrays. Additionally, near-field effects, electronics leakage, and transmitter distortions will be modeled to allow these waveform design techniques to be applied on a real system.

Regarding the scientific analyses in this research, a series of avenues exist for scientific advancement and increased understanding of mesoscale convective storm processes using systems such as PX-1000 and the AIR. With respect to PX-1000, low-powered SSPAs have become increasingly popular in recent years, meaning that these systems are likely to exist in many more locations in the coming years. SSPAs will even be used in future mobile tornado radars (development of a polarimetric atmospheric imaging radar, or PAIR, has been funded), making their applications increasingly important. The Moore case is an excellent example of pulse compression data quality, and has also contributed to understanding of a high-profile case in the Oklahoma City area.

The AIR's applications to vortex tilt and other three-dimensional storm structures are wide and varied due to the combination of rapid volumetric scanning and simultaneous RHI collection. The combination of high temporal and spatial resolutions allows for observation of storm-scale evolutions not observable with typical scanning weather radars. The observation of extremely short-lived storm processes, including tornadoes, is made possible in three dimensions due to very rapid scanning. The next steps for the AIR data presented in this research include rigorous analysis and comparison with other systems in order to determine any biases from digital beamforming. Adaptive beamforming techniques are an ideal fit for the AIR. Meteorological analysis of various case studies is a clear goal for the AIR. The future PAIR will ideally provide additional capabilities such as two-dimensional imaging and polarimetric data collection. As shown in the El Reno case, as well as the other major tornado cases, the implementation of a PAIR would allow for excellent debris analysis and tracking studies in tornadoes.

References

Ackroyd, M. H. and F. Ghani, 1973: Optimum mismatched filters for sidelobe suppression. *IEEE Trans. Aerospace and Electronic Sys.*, **AES-9**, 214–218.

Adam, J. A., 1988: Pinning defense hopes on Aegis. *Spectrum, IEEE*, **25**, 24–27.

Adlerman, E. J. and K. K. Droegemeier, 2005: The dependence of numerically simulated cyclic mesocyclogenesis upon environmental vertical wind shear. *Mon. Wea. Rev.*, **133**, 3595–3623.

Adlerman, E. J., K. K. Droegemeier, and R. Davies-Jones, 1999: A numerical simulation of cyclic mesocyclogenesis. *J. Atmos. Sci.*, **56**, 2045–2069.

Atkins, N. T., K. M. Butler, K. R. Flynn, and R. M. Wakimoto, 2014a: An integrated damage, visual, and radar analysis of the 2013 Moore Oklahoma EF5 tornado. *Bull. Amer. Meteor. Soc.*, **95**, 1549–1561.

Atkins, N. T., E. M. Glidden, and T. M. Nicholson, 2014b: Observations of wall cloud formation in supercell thunderstorms during VORTEX2. *Mon. Wea. Rev.*, in press.

Austin, G. L., 1974: Pulse compression systems for use with meteorological radars. *Radio Science*, **9**, 29–33.

Babaoglu, O., T. Binci, M. Jelasity, and A. Montresor, 2007: Firefly-inspired heartbeat synchronization in overlay networks. *Self-Adaptive and Self-Organizing Systems, First International Conference on*, 77–86.

Baden, J. M. and M. N. Cohen, 1990: Optimal peak sidelobe filters for biphase pulse compression. *International Radar Conference*, IEEE, Arlington, VA, 249–252.

Baird, C. and G. Rassweiler, 1976: Adaptive sidelobe nulling using digitally controlled phase-shifters. *Antennas and Propagation, IEEE Transactions on*, **24**, 638–649.

Barnes, S. L., 1964: A technique for maximizing details in numerical weather map analysis. *J. Appl. Meteor.*, **3**, 396–409.

Battan, L. J., 1973: *Radar Observation of the Atmosphere*. University of Chicago Press.

Beck, J. R., J. L. Schroeder, and J. M. Wurman, 2006: High-resolution dual-Doppler analyses of the 29 May 2001 Kress, Texas, cyclic supercell. *Mon. Wea. Rev.*, **134**, 3125–3148.

Bharadwaj, N. and V. Chandrasekar, 2012: Wideband waveform design principles for solid-state weather radars. *Journal of Atmospheric and Oceanic Technology*, **29**, 14–31.

Biggerstaff, M. I., L. J. Wicker, J. Guynes, C. Ziegler, J. M. Straka, E. N. Rasmussen, A. Doggett, L. D. Carey, J. L. Schroeder, and C. Weiss, 2005: The shared mobile atmospheric research and teaching radar: A collaboration to enhance research and teaching. *Bull. Amer. Meteor. Soc.*, **86**, 1263–1274.

Bluestein, H. B., 2013: *Severe Convective Storms and Tornadoes*. Springer-Verlag Berlin Heidelberg.

Bluestein, H. B., M. M. French, I. PopStefanija, R. T. Bluth, and J. B. Knorr, 2009: A mobile, phased-array Doppler radar for the study of severe convective storms. *Bull. Amer. Meteor. Soc.*, **91**, 579–600.

—, 2010: A mobile, phased-array Doppler radar for the study of severe convective storms. *Bull. Amer. Meteor. Soc.*, **91**, 579–600.

Bluestein, H. B., M. M. French, R. L. Tanamachi, S. Frasier, K. Hardwick, F. Junyent, and A. L. Pazmany, 2007a: Close-range observations of tornadoes in supercells made with a dual-polarization, X-band, mobile Doppler radar. *Mon. Wea. Rev.*, **135**, 1522–1543.

Bluestein, H. B. and M. L. Weisman, 2000: The interaction of numerically simulated supercells initiated along lines. *Mon. Wea. Rev.*, **128**, 3128–3149.

Bluestein, H. B., C. C. Weiss, M. M. French, E. M. Holthaus, R. L. Tanamachi, S. Frasier, and A. L. Pazmany, 2007b: The structure of tornadoes near Attica, Kansas, on 12 May 2004: High-resolution, mobile, Doppler radar observations. *Mon. Wea. Rev.*, **135**, 475–506.

Bluestein, H. B., C. C. Weiss, and A. L. Pazmany, 2003: Mobile Doppler radar observations of a tornado in a supercell near Bassett, Nebraska, on 5 June 1999. Part I: Tornadogenesis. *Monthly Weather Review*, **131**, 2954–2967.

—, 2004: The vertical structure of a tornado near Happy, Texas, on 5 May 2002: High-resolution, mobile, W-band, Doppler radar observations. *Mon. Wea. Rev.*, **132**, 2325–2337.

Blunt, S., M. Cook, J. Jakabosky, J. De Graaf, and E. Perrins, 2014a: Polyphase-coded FM (PCFM) radar waveforms, Part I: Implementation. *Aerospace and Electronic Systems, IEEE Transactions on*, **50**, 2218–2229.

Blunt, S., J. Jakabosky, M. Cook, J. Stiles, S. Seguin, and E. Mokole, 2014b: Polyphase-coded FM (PCFM) radar waveforms, Part II: Optimization. *Aerospace and Electronic Systems, IEEE Transactions on*, **50**, 2230–2241.

Blunt, S. D. and K. Gerlach, 2006: Adaptive pulse compression via MMSE estimation. *Aerospace and Electronic Systems, IEEE Transactions on*, **42**, 572–584.

Bodine, D. J., M. R. Kumjian, R. D. Palmer, P. L. Heinselman, and A. V. Ryzhkov, 2013: Tornado damage estimation using polarimetric radar. *Wea. Forecasting*, **28**, 139–158.

Bodine, D. J., R. D. Palmer, and G. Zhang, 2014: Dual-wavelength polarimetric radar analyses of tornadic debris signatures. *J. Appl. Meteor. Climatol.*, **53**, 242–261.

Boender, C. G. E., A. H. G. Rinnooy Kan, L. Strougie, and G. T. Timmer, 1982: A stochastic method for global optimization. *Mathematical Programming*, **22**, 125–140.

Boyd, S. P. and L. Vandenberghe, 2004: *Convex Optimization*. Cambridge University Press.

Bradford, M., 2001: *Scanning the Skies: A History of Tornado Forecasting*. University of Oklahoma Press.

Brandes, E. A., 1978: Mesocyclone evolution and tornadogenesis: Some observations. *Mon. Wea. Rev.*, **106**, 995–1011.

Brandes, E. A., G. Zhang, and J. Vivekanandan, 2004a: Comparison of polarimetric radar drop size distribution retrieval algorithms. *J. Atmos. Oceanic Technol.*, **21**, 584–598.

—, 2004b: Drop size distribution retrieval with polarimetric radar: Model and application. *J. Appl. Meteor.*, **43**, 461–475.

Bringi, V. N. and V. Chandrasekar, 2001: *Polarimetric Doppler Weather Radar: Principles and Applications*. Cambridge University Press.

Bringi, V. N., V. Chandrasekar, N. Balakrishnan, and D. S. Zrnić, 1990: An examination of propagation effects in rainfall on radar measurements at microwave frequencies. *J. Atmos. Oceanic Technol.*, **7**, 829–840.

Brooks, H. E., C. A. Doswell III, and M. P. Kay, 2003: Climatological estimates of local tornado probability for the United States. *Wea. Forecasting*, **18**, 626–640.

Brown, R. A., L. R. Lemon, and D. W. Burgess, 1978: Tornado detection by pulsed Doppler radar. *Mon. Wea. Rev.*, **106**, 29–38.

Brown, R. A. and V. T. Wood, 2012: Simulated vortex detection using a four-face phased-array Doppler radar. *Wea. Forecasting*, **27**, 1598–1603.

Brown, R. A., V. T. Wood, and D. Sirmans, 2000: Improved WSR-88D scanning strategies for convective storms. *Wea. Forecasting*, **15**, 208–220.

Brown, R. A., V. T. Wood, R. M. Steadham, R. R. Lee, B. A. Flickinger, and D. Sirmans, 2005: New WSR-88D volume coverage pattern 12: Results of field tests. *Wea. Forecasting*, **20**, 385–393.

Browning, K. A. and R. Wexler, 1968: The determination of kinematic properties of a wind field using Doppler radar. *J. Appl. Meteor.*, **7**, 105–113.

Bryan, K., P. Cunningham, and N. Bolshakova, 2006: Application of simulated annealing to the biclustering of gene expression data. *Information Technology in Biomedicine, IEEE Transactions on*, **10**, 519–525.

Bucci, N. J., H. S. Owen, K. A. Woodward, and C. M. Hawes, 1997: Validation of pulse compression techniques for meteorological functions. *IEEE Trans. Geosciences and Remote Sensing Letters*, **35**, 507–523.

Bucci, N. J. and H. Urkowitz, 1993: Testing of Doppler tolerant range sidelobe suppression in pulse compression meteorological radar. *International Radar Conference*, IEEE, Moorestown, NJ, 206–211.

Burgess, D., K. Ortega, G. Stumpf, G. Garfield, C. Karstens, T. Meyer, B. Smith, D. Speheger, J. Ladue, R. Smith, and T. Marshall, 2014: 20 May 2013 Moore, Oklahoma tornado: Damage survey and analysis. *Wea. Forecasting*, **29**, 1229–1237.

Burgess, D. W., M. A. Magsig, J. Wurman, D. C. Dowell, and Y. Richardson, 2002: Radar observations of the 3 May 1999 Oklahoma City tornado. *Wea. Forecasting*, **17**, 456–471.

Burgess, D. W., V. T. Wood, and R. A. Brown, 1982: Mesocyclone evolution statistics. *Preprints, 12th Conf. on Severe Local Storms*, Amer. Meteor. Soc., San Antonio, TX, 422–424.

Cao, Q., G. Zhang, E. A. Brandes, and T. J. Schuur, 2010: Polarimetric radar rain estimation through retrieval of drop size distribution using a Bayesian approach. *J. Appl. Meteor. Climatol.*, **49**, 973–990.

Carbone, R. E., M. J. Carpenter, and C. D. Burghart, 1985: Doppler radar sampling limitations in convective storms. *Journal of Atmospheric and Oceanic Technology*, **2**, 357–361.

Carswell, J., S. Bidwell, and R. Meneghini, 2008: A novel solid-state, dual-polarized, dual wavelength precipitation Doppler radar/radiometer. *International Geoscience and Remote Sensing Symp.*, IEEE, Boston, MA, 1014–1017.

Celis, M., J. E. Dennis, and R. A. Tapia, 1984: A trust region strategy for nonlinear equality constrained optimization. *Numerical Optimization*, Soc. Industrial Appl. Mathematics, Philadelphia, PA.

Chen, Y., S. Yang, G. Li, and Z. Nie, 2008: Adaptive nulling in time-modulated antenna arrays. *ISAPE, 8th International Symposium on*, 713–716.

Cheong, B. L., M. W. Hoffman, R. D. Palmer, S. J. Frasier, and F. J. López-Dekker, 2004: Pulse pair beamforming and the effects of reflectivity field variations on imaging radars. *Radio Science*, **39**, RS3014.

Cheong, B. L., R. Kelley, R. D. Palmer, Y. Zhang, M. Yeary, and T.-Y. Yu, 2013a: PX-1000: A solid-state polarimetric X-band weather radar and time-frequency multiplexed waveform for blind range mitigation. *IEEE Trans. Instrum. Meas.*, **62**, 3064–3072.

Cheong, B. L., J. M. Kurdzo, G. Zhang, and R. D. Palmer, 2013b: The impacts of multi-lag moment processor on a solid-state polarimetric weather radar. *36th Conf. on Radar Meteorology*, Amer. Meteor. Soc., Breckenridge, CO.

Cheong, B. L., J. D. Lee, T.-Y. Yu, S. Lee, R. D. Palmer, J. Heo, H. Kim, J. Yoo, S. J. Oh, G. W. Lee, B.-Y. Ye, J. E. Lee, and K.-Y. Nam, 2014: Observations of winter precipitation using the PX-1000. *8th European Conference on Radar in Meteorology and Hydrology*.

Cheong, B. L., R. D. Palmer, C. D. Curtis, T.-Y. Yu, D. S. Zrnic, and D. Forsyth, 2008: Refractivity retrieval using the phased-array radar: First results and potential for multimission operation. *Geoscience and Remote Sensing, IEEE Transactions on*, **46**, 2527–2537.

Chilson, P. B., W. F. Frick, P. M. Stepanian, J. R. Shipley, T. H. Kunz, and J. F. Kelly, 2012: Estimating animal densities in the aerosphere using weather radar: To Z or not to Z? *Ecosphere*, **3**, art72.

Cilliers, J. E. and J. C. Smit, 2007: Pulse compression sidelobe reduction by minimization of L_p-norms. *IEEE Trans. Aerospace and Electronic Sys.*, **43**, 1238–1247.

Clerc, M. and J. Kennedy, 2002: The particle swarm - explosion, stability, and convergence in a multidimensional complex space. *Evolutionary Computation, IEEE Transactions on*, **6**, 58–73.

Colorni, A., M. Dorigo, and V. Maniezzo, 1991: Distributed optimization by ant colonies. *European Conference on Artificial Intelligence*, 134–142.

Cook, C. E., 1960: Pulse compression-key to more efficient radar transmission. *Proceedings of the IRE*, **48**, 310–316.

Cook, C. E. and J. Paolillo, 1964: A pulse compression predistortion function for efficient sidelobe reduction in a high-power radar. *Proc. IEEE*, **52**, 377–389.

Crook, N. A., T. L. Clark, and M. W. Moncrieff, 1990: The Denver Cyclone. Part I: Generation in low Froude number flow. *J. Atmos. Sci.*, **47**, 2725–2742.

—, 1991: The Denver Cyclone. Part II: Interaction with the convective boundary layer. *J. Atmos. Sci.*, **48**, 2109–2126.

Crowe, C. C., W. A. Petersen, L. D. Carey, and D. J. Cecil, 2010: A dual-polarization investigation of tornado-warned cells associated with Hurricane Rita (2005). *Electronic J. Operational Meteor.*, **EJ4**.

Crum, T. and R. Alberty, 1993: The WSR-88D and the WSR-88D Operational Support Facility. *Bull. Amer. Meteor. Soc.*, **74**, 1669–1687.

Crum, T., S. Smith, J. Chrisman, R. Vogt, M. Istok, R. Hall, and B. Saffle, 2013: WSR-88D radar projects 2013 update. *EIPT, 29th Conference on*, Austin, TX.

Curtis, C. D., 2009: *Exploring the Capabilities of the Agile Beam Phased Array Weather Radar*. Ph.D. dissertation, University of Oklahoma.

Dantzig, G. B. and M. N. Thapa, 1997: *Linear Programming: 1: Introduction*. Springer.

Darkow, G. L. and J. C. Roos, 1970: Multiple tornado producing thunderstorms and their apparent cyclic variations in intensity. *14th Conf. on Radar Meteorology*, Amer. Meteor. Soc., Tucson, AZ, 305–308.

Daves-Jones, R. P., 1986: *Tornado Dynamics*. University of Oklahoma Press, 2nd edition, 167–221 pp.

Davies-Jones, R. P. and V. T. Wood, 2006: Simulated Doppler velocity signatures of evolving tornado-like vortices. *J. Atmos. Oceanic Technol.*, **23**, 1029–1048.

Dawson, D. T., E. R. Mansell, Y. Jung, L. J. Wicker, M. R. Kumjian, and M. Xue, 2013: Low-level ZDR signatures in supercell forward flanks: The role of size sorting and melting of hail. *J. Atmos. Sci.*, **71**, 276–299.

De Witte, E. and H. D. Griffiths, 2004: Improved ultra-low range sidelobe pulse compression waveform design. *IEEE Electronics Letters*, **40**, 1448–1450.

Dolan, B. and S. A. Rutledge, 2009: A theory-based hydrometeor identification algorithm for X-band polarimetric radars. *J. Atmos. Oceanic Technol.*, **26**, 2071–2088.

Dorigo, M., M. Birattari, and T. Stutzle, 2006: Ant colony optimization. *Computational Intelligence Magazine, IEEE*, **1**, 28–39.

Dorigo, M. and L. M. Gambardella, 1997: Ant colony system: A cooperative learning approach to the traveling salesman problem. *Evolutionary Computation, IEEE Transactions on*, **1**, 53–66.

Doviak, R. J., 2014: Comparison of weather and aircraft surveillance radar to determine key features for a MPAR (A basis for a cylindrical polarimetric phase array radar design). Technical report, National Severe Storms Laboratory.

Doviak, R. J., V. Bringi, A. Ryzhkov, A. Zahrai, and D. Zrnić, 2000: Considerations for polarimetric upgrades to operational WSR-88D radars. *J. Atmos. Oceanic Technol.*, **17**, 257–278.

Doviak, R. J. and D. S. Zrnić, 1993: *Doppler Radar and Weather Observations*. Dover Publications.

Dowell, D. C., C. R. Alexander, J. M. Wurman, and L. J. Wicker, 2005: Centrifuging of hydrometeors and debris in tornadoes: Radar-reflectivity patterns and wind-measurement errors. *Mon. Wea. Rev.*, **133**, 1501–1524.

Dowell, D. C. and H. B. Bluestein, 2002a: The 8 June 1995 Mclean, Texas, storm. Part I: Observations of cyclic tornadogenesis. *Mon. Wea. Rev.*, **130**, 2626–2648.

—, 2002b: The 8 June 1995 Mclean, Texas, storm. Part II: Cyclic tornado formation, maintenance, and dissipation. *Mon. Wea. Rev.*, **130**, 2649–2670.

Duh, F. B., C. F. Juang, and C. T. Lin, 2004: A neural fuzzy network approach to radar pulse compression. *IEEE Geoscience and Remote Sensing Letters*, **1**, 15–20.

Dunn, Z., M. Yeary, C. Fulton, and N. Goodman, 2015: Memory polynomial model for digital predistortion of broadband solid-state radar amplifiers. *Radar Conference, IEEE*, 1482–1486.

Eiben, A. E. and J. E. Smith, 2007: *Introduction to evolutionary computing*. Natural Computing, Springer Berlin Heidelberg, New York, Berlin, 2nd edition.

Evans, J. V., 1969: Theory and practice of ionosphere study by Thomson scatter radar. *Proc. IEEE*, **57**, 496–530.

Evans, J. V., R. A. Brockelman, R. F. Julian, W. A. Reid, and L. A. Carpenter, 1970: Determination of F-region vertical drifts at Millstone Hill. *Radio Science*, **5**, 27–38.

FAA, 2012: Multifunction phased array radar (MPAR) notional functional requirements document. Technical report, FAA.

Farin, G. E., 1996: *Curves and Surfaces for Computer-Aided Geometric Design: A Practical Guide*. Academic Press, Orlando, FL, 4th edition.

Finley, C. A. and B. D. Lee, 2004: High resolution mobile mesonet observations of RFD surges in the June 9 Basset, Nebraska supercell during Project ANSWERS 2003. *Preprints, 22nd Conf. on Severe Local Storms*, Amer. Meteor. Soc., Hyannis, MA, P11.3.

—, 2008: Mobile mesonet observations of an intense RFD and multiple RFD gust fronts in the May 23 Quinter, Kansas tornadic supercell during TWISTEX 2008. *Preprints, 24th Conf. on Severe Local Storms*, Amer. Meteor. Soc., Savannah, GA, P3.18.

Fogel, L. J., A. J. Owens, and M. J. Walsh, 1966: *Artificial Intelligence Through Simulated Evolution*. Wiley, Chichester, UK.

French, M. M., H. B. Bluestein, D. C. Dowell, L. J. Wicker, M. R. Kramar, and A. L. Pazmany, 2008: High-resolution, mobile Doppler radar observations of cyclic mesocyclogenesis in a supercell. *Mon. Wea. Rev.*, **136**, 4997–5016.

French, M. M., H. B. Bluestein, I. PopStefanija, C. A. Baldi, and R. T. Bluth, 2013a: Mobile, phased-array, Doppler radar observations of tornadoes at X band. *Mon. Wea. Rev.*, **142**, 1010–1036.

—, 2013b: Reexamining the vertical development of tornadic vortex signatures in supercells. *Mon. Wea. Rev.*, **141**, 4576–4601.

French, M. M., D. W. Burgess, E. R. Mansell, and L. J. Wicker, 2015: Bulk hook echo raindrop sizes retrieved using mobile, polarimetric Doppler radar observations. *J. Appl. Meteor. Climatol.*, in press.

Frick, W. F., P. M. Stepanian, J. F. Kelly, K. W. Howard, C. M. Kuster, T. H. Kunz, and P. B. Chilson, 2012: Climate and weather impact timing of emergence of bats. *PLoS ONE*, **7**, e42737.

Friday, E. W., 1994: The modernization and associated restructuring of the National Weather Service: An overview. *Bull. Amer. Meteor. Soc.*, **75**, 43–52.

Fudenberg, D., 1991: *Game Theory*. MIT Press.

Fujita, T. T., D. L. Bradbury, and C. F. V. Thullenar, 1970: Palm Sunday tornadoes of April 11, 1965. *Mon. Wea. Rev.*, **98**, 29–69.

Fujita, T. T. and H. R. Byers, 1977: Spearhead echo and downburst in the crash of an airliner. *Mon. Wea. Rev.*, **105**, 129–146.

Fulton, C. J., 2011: *Digital array radar calibration and performance monitoring techniques for direct conversion and dual polarization architectures*. Ph.D. dissertation, Purdue University.

Gass, S. I., 2003: *Linear Programming: Methods and Applications*. Dover Publications.

Ge, Z., P. Huang, and W. Lu, 2008: Matched NLFM pulse compression method with ultra-low sidelobes. *Proc. 5th European Radar Conf.*, IEEE, Amsterdam, Netherlands, 92–95.

George, J., N. Bharadwaj, and V. Chandrasekar, 2008: Considerations in pulse compression design for weather radars. *International Geoscience and Remote Sensing Symp.*, IEEE, Boston, MA, 109–112.

Gini, F. and M. Rangaswamy, 2008: *Knowledge Based Radar Detection, Tracking and Classification*. Wiley.

Glover, F., 1989: Tabu search - Part I. *ORSA Journal on Computing*, **3**, 190–206.

—, 1990: Tabu search - Part II. *ORSA Journal on Computing*, **1**, 4–32.

Gorgucci, E. and V. Chandrasekar, 2005: Evaluation of attenuation correction methodology for dual-polarization radars: Application to X-band systems. *J. Atmos. Oceanic Technol.*, **22**, 1195–1206.

Griffiths, H. D. and L. Vinagre, 1994: Design of low-sidelobe pulse compression waveforms. *IEEE Electronics Letters*, **30**, 1004–1005.

Grzych, M. L., B. D. Lee, and C. A. Finley, 2007: Thermodynamic analysis of supercell rear-flank downdrafts from Project ANSWERS. *Mon. Wea. Rev.*, **135**, 240–246.

Guerci, J. R., 2010: *Cognitive Radar: The Knowledge-Aided Fully Adaptive Approach*. Artech House.

—, 2011: Cognitive radar: The next radar wave? *Microwave Journal*, **54**, 22–36.

Harris, F. J., 1978: On the use of windows for harmonic analysis with the discrete Fourier transform. *Proceedings of the IEEE*, **66**, 51–83.

Hastings, R. M., Y. P. Richardson, and P. M. Markowski, 2014: Simulation of near-surface mesocyclogenesis during mergers between mature and nascent supercells. *27th Conf. on Severe Local Storms*, Amer. Meteor. Soc.

Haupt, R. L., 1997: Phase-only adaptive nulling with a genetic algorithm. *Antennas and Propagation, IEEE Transactions on*, **45**, 1009–1015.

Haykin, S., 2006: Cognitive radar: A way of the future. *Signal Processing Magazine, IEEE*, **23**, 30–40.

—, 2007: *Adaptive Radar Signal Processing*. Wiley.

—, 2012a: *Cognitive Dynamic Systems: Perception-Action Cycle, Radar and Radio*. Cambridge University Press.

—, 2012b: Cognitive dynamic systems: Radar, control, and radio. *Proceedings of the IEEE*, **100**, 2095–2103.

Heinselman, P. L., D. L. Priegnitz, K. L. Manross, T. M. Smith, and R. W. Adams, 2008: Rapid sampling of severe storms by the national weather radar testbed phased array radar. *Wea. Forecasting*, **23**, 808–824.

Heinselman, P. L. and S. M. Torres, 2011: High-temporal-resolution capabilities of the national weather radar testbed phased-array radar. *J. Appl. Meteor. Climatol.*, **50**, 579–593.

Herzegh, P. H. and A. R. Jameson, 1992: Observing precipitation through dual-polarization radar measurements. *Bull. Amer. Meteor. Soc.*, **73**, 1365–1374.

Hewitt, E. and R. E. Hewitt, 1979: *The Gibbs-Wilbraham phenomenon: An episode in Fourier analysis*, volume 2. Springer-Verlag.

Hirth, B. D., J. L. Schroeder, S. W. Gunter, and J. G. Guynes, 2012: Measuring a utility scale turbine wake using the TTUKa mobile research radars. *J. Atmos. Oceanic Technol.*, **29**, 765–771.

Hirth, B. D., J. L. Schroeder, and C. C. Weiss, 2008: Surface analysis of the rear-flank downdraft outflow in two tornadic supercells. *Mon. Wea. Rev.*, **136**, 2344–2363.

Holland, J., 1975: *Adaption in Natural and Artificial Systems*. The University of Michigan Press, Ann Arbor.

Horton, K. G., P. M. Stepanian, C. E. Wainwright, and A. K. Tegeler, 2015: Influence of atmospheric properties on detection of wood-warbler nocturnal flight calls. *International Journal of Biometeorology*, 1–10.

Houser, J. B., 2013: *Observations of Supercell Tornado Evolution using a Mobile, Rapid-Scan, X-Band Radar*. Ph.D. dissertation, University of Oklahoma.

Houser, J. B., H. B. Bluestein, and J. C. Snyder, 2015: Rapid-scan, polarimetric, Doppler-radar observations of tornadogenesis and tornado dissipation in

a tornadic supercell: The "El Reno, Oklahoma" storm of 24 May 2011. *Mon. Wea. Rev.*, **143**, 2685–2710.

Irwin, S. and T. Smith, 2009: Nowcasting wet microburst events with phased array radar. *2009 National Wea. Assoc. Meeting*, National Wea. Assoc., Norfolk, VA.

Isom, B., R. Palmer, R. Kelley, J. Meier, D. Bodine, M. Yeary, B.-L. Cheong, Y. Zhang, T.-Y. Yu, and M. I. Biggerstaff, 2013: The atmospheric imaging radar: Simultaneous volumetric observations using a phased array weather radar. *J. Atmos. Oceanic Technol.*, **30**, 655–675.

Jakabosky, J., S. D. Blunt, and T. Higgins, 2015: Ultra-low sidelobe waveform design via spectral shaping and LINC transmit architecture. *Radar Conference, IEEE*, 1021–1026.

Jakabosky, J., S. D. Blunt, and B. Himed, 2014: Optimization of "over-coded" radar waveforms. *Radar Conference, IEEE*, 1460–1465.

Jakabosky, J., L. Ryan, and S. Blunt, 2013: Transmitter-in-the-loop optimization of distorted OFDM radar emissions. *Radar Conference, IEEE*, 1–5.

Jameson, A. R., 1992: The effect of temperature on attenuation-correction schemes in rain using polarization propagation differential phase shift. *J. Appl. Meteor.*, **31**, 1106–1118.

Kanti Paul, B. and M. Stimers, 2014: Spatial analyses of the 2011 Joplin tornado mortality: Deaths by interpolated damage zones and location of victims. *Wea. Climate Soc.*, **6**, 161–174.

Karmarkar, N., 1984: A new polynomial time algorithm for linear programming. *Combinatorica*, **4**, 373–395.

Keeler, R. J. and C. A. Hwang, 1995: Pulse compression for weather radar. *International Radar Conference*, IEEE, Alexandria, VA, 529–535.

Keeler, R. J., C. A. Hwang, and A. S. Mudukutore, 1999: Pulse compression for phased array weather radars. Technical report, National Center for Atmospheric Research.

Kennedy, J. and R. Eberhart, 1995: Particle swarm optimization. *Neural Networks, IEEE Intl. Conf. on*, volume 4, 1942–1948.

Kirkpatrick, S., C. D. Gelatt, and M. P. Vecchi, 1983: Optimization by simulated annealing. *Science*, **220**, 671–680.

Klauder, J. R., A. C. Price, S. Darlington, and W. J. Albersheim, 1960: The theory and design of chirp radars. *Bell Syst. Technol. J.*, **39**, 745–809.

Klemp, J. B. and R. Rotunno, 1983: A study of the tornadic region within a supercell thunderstorm. *J. Atmos. Sci.*, **40**, 359–377.

Kosiba, K. and J. Wurman, 2010: The three-dimensional axisymmetric wind field structure of the Spencer, South Dakota, 1998 tornado. *J. Atmos. Sci.*, **67**, 3074–3083.

Kosiba, K., J. Wurman, Y. Richardson, P. Markowski, P. Robinson, and J. Marquis, 2013: Genesis of the Goshen County, Wyoming, tornado on 5 June 2009 during VORTEX2. *Mon. Wea. Rev.*, **141**, 1157–1181.

Kosiba, K. A. and J. Wurman, 2013: The three-dimensional structure and evolution of a tornado boundary layer. *Wea. Forecasting*, **28**, 1552–1561.

Kumjian, M. R., 2011: Precipitation properties of supercell hook echoes. *Electronic J. Severe Storms Meteor.*, **6**, 1–21.

Kumjian, M. R. and A. V. Ryzhkov, 2008: Polarimetric signatures in supercell thunderstorms. *J. Appl. Meteor. Climatol.*, **47**, 1940–1961.

—, 2009: Storm-relative helicity revealed from polarimetric radar measurements. *J. Atmos. Sci.*, **66**, 667–685.

Kumjian, M. R., A. V. Ryzhkov, V. M. Melnikov, and T. J. Schuur, 2010: Rapid-scan super-resolution observations of a cyclic supercell with a dual-polarization WSR-88D. *Mon. Wea. Rev.*, **138**, 3762–3786.

Kurdzo, J. M., D. J. Bodine, B. L. Cheong, and R. D. Palmer, 2015a: High-temporal resolution polarimetric X-band Doppler radar observations of the 20 May 2013 Moore, Oklahoma, tornado. *Mon. Wea. Rev.*, **143**, 2711–2735.

Kurdzo, J. M., B. L. Cheong, R. D. Palmer, G. Zhang, and J. Meier, 2014: A pulse compression waveform for improved-sensitivity weather radar observations. *J. Atmos. Oceanic Technol.*, **31**, 2713–2731.

Kurdzo, J. M., F. Nai, D. J. Bodine, R. D. Palmer, J. Lujan, A. Mahre, and A. D. Byrd, 2015b: Observations of severe local storms and tornadoes with the atmospheric imaging radar. *Radar Conference, AMS*.

Kurdzo, J. M., R. D. Palmer, F. Nai, D. J. Bodine, and B. L. Cheong, 2015c: Meteorological data results from the atmospheric imaging radar. *Radar Conference, IEEE*, 0799–0804.

Lazo, J. K., M. Lawson, P. H. Larsen, and D. M. Waldman, 2011: U.S. economic sensitivity to weather variability. *Bull. Amer. Meteor. Soc.*, **92**, 709–720.

Le, K. D., R. D. Palmer, B. L. Cheong, T.-Y. Yu, G. Zhang, and S. M. Torres, 2009: On the use of auxiliary receive channels for clutter mitigation with phased array weather radars. *Geoscience and Remote Sensing, IEEE Transactions on*, **47**, 272–284.

Lee, B. D., C. A. Finley, and C. D. Karstens, 2012: The Bowdle, South Dakota, cyclic tornadic supercell of 22 May 2010: Surface analysis of rear-flank downdraft evolution and multiple internal surges. *Mon. Wea. Rev.*, **140**, 3419–3441.

Lee, B. D., B. F. Jewett, and R. B. Wilhelmson, 2006: The 19 April 1996 Illinois tornado outbreak. Part II: Cell mergers and associated tornado incidence. *Wea. Forecasting*, **21**, 449–464.

Lee, E. T. Y., 1989: Choosing nodes in parametric curve interpolation. *Computer-Aided Design*, **21**, 363–370.

Lei, L., G. Zhang, R. J. Doviak, R. Palmer, B. L. Cheong, M. Xue, Q. Cao, and Y. Li, 2012: Multilag correlation estimators for polarimetric radar measurements in the presence of noise. *J. Atmos. Oceanic Technol.*, **29**, 772–795.

Lemon, L. R. and C. A. Doswell, 1979: Severe thunderstorm evolution and mesocyclone structure as related to tornadogenesis. *Mon. Wea. Rev.*, **107**, 1184–1197.

Leslie, L. M., 1971: The development of concentrated vortices: A numerical study. *J. Fluid Mechanics*, **48**, 1–21.

Levanon, N. and E. Mozeson, 2004: *Radar Signals*. Wiley.

Li, Z., Y. Zhang, S. Wang, L. Li, and M. Mclinden, 2015: Fast adaptive pulse compression based on matched filter outputs. *Aerospace and Electronic Systems, IEEE Transactions on*, **51**, 548–564.

Magsig, M. A. and J. T. Snow, 1998: Long-distance debris transport by tornadic thunderstorms. Part I: The 7 May 1995 supercell thunderstorm. *Mon. Wea. Rev.*, **126**, 1430–1449.

Mahre, A., R. D. Palmer, T.-Y. Yu, and J. M. Kurdzo, 2016: A study of high temporal and spatial resolution RHIs throgh outflow boundaries and squall lines using the atmospheric imaging radar. *EIPT, 31st Conference on*.

Mailloux, R. J., 2005: *Phased Array Antenna Handbook*. Artech House.

Majcen, M., P. Markowski, Y. Richardson, D. Dowell, and J. Wurman, 2008: Multipass objective analyses of Doppler radar data. *J. Atmos. Oceanic Technol.*, **25**, 1845–1858.

Markowski, P., Y. Richardson, J. Marquis, J. Wurman, K. Kosiba, P. Robinson, D. Dowell, E. Rasmussen, and R. Davies-Jones, 2012: The pretornadic phase of the Goshen County, Wyoming, supercell of 5 June 2009 intercepted by VORTEX2. Part I: Evolution of kinematic and surface thermodynamic fields. *Mon. Wea. Rev.*, **140**, 2887–2915.

Markowski, P. M., 2002: Hook echoes and rear-flank downdrafts: A review. *Mon. Wea. Rev.*, **130**, 852–876.

Markowski, P. M. and Y. P. Richardson, 2010: *Mesoscale Meteorology in Midlatitudes*. Wiley.

—, 2014: What we know and don't know about tornado formation. *Physics Today*, **67**, 26–31.

Markowski, P. M., J. M. Straka, and E. N. Rasmussen, 2002: Direct surface thermodynamic observations within the rear-flank downdrafts of nontornadic and tornadic supercells. *Mon. Wea. Rev.*, **130**, 1692–1721.

—, 2003: Tornadogenesis resulting from the transport of circulation by a downdraft: Idealized numerical simulations. *J. Atmos. Sci.*, **60**, 795–823.

Marquis, J., Y. Richardson, P. Markowski, D. Dowell, and J. Wurman, 2012: Tornado maintenance investigated with high-resolution dual-Doppler and EnKF analysis. *Mon. Wea. Rev.*, **140**, 3–27.

Marquis, J., Y. Richardson, J. Wurman, and P. Markowski, 2008: Single- and dual-Doppler analysis of a tornadic vortex and surrounding storm-scale flow in the Crowell, Texas, supercell of 30 April 2000. *Mon. Wea. Rev.*, **136**, 5017–5043.

McDonald, J. R. and K. C. Mehta, 2006: *A recommendation for an Enhanced Fujita scale (EF-Scale)*. Wind Science and Engineering Center, Texas Tech University.

McLaughlin, D., D. Pepyne, B. Philips, J. Kurose, M. Zink, D. Westbrook, E. Lyons, E. Knapp, A. Hopf, A. Defonzo, R. Contreras, T. Djaferis, E. Insanic, S. Frasier, V. Chandrasekar, F. Junyent, N. Bharadwaj, Y. Wang,

Y. Liu, B. Dolan, K. Droegemeier, J. Brotzge, M. Xue, K. Kloesel, K. Brewster, F. Carr, S. Cruz-Pol, K. Hondl, and P. Kollias, 2009: Short-wavelength technology and the potential for distributed networks of small radar systems. *Bulletin of the American Meteorological Society*, **90**, 1797–1817.

McTaggart-Cowan, R., L. F. Bosart, J. R. Gyakum, and E. H. Atallah, 2007: Hurricane Katrina (2005). Part I: Complex life cycle of an intense tropical cyclone. *Mon. Wea. Rev.*, **135**, 3905–3926.

Metropolis, N., A. W. Rosenbluth, M. N. Rosenbluth, A. H. Teller, and E. Teller, 1953: Equation of state calculations by fast computing machines. *Journal of Chemical Physics*, **21**, 1087–1092.

Michelson, M., W. Shrader, and J. Wieler, 1990: Terminal Doppler Weather Radar. *Microwave Journal*, **33**, 139–148.

Miranda, S., C. Baker, K. Woodbridge, and H. Griffiths, 2006: Knowledge-based resource management for multifunction radar: A look at scheduling and task prioritization. *Signal Processing Magazine, IEEE*, **23**, 66–76.

Moller, A. R., C. A. Doswell, M. P. Foster, and G. R. Woodall, 1994: The operational recognition of supercell thunderstorm environments and storm structures. *Wea. Forecasting*, **9**, 327–347.

Mucci, R. A., 1984: A comparison of efficient beamforming algorithms. *Acoustics, Speech and Signal Processing, IEEE Trans. on*, **32**, 548–558.

Mudukutore, A. S., V. Chandrasekar, and R. J. Keeler, 1998: Pulse compression for weather radars. *Geoscience and Remote Sensing, IEEE Transactions on*, **36**, 125–142.

Nai, F., S. Torres, and R. Palmer, 2013: Adaptive beamforming for weather observations using the atmospheric imaging radar. *Phased Array Systems and Technology, IEEE International Symposium on*, 709–713.

Neblett Fanfair, R., K. Benedict, J. Bos, S. D. Bennett, Y.-C. Lo, T. Adebanjo, K. Etienne, E. Deak, G. Derado, W.-J. Shieh, C. Drew, S. Zaki, D. Sugerman, L. Gade, E. H. Thompson, D. A. Sutton, D. M. Engelthaler, J. M. Schupp, M. E. Brandt, J. R. Harris, S. R. Lockhart, G. Turabelidze, and B. J. Park, 2012: Necrotizing Cutaneous Mucormycosis after a tornado in Joplin, Missouri, in 2011. *New England Journal of Medicine*, **367**, 2214–2225.

Nelder, J. A. and R. Mead, 1965: A simplex method for function minimization. *Computer Journal*, **7**, 308–313.

Obama, B. H., 2013: Presidential Memorandum – Expanding America's leadership in wireless innovation. Technical report, Office of the President of the United States.

Oh, I.-S., J.-S. Lee, and B.-R. Moon, 2004: Hybrid genetic algorithms for feature selection. *Pattern Analysis and Machine Intelligence, IEEE Transactions on*, **26**, 1424–1437.

O'Hora, F. and J. Bech, 2007: Improving weather radar observations using pulse-compression techniques. *Meteorol. Appl.*, **14**, 389–401.

Palmer, R. D., D. Bodine, M. Kumjian, B. Cheong, G. Zhang, Q. Cao, H. B. Bluestein, A. Ryzhkov, T.-Y. Yu, and Y. Wang, 2011: Observations of the 10 May 2010 tornado outbreak using OU-PRIME: Potential for new science with high-resolution polarimetric radar. *Bull. Amer. Meteor. Soc.*, **92**, 871–891.

Palmer, R. D., B. L. Cheong, M. W. Hoffman, S. J. Frasier, and F. J. López-Dekker, 2005: Observations of the small-scale variability of precipitation using an imaging radar. *J. Atmos. Oceanic Technol.*, **22**, 1122–1137.

Pang, C., P. Hoogeboom, F. Le Chevalier, H. W. J. Russchenberg, J. Dong, T. Wang, and X. Wang, 2015: A pulse compression waveform for weather radars with solid-state transmitters. *Geoscience and Remote Sensing Letters, IEEE*, **12**, 2026–2030.

Papoulis, A. and S. U. Pillai, 2002: *Probability, Random Variables, and Stochastic Processes*. Tata McGraw-Hill.

Park, H. S., A. V. Ryzhkov, D. S. Zrnić, and K.-E. Kim, 2009: The hydrometeor classification algorithm for the polarimetric WSR-88D: Description and application to an MCS. *Wea. Forecasting*, **24**, 730–748.

Park, S. G., V. N. Bringi, V. Chandrasekar, M. Maki, and K. Iwanami, 2005: Correction of radar reflectivity and differential reflectivity for rain attenuation at X band. Part I: Theoretical and empirical basis. *J. Atmos. Oceanic Technol.*, **22**, 1621–1632.

Pazmany, A. L., J. B. Mead, H. B. Bluestein, J. C. Snyder, and J. B. Houser, 2013: A mobile rapid-scanning X-band polarimetric (RaXPol) Doppler radar system. *J. Atmos. Oceanic Technol.*, **30**, 1398–1413.

Probert-Jones, J. R., 1962: The radar equation in meteorology. *Quart. J. Royal Met. Soc.*, **88**, 485–495.

Rechenberg, I., 1973: *Evolutionstrategie: Optimierung Technisher Systeme nach Prinzipien des Biologischen Evolution*. Frommann-Holzboog, Stuttgart.

Reinoso-Rondinel, R., T.-Y. Yu, and S. Torres, 2010: Multifunction phased-array radar: Time balance scheduler for adaptive weather sensing. *Journal of Atmospheric and Oceanic Technology*, **27**, 1854–1867.

Robinson, J. and Y. Rahmat-Samii, 2004: Particle swarm optimization in electromagnetics. *Antennas and Propagation, IEEE Transactions on*, **52**, 397–407.

Rockney, V., 1958: The WSR-57 radar. *Proc. Seventh Conf. on Weather Radar*, Amer. Meteor. Soc., Miami Beach, FL, F14–F20.

Ryzhkov, A., D. Burgess, D. Zrnić, T. Smith, and S. Giangrande, 2002: Polarimetric analysis of a 3 May 1999 tornado. *Preprints, 21st Conf. on Severe Local Storms*, Amer. Meteor. Soc., San Antonio, TX.

Ryzhkov, A. V., 2007: The impact of beam broadening on the quality of radar polarimetric data. *J. Atmos. Oceanic Technol.*, **24**, 729–744.

Ryzhkov, A. V., S. E. Giangrande, and T. J. Schuur, 2005a: Rainfall estimation with a polarimetric prototype of WSR-88D. *J. Appl. Meteor. Climatol.*, **44**, 502–515.

Ryzhkov, A. V., T. J. Schurr, D. W. Burgess, and D. Zrnić, 2005b: Polarimetric tornado detection. *J. Appl. Meteor. Climatol.*, **44**, 557–570.

Ryzhkov, A. V. and D. S. Zrnić, 1995: Comparison of dual-polarization radar estimators of rain. *J. Atmos. Oceanic Technol.*, **12**, 249–256.

—, 2005: Radar polarimetry at S, C, and X bands: Comparative analysis and operational implications. *32nd Conf. Radar Meteor.*, Amer. Meteor. Soc., Albuquerque, NM, volume 9R.3.

Schmidlin, T. W., 2006: On evacuation and deaths from Hurricane Katrina. *Bull. Amer. Meteor. Soc.*, **87**, 754–756.

Schultz, C. J., L. D. Carey, E. V. Schultz, B. C. Carcione, C. B. Darden, C. C. Crowe, P. N. Gatlin, D. J. Nadler, W. A. Petersen, and K. R. Knupp, 2012: Dual-polarization tornadic debris signatures Part I: Examples and utility in an operational setting. *Electronic J. Operational Meteor.*, **13**, 120–137.

Shanno, D. F., 1970: Conditioning of Quasi-Newton methods for function minimization. *Mathematics of Computation*, **24**, 647–656.

Shannon, C. E., 1949: Communication in the presence of noise. *Proceedings of the IRE*, **37**, 10–21.

Shapiro, A. and J. J. Mewes, 1999: New formulations of dual-Doppler wind analysis. *J. Atmos. Oceanic Technol.*, **16**, 782–792.

Shein, K. A., 2006: State of the climate in 2005. *Bull. Amer. Meteor. Soc.*, **87**, s1–s102.

Simmons, K. M. and D. Sutter, 2008: Tornado warnings, lead times, and tornado casualties: An empirical investigation. *Wea. Forecasting*, **23**, 246–258.

Skinner, P. S., C. C. Weiss, M. M. French, H. B. Bluestein, P. M. Markowski, and Y. P. Richardson, 2014: VORTEX2 observations of a low-level mesocyclone with multiple internal rear-flank downdraft momentum surges in the 18 May 2010, Dumas, Texas supercell. *Mon. Wea. Rev.*, **142**, 2935–2960.

Skinner, P. S., C. C. Weiss, L. J. Wicker, C. K. Potvin, and D. C. Dowell, 2015: Forcing mechanisms for an internal rear-flank downdraft momentum surge in the 18 May 2010 Dumas, Texas supercell. *Mon. Wea. Rev.*, **in press**.

Skolnik, M., 2002: *Introduction to Radar Systems*. McGraw-Hill, third edition.

Snow, J. T., 1982: A review of recent advances in tornado vortex dynamics. *Reviews of Geophysics*, **20**, 953–964.

—, 1984: On the formation of particle sheaths in columnar vortices. *J. Atmos. Sci.*, **41**, 2477–2491.

Snyder, J. C. and H. B. Bluestein, 2014: Some considerations for the use of high-resolution mobile radar data in tornado intensity determination. *Wea. Forecasting*, **29**, 799–827.

Snyder, J. C., H. B. Bluestein, V. Venkatesh, and S. J. Frasier, 2013: Observations of polarimetric signatures in supercells by an X-band mobile Doppler radar. *Mon. Wea. Rev.*, **141**, 3–29.

Snyder, J. C., H. B. Bluestein, G. Zhang, and S. J. Frasier, 2010: Attenuation correction and hydrometeor classification of high-resolution, X-band, dual-polarized mobile radar measurements in severe convective storms. *J. Atmos. Oceanic Technol.*, **27**, 1979–2001.

Snyder, J. C. and A. V. Ryzhkov, 2014: An automated detection for polarimetric tornado debris detection. *8th European Conference on Radar in Meteorology and Hydrology*, Garmisch-Partenkirchen, Germany.

Stensrud, D. J., L. J. Wicker, K. E. Kelleher, M. Xue, M. P. Foster, J. T. Schaefer, R. S. Schneider, S. G. Benjamin, S. S. Weygandt, J. T. Ferree, and J. P. Tuell, 2009: Convective-scale warn-on-forecast system. *Bull. Amer. Meteor. Soc.*, **90**, 1487–1499.

Stepanian, P. M. and K. G. Horton, 2015: Extracting migrant flight orientation profiles using polarimetric radar. *Geoscience and Remote Sensing, IEEE Transactions on*, in press.

Stumpf, G. J., 2013: The NWS/NSSSL damage survey of the 20 May Moore, Oklahoma tornado. Personal Communication.

Tanamachi, R. L., H. B. Bluestein, J. B. Houser, S. J. Frasier, and K. M. Hardwick, 2012: Mobile, X-band, polarimetric Doppler radar observations of the 4 May 2007 Greensburg, Kansas, tornadic supercell. *Mon. Wea. Rev.*, **140**, 2103–2125.

Taylor, J. W. and G. Brunins, 1975: Long-range surveillance radar for automatic control systems. *International Radar Conference*.

Torres, S., R. Adams, C. Curtis, E. Forren, I. Ivić, D. Priegnitz, J. Thompson, and D. Warde, 2013a: New weather-surveillance capabilities for NSSL's phased-array radar. *EIPT, 29th Conference on*, AMS.

Torres, S. M., R. Adams, C. Curtis, E. Forren, D. Forsyth, I. Ivić, D. Priegnitz, J. Thompson, and D. Warde, 2013b: A demonstration of multifunction capabilities on the national weather radar testbed phased-array radar. *Radar Meteorology, 36th Conference on*.

Torres, S. M., Y. F. Dubel, and D. S. Zrnić, 2004: Design, implementation, and demonstration of a staggered PRT algorithm for the WSR-88D. *Journal of Atmospheric and Oceanic Technology*, **21**, 1389–1399.

Trapp, R. J. and R. Davies-Jones, 1997: Tornadogenesis with and without a dynamic pipe effect. *J. Atmos. Sci.*, **54**, 113–133.

Trapp, R. J. and B. H. Fiedler, 1995: Tornado-like vortexgenesis in a simplified numerical model. *J. Atmos. Sci.*, **52**, 3757–3778.

Vasiloff, S. V., 2001: Improving tornado warnings with the Federal Aviation Administration's terminal Doppler weather radar. *Bull. Amer. Meteor. Soc.*, **82**, 861–874.

Wang, C. P., 1974: Standardization of the definition of the radar ambiguity function. *Aerospace and Electronic Systems, IEEE Transactions on*, **10**, 532–533.

Wang, P., H. Meng, and W. Xiqin, 2008: Suppressing autocorrelation sidelobes of LFM pulse trains with genetic algorithm. *Tsinghua Science and Technology*, **13**, 800–806.

Wang, S., Z. Li, Y. Zhang, B. Cheong, and L. Li, 2015: Implementation of adaptive pulse compression in solid-state radars: Practical considerations. *Geoscience and Remote Sensing Letters, IEEE*, **12**, 2170–2174.

Watson Jr., R. C., 2009: *Radar Origins Worldwide: History of Its Evolution in 13 Nations Through World War II*. Trafford.

Weadon, M., P. Heinselman, D. Forsyth, J. Kimpel, W. E. Benner, and G. S. Torok, 2009: Multifunction phased array radar. *Bull. Amer. Meteor. Soc.*, **90**, 385–389.

Weber, M., J. Cho, J. Flavin, J. Herd, and M. Vai, 2005: Multifunction phased array radar for US civil-sector surveillance needs. *Radar Meteorology, 32nd Conference on*.

Weber, M. E., J. Y. N. Cho, J. S. Herd, J. M. Flavin, W. E. Benner, and G. S. Torok, 2007: The next-generation multimission U.S. surveillance radar network. *Bull. Amer. Meteor. Soc.*, **88**, 1739–1751.

Weber, M. E. and M. L. Stone, 1995: Low altitude wind shear detection using airport surveillance radars. *Aerospace and Electronic Systems Magazine, IEEE*, **10**, 3–9.

Weiss, C. C., J. L. Schroeder, J. Guynes, P. S. Skinner, and J. Beck, 2009: The TTUKa mobile Doppler radar: Coordinated radar and in situ measurements of supercell thunderstorms during Project VORTEX2. *Preprints, 34th Conf. on Radar Meteorology*, Amer. Meteor. Soc., Williamsburg, VA, 11B.2.

Wen, C.-H., J. F. Doherty, and J. D. Mathews, 2004: Time-frequency radar processing for meteor detection. *Geoscience and Remote Sensing, IEEE Transactions on*, **42**, 501–510.

Whiton, R. C., P. L. Smith, S. G. Bigler, K. E. Wilk, and A. C. Harbuck, 1998: History of operational use of weather radar by U.S. weather services. Part I: The pre-NEXRAD era. *Wea. Forecasting*, **13**, 219–243.

Wicker, L. J. and R. B. Wilhelmson, 1995: Simulation and analysis of tornado development and decay within a three-dimensional supercell thunderstorm. *J. Atmos. Sci.*, **52**, 2675–2703.

Wilbraham, H., 1848: On a certain periodic function. *The Cambridge and Dublin Mathematical Journal*, **3**, 198–201.

Willoughby, H. E. and P. G. Black, 1996: Hurricane Andrew in Florida: Dynamics of a disaster. *Bull. Amer. Meteor. Soc.*, **77**, 543–549.

Wilson, J. W., R. D. Roberts, C. Kessinger, and J. McCarthy, 1984: Microburst wind structure and evaluation of Doppler radar for airport wind shear detection. *Journal of Climate and Applied Meteorology*, **23**, 898–915.

Wolfson, M., R. Delanoy, B. Forman, R. Hallowell, M. Pawlak, and P. Smith, 1994: Automated microburst wind-shear prediction. *Lincoln Laboratory Journal*, **7**, 399–426.

Wurman, J. and C. R. Alexander, 2005: The 30 May 1998 Spencer, South Dakota, storm. Part II: Comparison of observed damage and radar-derived winds in the tornadoes. *Mon. Wea. Rev.*, **133**, 97–119.

Wurman, J., D. Dowell, Y. Richardson, P. Markowski, E. Rasmussen, D. Burgess, L. Wicker, and H. B. Bluestein, 2012: The second verification of the origins of rotation in tornadoes experiment: VORTEX2. *Bull. Amer. Meteor. Soc.*, **93**, 1147–1170.

Wurman, J. and S. Gill, 2000: Finescale radar observations of the Dimmitt, Texas (2 June 1995), tornado. *Mon. Wea. Rev.*, **128**, 2135–2164.

Wurman, J. and K. Kosiba, 2013: Finescale radar observations of tornado and mesocyclone structures. *Wea. Forecasting*, **28**, 1157–1174.

Wurman, J., K. Kosiba, P. Markowski, Y. Richardson, D. Dowell, and P. Robinson, 2010: Finescale single- and dual-Doppler analysis of tornado intensification, maintenance, and dissipation in the Orleans, Nebraska, supercell. *Mon. Wea. Rev.*, **138**, 4439–4455.

Wurman, J. and M. Randall, 2001: An inexpensive, mobile, rapid-scan radar. *Preprints, 30th International Conf. on Radar Meteorology*, Amer. Meteor. Soc., Munich, Germany, P3.4.

Wurman, J., Y. Richardson, C. Alexander, S. Weygandt, and P. F. Zhang, 2007a: Dual-Doppler analysis of winds and vorticity budget terms near a tornado. *Mon. Wea. Rev.*, **135**, 2392–2405.

—, 2007b: Dual-Doppler and single-Doppler analysis of a tornadic storm undergoing mergers and repeated tornadogenesis. *Mon. Wea. Rev.*, **135**, 736–758.

Wurman, J., J. M. Straka, and E. N. Rasmussen, 1996: Fine-scale Doppler radar observations of tornadoes. *Science*, **272**, 1774–1777.

Yang, X. S., 2008: *Nature-Inspired Metaheuristic Algorithms*. Luniver Press.

Yichun, P., P. Shirui, Y. Kefeng, and D. Wenfeng, 2005: Optimization design of NLFM signal and its pulse compression simulation. *International Radar Conference*, IEEE, Arlington, VA, 383–386.

Youhua, W., Y. Weili, and Z. Guansheng, 1996: Adaptive simulated annealing for the optimal design of electromagnetic devices. *Magnetics, IEEE Transactions on*, **32**, 1214–1217.

Yu, T.-Y. and R. D. Palmer, 2001: Atmospheric radar imaging using multiple-receiver and multiple-frequency techniques. *Radio Science*, **36**, 1493–1503.

Yussouf, N. and D. J. Stensrud, 2008: Impact of high temporal frequency radar data assimilation on storm-scale NWP model simulations. *24th Conf. on Severe Local Storms*, Amer. Meteor. Soc., Savannah, GA, 9B.1.

Zahrai, A. and D. Zrnić, 1993: The 10-cm-wavelength polarimetric weather radar at NOAA's National Severe Storms Laboratory. *J. Atmos. Oceanic Technol.*, **10**, 649–662.

Zhang, G., R. J. Doviak, D. S. Zrnić, R. Palmer, L. Lei, and Y. Al-Rashid, 2011: Polarimetric phased-array radar for weather measurement: A planar or cylindrical configuration? *J. Atmos. Oceanic Technol.*, **28**, 63–73.

Zhang, G., S. Karimkashi, L. Lei, R. Kelley, J. Meier, R. Palmer, C. Futon, R. J. Doviak, A. Zahrai, D. S. Zrnic, and Y. Al-Rashid, 2013: A cylindrical polarimetric phased array radar concept – A path to multi-mission capability. *Phased Array Systems & Technology, 2013 IEEE Intl. Symp. on*, 481–484.

Ziegler, C. L., E. N. Rasmussen, T. R. Shepherd, A. I. Watson, and J. M. Straka, 2001: The evolution of low-level rotation in the 29 May 1994 Newcastle–Graham, Texas, storm complex during VORTEX. *Mon. Wea. Rev.*, **129**, 1339–1368.

Zrnić, D. and P. Mahapatra, 1985: Two methods of ambiguity resolution in pulse Doppler weather radars. *Aerospace and Electronic Systems, IEEE Transactions on*, **21**, 470–483.

Zrnić, D. S. and R. J. Doviak, 2005: System requirements for phased array weather radar. Technical report, National Severe Storms Laboratory.

Zrnić, D. S., R. J. Doviak, V. M. Melnikov, and I. R. Ivić, 2014: Signal design to suppress coupling in the polarimetric phased array radar. *J. Atmos. Oceanic Technol.*, **31**, 1063–1077.

Zrnić, D. S., J. F. Kimpel, D. E. Forsyth, A. Shapiro, G. Crain, R. Ferek, J. Heimmer, W. Benner, T. J. McNellis, and R. J. Vogt, 2007: Agile-beam phased array radar for weather observations. *Bull. Amer. Meteor. Soc.*, **88**, 1753–1766.

Appendix A : List of Acronyms

ACF	Autocorrelation Function
AF	Ambiguity Function
AGL	Above Ground Level
AIR	Atmospheric Imaging Radar
ARRC	Advanced Radar Research Center
ARSR	Air Route Surveillance Radar
ASR	Air Surveillance Radar
ATC	Air Traffic Control
C-band	IEEE band classification for $\tilde{5}$ cm-wavelength
CAPE	Convective Available Potential Energy
CAPPI	Constant Altitude Plan Position Indicator
CI	Convective Initiation
CIN	Convective Inhibition
CPPAR	Cylindrical Polarimetric Phased Array Radar
CPU	Central Processing Unit
DFT	Discrete Fourier Transform
DPE	Dynamic Pipe Effect
EF	Enhanced Fujita Scale Indicator
FA	Firefly Algorithm
FAA	Federal Aviation Administration
FFD	Forward Flank Downdraft
GA	Genetic Algorithm
GPU	Graphics Processor Unit
HP	High Precipitation

IEEE	Institute of Electrical and Electronics Engineers
I/Q	In-Phased/Quadrature
Ka-band	IEEE band classification for $\tilde{7}.5$ mm-wavelength
KFDR	Frederick, OK WSR-88D Radar
KTLX	Twin Lakes, OK WSR-88D Radar
KOUN	Norman, OK WSR-88D Development Radar
L-band	IEEE band classification for $\tilde{3}0$ cm-wavelength
LCL	Lifted Condensation Level
LLJ	Low-Level Jet
LFM	Linear Frequency Modulation
LRR	Low Reflectivity Ribbon
MCS	Mesoscale Convective System
ML	Mixed Layer
MLW	Mainlobe Width
MMC	Moore Medical Center
MPAR	Multi-Function Phased Array Radar
NLFM	Nonlinear Frequency Modulation
NFR	Notional Functional Requirements
NWRT	National Weather Radar Testbed
NWS	National Weather Service
OFM	Optimized Frequency Modulation
OU	University of Oklahoma
PAIR	Polarimetric Atmospheric Imaging Radar
PAR	Phased Array Radar
PECAN	Plains Elevated Convection at Night
PRF	Pulse Repetition Frequency

PRT	Pulse Repetition Time
PSL	Peak Sidelobe Level
PSO	Particle Swarm Optimization
PX-1000	Polarimetric X-band 1000 Radar
RaXPol	Rapid X-band Polarimetric Radar
RF	Radio Frequency
RFGF	Rear Flank Gust Front
RFGFS	Rear Flank Gust Front Surge
RFD	Rear Flank Downdraft
RHI	Range Height Indicator
ROC	Radar Operations Center
ROF	Roll-off Factor
S-band	IEEE band classification for $\tilde{1}0$ cm-wavelength
SA	Simulated Annealing
SHV	Simultaneous Horizontal/Vertical Polarization
SNR	Signal-to-Noise Ratio
SSPA	Solid-State Power Amplifier
STALO	Stable Local Oscillator
TB	Time-Bandwidth
TDWR	Terminal Doppler Weather Radar
TDS	Tornadic Debris Signature
TFM	Time-Frequency Multiplexing
TOKC	Oklahoma City, OK TDWR Radar
TWT	Traveling Wave Tube
UTC	Universal Time Code
USA	United States of America

VAD	Velocity Azimuth Display
VCP	Volume Coverage Pattern
VORTEX	Verification of the Origins of Rotation in Tornadoes Experiment
VWP	Velocity Azimuth Display Wind Profile
WEH	Weak Echo Hole
WoF	Warn on Forecast
W-band	IEEE band classification for $\tilde{3}$ mm-wavelength
WSR-57	Weather Surveillance Radar-1957
WSR-74	Weather Surveillance Radar-1974
WSR-88D	Weather Surveillance Radar-1988 Doppler
X-band	IEEE band classification for $\tilde{3}$ cm-wavelength

Appendix B : List of Commonly Used Symbols

A_e	effective aperture, m^2
B	bandwidth, Hz
c	speed of light, m s^{-1}
D	drop diameter, mm
F	fitness function
g	antenna gain
h	height, m
$H(\omega)$	frequency response of a filter
I	isolation, dB
K_w	complex dieletric factor, unitless
l	losses, unitless
M	number of samples
M_I	number of independent samples
N	noise power, W
$N(D)$	dropsize distribution
n_o	noise output, W
P	power, W
r	range, m
$R(T_s)$	autocorrelation
S	signal power, W
$S(\omega)$	frequency response of a signal
s_D	Doppler-shifted signal
S_i	incident power, W m^{-2}
s_o	signal output, W

t	time, s
T_l	lag time, s
T_s	pulse repetition time, s
u	zonal component of flow, m s^{-1}
v	meridional component of flow, m s^{-1}
V	resolution volume, m^3
v_a	Nyquist velocity, m s^{-1}
v_i	radial velocity increase, m s^{-1}
v_r	radial velocity, m s^{-1}
r_a	maximum unambiguous range, km
w	waveform signal
W	spectrum width, m s^{-1}
Z	reflectivity factor, mm^6 m^{-3}
Z_{DR}	differential reflectivity, dB
Z_{HH}	horizontal reflectivity factor, dBZ
Δr	range resolution, m
Δv_r	differential radial velocity, m s^{-1}
ζ	vorticity, s^{-1}
η	reflectivity, m^{-1}
θ	one-way half-power beamwidth
λ	wavelength, m
ν	Doppler shift, Hz
ρ_{HV}	cross-correlation coefficient, unitless
σ	target cross-section, m^2
$\sigma_{\hat{S}}$	standard deviation of S, W
σ_v	variance of the velocity field (W), m s^{-1}

σ_z	standard deviation of Z, dBZ
τ	pulse width, s
ϕ_{DP}	differential phase, rad

Index